Electromagnetic Time Reversal: Theory, Application to Fault Location in Power Networks and Experimental Validation

Zhaoyang WANG

■ École
polytechnique
fédérale
de Lausanne

2020

Lost time is never found again.
— Benjamin Franklin

往者不可谏，来者犹可追。
—《论语·微子》

To my parents.

Acknowledgments

This research work would not have been presented here without the help and support of many people around me, to only some of whom it is possible to give a particular mention in what follows in this passage.

My deepest gratitude goes first and foremost to my thesis directors, Prof. Farhad Rachidi and Prof. Mario Paolone, for granting me this precious opportunity to pursue my Ph.D. research under their supervision. I will never forget their careful guidance and unwavering support. They have been an example to me not only for their deep knowledge and academic attainments but also for their kindness and integrity.

I would like to extend my sincere thanks to the members of my jury, Prof. Ali Abur, Prof. Carlo Alberto Nucci, Prof. Anja Skrivervik, and also to Prof. Drazen Dujic for accepting the presidency of the jury. I am inspired by their encouraging and insightful comments. I would like to further thank their estimable participation in my private defense when the world is fighting coronavirus pandemic.

This thesis was carried out within the frame of the Swiss Centre for Competence in Energy Research on the Future Swiss Electrical Infrastructure (SCCER-FURIES) and the Swiss Federal Office of Energy (SFOE) Energy Research Section. Their financial support is acknowledged.

I would like to take this occasion to address my heartfelt thanks to Prof. Yan-zhao Xie, the supervisor for my Master's study at Xi'an Jiaotong University, for his constant support and the trust he has placed in me.

I am grateful to Prof. Marcos Rubinstein for his time in discussions, revision of papers, and kind help. I also owe a debt of gratitude to Dr. Reza Razzaghi for his inspiration at the beginning of my Ph. D. research as well as for his support continuing to the present.

Several other people with whom I have had the honor to collaborate deserve my acknowledgment, in particular, Dr. Asia Codino from Sapienza University of Rome, Dr. Shao-yin He and Qi Li from Xi'an Jiaotong University, Dr. Hamidreza Karami from Bu-Ali Sina University as well as Dr. Mohammad Azadifar, Zhe Chen and Francesco Gerini from EPFL.

Special thanks go to Dr. Rachid Cherkaoui for his passionate enthusiasm and maintaining a friendly atmosphere in the building of ELL. I am grateful to Andrée Moinat, Eulalia Durussel, and Sophie Flynn for their constant availability and kindness. My warm thanks go to

i

Acknowledgments

Stéphane Burri, Sylvain Robert, and Jean-Michel Buemi for their considerable help in solving experimental and technical issues.

I would like to express my thanks to Dr. Nicolas Mora for his long-term support, in particular, for helping me in exploring my way to Switzerland. Dr. Asja Derviškadić and Dr. Andreas Kettner, I appreciate their valuable advice to me on drafting and defending this thesis.

I will always remember and treasure the memories of the precious time I have shared with all the friends and colleagues of EMC, DESL, and PWRS laboratories over the past years: Dr. Gaspard Lugrin, Dr. Jun Guo, Amirhossein Mostajabi, Antonio Sunjerga, Dr. Mostafa Nick, Dr. Enrica Scolari, Dr. Marco Pignati, Dr. Fabrizio Sossan, Dr. Lorenzo Reyes, Dr. Mokhtar Bozorg, Dr. Guglielmo Frigo, and Yi-hui Zuo. I may forget to mention some names, but please know that I am grateful.

Last but not least, I extend my deepest and eternal gratitude to my beloved parents for their dedication and for always giving me unconditional support and confidence.

Lausanne, August 27, 2020   Zhaoyang Wang

Abstract

Reliable and efficient fault location functionality is increasingly required by modern electric power systems to ensure both security and quality of supply of electricity. Recently, the *electromagnetic time reversal* (EMTR) technique has been introduced as a useful complement to traditional fault location methods, taking advantage of the *time reversal* inherent property of refocusing time-reversed signals (e.g., electromagnetic waves) back to their original source. At the same time, both theoretical and technical challenging questions remain to be addressed before EMTR can be used as a mature fault location technique in real-world applications. On the one hand, it is needed to experimentally assess the performance of the existing EMTR based methods in particular with reference to real power system environments. The experimental study should also give consideration to hardware design to bridge the gap between the EMTR theory and its power system implementation. One the other hand, theoretical investigations have to be followed up to serve the purpose of improving and optimizing the performance of EMTR applied to fault location with regard to the requirements of location accuracy, efficiency, and so forth.

Within this context, the thesis is focused on the study of the theory of EMTR and its application to fault location in power networks. The theoretical and experimental contributions of the present thesis can be summarized as follows.

The thesis first challenges the widely accepted understanding that a *closed time-reversal cavity* is a purely theoretical concept and that its experimental realization is impossible. In the thesis, a theoretical proof, supported by experiments, is presented to demonstrate that a time-reversal cavity for electromagnetic waves can be realized using a transmission-line network. In addition, the *distortion* or *interfering* effect associated with the so-called diverging wave is discussed and an active realization of a *time-reversal sink* is presented.

With regard to the classical EMTR based fault location, in which the medium in the backward-propagation stage is identical to that in the forward-propagation stage (in a sense, being described as *matched media*), the thesis first assesses the performance of EMTR along with the fault current signal energy metric with reference to full-scale experiments, considering a field experiment on an unenergized distribution line, and a pilot test in a live power grid. In

Abstract

this regard, this is the first time that EMTR is validated in a real power system environment. An embedded controller based fault location system is developed and employed in the live pilot test, integrating the functions of fault detection, data acquisition, time-reversal processing, electromagnetic transients simulations, and fault location. In addition, the thesis proposes a new metric for identifying the focusing point of the back-injected transients using the time-correlation property. A comprehensive time-frequency domain analysis is performed, proving a *similarity* characteristic contained in the classical (matched-media based) EMTR fault location process. A novel *cross-correlation* metric is proposed to quantitatively represent the similarity characteristic and thus to identify the location of a fault occurrence.

The thesis presents experimental evidence suggesting that the focusing property of EMTR remains intact when a moderate lumped *mismatch* between the forward- and backward-propagation media exists. The concept of EMTR in *mismatched media* is used and applied for the first time to locate faults in power networks. It is proposed to remove the transverse branch representing a fault from the power network in the backward stage. The modified backward-propagation medium is proved to satisfy different frequency- and time-domain properties, which characterize the fault location by three proposed criteria (*bounded phase*, *mirrored minimum squared modulus* and *mirrored minimum energy*). More importantly, the proposed EMTR methods based on the derived mismatched-media criteria require only one single simulation for the backward propagation, therefore, reducing significantly the computational burden of running multiple independent backward simulations as it is in the classical methods.

Keywords: Closed time-reversal cavity, cross-correlation, electromagnetic time reversal, electromagnetic transients, electromagnetic waves, fault location, fault location system, matched media, mismatched media, power networks, similarity, time-correlation, time reversal, time-reversal mirror, time-reversal sink, transmission lines.

Résumé

La localisation fiable et efficace des défauts est de plus en plus requise dans les systèmes électriques modernes pour garantir à la fois la sécurité et la qualité de l'énergie. Récemment, le retournement temporel électromagnétique (EMTR - *Electromagnetic Time Reversal*) a été introduit comme un complément utile aux méthodes traditionnelles de localisation des défauts, tirant parti de la propriété inhérente du retournement temporel de refocaliser les signaux inversés dans le temps (par exemple, les ondes électromagnétiques) vers leur source d'origine. En même temps, des questions théoriques et techniques restent à résoudre avant que la technique puisse être utilisée comme un moyen de localisation de défaut dans des applications réelles. D'une part, il est nécessaire d'évaluer expérimentalement les méthodes classiques du retournement temporel électromagnétique, en particulier dans un environnement réel du réseau électrique. L'étude expérimentale devrait également envisager une implémentation matérielle pour la mise en œuvre de cette technique dans un réseau électrique. D'autre part, des recherches théoriques approfondies doivent être poursuivies afin d'améliorer et d'optimiser les performances du retournement temporel appliqué à la localisation des défauts en ce qui concerne les exigences de précision de localisation, d'efficacité de détection, etc.

Dans ce contexte, cette thèse est centrée sur l'étude de la théorie du retournement temporel électromagnétique et son application à la localisation des défauts dans les réseaux électriques. Les contributions théoriques et expérimentales de la thèse peuvent être résumées comme suit.

La thèse remet d'abord en cause le fait largement admis qu'une cavité à retournement temporel est un concept purement théorique et que sa réalisation expérimentale est impossible. Une preuve théorique appuyée par des résultats expérimentaux est présentée pour démontrer qu'une cavité à retournement temporel pour les ondes électromagnétiques peut être réalisée en utilisant un réseau de lignes de transmission. De plus, l'effet de distorsion associé à l'onde divergente est discuté et une réalisation active d'un puits à retournement temporel (*time reversal sink*) est présentée.

En ce qui concerne les méthodes classiques du retournement temporel électromagnétique dans lequels le milieu dans la phase de rétro-propagation est identique à celui dans la phase

Résumé

de la propagation directe, la thèse évalue d'abord les performances de la méthode classique EMTR qui utilise comme métrique de refocalisation l'énergie du signal du courant de défaut. Deux expériences à grande échelle sont conduites, la première sur une ligne de distribution non alimentée, et la deuxième consistant en un essai pilote dans un réseau électrique sous tension. Ces expériences constituent pour la première fois une validation expérimentale de la méthode EMTR dans un environnement réel. Un système de localisation des défauts basé sur un contrôleur intégré est développé et utilisé dans l'essai pilote, intégrant la fonction de détection des défauts, l'implémentation de l'algorithme du retournement temporel, ainsi que les simulations de transitoires électromagnétiques et la localisation des défauts. De plus, la thèse propose une nouvelle métrique pour identifier le point de focalisation des signaux rétro-injectés en utilisant la propriété de corrélation temporelle. Une analyse complète dans les domaines temporel et fréquentiel est effectuée, prouvant une caractéristique de similitude dans la procédure classique de localisation des défauts en utilisant EMTR. Une nouvelle métrique de corrélation croisée est proposée pour représenter quantitativement cette caractéristique de similitude et ainsi identifier l'emplacement du défaut.

La thèse présente également une expérience démontrant que la propriété de focalisation du retournement temporel électromagnétique reste intacte en cas de discordance modérée entre les milieux de propagation direct et inverse. Le concept du retournement temporel dans des milieux discordants (*mismatched media*) est utilisé et appliqué pour la première fois pour localiser les défauts dans les réseaux électriques. Il est en effet proposé de supprimer la branche transversale représentant le défaut du réseau électrique dans la phase de rétro-propagation. Il est démontré que le milieu de propagation ainsi modifié satisfait différentes propriétés dans les domaines temporel et fréquentiel, qui permettent d'identifier l'emplacement du défaut selon trois critères proposés. Plus important encore, les algorithmes de retournement temporel proposés basés sur les critères développés ne nécessitent qu'une seule simulation dans la phase de la rétro-propagation, réduisant ainsi considérablement le temps de calcul par rapport aux méthodes classiques, qui elles nécessitent l'exécution de plusieurs simulations.

Mots-clés : cavité à retournement temporel, corrélation croisée, retournement temporel électromagnétique, transitoires électromagnétiques, ondes électromagnétiques, localisation des défauts, système de localisation des défauts, milieux discordants, réseaux électriques, similitude, corrélation temporelle, miroir à retournement temporel, puits à retournement temporel, ligne de transmission.

Contents

Contents

Contents

List of Figures

List of Tables

1 Introduction

1.1 Context and Motivations

Power transmission and distribution grids, which evolve growing size and feature increasing complexity, are subject to various types of faults or failures of their components due to either technical or weather-related causes. Furthermore, power networks are going through a fast-changing evolution that is particularly reflected in the extensive use of smart grids technologies, which is needed to accommodate an increasing number of decentralized and intermittent generation units being widely integrated into the existing power networks. Power systems will certainly benefit from this development but, at the same time, they will require a higher level of reliability and resilience. Given this fact, fault location functionality with convincing performances in terms of response time, location accuracy as well as robustness against faults of diverse natures (e.g., fault types), uncertainties (e.g., in respect to line parameters), and measurement deficiency, is of paramount importance in present and future power systems.

Great effort has been directed to develop various strategies and techniques to address the fault location problem for transmission and distribution power networks, resulting in two major categories of fault location methods based on either *i)* analyzing fundamental-frequency voltages and currents, mainly using impedance measurement, or *ii)* analyzing fault-originated traveling waves (either voltages or currents). However, in spite of the availability of a considerable amount of literature, which reports unceasing progress in this field, the problem of fault location still represents a challenge for both categories of methods. Generally, the fault location performance of these methods, in particular location accuracy, can be affected by different factors, such as load-flow unbalance, presence of shunt reactors or series capacitors, presence of dispersed generation, topological complexity and inhomogeneity of power networks, fault characteristics (e.g., fault type and fault impedance), and so forth. The fault location performance can be also negatively affected by insufficient and inaccurate measurements. Very recently, starting from the 2010s, *electromagnetic time reversal* has been applied to the problem of fault location with promising results.

Electromagnetic time reversal refers to the *time reversal* theory applied to the field of electromagnetism. Most laws of nature, including those of electromagnetism, are invariant under the time-reversal operation. Even though time-reversal invariance was a known concept for a century or so, its engineering applications began only in the 1990s with Fink and his co-workers who first theoretically and experimentally studied time reversal in the field of acoustics and, later, in electromagnetism. By proposing the fundamental concept of a *closed time-reversal cavity*, Fink et al. presented time reversal as a powerful approach of refocusing time-reversed signals (e.g., acoustic or electromagnetic waves) to the original source in a propagative medium, which can be inhomogeneous. Moreover, illustrating the focusing property by a *time-reversal mirror* leads time reversal to emerge as a promising technique in source-location identification and find potential applications in various fields of engineering, including the fault location in power systems.

Taking advantage of the time-reversal invariance of the telegrapher's equations governing wave propagation along transmission lines, electromagnetic time reversal has been applied to the fault location problem since 2012. Although the fault location methods relying on electromagnetic time reversal belong to the traveling-wave based methodology, it has been shown that electromagnetic time reversal is characterized by a superior performance with respect to the existing methods in terms of accuracy, applicability as well as robustness against uncertainties and faults of diverse natures. More importantly, electromagnetic time reversal has the unique feature of being able to locate faults using a single observation point (generally located at the secondary winding of a substation transformer), even for power networks that are characterized by inhomogeneity as well as multiple branches/nodes. On the other hand, electromagnetic time reversal is still an emerging technique in fault location, thus requiring a continuing study on its theoretical foundations as well as advancing it towards a mature application in power systems.

Within this context, the thesis is focused on an in-depth study on the theory of electromagnetic time reversal and its application to fault location in power networks.

In regard to the theory of electromagnetic time reversal, the thesis demonstrates the possibility of realizing a *closed time-reversal cavity* for electromagnetic waves in transmission-line networks, challenging the widely accepted understanding that an exact experimental realization of a time-reversal cavity is impossible. In addition, the thesis proposes to study the focusing property of electromagnetic time reversal in a scattering medium, particularly considering a moderate lumped *mismatch* between the media respectively in the forward- and backward-propagation stages.

The existing electromagnetic time reversal based fault location methods are generally named classical or *matched-media* based methods, in the sense that the two media in the forward- and backward-propagation stages are identical (i.e., matched). The thesis proposes to make use of real power system environments to experimentally assess the performance of classical EMTR methods. Moreover, the thesis discusses an extended use of the underlying *time-correlation*

property in matched media to formulate alternative properties and methods to characterize the location of a fault occurrence.

Addressing the challenge of enhancing matched-media based methods with special attention to improving computation efficiency, the thesis discusses the possibility of illustrating the concept of *mismatched media* in the fault location problem. In particular, it is proposed to consider a modified power network topology in the backward stage representing a lumped mismatch between the media in the fault occurrence stage (i.e., forward stage) and in the fault location stage (i.e., backward stage).

1.2 Thesis Outline

The Thesis is organized as follows.

Chapter 2 first introduces the theoretical basis and classical applications of the time-reversal technique, with special attention to time reversal in electromagnetism. The state-of-the-art in fault detection and location in power systems is presented, including the existing electromagnetic time reversal based fault location methods.

Chapter 3 reports, for the first time, the experimental realization of a *closed time-reversal cavity*. A time-reversal cavity for electromagnetic waves is first discussed. Then, general consideration for realizing a time-reversal cavity in transmission-line networks is given. A Y-shaped inhomogeneous coaxial-cable network is proposed to illustrate the concept. The solutions of the wave equations, which physically describe the time-reversal forward- and backward-propagation processes in the Y-shaped cable network, are derived. Next, the behavior of the proposed time-reversal cavity is numerically and experimentally inferred. The so-called *interfering* (or *distortion*) effect caused by the diverging waves in the backward stage are discussed. An active realization of a *time-reversal sink* is proposed and experimentally realized to effectively overcome such interfering effect.

Chapter 4 presents experimental studies on classical electromagnetic time reversal (*matched-media* based) fault location techniques, with special attention to the method using the fault current signal energy metric. A field experiment and a pilot test are presented, validating the fault current signal energy metric in real power environments and especially evaluating its fault location performance with respect to realistic faults of diverse natures, such as fault types and fault impedance. The chapter also presents the development of a fault location system addressing the technical challenge of efficiently implementing electromagnetic time reversal based fault location methods in power systems by a suitable hardware platform coupled with a proper sensing and triggering unit.

Chapter 5 devotes attention to extending the classical electromagnetic time reversal methods through an alternative use of the *time-correlation* property. An integrated time-frequency domain analysis is first presented to prove a *similarity* characteristic existing in the matched-

media based fault location procedure. A novel fault location metric is proposed, calculating the *cross-correlation* between the back-injected time-reversed transient signal and the simulated fault current signal to quantify the level of the time-domain similarity and to identify the fault location. The similarity property and the fault location performance of the proposed cross-correlation metric are validated first through simulation case studies and then using experimentally acquired fault-originated transients in response to various realistic fault events in a live distribution feeder.

Chapter 6 presents two aspects of research associated with electromagnetic time reversal in *mismatched* or *changing media*. First, the electromagnetic time reversal focusing property in lumped mismatched-media is experimentally studied using a dielectric-rod set-up. Next, the concept of electromagnetic time reversal in mismatched media is illustrated with respect to locating faults in power networks. The thesis proposes to consider a modified boundary condition at the fault location, or more specifically to eliminate the need for reproducing a fault event in the backward stage. The thesis mathematically formulates and validates several mismatched-media based properties, which are respectively denominated as *bounded phase*, *mirrored minimum squared modulus*, and *mirrored minimum energy*, allowing the identification of the fault location using a single run of the backward-propagation simulation.

Chapter 7 summarizes the main findings of the present studies and future perspectives.

2 Electromagnetic Time Reversal and Its Fault Location Application in Power Networks

Time reversal constitutes a cornerstone of a range of topics in physics. The earliest introduction of time reversal in literature might date back to 1957, in which B. Bogert experimentally demonstrates the capability of time reversal to correct the delay distortion in slow-speed television and signature transmission [1]. Indeed, the broad acknowledgment of the concept of time reversal arises from its related techniques being extensively applied in various fields of engineering. It includes the recent efforts applying time reversal to fault location in power systems.

This chapter first introduces the theoretical basis and classical applications of the time-reversal technique, with special attention given to time reversal in electromagnetism. Meanwhile, the state of the art in fault detection and location in power systems, including the existing electromagnetic time reversal based fault location techniques, is discussed.

2.1 Time-Reversal Theory

2.1.1 Time reversal and time-reversal invariance

The concept of *time reversal* can be interpreted from different perspectives, while the involved basic data-processing consists of reversing in time a given time-dependent physical quantity $s(t)$ according to the operation

$$s(t) \overset{\text{TR}}{\longmapsto} s(-t). \tag{2.1}$$

It is implied that $s(t)$ is a causal function in the sense that it is defined on a finite time interval T_s such that

$$s(t) = 0, \quad (t < 0, \text{ and } t > T_s). \tag{2.2}$$

The time-domain operation of reversing the chronological sequence of $s(t)$ corresponds to the complex conjugate operation (denoted by the symbol $*$) in the frequency domain:

$$S(j\omega) \overset{\text{TR}}{\longmapsto} \left[s(j\omega) \right]^*, \tag{2.3}$$

where $S(j\omega)$ is the Fourier transform of $s(t)$.

Note that, to ensure causality, the time-reversal operation in the time domain is more practically realized by

$$s(t) \overset{\text{TR}}{\longmapsto} s(T - t), \tag{2.4}$$

with T being the time window over which $s(t)$ is observed. It is satisfied that

$$T \geqslant T_s. \tag{2.5}$$

Another underlying concept of *time-reversal invariance* is discussed in parallel with the operation of time reversal. It is found that the time-reversal invariance is readily described and universally embodied in most laws of nature, either in a strict or in a soft sense [2].

With reference to a given physical system wherein $s(t)$ evolves, it is assumed that the behavior of $s(t)$ can be described by certain underlying equations, which describe system governing laws, such as the wave equations for acoustic or electromagnetic waves. The condition of time-reversal invariance in the strict sense can be stated as follows [2].

Definition 1 Strict time-reversal invariance condition

A system is time-reversal invariant with respect to a physical quantity (i.e., system state variable) in the strict sense if, given a solution $s(t)$ to its underlying equations, the time-reversed function

$$g(t) = s(-t) \tag{2.6}$$

is also a solution.

Let us consider, for example, the scalar acoustic pressure field $p(\boldsymbol{r}, t)$ propagating in the transient regime (at an arbitrary location $\boldsymbol{r}$) in free space, which satisfies the wave equation [3, 4]:

$$\left(\nabla^2 - \frac{1}{c^2}\frac{\partial^2}{\partial t^2}\right)p(\boldsymbol{r}, t) = 0, \tag{2.7}$$

where ∇^2 is the Laplace operator and c the sound speed.

It can be observed that the wave equation contains a second-order derivative operator with respect to time t. As an immediate consequence, if $p(\boldsymbol{r}, t)$ is a solution of the wave equation, then the time-reversed function $p(\boldsymbol{r}, -t)$ also satisfies the wave equation. In this respect, the acoustic wave propagation in free space (or in a lossless medium) is time-reversal invariant.

Some physical laws do not satisfy the strict time-reversal invariance but they do satisfy the so-called soft time-reversal invariance, which can be defined as follows [2].

Definition 2   Soft time-reversal invariance condition

A system is time-reversal invariant with respect to a physical quantity (i.e., system state variable) in the soft sense if, given a solution $s(t)$ to its underlying equations, the time-reversed function after certain physically-valid operations (denoted by $f[\cdot]$) as

$$h(t) = f[s(-t)] \tag{2.8}$$

is also a solution.

The basic equations of electromagnetism appear to be time-reversal invariant in the soft sense. This will be interpreted in the later sections.

2.1.2   Time-reversal focusing properties

Time reversal is an established concept in physics. Its popularization in contemporary scientific communities is largely owing to the comprehensive theoretical and experimental study on the time-reversal inherent focusing property, which has lead to the concept of a *closed time-reversal cavity* proposed by Fink et al. in the early 1990s [3, 5, 6, 7]. Such a concept interprets the principle of time-reversed (acoustic) waves refocusing on their original source and further underlies the subsequent engineering applications in various fields.

As discussed earlier, the propagation behavior of acoustic waves features the time-reversal invariance in the strict sense. Thus, for acoustic waves generated by a point source and possibly reflected, scattered and distorted in a propagative medium, the focusing property states that the time-reversed waves being back injected retrace the paths that the waves have followed in the forward-propagation stage and eventually converge in synchrony on the original source location as if time goes backwards.

Chapter 2. Electromagnetic Time Reversal and Its Fault Location Application in Power Networks

A time-reversal cavity is proposed as a two-step procedure to achieve the focusing property [3, 6]. As illustrated in Fig. 2.1, a closed surface in three dimensions (3D) is assumed to enclose a point-like source and its surrounding medium, which can be inhomogeneous. In the forward-propagation stage (also named recording step [3], see Fig. 2.1a), the source generated and distorted (by the surrounding inhomogeneous medium) waves are recorded by an infinite number of elementary transducers located on the imaginary surface of the cavity. In the backward-propagation stage (also named reconstructing step [3], see Fig. 2.1b), those recorded waves are time reversed and back injected to propagate inward from the respective elementary transducers at the cavity surface, finally converging at the source location.

(a)   (b)
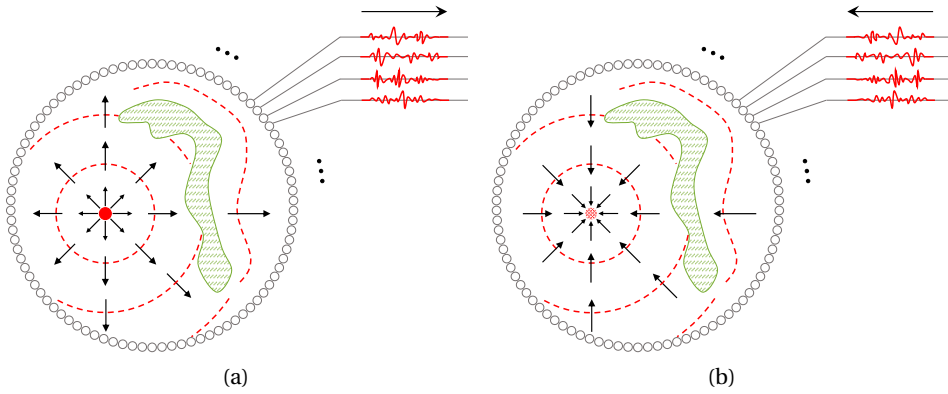
Figure 2.1 – Two-dimensional illustration to a time-reversal cavity for (a) forward-propagation stage: recording step and (b) backward-propagation stage: reconstructing step (adopted from [3]).

It can be noticed that a time-reversal cavity is a conceptual description that appears difficult to be implemented, since it is not feasible to fully cover a source in three dimensions and to record each one of the propagated wavefronts at the closed cavity surface. In practice, a time-reversal cavity is alternatively realized by means of a one-dimensional (1-D) or two-dimensional (2-D) transducer array, namely the so-called a *time-reversal mirror* (e.g., [3, 8, 9]), as schematically described in Fig. 2.2. A time-reversal mirror makes use of a limited number of transducers, which are arranged at one side of the source. It is shown that proper spatial distribution of the transducers on a limited angular aperture to sample sufficient wavefronts renders the time-reversal focusing property achievable.

The focusing property of time reversal has lead to extensive research continuing to today on time-reversal theory and its application in various fields of physics including acoustics, optics, and so forth [10, 11].

The initial series of studies (e.g., [3, 6, 8, 9, 12, 13]) investigated the time-reversal mirror as a realistically-attainable measure to realize the time-reversal focusing property. The follow-up research was oriented towards illustrating the efficiency of the concept, drawing considerable attention to investigating its performance in complex media (e.g., inhomogeneity). It has been
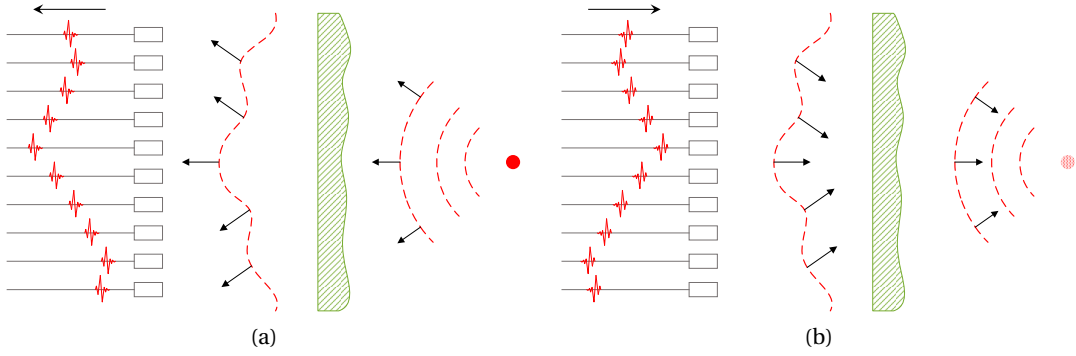
Figure 2.2 – Illustration to a time-reversal mirror for (a) forward-propagation stage: recording step and (b) backward-propagation stage: reconstructing step (adopted from [3]).

shown that an increasing number of propagative paths, which results from the presence of multiple reflection, refraction, and scattering (e.g., [14, 15, 16, 17, 18, 19]), allows reducing the size of the time-reversal mirror (i.e., a small physical aperture size or a reduced number of transducers) to refocus the backward-propagated waves to the source and being able to further demonstrate achieving the super resolution (in terms of focal spot size), in a sense, over the Rayleigh limit [20, 21, 22, 23, 24].

Moreover, in spite of the impressive efficiency of the time-reversal mirror, Draeger et al. further demonstrated that, in a special scenario of a closed reflecting boundary, the time-reversal focusing property can be achieved by a time-reversal mirror merely composed of a single transducer [25, 26, 27].

Time reversal also has been proven to be effective in selectively focusing on multiple targets and in multiple signal classification. The time-reversal operator decomposition (DORT) method, based on the theory of an iterative time-reversal mirror (e.g., [13]), analyzes eigenmodes of a diagonalized time-reversal operator to detect and identify multiple well-resolved targets (or scatterings) of different reflectivity [28, 29, 30, 31]. Devaney et al. later developed another group of matrix formalism methods named time-reversal imaging with multiple signal classification (TR-MUSIC) [32, 33, 34, 35, 36, 37]. As similar to the DORT method, TR-MUSIC based techniques are designed to image a medium, either homogeneous or inhomogeneous, wherein M targets are embedded, employing $N(> M)$ active transducers. TR-MUSIC appears to be an effective solution to resolving closely spaced targets or realizing selective detection and focusing on the reflectors with unknown or similar reflective characteristics.

In the wake of the theoretical and experimental studies, time reversal has also become a mature engineering technique with unprecedented performance compared to traditional ones. The representative applications belong to

i) biomedicine (e.g., [38, 39, 40, 41, 42]),

ii) geophysics (e.g., [43, 44, 45, 46, 47, 48]), and

iii) electromagnetism.

The theory of time reversal in electromagnetism and associated applications are briefly presented in the next section.

2.1.3   Electromagnetic time reversal

After the foundation studies in the field of acoustics, time reversal was later introduced into electromagnetism (e.g., [2, 49, 50, 51, 52, 53]), under the general denomination of electromagnetic time reversal (EMTR).

Let us now recall Maxwell's equations and examine their time reversibility. There are [54]

$$\nabla \times \boldsymbol{E}(\boldsymbol{r}, t) = -\mu(\boldsymbol{r}) \frac{\partial \boldsymbol{H}(\boldsymbol{r}, t)}{\partial t}, \tag{2.9}$$

$$\nabla \times \boldsymbol{H}(\boldsymbol{r}, t) = \epsilon(\boldsymbol{r}) \frac{\partial \boldsymbol{E}(\boldsymbol{r}, t)}{\partial t} + \boldsymbol{J}(\boldsymbol{r}, t), \tag{2.10}$$

$$\nabla \cdot \big[\epsilon(\boldsymbol{r}) \boldsymbol{E}(\boldsymbol{r}, t)\big] = \rho(\boldsymbol{r}, t), \tag{2.11}$$

$$\nabla \cdot \big[\mu(\boldsymbol{r}) \boldsymbol{H}(\boldsymbol{r}, t)\big] = 0, \tag{2.12}$$

where $\boldsymbol{E}(\boldsymbol{r}, t)$ and $\boldsymbol{H}(\boldsymbol{r}, t)$ are the electric and the magnetic fields, respectively. $\mu(\boldsymbol{r})$ and $\epsilon(\boldsymbol{r})$ are the magnetic permeability and the electric permittivity, respectively. $\boldsymbol{J}(\boldsymbol{r}, t)$ is the electric current density. $\rho(\boldsymbol{r})$ is the charge density.

Assuming that $\boldsymbol{E}(\boldsymbol{r}, t)$ and $\boldsymbol{H}(\boldsymbol{r}, t)$ represent the solutions to the electric and magnetic fields, the time-reversed functions appear to be $\boldsymbol{E}(\boldsymbol{r}, -t)$ and $\boldsymbol{H}(\boldsymbol{r}, -t)$, respectively. Maxwell's equations for the time-reversed functions read

$$\nabla \times \boldsymbol{E}(\boldsymbol{r}, -t) = \mu(\boldsymbol{r}) \frac{\partial \boldsymbol{H}(\boldsymbol{r}, -t)}{\partial (-t)}, \tag{2.13}$$

$$\nabla \times \boldsymbol{H}(\boldsymbol{r}, -t) = -\epsilon(\boldsymbol{r}) \frac{\partial \boldsymbol{E}(\boldsymbol{r}, -t)}{\partial (-t)} + \boldsymbol{J}(\boldsymbol{r}, -t), \tag{2.14}$$

$$\nabla \cdot \big[\epsilon(\boldsymbol{r}) \boldsymbol{E}(\boldsymbol{r}, -t)\big] = \rho(\boldsymbol{r}, -t), \tag{2.15}$$

$$\nabla \cdot \big[\mu(\boldsymbol{r}) \boldsymbol{H}(\boldsymbol{r}, -t)\big] = 0, \tag{2.16}$$

Maxwell's equations are different from the foregoing acoustic wave equation in the sense that the behavior of the electric and the magnetic fields is not simply regulated by a second-order time derivative operation. It is clear that the equations (2.13) and (2.14) are not readily time-reversal invariant. However, it is physically valid that, under time reversal, the sign of the charge velocity should be changed. Consequently, the associated current density should change its sign as well. Moreover, the magnetic field $\boldsymbol{H}(\boldsymbol{r}, t)$ should see a change of sign as a

result of the sign change of the current density. To sum up, the following transformations are required to make Maxwell's equations time-reversal invariant in the soft sense: [2, 55, 56]

$$\rho(\boldsymbol{r},\,t) \stackrel{\mathrm{TR}}{\longmapsto} \rho(\boldsymbol{r},\,-t)\,, \tag{2.17}$$

$$\boldsymbol{E}(\boldsymbol{r},\,t) \stackrel{\mathrm{TR}}{\longmapsto} \boldsymbol{E}(\boldsymbol{r},\,-t)\,, \tag{2.18}$$

$$\boldsymbol{J}(\boldsymbol{r},\,t) \stackrel{\mathrm{TR}}{\longmapsto} -\boldsymbol{J}(\boldsymbol{r},\,-t)\,, \tag{2.19}$$

$$\boldsymbol{H}(\boldsymbol{r},\,t) \stackrel{\mathrm{TR}}{\longmapsto} -\boldsymbol{H}(\boldsymbol{r},\,-t)\,. \tag{2.20}$$

Electromagnetic time reversal, making use of the focusing property of electromagnetic waves, has emerged as a very promising technique in various applications including

i)   focusing and amplification of electromagnetic waves (e.g., [49, 57]),
ii)   medical imaging (e.g., [58, 59, 60]),
iii) target detection and location (e.g., [61, 62, 63]),
iv)   communications (e.g., [64, 65]),
v)   EMC testing (e.g., [66, 67]),
vi)   soft fault location (e.g., [68, 69, 70, 71, 72]),
vii) lightning discharge location (e.g., [73, 74, 75, 76]), and
viii) lightning-originated flashover location (e.g., [77, 78]).

Recently, electromagnetic time reversal has also been successfully applied to address the fault detection and location problem in power systems [79, 80, 81, 82, 83, 84, 85, 86, 87]. The principle and methods are detailed in the following section.

2.2   Fault Location in Power Networks

2.2.1   Introduction

Electric power transmission and distribution networks are prone to a range of faults, which are initiated by weather-related causes including lightning, storms, freezing rain, etc. as well as by unintentional contact to power lines by falling or flying objects, such as trees or animals [88, 89]. In addition to the foregoing natural factors, power networks are also subject to faults as a result of technical failures, such as insulation deterioration or breakdown [88, 89]. Those various occurrence mechanisms result in power system faults being of diverse natures, which include fault impedance, fault inception angle, fault type, and so forth.

Within this context, a reliable and efficient fault detection and location functionality is increasingly emphasized in power system operation to ensure the security and quality of power supply [88, 89, 90, 91, 92, 93].

Chapter 2. Electromagnetic Time Reversal and Its Fault Location Application in Power Networks

In power transmission grids, facing its expanding size, fault location functionality is expected to provide a fast response in terms of identifying the faulty line sections and indicating the most-likely fault location with reasonable accuracy. In this respect, fault location is of fundamental importance in expediting fault clearance and restoration of a secure grid topology and eventually preventing severe cascading consequences. On the other hand, with reference to power distribution networks, its inherent complexity (e.g., with respect to topology or load condition), together with the increasing integration of distribution generators, calls for fault location to be a reliable and accurate process coping with frequent occurrences of faults of varied natures. In comparison, fault location functionality in distribution networks is more associated with power quality, for example, to accelerate power restoration and minimize the duration of power supply interruptions.

The procedures realizing the power system fault location functionality are collectively named *fault location methods* or *techniques*. To sum up, power system operation requires fault location methods to address the challenges mainly including:

i) *Accuracy.* It refers to the capability of pinpointing the exact fault location or identifying the faulty lines and the true fault location with user-accepted accuracy. Different factors can influence fault location accuracy, like inaccuracy and uncertainty of line parameters, presence of non-linear components (e.g., series capacitor), load-flow unbalance, insufficient accuracy of numerical models, and so forth. The capacity is also limited by errors and insufficiency in measurements.

ii) *Efficiency.* The time used to implement the fault location functionality should be directly linked to the allowed power grid restoration time. The time constraint for fault location is generally longer than that for fault protection for the needs of achieving a higher location accuracy, which might rely on time-consuming processing. Even though, a prompt fault response, namely a shorter time delay between a fault occurrence and the realization of the fault location functionality, is always desired.

iii) *Robustness.* This feature evaluates the applicability of a fault location method in transmission and distribution networks with reference to different degrees of topological complexity and inhomogeneity. It also assesses the fault location performance of a method with respect to uncertainties (e.g., in terms of line parameters and models), measurement introduced error, fault type, fault impedance, and so forth.

iv) *Feasibility.* This feature evaluates a fault location method from the viewpoint of power system practice, taking account of whether the method can be deployed into existing protection relays or requires stand-alone fault locators as well as whether it demands off-line programs to conduct a post-fault analysis. Besides, fault location methods based on relatively-high measurement bandwidth, sophisticated data processing or time alignment (e.g., by means of GPS) might increase the application complexity.

2.2.2 Fault location methods

In order to address the fault location problem in power systems, a considerable number of researchers have devoted great effort to fault location methods since the 1950s [94]. Consequently, various procedures for fault location assessment have been proposed for both transmission and distribution power networks and, in this respect, three main categories can be identified as [88]

i) impedance and fundamental-frequency component based methods,
ii) traveling wave and high-frequency component based methods, and
iii) knowledge based methods.

1) *Impedance and fundamental-frequency component based methods*

The first category of fault location methods is based on the measurement of the power system fundamental-frequency voltages and/or currents at power network terminal(s). The faulty line impedance is calculated as a measure of the distance between the measurement end(s) and the fault location.

Methods belonging to the first category can be further classified in accordance with the number of employed measurement ends (terminals):

a) single-end measurement methods (e.g., [95, 96, 97, 98, 99, 100, 101]),
b) double-end measurement methods (e.g., [102, 103, 104, 105, 106, 107, 108, 109, 110]),
c) multi-end measurement methods (e.g., [111, 112, 113, 114, 115, 116, 117, 118]).

Note that the double- and multi-end measurements for the methods of sub-categories *b*) and *c*) can be either synchronized (e.g., [106, 107, 108, 109, 110, 112, 113, 114, 115, 116]) or unsynchronized based (e.g., [102, 103, 104, 105, 111, 117]).

In comparison, the single-end measurement based methods bring the advantages of less-complexity of algorithms as well as lower cost of data collection. However, the location accuracy of these methods can be degraded by the single or combined effect of fault impedance, sensitive loads, inhomogeneity of power networks as well as the factors related to measurement uncertainties [88, 89]. The double- and multi-end measurement based methods are developed with the purpose of enhancing the fault location performance of the methods belonging to the first sub-category. The use of data acquisition (either synchronized or unsynchronized) and communication exchange among multiple ends, to a great extent, overcomes the foregoing negative effect and, therefore, improves the fault location accuracy.

Given the above-mentioned factors, higher fault location accuracy yielded by the impedance-based methods depends on the availability of double- and multi-end measurements. This would come at the expense of increasing technical and economic complexity. Meanwhile, the reliability of those methods is closely related to the accuracy and the stability of measurement blocks, particularly communication links and common time references. Last but not least, with

special reference to active distribution networks (ADNs), the applicability of those methods remains challenging. For instance, nodal infeed from dispersed energy resources (DERs) connected to medium voltage networks induces error in estimating the fault distance [89, 119].

2) *Traveling wave and high-frequency component based methods*

Traveling wave-based methods analyze the transient voltage (and/or current) waves along a faulty power network [120, 121, 122, 123, 124]. In contrast to the former category of fundamental-frequency component based methods, traveling wave-based methods extract the high-frequency components of the fault-originated transient signals. The time-domain and/or the frequency-domain features of the high-frequency components are investigated to infer the location of a fault occurrence [125, 126]. For instance, one of the earlier applications analyzed the cross-correlation between the incident and reflected traveling waves [120].

The traveling wave-based fault location methods are generally considered to be accurate meanwhile insensitive to fault type and fault impedance [88]. More importantly, since this category of methods uses the high-frequency components of the fault-originated transient voltages/currents, it is immune to power-frequency phenomena (e.g., current transformer saturation), and thus, less influenced by the power–frequency injections of dispersed energy resources (DERs) [88, 127].

According to the number of utilized measurement ends, these methods can be classified into the sub-categories as:

a) single-end measurement methods (e.g., [125, 126, 128, 129]), and
b) double-/multi-end measurement methods (e.g., [130, 131, 132, 133, 134, 135, 136]).

The underlying principle of traveling wave-based methods consists of detecting wavefronts and identifying the respective arrival instants at power network terminal(s) [88]. For single-end measurement based methods, the arrival instants of the initial wavefront and the subsequent ones are determined at one single end of a power network. The first-arriving wavefront corresponds to the traveling wave originated by the fault itself. The delay between the first wavefront and the subsequent reflected ones can be used to identify the distance between the measurement end and the fault location [128, 129]. With regard to double-end measurement based methods, the difference in the times of arrival of the traveling waves at the two terminals is used to determine the fault location. In this case, the measurement using a common time reference is assumed [130, 137]. Some newly-developed methods appear to be effective using two-terminal unsynchronized data (e.g., [131, 132, 133, 134, 135]), rendering the implementation straightforward and less costly.

The fault location performance of traveling wave-based methods heavily relies on detecting and distinguishing the wavefront originated by the fault from the reflected ones associated with the fault location or/and power network terminals and junctions. The location accuracy can be limited by

a) insufficient sampling rate,

b) insufficient measurement bandwidth,

c) uncertainties in power network characteristics (e.g., line parameters), and

d) imprecision of time stamping or loss of time alignment for those based on synchronized measurement.

In addition to the aforementioned affecting factors, in some particular cases of

a) a fault with an inception angle close to zero degree and

b) a close-up fault,

the traveling-wave based methods appear to be less effective in interpreting fault information due to the difficulties in detecting fault-originated traveling waves as well as in separating the wavefronts that overlap each other.

Coping with these limitations, wavelet transform (WT) among the traveling-wave methodology emerges as a powerful tool of transient analysis in power systems [123, 127, 138, 139, 140, 141]. The attractive feature of wavelet transform in processing fault-originated traveling waves is the adaptive adjustment of the time-window length according to the temporal duration or frequency content of the transients under study [123, 125, 127, 142, 143, 144]. This way, more accurate identification of the arrival instants of the initial and reflected wavefronts can be achieved. In comparison, the continuous wavelet transform (CWT) based fault location method is considered to be more efficient in providing detailed fault information since it smoothly shifts the analyzed wavelet over the full domain of the fault-originated transients rather than the shift in the dyadic grids in the discrete wavelet transform (DWT) based analysis. Meanwhile, in virtue of the capability of wavelet transform integrated time-frequency analysis, traveling-wave based fault location can be straightforwardly carried out in the frequency domain, avoiding the problem of identifying and differentiating successive wavefronts and respective arriving instants [125]. The main limitation associated with the wavelet transform based methods is about computation complexity and requirement of large measurement bandwidth. Moreover, the fault location performance is also dependent on the selection of the mother wavelet or the construction of specific ones using the attributes of fault-originated transients [127].

3) Knowledge based methods

With the recent remarkable progress in computer science, the knowledge-based fault location methods have become an alternative to the previous two categories of traditional techniques. These methods can be grouped into:

a) artificial intelligence based methods (e.g., [145, 146, 147]),

b) statistical analysis based methods (e.g., [148, 149]), and

c) hybrid methods (e.g., [150, 151, 152]).

Chapter 2. Electromagnetic Time Reversal and Its Fault Location Application in Power Networks

The artificial intelligence-based methods apply techniques mainly including artificial neural networks (ANNs), fuzzy logic (FL), expert systems (ES) and genetic algorithm (AE). In some methods, the fault location is identified by matching measured data with historically accumulated ones. Studies suggest that hybrid methods, which use a combination of different types of algorithms, allow a more accurate estimation of the fault location. The knowledge-based methods still progress in parallel with the continuing study of the conventional impedance- and traveling wave-based fault location techniques.

2.2.3   Electromagnetic time reversal application to fault location

Before addressing the fault location in power networks, we first discuss the voltage/current wave behavior under the time-reversal operation. Assuming the line longitudinal coordinate as x, the voltage and current wave vectors for multi-conductor transmission lines, such as three-phase systems, are denoted by $V(x, t)$ and $I(x, t)$, respectively. We make reference to the multi-conductor transmission-line equations [153]:

$$\frac{\partial^2}{\partial x^2} V(x, t) - \left[R'G' \right] V(x, t) - \left[R'C' + L'G' \right] \frac{\partial}{\partial t} V(x, t) - \left[L'C' \right] \frac{\partial^2}{\partial t^2} V(x, t) = \mathbf{0}, \qquad (2.21)$$

$$\frac{\partial^2}{\partial x^2} I(x, t) - \left[G'R' \right] I(x, t) - \left[C'R' + G'L' \right] \frac{\partial}{\partial t} I(x, t) - \left[C'L' \right] \frac{\partial^2}{\partial t^2} I(x, t) = \mathbf{0}, \qquad (2.22)$$

where R', G', L' and C' are the per-unit-length matrices of resistance, conductance, inductance and capacitance, respectively.

It is clear that the multi-conductor transmission-line equations do not satisfy the time-reversal invariance, because of the existence of the first-order partial derivative with respect to temporal variable t. However, by assuming that the lines are lossless with $R' = \mathbf{0}$ and $G' = \mathbf{0}$, it can be readily shown that the equations are time-reversal invariant, namely

$$\frac{\partial^2}{\partial x^2} V(x, -t) - \left[L'C' \right] \frac{\partial^2}{\partial t^2} V(x, -t) = \mathbf{0}, \qquad (2.23)$$

$$\frac{\partial^2}{\partial x^2} I(x, -t) - \left[C'L' \right] \frac{\partial^2}{\partial t^2} I(x, -t) = \mathbf{0}. \qquad (2.24)$$

The time-reversibility of the transmission-line equations underlies the electromagnetic time reversal as a potential technique to locate transient disturbance (i.e., an injection of energy) in power networks. In 2013, Razzaghi et al. proposed, for the first time, electromagnetic time reversal as a fault location method in power systems (e.g., [79]), developing the metric of fault current signal energy to determine the focal spot. One of the attractive peculiarities of the electromagnetic time reversal method is that it explores the possibility of locating faults using a single-end measurement. Lugrin et al. have also presented an analysis of the impact of line losses on the performance of the electromagnetic time reversal based fault location

method [154, 155]. Three backward-propagation models have been proposed and discussed. It has been shown that a lossy backward-propagation model, for which the transmission-line equations are not rigorously time-reversal invariant, still results in accurate fault location.

To better interpret the electromagnetic time reversal fault location method, we first review the electromagnetic transient processes associated with a fault event in power systems.

After a fault occurs in power networks, the fault-originated traveling waves propagate from the fault location towards the network terminals. Those traveling waves get reflected at discontinuities along the network (e.g., the junctions between main feeder and laterals), network ends as well as the fault location. The boundary conditions at the three categories of locations can be described by the respective voltage/current reflection coefficients, whose values depend on the line characteristic impedance and the input impedance of the connected power components [153]. To be specific, taking the voltage reflection coefficient, denoted by ρ^v, as an example (e.g., [125, 156, 157]),

i) At the *fault location*, ρ^v is close to -1 since the fault impedance is generally significantly small in comparison with the characteristic impedance of typical power overhead lines or underground cables.

ii) At the *power network terminals*, which are connected to power transformers, ρ^v is close to $+1$. The electromagnetic transients originated by faults are characterized by a spectrum with frequencies in the order of tens to hundreds of kilohertz, at which the transformer input impedance has the magnitudes of some tens to hundreds of kiloohms [156, 157]. As a consequence, the terminals behave approximately as open circuits for the incident traveling waves.

iii) At the *discontinuities*, ρ^v varies in accordance with the respective characteristic impedance of the line/cable along which the incident traveling waves propagate and the line/cable connected to the junction.

As introduced earlier, Draeger et al. have shown that, in the case of acoustic waves, it is possible to achieve the time-reversal focusing property using a single-channel (end) measurement for a closed reflective cavity [25, 26, 27]. The property was later validated for electromagnetic waves [53]. Considering the fault-originated traveling waves, a power network with boundary conditions (at the terminals) showing ρ^v close to $+1$ can be considered as a closed reflective cavity. Moreover, Derode et al. have demonstrated that the more complex the propagative medium, such as a high degree of inhomogeneity or multiple scattering, the better the time-reversal focusing quality (e.g., a higher resolution) [14, 16]. As known, power transmission and distribution networks consisting of multi conductors (e.g., three-phase systems) are generally configured in a topology of multi-branches and multi-nodes (e.g., junctions). Besides, the power networks are also commonly composed of a mixture of overhead lines and underground cables, and thus, feature inhomogeneity.

Chapter 2. Electromagnetic Time Reversal and Its Fault Location Application in Power Networks

The above-discussed advantages make the electromagnetic time reversal technique an efficient tool to locate power-system faults, especially considering the fact that it requires only a single-end measurement [79]. The step-by-step algorithm of the method will be introduced in Section 4.1. In brief, the fault location is implemented using a two-step procedure composed of the processing respectively belonging to the forward-propagation stage (also named *direct time*) and the backward-propagation stages (also named *reversed time*):

i) In the forward-propagation stage, the fault-originated transients are measured at a single observation point.

ii) In the backward-propagation stage, the measured transients are time reversed and back injected by simulation into a numerical model of the target power network. The fault location is identified using an appropriate criterion or metric, such as the fault current signal energy [79], to quantify the refocusing of the backward-propagated waves.

One of the fundamental hypotheses of time reversal is that the propagative media in the stages of the forward- and backward-propagation are identical, in a sense, being generally described as *matched media* [3, 8]. By realizing the matched-media condition, the time-reversed waves are able to constructively converge at the source location

However, for the fault location problem, the true fault location is the desired solution, being unknown in the backward-propagation stage. Given this, the backward propagation relies on first defining a set of *a priori* guessed fault locations and then reproducing a fault occurrence at each of those locations [79, 84, 85]. The matched-media condition in the fault location problem consists of the power-network topology in the fault occurrence stage, namely the direct time, is identical to that in the fault location stage, namely the reversed time. The spatial reciprocity determines that the matched-media condition is satisfied if and only if the guessed fault location coincides with the true fault location [158]. With the constructive convergence of the time-reversed backward-propagated transients, the true fault location is therefore characterized by the largest energy concentration [79].

The fault current signal energy appears to be the most representative fault location metric using electromagnetic time reversal. Its applicability has been numerically validated with reference to various types of power networks, which feature inhomogeneity, topological complexity (e.g., radial distribution feeder), non-linear characteristics (e.g., series compensated transmission lines), power injection of dispersed energy resources, and so forth [2, 79, 80]. The proposed method was also experimentally validated in a laboratory environment using a reduced-scale coaxial cable set-up [79].

To sum up, although the electromagnetic time reversal based fault location method belongs to traveling wave-based techniques, it has been shown to be capable of demonstrating superior fault location performance compared to existing methods in terms of [2, 79]

i) using single-end measurement even with the presence of inhomogeneity and multi-laterals in power networks,

ii) wide applicability (e.g., in active distribution networks),

iii) high location accuracy, namely pinpointing the precise fault location rather than identifying the fault passage,

iv) robustness against fault impedance and fault type, and

v) robustness against quantization error and noise.

3 A Closed Time-Reversal Cavity for Electromagnetic Waves in Transmission-Line Networks

A closed time-reversal cavity has been considered a purely theoretical concept whose experimental realization was assumed to be impossible. In the study presented in this chapter, we demonstrate that it is, in fact, possible to realize a closed time-reversal cavity for electromagnetic waves using a network of transmission lines. The network is excited by either lumped voltage or current sources at arbitrary locations, and it is terminated on matched impedance. This system is an exact closed time-reversal cavity in the sense that, in the backward-propagation stage, by back-injecting, at each line terminal, the time-reversed voltage or current that is measured as a response to the source excitation, a time-reversed copy of the voltage or current distribution in the forward-propagation stage is obtained.

We report for the first time an experimental realization of a time-reversal cavity formed by a network of inhomogeneous transmission lines, in which the spatial and temporal signal distribution along the network is reproduced as in a sequence of the system state (i.e., voltages and/or currents along the lines) being played in reverse. In addition, the time-reversal cavity inherent wave propagation properties are comparatively discussed in the realization of using transmission-line networks. We also discuss the interfering or distortion effect arising from the so-called diverging wave for observation points in the vicinity of the source. An active realization of a time-reversal sink is proposed, effectively overcoming the interfering effect.

The content of this chapter heavily draws from [159].

3.1 A Closed Time-Reversal Cavity for Electromagnetic Waves

The concept of a *closed time-reversal cavity* was proposed by Cassereau and Fink (e.g, [3, 6]) for acoustic waves, and it was later extended to electromagnetic waves using the Lorentz reciprocity principle. A time-reversal cavity derives the concept of a *time-reversal mirror* (e.g., [8, 9, 12, 13]) that a technique to refocus waves in a propagative medium back to the original source. A closed time-reversal cavity for electromagnetic waves can be briefly described as follows.

Consider a situation wherein a source is situated in a linear, non-magnetic, and time-invariant medium. Note that the medium can be inhomogeneous (see Fig. 3.1). Assume a closed, three-dimensional (3-D) surface *S* surrounding the source and its ambient medium (Fig. 3.1a). The source emits an electromagnetic pulse. Suppose that we are able to determine the tangential fields generated by the source at any point on this surface (Fig. 3.1b). Making use of the equivalence theorem, it is possible to replace the source with equivalent electric and magnetic current sources (on the surface *S* (Fig. 3.1c). Time reversing the equivalent sources on the surface results in the time reversal of the electromagnetic fields within the surface (Fig. 3.1d). An observer would see the fields propagate inwards, retracing the exact path the waves had followed as in a film being played in reverse or, equivalently, as if the observer were traveling backwards in time. The fields would then converge back to their original starting location.

The concept of the closed time-reversal cavity allows, therefore, refocusing a wave back to its source, using a two-stage procedure. In the forward(-propagation) stage, known as *direct time* (abbreviated as DT) in the time-reversal theory, the electromagnetic fields generated by the source are determined, either theoretically or experimentally, over the surface *S* forming the cavity. Then in the backward(-propagation) stage, known as *reversed time* (abbreviated as RT), the original source is removed from the medium and equivalent time-reversed sources (named secondary sources) on the surface are applied. The resulting field in the backward-propagation stage will be a time-reversed copy of that of the forward-propagation stage and, thus, it will converge back to the source.

It is generally assumed that the closed time-reversal cavity is impossible to achieve experimentally (e.g., [3]) because it requires an infinite number of observation points (e.g., transducers) covering a closed 3-D surface around the medium to obtain information about all wavefronts propagating in all directions [3, 27]. Indeed, in practice, the source-generated fields (e.g., acoustic or electromagnetic) can only be measured using a limited number of sensors (in a layout over a finite angular aperture, namely a time-reversal mirror) and, even though the focusing property of time reversal remains intact (e.g., [3, 26, 27]), the field distribution resulting from the injection of the time-reversed fields back into the medium will not be an exact time-reversed copy of the fields evolving in the forward stage.

We demonstrate that the closed time-reversal cavity for electromagnetic waves can, in fact, be realized using a transmission-line network. Such a time-reversal cavity requires a finite number of observation points located at the network terminals.

Figure 3.1 – Schematic description of a closed time-reversal cavity for electromagnetic waves. (a) Assume a closed, three-dimensional surface S surrounding a source and its ambient inhomogeneous medium. (b) The tangential fields generated by the source at any point on the surface S are determined. (c) The source is replaced by equivalent electric and magnetic current sources J_S and M_S. (d) Time reversing the equivalent sources on the surface results in time reversing the electromagnetic fields within that surface.

3.2 Realization of a Closed Time-Reversal Cavity Using a Network of Transmission Lines

3.2.1 General consideration

Consider a transmission-line network formed by coaxial shielded cables with an arbitrary topology as shown in Fig. 3.2a. Such networks can be found in various applications, for example, in electronic and communications circuits and underground power networks. Let the transmission-line network be excited by an impulsive voltage or current source located at an arbitrary point along one of the line branches (see the red dot along Branch 1 in Fig. 3.2b). Consider also a closed surface S (dotted line in Fig. 3.2) that surrounds the network passing through each one of its terminals. Note that the network can be inhomogeneous and non-uniform in the sense that the transmission lines that form the network can have different characteristics, such as propagation speed and cross-section dimension. Note also that the network can have any number of branches and nodes, and any number of sources, either voltage or current.
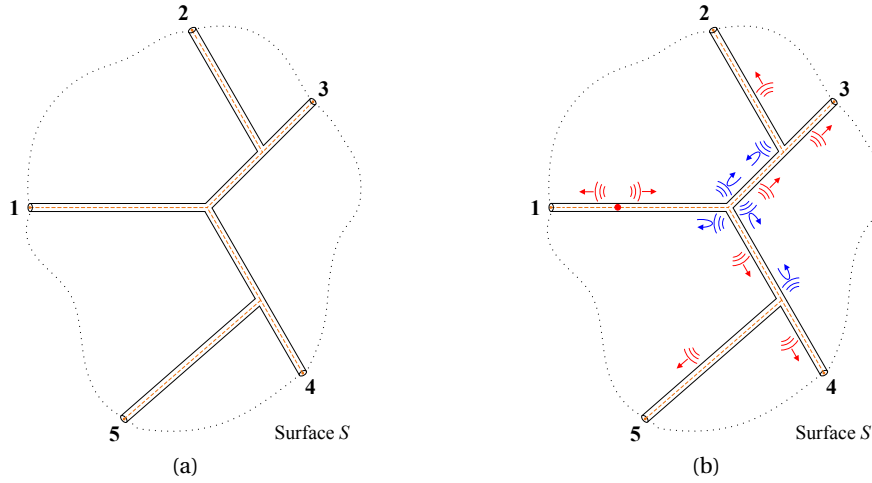
Figure 3.2 – Generic description of a closed time-reversal cavity in a multi-terminal multi-node coaxial-cable network. (a) A closed surface S represented by a dotted line surrounds the network passing through each terminal of the network (labeled 1 to 5). (b) The coaxial-cable network is excited by a voltage or current pulse source (represented by the red dot). The transmitted electromagnetic waves (in red color) propagate along the network. At the inner nodes, parts of the waves are transmitted to connected branches and parts of them, shown in blue, are reflected back.

Applying the concept of the closed time-reversal cavity to the case of Fig. 3.2 implies considering a matched load at each line terminal in such a way that electromagnetic energy only goes outward from the cavity.

The electromagnetic field propagation in such a system is confined within the cable (i.e., in the space between the inner conductor and the sheath). Furthermore, as long as the transverse dimensions of the cables forming the network are electrically small[1], the wave propagating along the conducting cables is transverse electromagnetic (TEM) [153, 160]. Therefore, inside the match-bounded cable network, the voltage/current wave is a scalar quantity, which propagates along the longitudinal directions of the cables. As a result, the field characteristics at every terminal are totally determined by the measured output signal (either current or voltage).

Furthermore, the only locations on the surface S at which electromagnetic fields are nonzero are at the line terminals. In other words, the considered system allows realizing a closed time-reversal cavity using a finite number of measurements equal to the number of network terminals. The current or voltage distribution along the network, resulting from the back-injection of the time-reversed signal from each terminal, will be an exact time-reversed copy of the temporal evolution in the forward-propagation stage.

---

[1]For example, a communication cable of about 1-cm diameter is electrically small for signals with the frequency content of up to a few GHz.

3.2.2   Illustration of the concept of a closed time-reversal cavity using a Y-shaped transmission-line network

Based on the generic description of a closed time-reversal cavity in a multi-terminal multi-node cable network (see Fig. 3.2), an inhomogeneous Y-shaped network is considered to illustrate the concept (see Fig. 3.3).

(a)

(b)
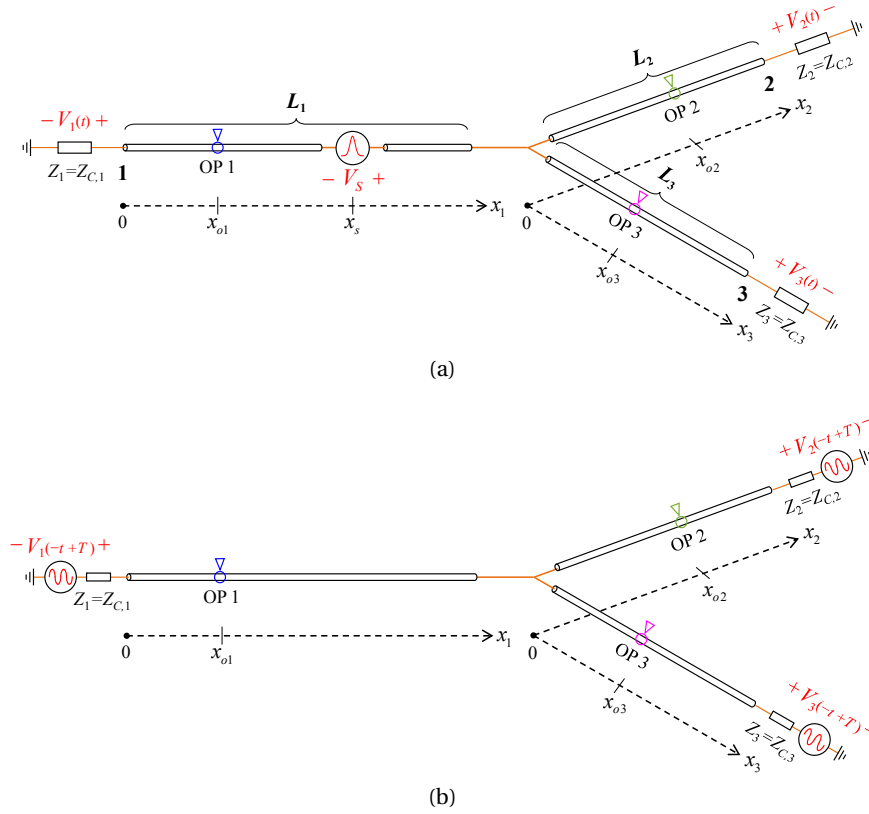
Figure 3.3 – Realization of a closed time-reversal cavity in a Y-shaped inhomogeneous coaxial-cable network. (a) Forward-propagation stage: *direct time*. (b) Backward-propagation stage: *reversed time*.

As illustrated in Fig. 3.3a, in the forward-propagation stage, a voltage pulse is injected into the inner conductor of the coaxial cable at a given location along Line branch 1 (along the x_1 axis) and induced voltage responses are observed at the three network terminals (labeled 1 to 3). In the backward-propagation stage (see Fig. 3.3b), the recorded voltages are time reversed and synchronously back injected into the network from the respective line terminals. In order to show that the temporal and spatial signal distribution along the network can be re-produced in reverse, three arbitrary observation points (identified as OP 1-3 in Fig. 3.3) are exemplified.

3.3 Time-Reversal Cavity Inherent Wave Propagation Properties: from Acoustic Waves to Transverse Electromagnetic Waves

The demonstration of the proposed cable network being exactly a closed time-reversal cavity is through formulating that the voltage/current wave propagation along the transmission-line network fully conforms to the wave propagation property inherent to a generic time-reversal cavity.

3.3.1 Time-reversal cavity in free space

For the sake of comparison, we make reference to the context initiating the concept of the closed time-reversal cavity, which consists of refocusing time-reversed acoustic scalar pressure fields to the original source [5, 6, 7]. The wave propagation properties of the time-reversal cavity in free space are first briefly reviewed. To ensure the time-reversal invariance of the wave equations, the following derivation assumes a lossless propagative medium.

Consider a point-like acoustic source located at the origin of the space coordinate system in free space. The generated scalar pressure field[2] $p^{\mathrm{DT}}(\boldsymbol{r}, t)$ observed in the forward-propagation stage at an arbitrary location $\boldsymbol{r}$ inside the time-reversal cavity satisfies the wave equation:

$$\left(\nabla^2 - \frac{1}{c^2}\frac{\partial^2}{\partial t^2}\right)p^{\mathrm{DT}}(\boldsymbol{r}, t) = -\phi(t)\cdot\delta(\boldsymbol{r}) + \mathscr{A}(\boldsymbol{r})\left[p^{\mathrm{DT}}(\boldsymbol{r}, t)\right], \tag{3.1}$$

where ∇^2 is the Laplace operator, c the sound speed and $\delta(\boldsymbol{r})$ the Dirac distribution in the 3-D space. $\phi(t)$ describes the temporal variation of the source excitation. It is implied that $\phi(t)$ is a causal function defined on a finite time interval T_ϕ [i.e., $\phi(t) = 0$ for $t < 0$ and $t > T_\phi$]. The formal linear operator $\mathscr{A}(\boldsymbol{r})$ accounts for the interaction between $p^{\mathrm{DT}}(\boldsymbol{r}, t)$ and inhomogeneity present in the medium.

Given that the cavity surface S is assumed not to perturb the propagation of the pressure field, namely the infinite free-space hypothesis holds, the solution of (3.1) can be expressed by a volume integral over the volume V enclosed by the cavity surface S as

$$p^{\mathrm{DT}}(\boldsymbol{r}, t) = \int_V \left\{\phi(t)\cdot\delta(\boldsymbol{r}_o) + \mathscr{A}(\boldsymbol{r}_o)\left[p^{\mathrm{DT}}(\boldsymbol{r}_o, t)\right]\right\} \otimes G(\boldsymbol{r}, \boldsymbol{r}_o, t)\,\mathrm{d}^3\boldsymbol{r}_o, \tag{3.2}$$

where $\boldsymbol{r}_o$ represents an arbitrary location on the cavity surface, $G(\boldsymbol{r}, \boldsymbol{r}_o, t)$ is the free-space Green's function and $\otimes$ is the time-domain convolution operator.

We are allowed to focus on a homogeneous propagative medium for the needs of inferring the representative property of a closed time-reversal cavity in free space. In this case, the solution

---

[2]The superscript DT and RT are used to indicate respectively that the signals are present in the forward- and backward-propagation stages of a closed time-reversal cavity.

(3.2) is obtained in a concise form as

$$p^{\mathrm{DT}}(\boldsymbol{r}, t) = \frac{1}{4\pi|\boldsymbol{r}|} \cdot \phi\left(t - \frac{|\boldsymbol{r}|}{c}\right).$$

(3.3)

In the backward-propagation stage, using the time-reversed components of the pressure fields recorded in the forward stage, the secondary sources on the cavity surface are generated as

$$p^{\mathrm{DT}}(\boldsymbol{r}_o, \ T - t).$$

(3.4)

Note that, to ensure causality, the time-reversal operation is given by the transformation

$$t \Longrightarrow T - t, \qquad T > T_\phi + d_m/c,$$

(3.5)

where T is the time window over which the pressure fields are recorded and d_m refers to the maximum distance between the origin and the points on the surface. The duration T is required to be long enough to record the complete pressure field at any location on the cavity surface.

In the backward-propagation stage, the pressure field generated by the secondary sources [e.g., $p^{\mathrm{DT}}(\boldsymbol{r}_o, \ T - t)$] inside the cavity can be calculated by

$$p^{\mathrm{RT}}(\boldsymbol{r}, t) = \int_S \left[G(\boldsymbol{r}, \boldsymbol{r}_o, t) \otimes \frac{\partial}{\partial \boldsymbol{n}_o} p^{\mathrm{DT}}(\boldsymbol{r}_o, \ T - t) - p^{\mathrm{DT}}(\boldsymbol{r}_o, \ T - t) \otimes \frac{\partial}{\partial \boldsymbol{r}_o} G(\boldsymbol{r}, \boldsymbol{r}_o, t) \right] \mathrm{d}^2 \vec{r}_o, \quad (3.6)$$

where $\boldsymbol{n}_o$ is the normal vector to the cavity surface S oriented outward at an arbitrary location $\boldsymbol{r}_o$ on S. The solution of (3.6) is yielded as

$$p^{\mathrm{RT}}(\boldsymbol{r}, t) = \underbrace{\frac{1}{4\pi|\boldsymbol{r}|} \cdot \phi\left(T - t - \frac{|\boldsymbol{r}|}{c}\right)}_{Converging} \underbrace{- \frac{1}{4\pi|\boldsymbol{r}|} \cdot \phi\left(T - t + \frac{|\boldsymbol{r}|}{c}\right)}_{Diverging}.$$

(3.7)

Examining equation (3.7), it can be seen that the solution is composed of two terms:

i) A *converging* term that corresponds to the propagation of the time-reversed wave back to the source. This term is an exact time-reversed copy of the field originally generated in the forward stage [see (3.3)].

ii) A *diverging* term that follows the *converging* wave, later arriving at the source location. The *diverging* term does not have any counterpart in the forward stage [see (3.3)].

3.3.2 Time-reversal cavity in transmission-line networks

In this Section, wave equations are solved to describe the time-reversal forward- and backward-propagation processes in the Y-shaped cable network of Fig. 3.3. Without loss of generality, the

derivation focuses on the voltage wave. Again, let us assume for now a lossless transmission line.

We use voltage reflection coefficients in the transmission-line theory to describe the boundary conditions at the network terminals and at the junction of the three line branches. Taking into account directionality, the voltage reflection coefficient at the junction can be defined as

$$\rho_{j,k}^i = \frac{Z_{j,k} - Z_{C,i}}{Z_{j,k} + Z_{C,i}}, \quad i \in U = \{1, 2, 3\}, \quad j, k = \complement_U i, \tag{3.8}$$

where the superscript i corresponds to the number of the line branch, along which incident voltage waves propagate, and the subscript pair j, k combines the numbers of the other two lines connected to the junction. $Z_{C,i}$ refers to the line characteristic impedance and $Z_{j,k}$ is the input impedance of the other two line branches seen from the junction. Note that, under the lossless-line assumption, $Z_{C,i}$ appears to be frequency independent. The input impedance, for a matched transmission line, being equal to its characteristic impedance, $Z_{j,k}$ can be thus calculated as:

$$Z_{j,k} = \frac{Z_{C,j} \cdot Z_{C,k}}{Z_{C,j} + Z_{C,k}}. \tag{3.9}$$

In the forward-propagation stage (see Fig. 3.3a), responding to the series voltage source $V_S(t)$ exciting the coaxial-cable network at $x_1 = x_s$, the voltage waves recorded at the line terminals (representing the cavity surface) read:

$$V_1(t) = -\frac{1}{2} V_S\left(t - \frac{x_s}{v_1}\right) + \rho_{2,3}^1 \cdot \frac{1}{2} V_S\left(t - \frac{L_1 - x_s}{v_1} - \frac{L_1}{v_1}\right), \tag{3.10}$$

$$V_2(t) = \left(1 + \rho_{2,3}^1\right) \cdot \frac{1}{2} V_S\left(t - \frac{L_1 - x_s}{v_1} - \frac{L_2}{v_2}\right), \tag{3.11}$$

$$V_3(t) = \left(1 + \rho_{2,3}^1\right) \cdot \frac{1}{2} V_S\left(t - \frac{L_1 - x_s}{v_1} - \frac{L_3}{v_3}\right), \tag{3.12}$$

which are obtained considering the matched boundary condition at each network terminal, namely $Z_i = Z_{C,i}$, resulting in the voltage reflection coefficient equal to zero. Z_i is the terminal impedance. v_i refers to the wave propagation speed along the corresponding line branch.

We now take the voltage wave at the observation point $x_1 = x_{o1}$ located between $x_1 = 0$ and the source point $x_1 = x_s$ as an example:

$$V_{x_{o1}}^{\mathrm{DT}}(t) = \overbrace{-\frac{1}{2} V_S\left(t - \tau_1'\right)}^{\textit{Incident}} + \rho_{2,3}^1 \cdot \frac{1}{2} V_S\left(t - \tau_1''\right), \quad (x_{o1} < x_s), \tag{3.13}$$

with the propagation delays respectively being

$$\tau_1' = \frac{x_s - x_{o1}}{v_1} \tag{3.14}$$

and

$$\tau_1'' = \frac{2L_1 - x_s - x_{o1}}{v_1}.$$
(3.15)

For the ease of the following discussion, we especially indicate in (3.13) the voltage wave that first arrives at $x_1 = x_{o1}$ as the *incident* term to manifest that it is originally generated by the source $V_S(t)$.

According to the time-reversal operation under causality, we denote the time-reversed copy of $V_i(t)$ as

$$V_i^{\text{tr}}(t) = V_i(T - t).$$
(3.16)

Following the previous use, T is the time window over which $V_i(t)$ is recorded.

In the backward-propagation stage (see Fig. 3.3b), the synchronous excitation of the secondary sources, namely $V_i^{\text{tr}}(t)$ with i being 1 to 3, generates the voltage wave at $x_1 = x_{o1}$ through

$$V_{x_{o1}}^{\text{RT}}(t) = \sum_{i=1}^{3} V_{x_{o1}}^{\text{RT}:V_i^{\text{tr}}}(t),$$
(3.17)

where the term V_i^{tr} in the superscript indicates the individual contribution of $V_i^{\text{tr}}(t)$ being separately back injected from its corresponding terminal. It can be readily obtained[3]:

$$V_{x_{o1}}^{\text{RT}:V_1^{\text{tr}}}(t) = \frac{1}{2} \cdot 2V_1^{\text{tr}}\left(t - \frac{x_{o1}}{v_1}\right) + \rho_{2,3}^1 \cdot \frac{1}{2} \cdot 2V_1^{\text{tr}}\left(t - \frac{L_1}{v_1} - \frac{L_1 - x_{o1}}{v_1}\right),$$
(3.18)

$$V_{x_{o1}}^{\text{RT}:V_2^{\text{tr}}}(t) = \left(1 + \rho_{1,3}^2\right) \cdot \frac{1}{2} \cdot 2V_2^{\text{tr}}\left(t - \frac{L_2}{v_2} - \frac{L_1 - x_{o1}}{v_1}\right),$$
(3.19)

$$V_{x_{o1}}^{\text{RT}:V_3^{\text{tr}}}(t) = \left(1 + \rho_{1,2}^3\right) \cdot \frac{1}{2} \cdot 2V_3^{\text{tr}}\left(t - \frac{L_3}{v_3} - \frac{L_1 - x_{o1}}{v_1}\right).$$
(3.20)

Substituting (3.18) to (3.20) into (3.17) produces (3.21):

$$2V_{x_{o1}}^{\text{RT}}(t) = -V_S\left(T - t - \tau_1'\right) + \rho_{2,3}^1 \cdot V_S\left(T - t - \tau_1''\right) - \rho_{2,3}^1 \cdot V_S\left(T - t + \tau_1''\right) + \left(\rho_{2,3}^1\right)^2 \cdot V_S\left(T - t + \tau_1'\right)$$
$$+ \left(1 + \rho_{1,3}^2\right) \cdot \left(1 + \rho_{2,3}^1\right) \cdot V_S\left(T - t + \tau_1'\right)$$
$$+ \left(1 + \rho_{1,2}^3\right) \cdot \left(1 + \rho_{2,3}^1\right) \cdot V_S\left(T - t + \tau_1'\right).$$
(3.21)

According to the boundary condition at the junction, namely

$$\rho_{2,3}^1 + \rho_{1,3}^2 + \rho_{1,2}^3 = -1,$$
(3.22)

---

[3]When $V_i^{\text{tr}}(t)$ is back injected as the secondary source, a voltage division ratio of $1/2$ caused by the matched boundary condition at the network terminal is introduced. As it can be seen in (3.18) to (3.20), $V_i^{\text{tr}}(t)$ is multiplied by 2 to offset the dividing effect and to be consistent with the generic definition of the closed time-reversal cavity.

$V_{x_{o1}}^{\mathrm{RT}}(t)$ is simplified as:

$$V_{x_{o1}}^{\mathrm{RT}}(t) = \underbrace{\rho_{2,3}^1 \cdot \frac{1}{2} V_S\big(T - t - \tau_1''\big) \overbrace{- \frac{1}{2} V_S\big(T - t - \tau_1'\big)}^{Incident^{\mathrm{TR}}}}_{Converging} + \underbrace{\frac{1}{2} V_S\big(T - t + \tau_1'\big) - \rho_{2,3}^1 \cdot \frac{1}{2} V_S\big(T - t + \tau_1''\big)}_{Diverging}.$$

(3.23)

Following a similar approach, we can derive the solutions for the voltage waves observed along Line branch 2 (i.e., at the observation point $x_2 = x_{o2}$) in the forward- and backward-stages:

$$V_{x_{o2}}^{\mathrm{DT}}(t) = \big(1 + \rho_{2,3}^1\big) \cdot \frac{1}{2} V_S(t - \tau_2),$$

(3.24)

with

$$\tau_2 = \frac{L_1 - x_s}{v_1} + \frac{x_{o2}}{v_2}$$

(3.25)

and

$$V_{x_{o2}}^{\mathrm{RT}}(t) = \underbrace{\big(1 + \rho_{2,3}^1\big) \cdot \frac{1}{2} V_S\big(T - t - \tau_2\big)}_{Converging} \underbrace{- \big(1 + \rho_{2,3}^1\big) \cdot \frac{1}{2} V_S\big(T - t + \tau_2\big)}_{Diverging}.$$

(3.26)

Given that the excitation source is located along Line branch 1, the voltage wave expression obtained at the observation point $x_3 = x_{o3}$ along Line branch 3 has a similar form as that at $x_2 = x_{o2}$:

$$V_{x_{o3}}^{\mathrm{DT}}(t) = \big(1 + \rho_{2,3}^1\big) \cdot \frac{1}{2} V_S(t - \tau_3),$$

(3.27)

$$V_{x_{o3}}^{\mathrm{RT}}(t) = \underbrace{\big(1 + \rho_{2,3}^1\big) \cdot \frac{1}{2} V_S\big(T - t - \tau_3\big)}_{Converging} \underbrace{- \big(1 + \rho_{2,3}^1\big) \cdot \frac{1}{2} V_S\big(T - t + \tau_3\big)}_{Diverging},$$

(3.28)

where

$$\tau_3 = \frac{L_1 - x_s}{v_1} + \frac{x_{o3}}{v_3}.$$

(3.29)

We now use the expressions (3.27) and (3.28) to interpret the property of the voltage wave propagation in the forward- and backward-propagation stages. As it is similar to the case of the acoustic waves, the voltage wave observed in the backward-propagation stage consists of two correlative components, which arrive at the observation point one after the other. The later-arriving component [i.e., the second term in (3.28)] is an inverted and time-delayed copy of the first voltage wave. The two components are respectively generated by the processes of the time-reversed terminal responses (back injected by the secondary sources) converging to and diverging from the original source location. For this reason, the two components are referred to, respectively, as the *converging* and *diverging* terms in (3.28), in agreement with the terminology used in (3.7) [3, 5, 7].

In addition, for the reason that the second term of the *converging* voltage wave in (3.23) is a time-reversed copy of the *incident* wave in (3.13), it is specially indicated by the notation *incident*$^{\text{TR}}$.

It is important to note that only the converging wave in the backward-propagation stage behaves as a time-reversed copy of the voltage wave in the forward-propagation stage, whereas the diverging component does not have its counterpart in the forward stage. This can be clearly seen by comparing equations (3.23), (3.26) and (3.28) with their forward-stage counterparts, namely equations (3.13), (3.24) and (3.27), respectively.

Recall the previously-formulated expressions (3.3) and (3.7) describing the wave behaviors of the closed time-reversal cavity in free space. As indicated, the pressure filed in the backward-propagation stage intrinsically contains the converging and diverging components. Moreover, the earlier-arriving converging component is a mirror image of the source originally-generated field with respect to the recording time-window length T. Besides, it is also noted that the later-arriving diverging component is an inverted and time-delayed copy of its converging counterpart.

The derived solutions of the voltage waves exhibit a similar structure like (3.3) and (3.7), thus analogously achieving the foregoing wave propagation property. We thereby analytically show that a bounded, matched transmission-line network is an exact closed time-reversal cavity.

We now discuss the *interfering*[4] effect caused by the diverging wave for observation points located in the region near the source location.

For the ease of explanation, the components of $V_{x_{o1}}^{\text{RT}}$ in (3.23) are arranged in chronological order according to the instants when they respectively arrive at the observation point $x_1 = x_{o1}$. We denote by τ the difference between the instants of the converging and diverging components respectively arriving at $x_1 = x_{o1}$. It can be seen that τ is twice as long as the prorogation delay of τ_1'. An immediate consequence of this fact is that the diverging voltage wave overlaps with the converging one at the location, which is characterized by a relatively small τ_1'. The two voltage waves are completely separated in time if τ is greater than T_S, namely the temporal duration of the voltage source $V_S(t)$. Thus, this interference would affect only the observation point that is located around the source and is characterized by the abscissa $x_1 = x_{o1}$ satisfying

$$|x_{o1} - x_s| \leqslant \frac{1}{2} v_1 \cdot T_S. \tag{3.30}$$

Here, without loss of generality, we assume that Line branch 1 is long enough so that the interfering region is confined along the line branch where the source excitation is originally injected.

---

[4]Note that Fink and co-workers used the term distortion in their papers (e.g., [3, 5, 7]). We prefer instead to use hereinafter the term of interfering to avoid any confusion with the concept of distortion in communication systems.

This conclusion is also analogous to that of the time-reversal cavity in free space wherein the interfering effect is confined in the region where [3, 5, 7]

$$|\boldsymbol{r} - \boldsymbol{0}| = |\boldsymbol{r}| \leqslant \frac{1}{2} c \cdot T_\phi. \tag{3.31}$$

In summary, the closed time-reversal cavity inherent wave propagation property can be stated in a strict sense by

$$V^{\mathrm{RT},c.}(x,t) = V^{\mathrm{DT}}(x, T - t), \quad (x > x_s \pm \frac{1}{2} v_1 \cdot T_S), \tag{3.32}$$

where $V^{\mathrm{RT},c.}(x,t)$ represents the converging component of the voltage wave at a generic location x along the network.

3.4 Numerical and Experimental Validation

The preceding analysis demonstrates the realization of a closed time-reversal cavity in transmission-line networks. It has been shown that the voltage wave resulting from the converging process in the backward stage is a time-reversed copy of the voltage wave that is originally generated by the source in the forward stage. This section further presents the numerical and experimental validation of the proposed time-reversal cavity. To this end, the generic Y-shaped inhomogeneous cable network of Fig. 3.3 is experimentally realized using the set-up described in Fig. 3.4.

The proposed cable network is composed of three line branches and five segments of coaxial cables. As detailed in Table 3.1, Line branches 1 and 2 are RG-58 coaxial cables, which are respectively 45 m and 26 m in length. Note that, Line branch 3 contains a mix of three line segments comprising RG-59 and RG-179 coaxial cables. The main parameters of the adopted RG-58, -59 and -179 standard coaxial cables are summarized in Table 3.2. The three types of cables feature different characteristic impedance, wave propagation speeds, and cross-sectional dimensions. As a result, the considered cable network is characterized by a high degree of inhomogeneity.

Table 3.1 – Configuration of the experimental set-up realizing a time-reversal cavity

Line branch	Cable	Length	
1 (along the x_1 axis)	RG-58	L_1	45 m
2 (along the x_2 axis)	RG-58	L_2	26 m
	RG-59	L_{3-1}	14 m
3 (along the x_3 axis)	RG-179	L_{3-2}	4 m
	RG-59	L_{3-3}	4 m
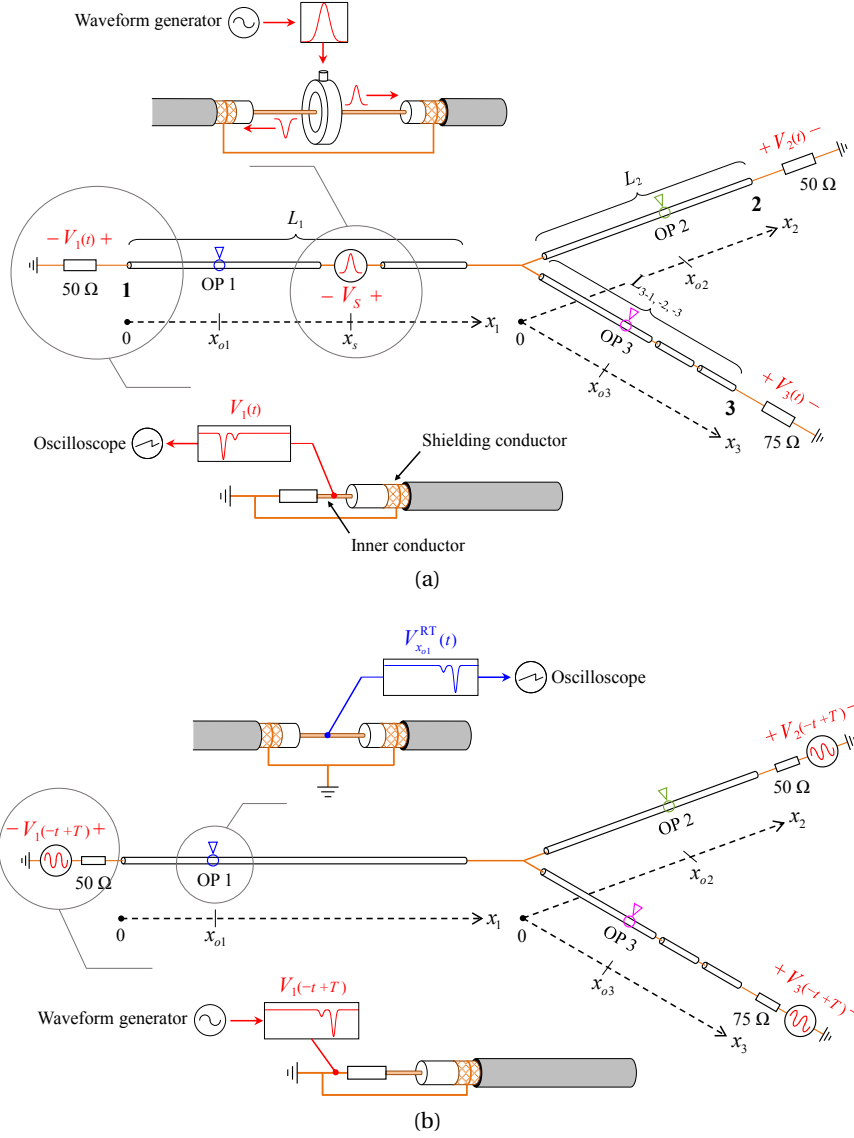
Figure 3.4 – Experimental set-ups realizing a closed time-reversal cavity in a Y-shaped inhomogeneous coaxial-cable network. (a) Forward-propagation stage: *direct time*. (b) Backward-propagation stage: *reversed time*.

Table 3.2 – Main parameters of RG-58/59/179 standard coaxial cables

	RG-58	RG-59	RG-179
Characteristic impedance (Ω)	50	75	75
Propagation speed (% of the speed of light)	66	65.8	69
Nom. attenuation (dB/m) ($f \leq 35$ MHz)	0.07	0.06	0.14
Diameter of inner/shielding conductor (mm/mm)	0.9/3.6	0.58/4.5	0.31/2

Matching the coaxial-cable network under study consists of terminating RG-58 cable and RG-59 cables with lumped resistors of 50 Ω and 75 Ω, respectively. Note that matched impedance is only required at the external terminations.

Figure 3.5 illustrates the profile of a modified Gaussian pulse of

$$A \cdot e^{-4\pi \cdot \frac{(t-t_0)^2}{\tau^2}}, \tag{3.33}$$

which is adopted as the excitation signal of the series voltage source $V_S(t)$ being injected into the network in the forward-propagation stage. In (3.33), A and t_0 respectively specify the maximum amplitude and the time delay of the Gaussian pulse, being assigned 120 mV and 60 ns, as it can be seen in Fig. 3.5. Meanwhile, τ determines the $1/e$ width of the pulse as $\tau/\sqrt{\pi}$. In the study, τ was set at 68 ns, resulting in the $1/e$ pulse width of the injected pulse as about 38 ns. In this respect, the width is sufficiently small in the light of the propagation delays of the line branches.
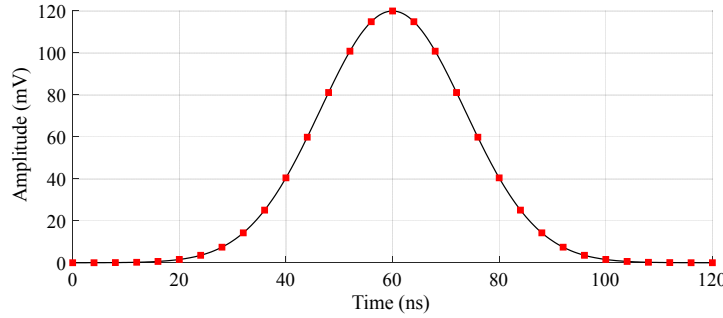
Figure 3.5 – Modified Gaussian pulse as the excitation signal of the series voltage source $V_S(t)$. The red squares show the sampling points that correspond to the 250 MSamples/s sampling rate of the adopted arbitrary waveform generator.

3.4.1 Numerical validation

The voltage wave propagation along the Y-shaped inhomogeneous cable network, which represents a closed time-reversal cavity, was first numerically simulated within the EMTP-RV environment [161, 162]. In the numerical simulations, losses in the coaxial cables were still disregarded as the foregoing derivation has assumed. This way, the time-reversal invariance of the wave equations is strictly satisfied.

In accordance with the set-up described in Fig. 3.4a, Fig. 3.6 presents the terminal voltages $V_i(t)$ (i being 1 to 3) simulated in the forward-propagation stage of the time-reversal cavity. The series voltage source $V_S(t)$ injected the Gaussian pulse at $x_1 = x_s = 28$ m, giving rise to the voltage wave propagating towards the network terminals. The voltage responses at the terminals were observed in a time window T of 800 ns. The voltages $V_i(t)$ were then time reversed and shifted in time by T as $V_i(T-t)$. The two sets of waveforms are superimposed in Fig. 3.6. The original waveforms $V_i(t)$ and their time-reversed images $V_i(T-t)$ are symmetrical

with respect to the middle point of the time window T (i.e., $t = 400$ ns). For simulating the backward propagation, the time-reversed voltages $V_i(T - t)$ were synchronously back injected into the network.
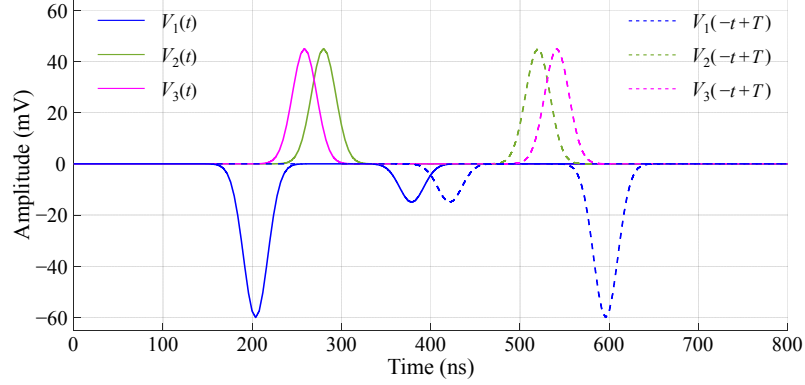
Figure 3.6 – Simulated terminal voltage waveforms $V_i(t)$ in the forward-propagation stage of the closed time-reversal cavity. The terminal responses are time reversed as $V_i(T - t)$, which are plotted in dashed lines.

In view of the line parameters reported in Tables 3.1 and 3.2, the interfering effect caused by the diverging process in the Y-shaped cable network can be eliminated by considering the observation points with a coordinate, satisfying either $x_1 \leq 16$ m or $x_1 \geq 40$ m. Fig. 3.7 presents the simulated voltage waves in the forward-propagation stage (solid lines) and the backward-propagation stage (dashed lines) at the three observation points, which were located along the three line branches with the coordinates being $x_1 = x_{o1} = 4$ m, $x_2 = x_{o2} = 17$ m and $x_3 = x_{o3} = 12$ m, respectively. As analyzed previously, the observed voltage waves contributed by the converging process in the backward stage are exact time-reversed copies of the voltage waves propagating in the forward stage.
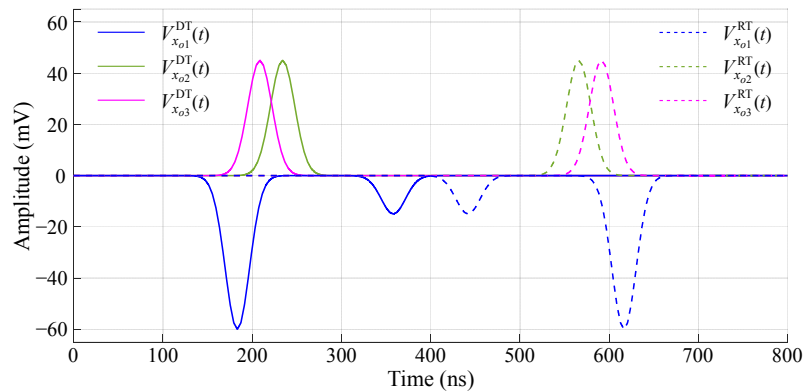
Figure 3.7 – Simulated voltage waveforms of the considered observation points. Solid lines: forward-stage voltages. Dashed lines: backward-stage voltages.

3.4.2   Experimental validation

The proposed Y-shaped coaxial-cable network realizing a closed time-reversal cavity was validated experimentally. The expanded views in Fig. 3.4 describe the involved experimental devices and approaches.

The main specifications of the devices used in the experiment are summarized in Table 3.3. Note that the spectrum of the Gaussian pulse of Fig. 3.5 extends to significant frequencies of up to a few megahertz.

Table 3.3 – Main characteristics of the experimental instruments

	CP[a]	AWG[b]	Osc.[c]
Bandwidth	200 MHz	125 MHz	350 MHz
Sampling rate	–	250 MS/s	2.5 GS/s
Vertical resolution	–	16 bit	14 bit

[a]Current probe, [b]Arbitrary waveform generator and [c]Oscilloscope .

In the forward-propagation stage, an arbitrary waveform generator was used in combination with a Pearson 1 V/A (50 turns) broadband current transformer for the generation and injection of a voltage pulse into the inner conductor of the coaxial cable (see Fig. 3.4a). Corresponding to the simulation scenario, the current probe was positioned along Line branch 1 at $x_1 = x_s = 28$ m. With the injection of a signal from the secondary coil, the current probe behaves as a voltage transformer with a transformation ratio of 50:1. Therefore, the same Gaussian pulse shown in Fig. 3.5 was applied to the secondary coil of the current probe but with a peak value of 6 V. This way, the generated voltage pulse, which is equivalent to the excitation of the series voltage source $V_S(t)$ in the inner conductor in Fig. 3.4a, remains a peak value of 120 mV. At the matched line terminals, the induced voltage responses were recorded by means of an oscilloscope.

The measured terminal voltages are shown in Fig. 3.8. In the same figure, the simulated counterparts are also presented in black lines for the sake of comparison. It can be seen that, except for the peak values that are attenuated in the measured signals, the overall simulated and measured waveforms are in high-grade agreement. The attenuation is essentially due to the losses in the cables, which were not considered in the simulations.

As described in Fig. 3.4b, in the backward-propagation stage, the responses acquired in the forward stage at the network terminals were reversed in time and synchronously back injected into the network from the respective terminals using an arbitrary waveform generator.

Figure 3.9 presents the voltages measured in the forward stage (solid lines) and in the backward stage (dashed lines) at the three considered observation points. It is evident that the observed signals in the backward stage (more precisely the converging process) are nearly-perfect time-
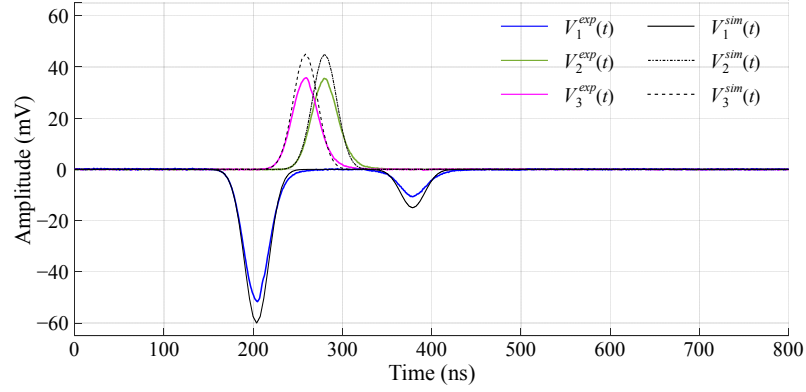
Figure 3.8 – Experimentally-recorded terminal voltage waveforms $V_i(t)$ (indicated by the superscript *exp* in the legend) in the forward-propagation stage. The simulated waveforms (indicated by the superscript *sim*) are shown in black (solid for V_1, dash-dotted for V_2 and dashed for V_3).
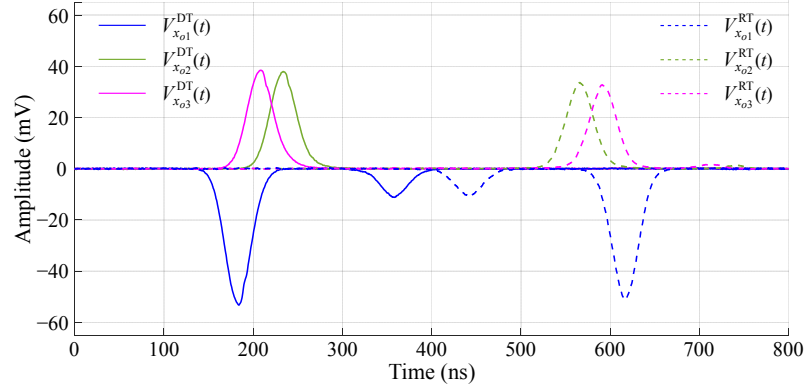
Figure 3.9 – Experimentally-recorded voltage waveforms of the considered observation points. Solid lines: forward-propagation stage voltages. Dashed lines: backward-propagation stage voltages.

reversed copies of the ones originally present in the forward stage. The difference between the two stages' voltages is the slight attenuation in amplitude, which stems from losses in the cables. Note that by considering an inverted-loss medium in the backward stage [154, 155], the attenuation effect can be compensated.

3.5 Discussion

The preceding results have validated the wave propagation property of the closed time-reversal cavity realized by the Y-shaped cable network. The observation refers to the locations that are out of the region affected by the interfering diverging wave. The discussion in this section focuses on the locations that neighbor the original source location $x_1 = x_s$.

3.5.1 Interfering effect of diverging voltage waves

Given the previous analysis, the interfering region for the proposed time-reversal cavity is bounded at $x_1 = x_s \pm 12$ m. Figs. 3.10a and 3.10b depict the voltage waves measured at the locations $x_1 = x_s \pm \Delta x$ with Δx being 1, 2 and 5 m, respectively. As formulated previously, if the observation point is within the interfering region, the backward stage voltage wave is not a time-reversed copy of its counterpart in the forward stage anymore.

(a)

(b)
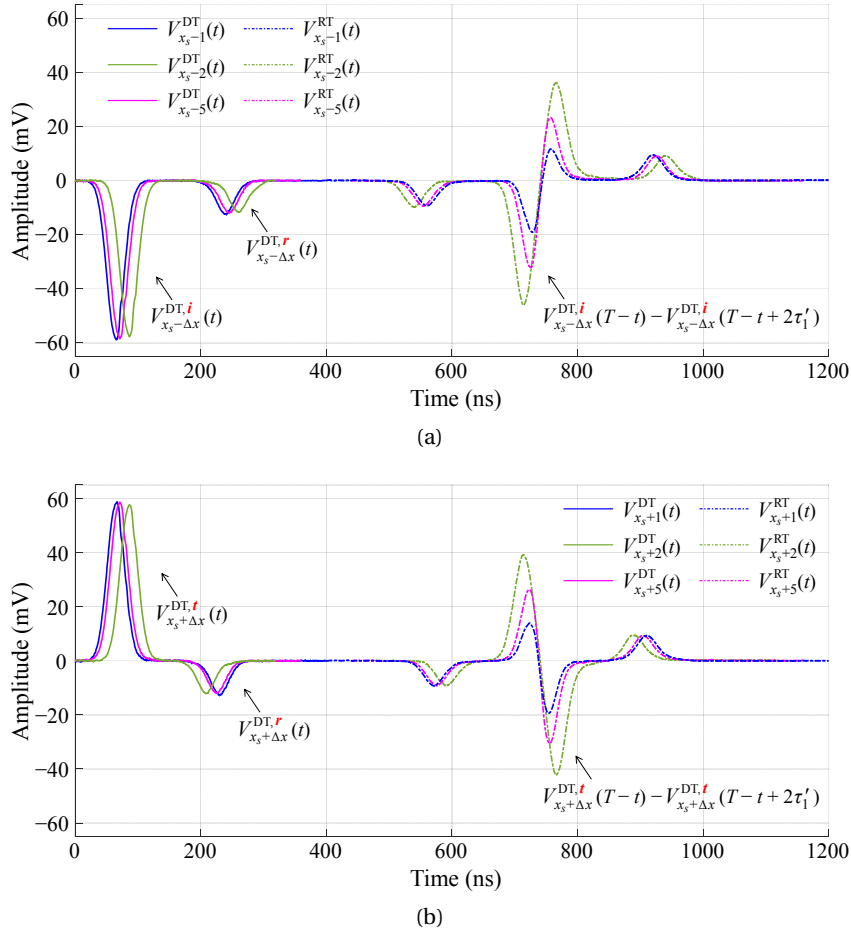
Figure 3.10 – Experimentally-recorded voltage waveforms of the observation points that neighbor the source location $x_1 = x_s$. Solid lines: voltages in the forward stage. Dashed lines: voltages in the backward stage. The observation points are on (a) the side $x_1 < x_s$ and (b) the side $x_1 > x_s$.

The forward-stage voltage wave can be decomposed into two terms (see Fig. 3.10):

i) the incident voltage wave generated by the source, which is denoted by the superscript '*i*', and

ii) the reflected voltage wave from the junction point, which is denoted by the superscript '*r*'.

The incident voltage wave has the same shape as the series excitation source $V_S(t)$ but with an amplitude reduced by a factor 2 due to the division of the excitation voltage. As it can be seen in Figs. 3.10a and 3.10b, the incident voltage wave has either a positive or negative polarity depending on whether the observation point is located on the right side (i.e., $x_1 > x_s$) or left side (i.e., $x_1 < x_s$) of the series voltage source.

In the backward-propagation stage, taking the locations at $x_1 = x_s - \Delta x$ as an example, the interfering effect results from the time-reversed incident wave $V^{\mathrm{DT},i}_{x_s - \Delta x}(T - t)$ overlapping with its inverted and time-shifted copy, showing the temporal evolution of the distorted voltage wave being shaped like a derivative of a negative pulse (see Fig. 3.10a). This fact is consistent with that the incident voltage wave is of negative polarity on the side of $x_1 < x_s$. As shown in Fig. 3.10b, such temporal derivative attribute is similarly obtained at the locations $x_1 = x_s + \Delta x$, corresponding to that the incident voltage wave is turned positive on the side of $x_1 > x_s$. The results also demonstrate that only the incident component [i.e., the 'incident' term in (3.23)] that is originally generated by the source itself is interfered by the diverging voltage wave in the backward stage.

It is worth noting that the discussed voltage wave property is analogous to the diverging process of the time-reversal cavity in free space. Indeed, reviewing expression (3.7) and limiting $|\boldsymbol{r}|$ to 0, the backward-stage pressure field in the interfering region is in a pattern of the temporal derivative of the excitation function $\phi(t)$.

Also, note that in spite of the overlap between the converging and diverging voltage waves, it is still possible to locate the position of the source. Taking advantage of the time-reversal temporal-spatial correlation property, $V^{\mathrm{DT},i}_{x_s}(T - t)$ and its inverted copy inherently arrive in phase at the source location $x_1 = x_s$, resulting in a complete offset. This way, the original source point can be exclusively distinguished from its neighboring locations, for example, by means of an algorithm assessing the energy of the voltage wave along the network. Fig. 3.11 shows the normalized voltage energy as a function of the distance to the network terminal $x_1 = 0$. Obviously, the source location, namely $x_1 = 28$ m, features the global minimum voltage energy among the observation points distributed along the network.

3.5.2 A closed time-reversal cavity in transmission-line networks with a time-reversal sink

Rosny and Fink have proposed in acoustics the concept of a *time-reversal sink* to overcome the interfering effect caused by the diverging waves in the region near the source location [53, 163]. According to this concept, during the backward-propagation stage of the time-reversal process, the source is replaced by a sink that absorbs the incident wave. A passive realization of a time-reversal sink is quite challenging. However, if the source excitation is known, the sink can be experimentally realized by an active source that generates an additive inverse of the diverging wave in the backward stage, compensating, therefore, the interfering effect caused by the diverging process.
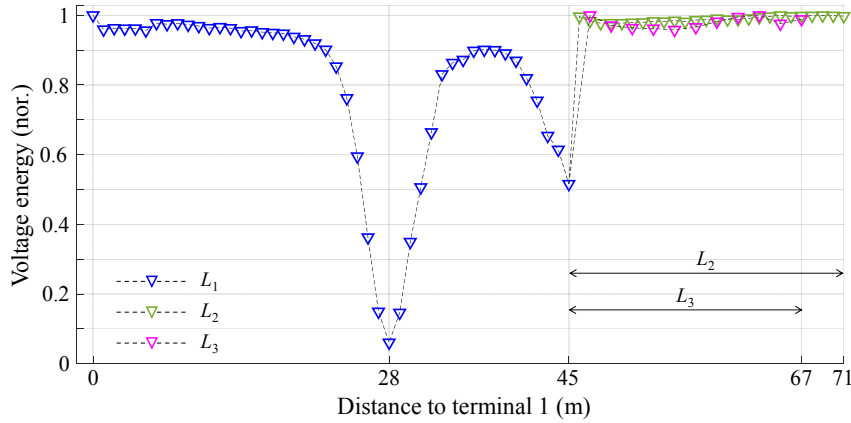
Figure 3.11 – Normalized energy of the voltage experimentally-recorded along the network. The spacings of the observation points are respectively 1 m along Line branches 1 and 2 while 2 m along Line branch 3. The normalization is based on the maximal voltage energies calculated for the respective line branches.

Assume that the original source remains active in the backward-propagation stage but with a time-reversed variation, namely $V_S(T - t)$ for the proposed case of the time-reversal cavity in transmission- line networks. Mathematically, solving the wave equation taking into account the active time-reversal sink in the backward stage, it can readily be shown that the voltage wave generated by the time-reversed source is identical to the diverging term in (3.23) but with opposite polarity.

Figure 3.12 compares the distorted voltage wave experimentally recorded at the location $x_1 = x_s - 1$ as an example with the one measured in presence of the active source $V_S(T - t)$, which represents a time-reversal sink. As it can be observed, even when the voltage wave is recorded at a location quite adjacent to the source point, its waveform in the backward-propagation stage is nearly a time-reversed copy of the voltage wave in the forward-propagation stage, as the diverging voltage wave has been compensated.

Thus, the so-called time-reversal sink applies the additional source generated wave to interfere destructively with the backward-stage diverging wave, keeping the converging component intact.

3.6 Conclusion

The study presented in this chapter demonstrated that a closed time-reversal cavity for electromagnetic waves can be realized using a transmission-line network. Such a time-reversal cavity requires a finite number of observation points located at the terminals of the network. A time-reversed copy of the system state (e.g., voltage wave distributions) originated by a source in the forward-propagation stage can be obtained by time-reversing the responses at the terminals and back injecting them into the network.
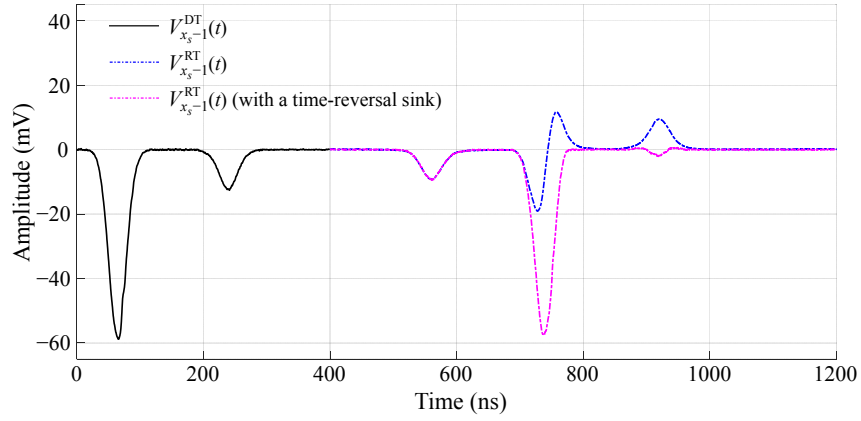
Figure 3.12 – Experimentally-recorded voltage waveforms at the location $x_1 = x_s - 1$ in the forward-propagation stage and the backward-propagation stage (with and without a *time-reversal sink*).

In the experimental realization of the time-reversal cavity, the resulting distribution was affected by an attenuation caused by losses in the coaxial cables. Indeed, the wave equations in transmission lines are time-reversal invariant for lossless lines. When the network is lossy, the time-reversal invariance will hold when an inverted-loss medium is considered in the backward-propagation model [154, 155]. An inverted-loss medium can be considered in a straightforward way in numerical simulations as long as the line losses are well characterized.

We showed, in this study, that the past behaviors of signals along a transmission-line network can be reproduced in the future. To achieve this, only a finite number of responses need to be monitored at the network terminals. We also discussed the interfering effect of the so-called diverging wave for observation points in the vicinity of the source. We proposed an active realization of a time-reversal sink, using the time-reversed source generated wave to interfere destructively with the backward-stage diverging wave.

The proposed closed time-reversal cavity in transmission lines can find useful applications, for instance, online monitoring of communication networks, which work generally under matched conditions. Such networks can also include point-to-point wireless communication systems, which can be represented by their equivalent models in the backward stage. The synchronized measurement of signals at every network terminal would allow detecting anomalies and locating their source. The technique can also be used in various other applications such as:

i) preventive maintenance and monitoring of cables to detect and locate incipient faults, before their occurrence;
ii) detecting and locating intentional electromagnetic interference (IEMI) attacks [164, 165];
iii) facilitating the investigation of incidents in flight-data recorders.

4 Electromagnetic Time Reversal Based Fault Current Signal Energy Metric: Analysis and Experimental Validation

The application of electromagnetic time reversal (EMTR) in the context of the fault location problem in power systems was first studied in [79], proposing the use of fault current signal energy (FCSE) as discriminating metric to determine the most likely location of a fault. Indeed, the first experimental validation of the EMTR-FCSE metric has been reported along with pioneering the metric in the publication of [79]. However, the experiment was limited to laboratory environments in terms of : i) use of a reduced-scale experimental set-up composed of low-power signal cables, ii) use of hardware-emulated faults, and iii) use of conventional laboratory instruments for measurements.

Indeed, to the best of our knowledge, prior to the study presented in this chapter, there was a lack of experimental evidence about verifying EMTR-based fault location methods by using full-scale transmission lines. The study represents the first field experiment and the first pilot test in real power system environments, validating the EMTR-FCSE metric and evaluating its performance with respect to faults of diverse natures, such as fault types, fault inception angles, and so forth. Besides, the study is also devoted to addressing the technical challenge of developing a dedicated hardware system suitable for the efficient implementation of EMTR-based fault location methods in power systems.

The chapter includes results of publications [83, 84, 86, 166].

4.1 Electromagnetic Time Reversal Using Fault Current Signal Energy Metric

The so-called classical electromagnetic time reversal (EMTR) fault location methods refer to the category of methods realizing the fault location functionality by conforming to the principle of *matched media* in the time-reversal theory. The principle requires the backward-propagation medium to be identical to that in the forward-propagation stage. Among these efforts, the fault current signal energy appears the most representative metric [79]. In what follows, the EMTR fault location technique using the FCSE metric will be referred to as the EMTR-FCSE method.

In this section, we briefly introduce the time-domain algorithm to implement the FCSE metric.

First, responding to a fault occurrence in power networks, the fault-originated transient voltage (or current) signal is measured at a given single observation point as

$$S_{ph}^{\mathrm{DT}}(t), \ t \in [t_{trigger}, t_{trigger} + T], \tag{4.1}$$

with $ph = a, b, and c$ for a three-phase system. $t_{trigger}$ is the acquisition triggering instant and T is the length of the time window over which $S_{ph}^{\mathrm{DT}}(t)$ is recorded. T is assumed to be sufficiently long to damp out $S_{ph}^{\mathrm{DT}}(t)$. The superscript DT (abbreviation of *direct time*) indicates that the signal is observed in the time-reversal forward-propagation stage. In the case of fault location, the *direct time* refers to the stage in which a fault occurs.

It is worth observing that $S_{ph}^{\mathrm{DT}}(t)$ contains the network steady-state frequency (e.g., 50 Hz) component and the superimposed fault-originated high-frequency transients $\tilde{S}_{ph}^{\mathrm{DT}}(t)$.

Then, the extracted transients with a duration of T_w^{DT} are reversed in time as

$$\tilde{S}_{ph}^{\mathrm{DT}}(t) \xrightarrow{\mathrm{TR}} S_{ph}^{\mathrm{TR}}(t): \ S_{ph}^{\mathrm{TR}}(t) = \tilde{S}_{ph}^{\mathrm{DT}}(-t + T_w^{\mathrm{DT}}), \ t \in [0, T_w^{\mathrm{DT}}]. \tag{4.2}$$

Next, the true fault location being unknown, a number of *a priori* guessed fault locations, with a density associated with a desired fault location accuracy, are defined:

$$x_{\mathbb{G}} = \left\{ x_g \,\middle|\, x_{g,1}, x_{g,2}, \dots \right\}. \tag{4.3}$$

For each x_g, the backward propagation is simulated by back injecting the time-reversed transients $S_{ph}^{\mathrm{TR}}(t)$ from the original observation point into a model, which numerically represents and simulates the target power network. By simulating a fault occurrence, the current flowing through the transverse branch at x_g is computed as

$$I_{x_g}^{\mathrm{RT}}(t), \ t \in [0, T_w^{\mathrm{RT}}], \tag{4.4}$$

where T_w^{RT} is the duration of $I_{x_g}^{\text{RT}}(t)$. Similarly, the superscript RT (abbreviation of *reversed time*) represents the backward-propagation stage.

The FCSE metric calculates the energy of the fault current signal $I_{x_g}^{\text{RT}}(t)$. In practice, both acquired and simulated signals are discretely sampled. The FCSE metric is thus calculated by

$$\text{FCSE}(x_g) = \sum_{i=0}^{M} \left[I_{x_g}^{\text{RT}}(i \cdot \Delta t) \right]^2 \cdot \Delta t, \ T_w^{\text{RT}} = M \cdot \Delta t, \tag{4.5}$$

where Δt is the sampling interval.

In the last step, among the guessed fault locations $x_{\mathbb{G}}$, the FCSE metric determines the most-likely fault location as the one with the maximum energy concentration through

$$x_{f, estimated} = arg\big|_{x_{\mathbb{G}}} \quad Max\big[\text{FCSE}(x_{\mathbb{G}})\big] \ . \tag{4.6}$$

It can be noticed that the EMTR-FCSE metric relies on multiple independent electromagnetic transient (EMT) simulations at respective guessed fault locations.

The above-introduced step-by-step processing is summarized in a pseudo-algorithm reported in Table 4.1.

Table 4.1 – Pseudo-algorithm of the EMTR-FCSE metric

Input: network topology and parameters   guessed fault locations $x_{\mathbb{G}} = \big\{ x_g \,\big|\, x_{g,1}, x_{g,2}, \ldots \big\}$
$S_{ph}^{\text{DT}}(t), \ t \in [t_{trigger}, t_{trigger} + T]$ $S_{ph}^{\text{TR}}(t), \ t \in [0, T_w^{\text{DT}}]$
for each *a priori* guessed fault location $x_g \in x_{\mathbb{G}}$ **do**   1: simulate the fault current $I_{x_g}^{\text{RT}}(t)$ using network model and $S_{ph}^{\text{TR}}(t)$ 2: compute the metric $\text{FCSE}(x_g)$ **end** $x_{f, estimated} = arg\big|_{x_{\mathbb{G}}} \quad Max\big[\text{FCSE}(x_{\mathbb{G}})\big]$
Output: $x_{f, estimated}$

Indeed, the existing research has produced a number of simulation case studies discussing the FCSE metric in terms of location accuracy and robustness. In comparison, very limited effort has been made to experimental studies in actual power grids. In what follows, we present two types of experimental validation. For the first time, the applicability and fault location performance of the EMTR-FCSE metric are discussed with reference to field experiments and pilot tests carried out in real power system environments.

4.2 Field Experiment on an Unenergized Distribution Line

In November 2016, the EMTR-FCSE method was, for the first time, experimentally studied in a real power system environment. A field experiment was performed on a 10-kV power distribution network in Shanxi Province, China.

4.2.1 Experimental set-up and approaches

1) Experimental set-up

The experimental set-up is schematically represented in Fig. 4.1. This field experiment used a 677-m long overhead-line section, which spans a total of 11 towers numbered 22 to 32, configured as a double-circuit distribution network. The experiment was carried out using one of the three-phase circuits. Another circuit was left open at both terminals during the experiment.
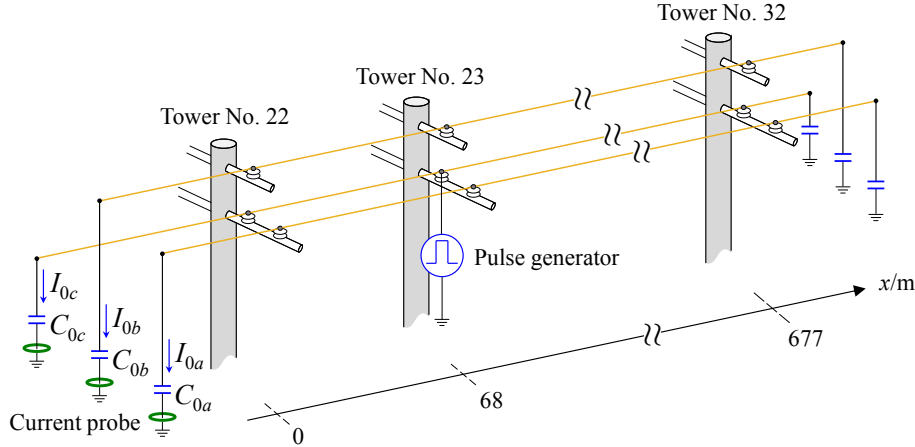
Figure 4.1 – Schematic representation of the experimental set-up based on a 10-kV power distribution network. Another three-phase circuit (not shown in this diagram) was in open-circuit at both ends.

The picture of the overhead-line tower and its cross-section geometry are presented in Fig. 4.2. The overhead-line conductors are made of steel-reinforced aluminum with a conductivity of 3.5×10^7 S/m and a diameter of 18.4 mm. Besides, the measured soil conductivity is about 0.1 S/m.

At the line terminals (i.e., the towers numbered 22 and 32), the three-phase overhead lines were grounded through lumped capacitors (denoted by C_{0a}, C_{0b}, and C_{0c} in Fig. 4.1). These capacitors emulate the high-frequency impedance of power transformers. Indeed, the fault-originated electromagnetic transients in power systems are generally characterized by a spectrum with frequencies in the order of tens to hundreds of kilohertz [156]. Given this, a power transformer can be represented, to a first approximation, by its winding-to-ground
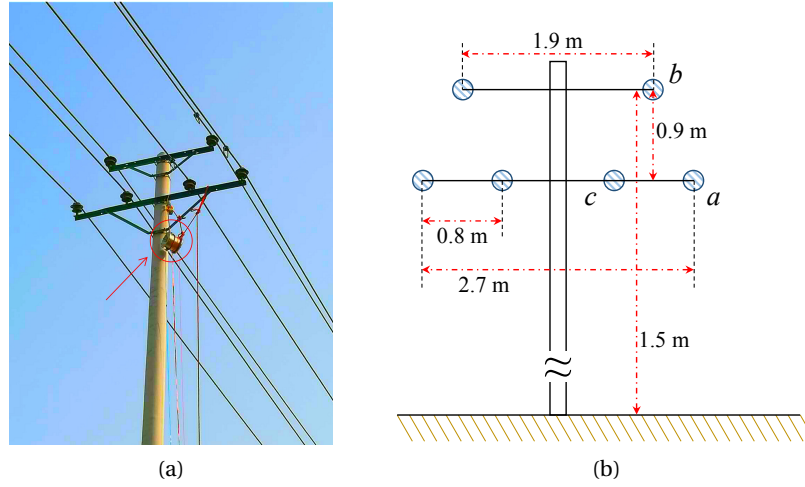
Figure 4.2 – Picture and cross-section geometry of the overhead-line tower. (a) Picture of Tower No. 23 at which the pulse generator (marked with the red circle) was connected to one of the phase conductors. (b) Cross-section geometry.

capacitance C_t. Additionally, power transformers are generally connected to a bus through bushings, whose high-frequency electrical characteristics are also dominated by a line-to-ground capacitance C_b. Therefore, the characteristics of a power transformer (seen from the incoming-line side) can be approximated by the parallel circuit of C_t and C_b.

According to actual measurements on 10-kV-level transformers operating on the local power distribution network, the capacitance values of C_t and C_b were found to be in the range of 800 to 900 pF and 450 to 550 pF, respectively. As a result, a 1500-pF thin-film capacitor (per phase) was used to model the power transformer in the field experiment.

2) Fault emulation

The first experiment focused on the validation of the FCSE metric using full-scale power networks. The data acquisition (e.g., measurements on electromagnetic transient signals) was still by means of conventional laboratory instruments (e.g., current probes). Given this, the distribution line in the experiment was unenergized and the fault emulation was realized by injecting a voltage pulse into the overhead-line conductor (see Fig. 4.1). The waveform of the pulse was designed to dominate a wide enough frequency band to cover the typical frequency spectrum of the electromagnetic transients generated by a fault in power systems.

To this end, a compact capacitor-discharging type pulse generator was developed (see Fig. 4.3). The pulse generator can be equivalently represented by a *RLC* circuit (see Fig. 4.3c), in which the capacitance C of the energy-storage capacitor is 6.97 nF. The coaxial structure of the generator restricts the discharging-circuit inductance L to some hundreds of nanohenries. In the experiment, the output end of the generator was connected to the line conductor of Phase *c*, which was assumed to be the faulty phase. The discharging-voltage of the generator was controlled by a spark gap switch (see Fig. 4.3b). Compressed air was used as a dielectric in the

(a)   (b)   (c)
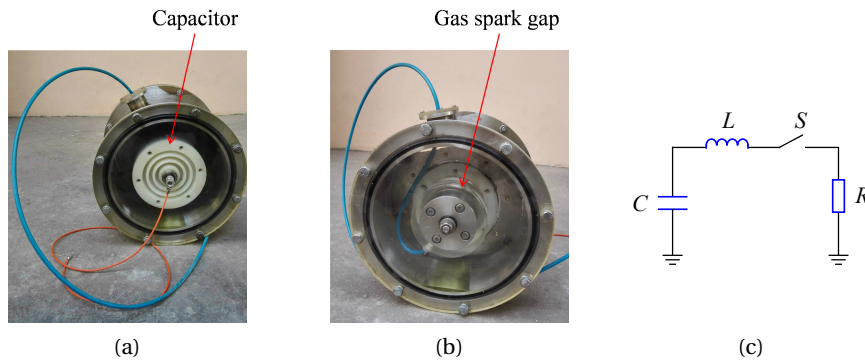
Figure 4.3 – Pictures and equivalent circuit of the capacitor-discharging type pulse generator. (a) Front view. (b) Back view. (c) Equivalent circuit.

(a)

(b)
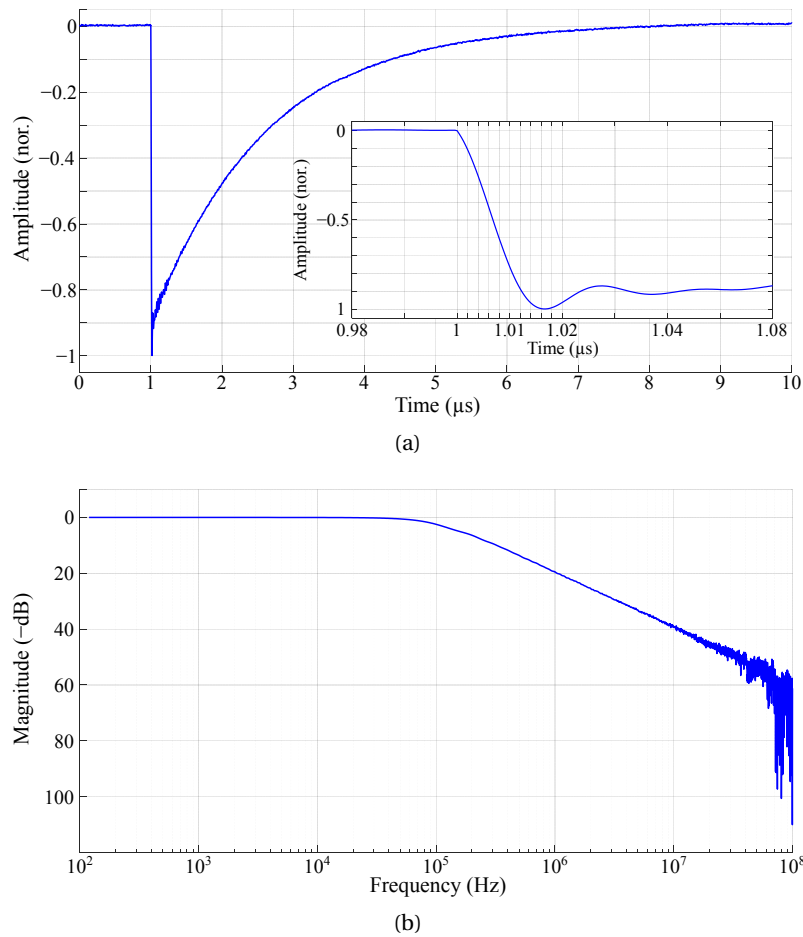
Figure 4.4 – Normalized waveform and magnitude spectrum of the voltage pulse characterized by a rise time and a full width at half maximum of 12 ns and 960 ns, respectively. (a) Waveform. (b) Magnitude spectrum.

switch. In the experiment, the peak value of the voltage pulse reached about 10 kV.

In the laboratory environment, we used a 200-Ω metal oxide film resistor as the load R of the pulse generator to emulate its discharging situation during the field experiment. This resistance approximates the actual input impedance seen by the pulse generator. More precisely, R appears to be about half the characteristic impedance of the single-phase overhead line formed by Phase c and the ground, meanwhile ignoring the other conductors and the mutual coupling. As shown in Fig. 4.4a, the produced double-exponential pulse features a rise time t_r of 12 ns (see the inset in Fig. 4.4a) and a full width at half maximum (FWHM) of about 1 μs. According to Fig. 4.4b, the spectrum of the pulse extends to significant frequencies up to a few megahertz.

4.2.2 Experimental results and analysis

Recalling the set-up described in Fig. 4.1, a solid-fault event was emulated along the distribution line by injecting a voltage pulse (with the nominal parameters t_r = 12 ns and FWHM = 960 ns) into the line conductor of Phase c at the overhead-line tower numbered 23. The single observation point was situated at Tower No. 22, which was 68 m away from the assumed fault location.

The terminal response to the pulse injection was measured in the form of the current signals flowing through the grounding capacitors (i.e., C_{0a} to C_{0c}). Pearson 8585C current probes were employed to undertake the measurement. The data acquisition task was fulfilled by a Tektronix DPO 3054 oscilloscope. The main specifications of the experimental instruments are reported in Table 4.2.

Table 4.2 – Main specifications of the experimental instruments

	Model	Parameter	Value
Current probe	Pearson 8585C	Sensitivity	0.5 V/A
		Bandwidth	200 MHz
Oscilloscope	Tektronix DPO 3054	Sampling rate	2.5 GS/s
		Vertical resolution	11 bits
		Bandwidth	500 MHz
Impedance analyzer	Wayne Kerr 6520B	Precision	±0.05%

A numerical model of the experimental set-up was developed in the EMTP-RV simulation environment [161, 162]. The 677-m long overhead-line was modeled using the constant-parameter (CP) line module. Note that, for achieving an accurate reflection of the actual situation, both circuits of the distribution line were modeled. As regards the line boundary condition, the terminal elements composed of the thin-film capacitor and its leading wires were described using a RLC equivalent circuit, whose parameters were determined by actual

measurements using an impedance analyzer and considering a frequency range from DC to 20 MHz. The inferred values for R, L and C are respectively 433.75 mΩ, 1.5025 μH and 1.4995 nF.

In what follows, the experimental results corresponding to the set-up configurations of single-phase and three-phase are presented and discussed.

1) *Single-phase configuration*

The first experiment considered a single-phase configuration wherein only Phase c was terminated at each end on a 1500-pF thin-film capacitor, whereas the other two phases were left open at both terminals. Fig. 4.5 shows the recorded transient current signal in response to the injection of the voltage pulse at Tower No. 23.
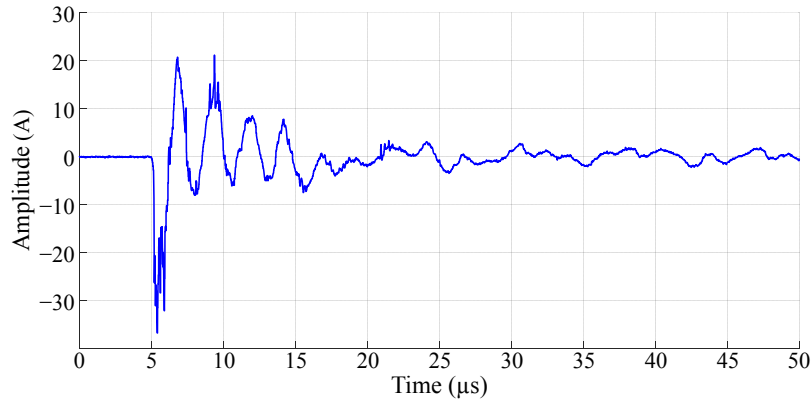
Figure 4.5 – Experimentally-recorded current waveform of Phase c at Tower No. 22 in the single-phase configuration.

The current signal in Fig. 4.5 was time reversed and back injected into the numerical model of the experimental set-up in EMTP-RV. Then the fault current was simulated at each of a series of *a priori* guessed fault locations $x_{\mathbb{G}}$. For the experiment case, we defined the location of each tower as a guessed fault location. For the sake of comparison, the fault current was also simulated for the other two phases (a and b) whose line terminals were left open.

Fig. 4.6 reports the calculated fault current signal energy as a function of the guessed fault location. In agreement with the EMTR-FCSE metric, Phase c of Tower No. 23, where the voltage pulse was originally imposed, is evidently characterized by the highest energy. It is also worth noticing that the induced currents appear at the other two phases as a result of the mutual coupling among the phases. However, the induced energy level is comparatively low.
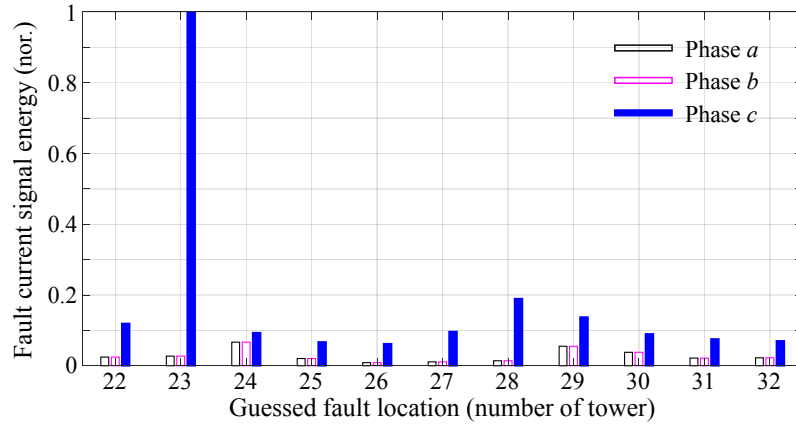
Figure 4.6 – Normalized fault current signal energy as a function of the guessed fault location for the single-phase configuration. The normalization results in the maximum energy among the guessed fault locations (defined along the three phases) as the unit value.

2) *Three-phase configuration*

In the second experiment, all three phases of the circuit were grounded through the capacitors at both ends, as it is described in Fig. 4.1. With the injection of the voltage pulse at Phase *c*, the experimental set-up emulated a single-phase-to-ground fault occurrence. Fig. 4.7 shows the fault-originated transient current signals measured at the terminal tower numbered 22 after triggering the voltage pulse. In the backward-propagation simulation, the time-reversed copies of the currents were synchronously back-injected into the EMTP-RV model from their respective observation points at Tower No. 22.
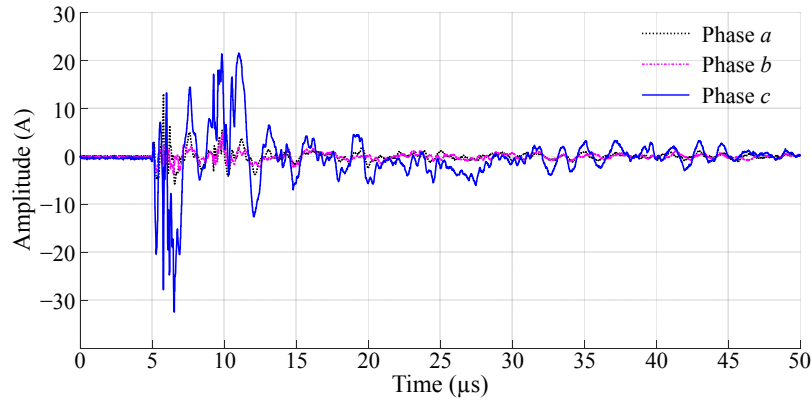
Figure 4.7 – Experimentally-recorded three-phase current waveforms at Tower No. 22 in the three-phase configuration.

In Fig. 4.8, the calculated fault current signal energies are presented. Among the guessed fault locations, Phase *c* of Tower No. 23 appears to be the location of the maximum energy. Compared to the previous case, the three-phase configuration also takes accounts of the

additional coupling effects caused by the common-grounded capacitors at the two terminals. As mentioned earlier, this approximates the operating condition of power transformers connected to buses or loads at power network terminals. Even so, the EMTR-FCSE metric is still validated.
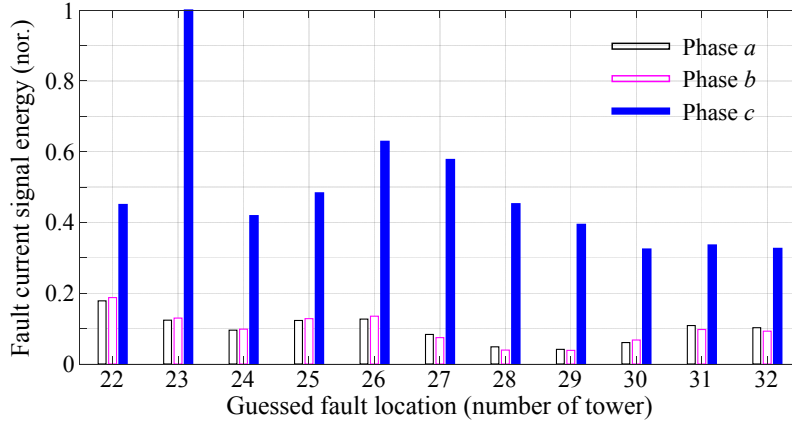
Figure 4.8 – Normalized fault current signal energy as a function of the guessed fault location for the three-phase configuration. The normalization results in the maximum energy among the guessed fault locations (defined along the three phases) as the unit value.

4.3 Embedded Controller Based Fault Location System Implementing EMTR-FCSE Metric

The field experiment and the earlier-performed reduced-scale experiment (e.g., [79]) both relied on laboratory instruments and, thus, manual operations were inevitably involved in each of the procedures from data acquisition to implementation of EMTR-based fault location methods. From the perspective of practical application, it is preferable to realize an automatic operation (making use of suitable hardware units/platforms), which is capable of integrating the functions of the whole process, namely from detecting a fault occurrence to reporting an estimation of the most-likely fault location.

Addressing such demands, the present study realized the deployment of the EMTR-FCSE method into an embedded controller coupled with a suitable sensing and triggering system. A ruggedized prototype of an EMTR-based fault location system was developed and later applied in a pilot trial, integrating the functions of fault detection, data acquisition, time-reversal processing, and electromagnetic transients (EMT) simulations. Note that the fault location system can be readily adapted to a diversity of fault location methods, either EMTR based or not. In view of the non-trivial aspects related to this deployment, details about the development are given here below.

The block diagram of the fault location system is shown in Fig. 4.9. It is composed of:

i) a sensing and measurement unit,
ii) a data acquisition unit,
iii) a triggering block, and
iv) an embedded platform (to perform EMTR-based fault location process).
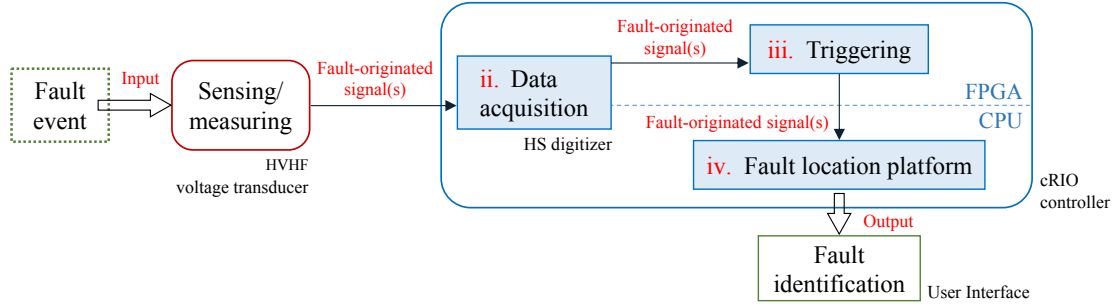
Figure 4.9 – Block diagram of the embedded controller based fault location system. The upstream procedures *i*) to *iii*) deliver fault-originated transient signals to the platform *iv*) implementing the EMTR-based fault location process.

Figure 4.9 also explains the adopted hardware support for the respective blocks, which mainly includes a National Instruments (NI) CompactRIO embedded controller, a NI high-speed (HS) digitizer and an ALTEA high-voltage high-frequency (HVHF) voltage transducer. With regard to the processing units, both the CPU processor and reconfigurable FPGA of the controller are used. As it can be seen, the data acquisition capability is dependent on both units, while the blocks *iii*) and *iv*) are supported by the FPGA and the CPU of the controller respectively. The LabVIEW programming environment is used to develop the logic of the blocks *ii*) to *iv*).

4.3.1 Sensing/measuring unit

For measuring fault-originated electromagnetic transient signals and delivering the signals to the input/output (I/O) module of the data acquisition block, the sensing/measuring instruments are expected to be capable of: *i*) having a sufficient bandwidth to cover the frequency spectra of the electromagnetic transients associated with power system faults and *ii*) transforming the measured fault responses (typically more than ten kilovolts) to the withstand voltage level of low-power signal cables (e.g., RG-58 standard cable). Given the above consideration, an ALTEA 18-kV high-frequency voltage transducer was employed. Fig. 4.10 shows the transducer installed in the primary substation (serving as the observation point) of a medium voltage distribution feeder.

The rated primary and secondary voltages of the transducer are respectively 18 kV and 18 V. The transducer features a frequency band up to 500 kHz with zero phase displacement and,

Figure 4.10 – 18-kV voltage transducer installed in the primary substation of a medium voltage distribution network (courtesy of Murielle Gerber, EPFL). The distribution network was employed in the pilot test of EMTR-based fault location methods.

thus, is suitable for acquiring fault-originated transient signals in general fault occurrences. Note that the transients resulting from a fault that occurs near the measurement unit (i.e., the substation serving as an observation point) might present its components at frequencies up to the order of megahertz. In this case, post-phase correction can be applied using the transducer's transfer function, which is characterized up to a frequency of 4.5 MHz (3-dB bandwidth).

4.3.2 Data acquisition unit

To sample the acquired signals from the voltage transducer, a NI 4-channel high-speed digitizer was utilized. This module has independent analog-to-digital (ADC) converters with a 14-bit resolution and can operate in two acquisition modes: continuous mode and record mode. In the continuous mode, the module transfers real-time data at an aggregate rate of 4 MSamples/s across all channels. In the record mode, the module stores samples into inboard memory at up to 20 MSamples/s/ch. It is also possible to combine these two modes for advanced triggering systems. This feature was exploited to develop a suitable triggering system to detect fault occurrences in power systems (see details in the next section).

4.3.3 Triggering block

There is a need for a proper triggering system to detect the high-frequency transients resulting from a fault occurrence. Since these transients are superimposed to the network steady-state frequency component (e.g., of 50 Hz), a simple threshold-triggering criterion is generally inadequate. The adopted triggering approach (e.g., [167, 168]) is briefly described in what follows.

According to the logic structure of the triggering block shown in Fig. 4.11, first, the ADC module of the digitizer is operated in the continuous mode, in which it transfers in real-time the data at the rate of 1 MSamples/s. These data [i.e., $S(t)$ in Fig. 4.11] are used as input to a first-order Butterworth low-pass (LP) digital IIR (infinite impulse response) filter, which

outputs the low-frequency components [i.e., $S_l(t)$] of the original transient signal. The LP cut-off frequency can be generally set as 1 kHz. The filtered signal is subtracted from the original one, resulting in a processed signal containing only the high-frequency components [i.e., $S_h(t)$] characterized by a frequency spectrum larger than the cut-off frequency. Then, when the absolute value of the obtained signal is greater than a predefined threshold value (i.e., $\hat{S}$), it activates the recording mode of the digitizer. For example, $\hat{S}$ can be set as 0.1 p.u. of the network phase-to-ground voltage ([167, 168]).
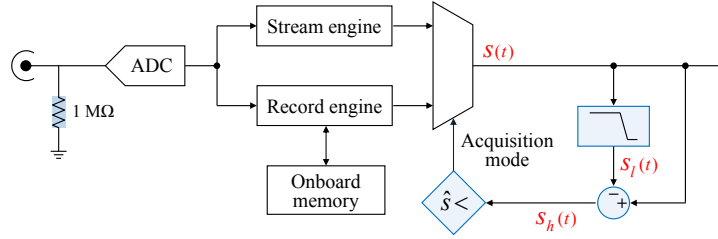
Figure 4.11 – Block diagram of the triggering block.

4.3.4 Fault location platform

The EMTR-FCSE method is numerically implemented on the cRIO embedded controller, which uses a dual-core Intel Core processor and supports Windows Embedded Standard 7 operating system. These features allow executing third-party Windows-based simulation software on this chassis. For the developed prototype, the EMTP-RV simulation environment (e.g., [161, 162]) is considered to model target power networks and conduct the EMT simulations in the backward-propagation stage of EMTR.

The platform processes the fault-originated transient signals delivered by the triggering block and provides fault information (e.g., fault phase and fault location) as output, as illustrated in Fig. 4.12.
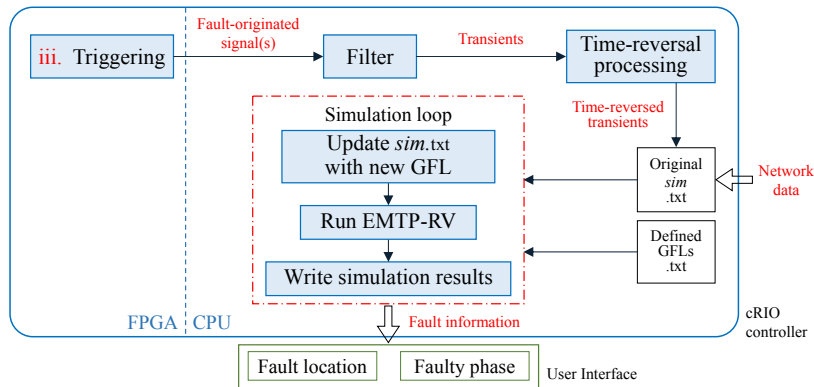
Figure 4.12 – Block diagram of the fault location platform.

Chapter 4. Electromagnetic Time Reversal Based Fault Current Signal Energy Metric: Analysis and Experimental Validation

First, the target power network is numerically represented using the knowledge of its electrical and geometrical parameters as well as boundary conditions. Based on the simulation model, EMTR-RV generates the corresponding simulation file *sim* (.txt)[1], which contains information about network topology, components, and their parameters. The original simulation file is updated by reading the time-reversed transients.

Next, the backward propagation is simulated for every *a priori* defined guessed fault location. To be specific, the fault is modeled by a switch operation. Therefore, for each independent simulation corresponding to a guessed fault location, the simulation file is once again updated by changing the connection node of the switch element. Then, EMTP-RV reads the simulation file containing the time-reversed signals as well as the updated switch information and then runs the loop of simulating the fault current signal.

Afterward, the generated simulation data are stored in the internal storage of the platform, and the fault current (switch current) vector of each guessed fault location is extracted from the output data. Subsequently, the FCSE metric is calculated to identify the maximum likelihood fault point.

It is worth mentioning that the fault location platform communicates with EMTP-RV through Windows command prompts. Moreover, a JavaScript is coded in the EMTP-RV console for commanding the loop simulations. These efforts allow the developed system to function from fault occurrence detection to fault information announcement in a fully-automatic and unattended manner.

As shown in Fig. 4.13, a prototype of the embedded controller based fault location system was deployed in the primary substation of a medium-voltage distribution feeder, undertaking the tasks of measurements and fault location in the pilot test.
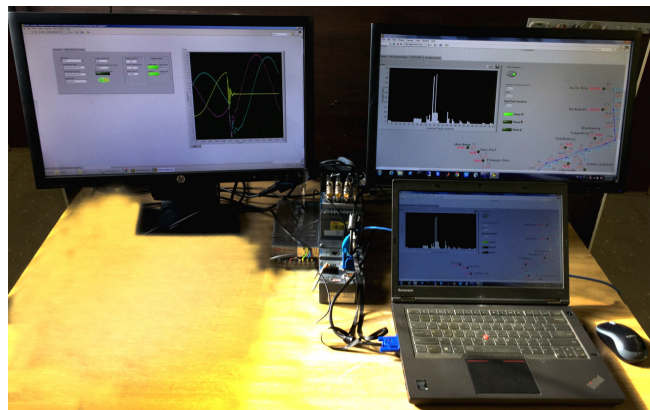
Figure 4.13 – A prototype of the embedded controller based fault location system deployed in the primary substation of the pilot distribution feeder.

---

[1] EMTP-RV converts simulation settings and modelings (with the graphical user interface) into a simulation file, which contains the descriptive texts about simulated network topology and parameters, device models, simulation functions, and so forth.

4.4 Pilot Test on a Live Distribution Feeder

Encouraged by the promising performance of the classical EMTR-FCSE method in the field experiment, the experimental study proceeded to further validate the method with reference to real fault events in live power networks. To this end, a series of pilot tests have been conducted since 2017.

Compared to the first full-scale experiment in China, the pilot trial was performed using a live power distribution network subject to real faults. In this respect, the following observations are in order.

i) The distribution network is characterized by a topology of multiple branches and strong inhomogeneity (i.e., mixed overhead lines with underground cables). One of the unique features of the EMTR-based fault location method is that it only requires single-end measurement. The conducted pilot test allows demonstrating this unique feature for the first time on such a topologically-complex and inhomogeneous grid.

ii) A range of faults of very different natures (e.g., in terms of fault type and fault impedance) is intentionally triggered when the pilot distribution network is under normal operating conditions.

iii) The pilot test is also designed to evaluate the developed fault location system. By equipping the primary substation of the pilot network with a prototype of the fault location system, the fault detection and location procedure allowed to be executed in a highly automatic and efficient manner.

4.4.1 Pilot networks

The pilot network is a radial medium voltage distribution feeder, located in the region of Fribourg, Switzerland, which connects two distribution substations. It is operated with a resonant neutral (i.e., Petersen coil). A schematic description of the network is presented in Fig. 4.14. The tested distribution feeder consists of 11.9-km long double-circuit lines (overhead lines) operating at 18/ 60 kV and multiple 18-kV three-phase laterals branching from the main feeder. The branched lines are overhead lines, underground cables, or mixed configuration, with lengths ranging from tens of meters to a few kilometers.

The medium voltage side of the primary substation (i.e., substation A in Fig. 4.14) feeding the network was selected to serve as the single observation/monitoring station and was equipped with the front-end voltage transducer together with the fault location platform described before.

Four categories of locations along the network were considered as the guessed fault locations, which include: *i*) junction between two overhead lines (along the main feeder), *ii*) junction between two underground cables, *iii*) junction between the main feeder and a branch lateral
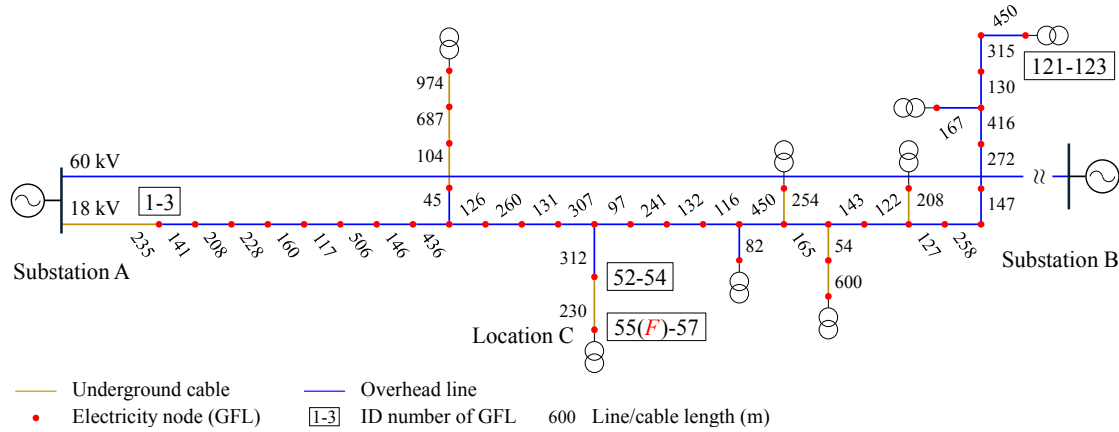
Figure 4.14 – Schematic description of the distribution network employed in the pilot test. All the electricity nodes (e.g., overhead-line towers along feeder and junctions between feeder and branch laterals) in the network are defined as guessed fault locations, which are numbered from 1 (i.e., Phase *a* at the initial terminal of the outlet cable from substation A) to 123 (i.e., Phase *c* at the most distant load terminal).

and *iv*) terminal of branch lateral connected to load. As a result, a total of 123 guessed fault locations were *a priori* defined.

The numerical representation of the pilot distribution network was given in the EMTP-RV simulation environment making use of the constant-parameter (CP) line module [161, 162]. As to the power transformers located at the two substations (A and B) as well as at the load terminals, they were modeled considering their high-frequency input impedance of the secondary winding. To be precise, the network was grounded through a 10-kΩ resistor per phase at the above-mentioned terminals.

4.4.2   Fault cases

The pilot test was carried out by intentionally triggering a single-phase-to-ground fault along one of the network laterals, as this is the most common fault type in distribution networks. Besides, as known, fault impedance can vary in a wide range and may introduce significant errors in some fault location methods. Therefore, both solid and resistive faults were emulated in the test.

Moreover, the pilot test also took account of various fault causes. In addition to permanent faults consequent upon a short circuit between a phase conductor and the ground, the test also covered transient fault events due to single and intermittent phase-to-ground arcing discharges, respectively.

In the test, the short-circuit solid fault was realized by a switching maneuver using an ABB 24-kV medium-voltage switchgear. The arcing-fault emulator was composed of a spark gap with two electrodes separated by the distances of 14 cm and 3.5mm for the single- and intermittent-

Figure 4.15 – Two types of fault emulators with spark gaps used in the pilot test. (a) A 14-cm long spark gap for the single-arcing fault and (b) a 3.5-mm long spark gap for the intermittent-arcing fault.

arcing faults, respectively, as shown in Fig. 4.15. In the above-mentioned fault cases, the equivalent impedance of the phase-to-ground channel/arc remained significantly smaller than the characteristic impedance of the lines/cables in the tested distribution network. The resistive fault was emulated by means of adding a 30-Ω (water) resistor into the discharge circuit of the voltage switchgear. Note that the considered impedance value is typically witnessed in resistive faults that occur in the tested distribution network.

The tested fault cases are summarized in Table 4.3.

Table 4.3 – Emulated single-phase-to-ground fault cases in the pilot test

Fault type	Fault impedance	Fault cause
Solid fault	Approx. $0\ \Omega$	Short circuit Single-arcing discharge Intermittent-arcing discharge
Resistive fault	$30\ \Omega$	Short circuit

4.4.3 Off-line validation

Prior to performing the on-line live tests, a solid (single-phase-to-ground) short-circuit fault was studied first for the purpose of assessing the accuracy of modeling the tested network in the EMTP-RV environment. The fault was triggered at the line-cable mixed lateral terminal indicated as Location C (see Fig. 4.14), which was about 3.6 km away from the monitoring substation A. Then, an identical fault case was simulated using the network model in the EMTP-RV environment.

Figure 4.16 compares the measured fault-originated high-frequency voltage transients of the faulty phase with the simulation counterpart. The filter sub-block of the fault location platform functions in extracting the high-frequency transients from the transient signal, in which the
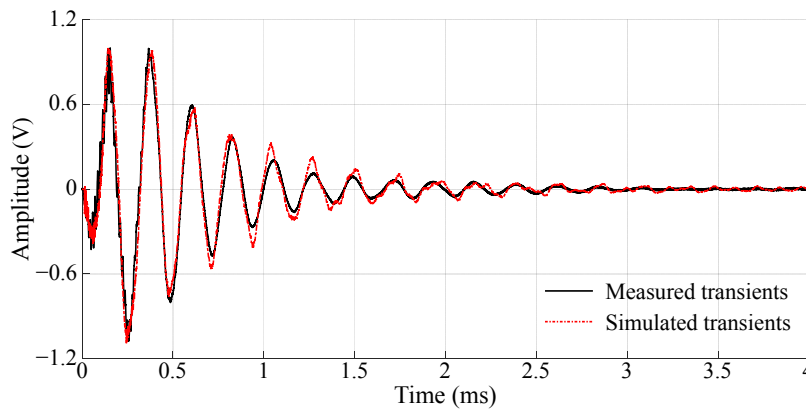
Figure 4.16 – Fault-originated transients respectively obtained from the on-line measurement and the off-line simulation.

high-frequency transients are superimposed to 50-Hz fundamental frequency component. According to the spectrum analysis module integrated into the filter sub-block, the measured fault response exhibits its high-frequency components at frequencies above 3 kHz. Given this, a 4th-order Butterworth high-pass IIR filter with a cutoff frequency of 3 kHz was used.

For the sake of comparison, both waveforms in Fig. 4.16 are normalized with reference to the respective maximum amplitudes. As it can be observed, the simulated signal reaches an impressive agreement with the measured one. The frequency-domain components of the high-frequency transients are mainly concentrated at 4.452 kHz (measured transients) and 4.456 kHz (simulated transients), respectively. As known, this frequency (also known as fault switching frequency) is a function of the time delay caused by voltage/current wave propagating from the fault location to the observation point. With regard to the traveling-wave based analysis, the model can be considered to accurately represent the tested network in the simulation environment.

It is worth mentioning that the time step of the corresponding simulation in EMTP-RV was set to 50 ns, which is in accordance with the maximum sampling rate (20 MSamples/s) of the fault location system. It is determined by the data acquisition block. The filtering and simulation settings mentioned above were also applied to the later on-line tests.

4.4.4 On-line tests

As summarized in Table 4.3, two types of single-phase-to-ground faults were triggered at a specific location (i.e., Location C in Fig. 4.14) in the live network. In the backward-propagation stage, a total of 123 electrical nodes were identified as the guessed fault locations. The fault current signal was simulated at each of those locations.

1) Solid fault

a) Short-circuit fault

Figure 4.17 depicts the transient voltage signals measured at the observation substation A when a short-circuit fault was generated at location C (see Fig. 4.14). The fault occurred during the positive half period of Phase *a*. As it can be seen, a 25-ms time window was set to record the full transient process.
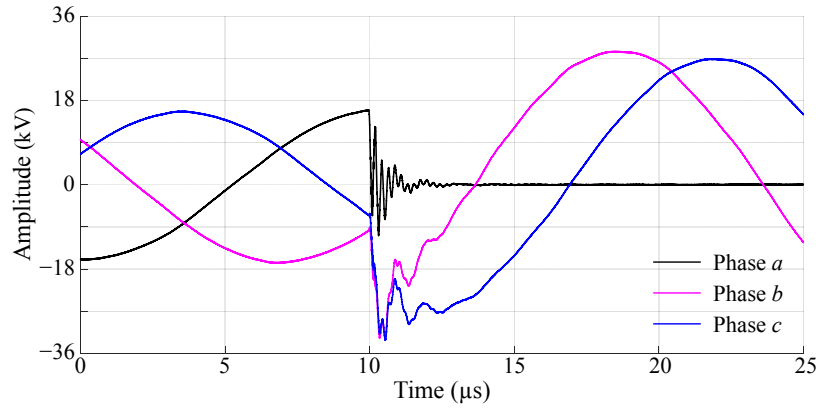
Figure 4.17 – Transient voltage signals measured in response to a solid short-circuit fault occurring in location C.

In order to improve the computation efficiency, it is preferable to define the temporal length of the forward-stage time window (i.e., T_w^{DT}) as short as possible to cut off the tail section of the transients whose amplitudes are near zero. Fig. 4.18 depicts the high-frequency transients of the faulty phase within a duration of 2 ms. The transients of non-faulty phases (i.e., Phases *b* and *c*) are not shown, yet the same processing was also applied to these signals.

The extracted three-phase high-frequency transients were inverted in time and synchronously back-injected into the network model to simulate the fault current at each of the guessed fault locations.

Figure 4.19 illustrates the calculated current energy as a function of the assigned identification number of the guessed fault location each. Note that the positions of Phases *a*, *b* and *c* of the underground cable at the location C are numbered from 55 to 57. It can be observed that Node 55, corresponding to the true fault location of the faulty phase (labeled with F in Fig. 4.14), is
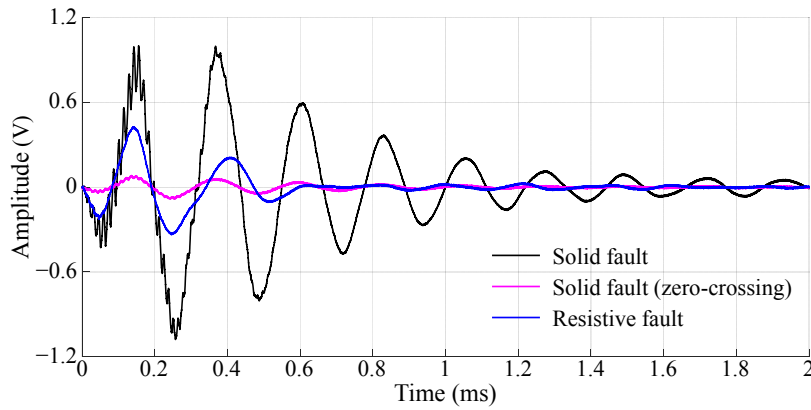
Figure 4.18 – Fault-originated high-frequency transients (of the faulty phase) truncated to a 2-ms duration.
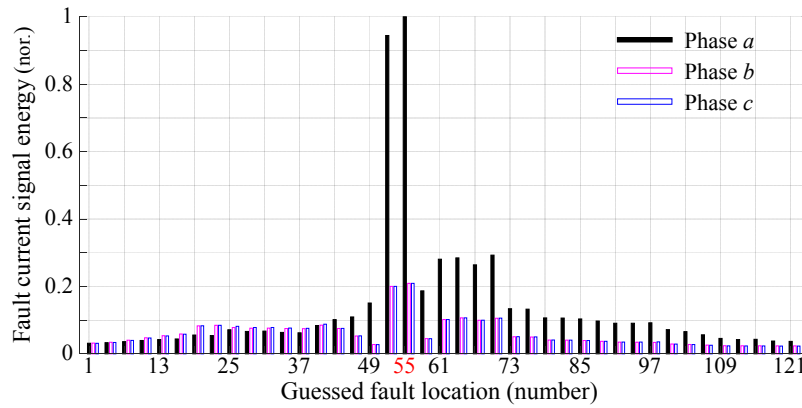
Figure 4.19 – Fault current signal energy calculated in the solid short-circuit fault case as a function of the guessed fault location. The normalization is performed with respect to the calculated maximal energy. The true fault location is numbered 55 in the backward-propagation model.

clearly characterized by the maximum energy among the defined 123 guessed fault locations. Thereby, both the faulty phase and the exact location are determined accurately according to the EMTR-FCSE metric.

b) Single-arcing fault

Figure 4.20a presents the transient voltage signals measured in response to a solid type of single-arcing fault occurrence. The fault was triggered by an arc ignition between the 14-cm spaced electrodes of the spark gap during the negative half period of Phase *a*. Like the previous case, the fault occurred at the node numbered 55. Fig. 4.20b demonstrates the applicability of the fault location system implementing the EMTR-FCSE the metric in dealing with such arcing faults. As it can be seen, the maximum of the fault current signal energies indicates the true fault position as well as the faulty phase.

(a)

(b)
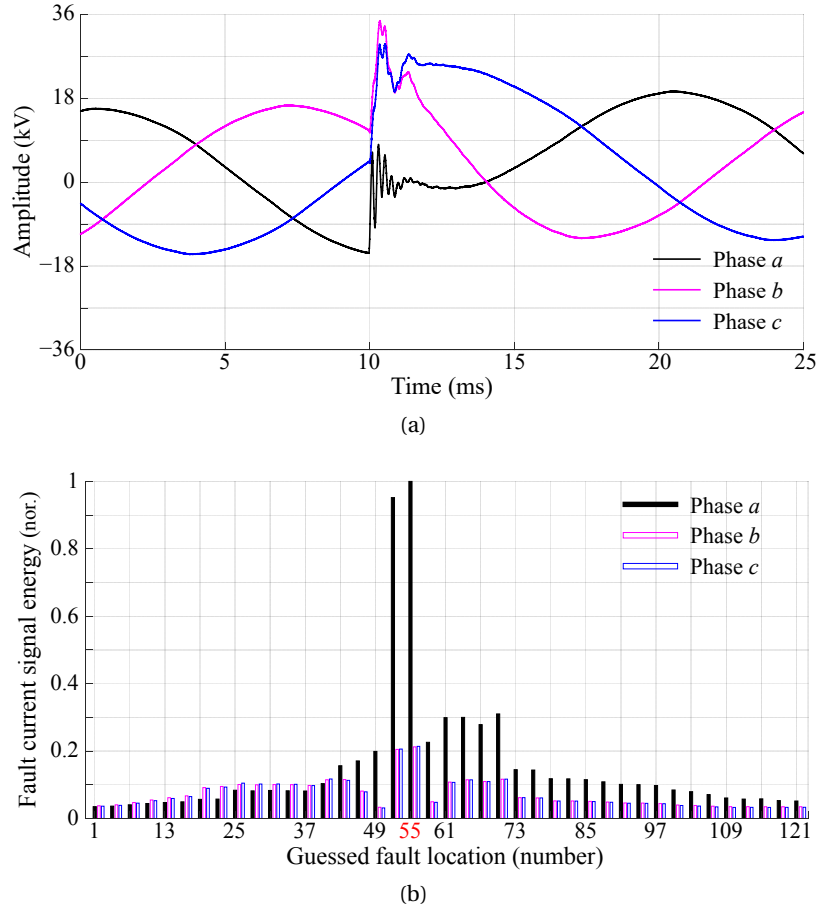
Figure 4.20 – (a) Transient voltage signals and (b) fault current signal energies of the single-arcing fault case. The previously-introduced normalization approach is applied. The true fault location is numbered 55 in the backward-propagation model.

c) Intermittent-arcing fault

The intermittent-arcing discharge in the pilot test was specified with a double arc ignition during one 20-ms period. The inter-electrode distance of the fault emulator was reduced to 3.5 mm. The intermittent-arcing fault originated transient voltage signals are plotted in Fig. 4.21a. Still, the fault was triggered at the lateral terminal numbered 55 among the guessed fault locations.

As it can be seen, unlike the previous cases, two transient processes occurred due to the first and subsequent phase-to-ground arcing discharges. In the backward-propagation stage, the simulations were first carried out using a 2-ms time window (T_w^{DT}) as it is in the previous case, in which only the initial transients were time reversed and back injected. Then, the time window was extended to 12 ms, taking the full transients into account. The obtained distributions of the fault current signal energies are shown in Fig. 4.21b wherein the normalization is made with reference to the calculated maximum energy when the full transients (in

(a)

(b)
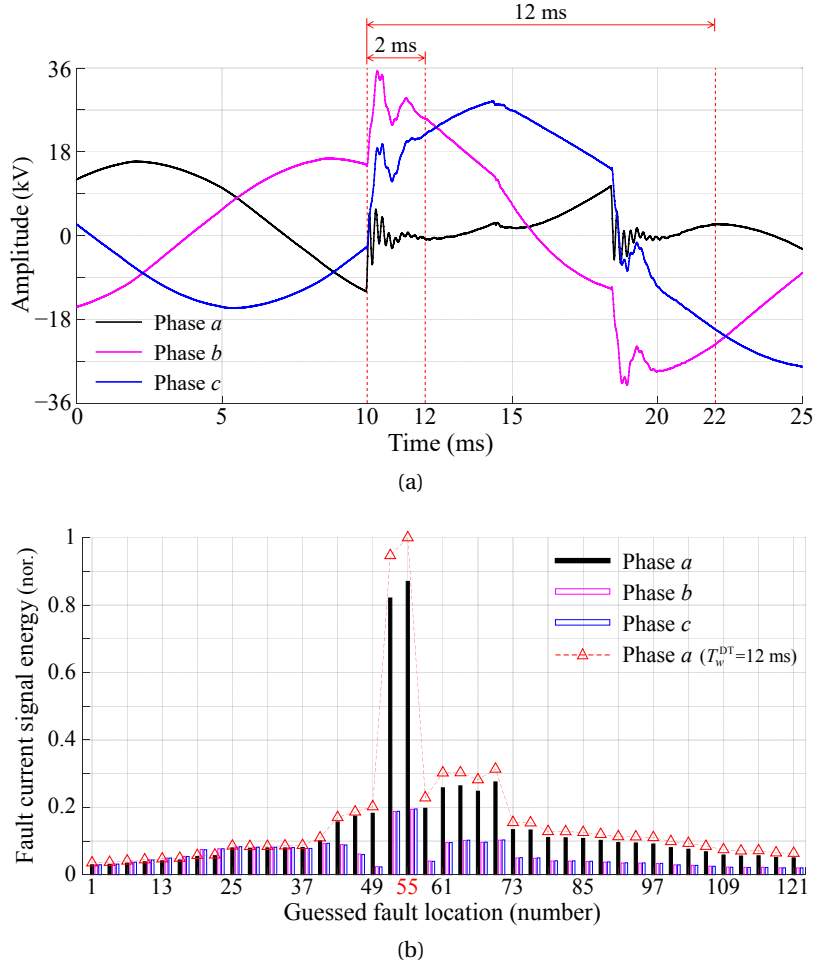
Figure 4.21 – (a) Transient voltage signals and (b) fault current signal energies of the inter-mittent-arcing fault case using the initial transients in 2 ms (represented with bars) and the full transients in 12 ms (represented with marked dashed line). The normalization is with reference to the maximum energy resulted from using the full transients. The real fault location is numbered 55 in the backward-propagation model.

$T_w^{\mathrm{DT}} = 12$ ms) are considered. It is worth observing that, when comparing the energies of the fault current signals resulting from the respective time window settings, the differences turn out to be mainly at a quantitative level and, in both cases, the location of the fault and the faulty phase are clearly pinpointed.

2) Resistive fault

For the resistive fault case, a 30-Ω water resistor was connected in series with the fault emulator. The acquired transient voltage signals are depicted in Fig. 4.22a. Like the previous case, the fault occurred at Location C.

(a)

(b)
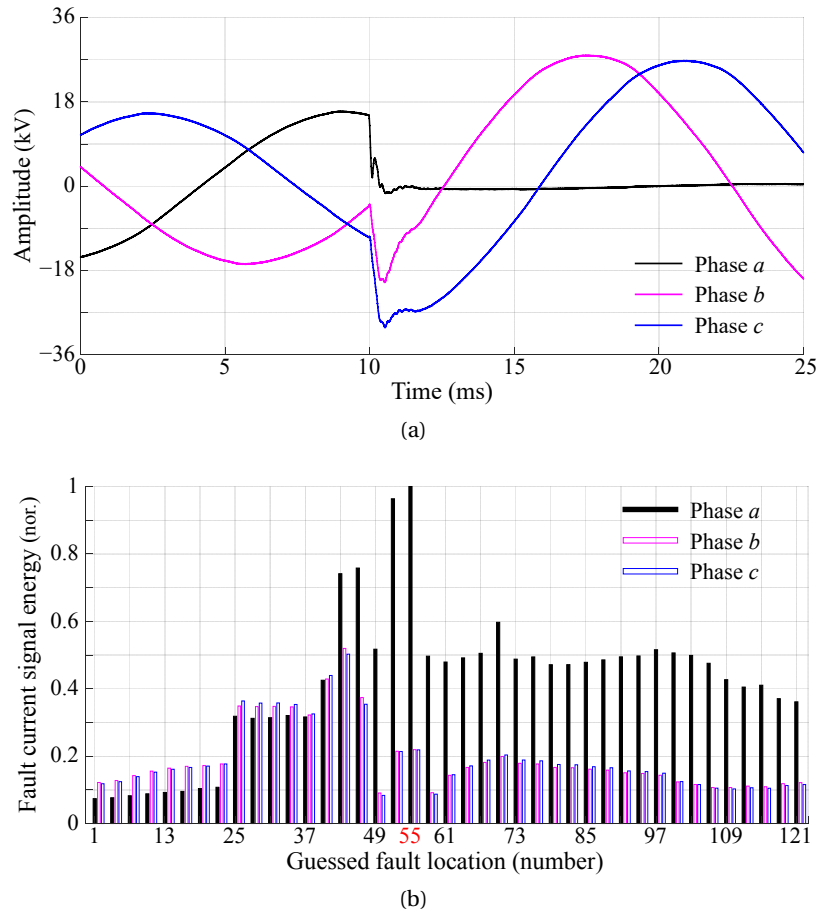
Figure 4.22 – (a) Transient voltage signals and (b) fault current signal energies of the resistive fault case wherein the fault impedance is 30 Ω. The previously-introduced normalization approach is applied. The true fault location is numbered 55 in the backward-propagation model.

By ignoring the presence of the mutual coupling between the conductors, the faulty phase of the underground cable has a characteristic impedance of 14.6 Ω (i.e., considering the faulty phase as a single coaxial cable), thereby the voltage reflection coefficient at the fault location is positive, unlike the case of a solid fault wherein the reflection coefficient appears negative. As it can be seen in Fig. 4.18, the high-frequency transients generated by the resistive fault have much faster damping compared to the solid fault case of Fig. 4.17. This also results in a different distribution of the fault current signal energies at the guessed fault locations, as it can be observed in Fig. 4.22b. Nevertheless, the true fault location and the faulty phase are again accurately identified.

4.4.5   Analysis: performance assessment

1) Performance assessment: fault location accuracy

In practice, for the sake of minimizing the computation time, the EMTR-based fault location process can be conducted successively in two steps. In the first step, only the so-called electricity nodes (e.g., overhead-line towers along the main feeder, junctions between the main feeder and lateral branches) are considered as guessed fault locations. For the tested distribution network, a total of 123 electricity nodes are defined (see Fig. 4.14). This first step identifies, in a relatively short time, the faulty line/cable. Then, an off-line analysis further subdivides the faulty line/cable into shorter sections according to user-desired location accuracy.

As the results have been presented for the previous cases, the calculated fault current energies show a second peak at the guessed fault location numbered 52, which is adjacent to the true fault location (i.e., the guessed fault location No. 55). The guessed fault locations No. 52 and No. 55 are the two ends of the 230-m long faulty underground cable (see Fig. 4.14). The cable was subdivided into 23 sections in order to reach a location accuracy of 10 m. Accordingly, the off-line simulations were performed with a finer time step of 5 ns, which is smaller than one-tenth of the wave propagation delay of the 10-m cable section.
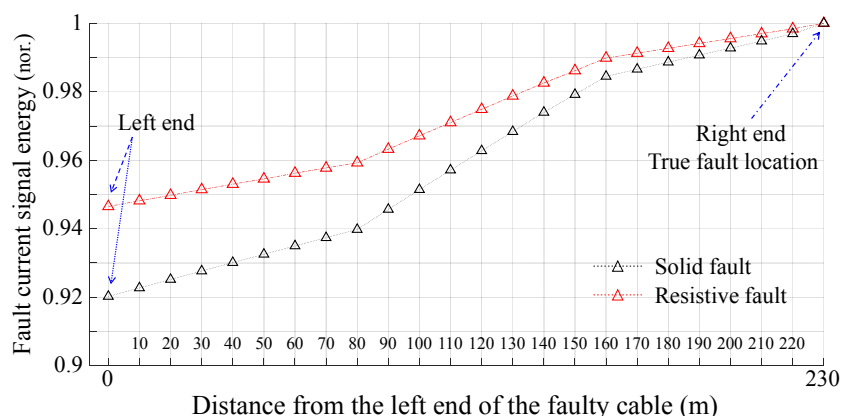
Figure 4.23 – Fault current signal energy as a function of the distance from the left end of the faulty cable.

In Fig. 4.23, the normalized fault current signal energy is presented as a function of the distance from the left end of the faulty cable. It is shown that the energy reaches its maximum at the true fault location (i.e., the right end of the cable) in the emulated solid fault case of (Fig. 4.17) and in the resistive fault case (of Fig. 4.22a) as well. Because of the highly similar behaviors compared with that of the solid fault case, the fault current signal energies calculated for the cases of arcing faults are not presented in Fig. 4.23.

The off-line analysis demonstrates that the EMTR-FCSE metric reaches a better-than-10-m location accuracy for the tested faults. Yet, achieving such accuracy level requires considerable computation time in the backward-propagation simulations and, thus, higher achievable accuracy was not tested.

2) Performance assessment with respect to fault inception angle

In the pilot test, a special fault case with a near-zero fault inception angle was intentionally triggered with the purpose of assessing the fault location performance of the FCSE metric in dealing with such zero-crossing faults. According to the waveforms depicted in Fig. 4.24a, the fault was generated when the faulty phase (i.e., Phase a) voltage just crossed the zero amplitude. As known, such faults can be challenging for some traveling-wave based fault location methods due to the difficulty in distinguishing the fault switching frequency as well as the decreased signal-to-noise ratio of the extracted high-frequency transients.

(a)

(b)
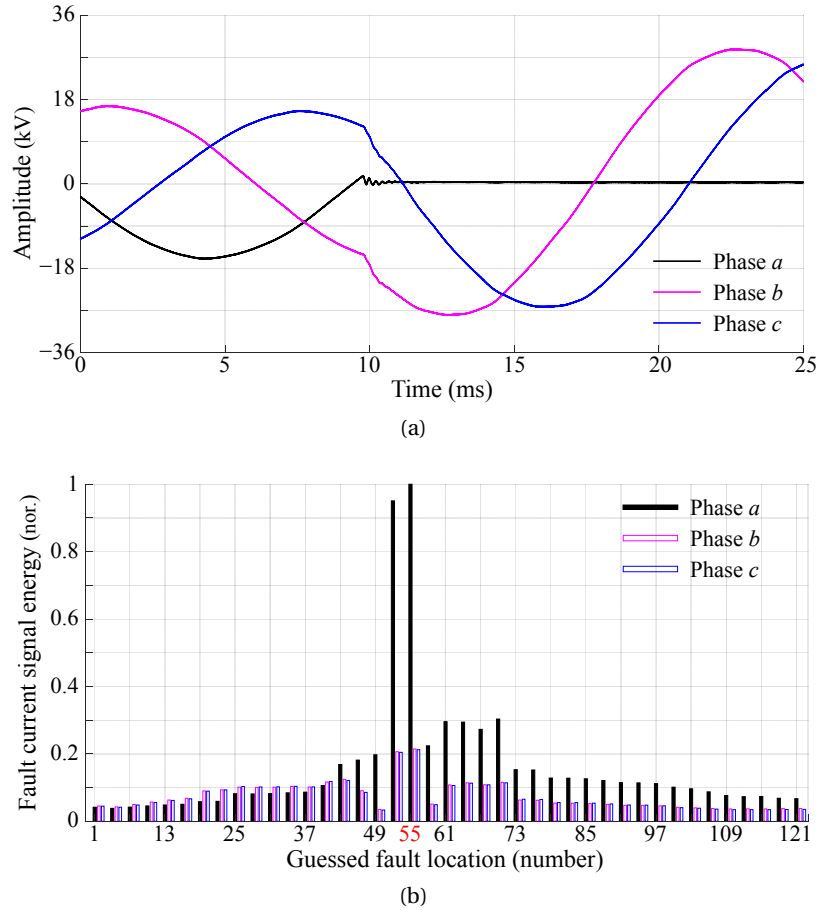
Figure 4.24 – (a) Transient voltage signals and (b) fault current signal energies of the zero-crossing short-circuit fault case. The previously-introduced normalization approach is applied. The true fault location is numbered 55 in the backward-propagation model.

The extracted transients of the zero-crossing fault case are also shown in 4.18, exhibiting a relatively weaker oscillation compared with those of the short-circuit fault case of Fig. 4.17. Despite this, the fault location platform was able to detect the fault occurrence. More importantly, as it is illustrated in Fig. 4.24b, the calculated FCSE metric exhibits a very similar pattern as the one obtained in the case of Fig. 4.17. The true fault location can be identified with the pronounced maximum of the fault current signal energies. This result demonstrates the capability of the EMTR-FCSE metric in identifying such a zero-crossing type of fault.

3) *Performance assessment with respect to time-window length*

The study in [169] analyzed the influence of the length of the observation time window on the performance of the EMTR-FCSE metric. In the simulated fault case of [169], the entire fault-generated transient signals were 200-ms long. The fault location was identified when a limited time window (T_w^{DT}) was applied to truncate the full transients to a few milliseconds, in which only the initial transients were contained.

The pilot test also assessed the fault location performance of the EMTR-FCSE metric considering different time window lengths. The above-presented results refer to the use of a 2-ms time window (T_w^{DT}), in which the fault-originated transients have sufficiently decayed (see Fig. 4.18). In the off-line analysis, the time window length was further reduced to 1 ms, which approximates a few oscillation periods of the transients. Even in this situation, for all the tested faults, the fault location could still be accurately identified by the FCSE metric.

Taking the solid fault case of Fig. 4.17 and the resistive fault case of Fig. 4.22a as examples, Fig. 4.25 compares the calculated fault current energies based on the time-window lengths of 1 ms and 2 ms, respectively. For the sake of clarity, Fig. 4.25 does not depict those energies of the non-faulty phases (*b* and *c*) under the 2-ms setting, which have been presented in the previous section. As it can be observed, the reduction of the time-window length does not substantially change the patterns of the energy distribution at the guessed fault locations.

(a)

(b)
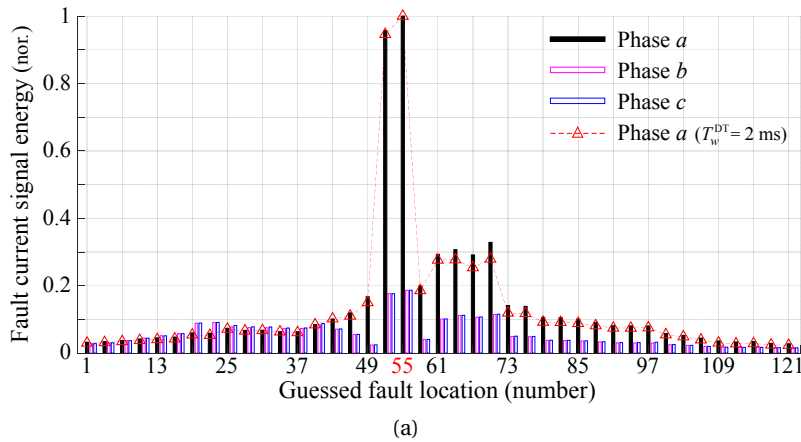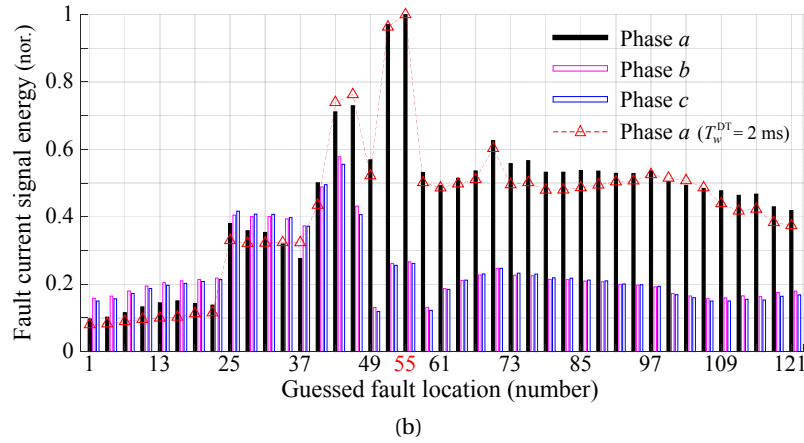
Figure 4.25 – Fault current signal energies calculated using the fault-originated transients over two different time windows of 1 ms (represented with bars) and 2 ms (represented with marked dashed line), respectively. (a) The solid fault case of Fig. 4.17. (b) The resistive fault case of Fig. 4.22a.

4.5   Conclusion

In this chapter, we presented and analyzed the results of two types of experimental campaigns that served the purpose of validating the EMTR-FCSE metric and evaluating its fault location performance, especially making use of actual power grids.

The first experimental validation utilized a full-scale unenergized 677-m-long, 10-kV double-circuit distribution line. A fault occurrence was emulated by injecting a voltage pulse into one line conductor of the three-phase circuit. The frequency spectrum of the injected voltage pulse was specified such that its originated electromagnetic transients were compatible with typical power system faults. It was shown that the EMTR-FCSE metric accurately identified the fault location as well as the faulty phase in the configured one- and three-phase experimental scenarios.

Later, the experimental study was extended to a pilot test based on a live distribution feeder. Compared to the first full-scale experiment, the complexity of the power-network topology was enhanced in the pilot test, in which a radial distribution feeder with multiple branches and multiple nodes was considered. The distribution network contained a mix of overhead lines and underground cables, therefore, incorporating strong inhomogeneity. More importantly, the pilot test evaluated the performance of the EMTR-FCSE metric in dealing with various realistic faults. The pilot test involved two types of single-phase-to-ground faults, including solid and resistive (with 30-Ω fault impedance) fault cases. The pilot test also took account of the common fault mechanism. The emulated faults were respectively caused by a short circuit, a single-arcing discharge, and an intermittent-arcing discharge.

The faults were artificially triggered at an overhead line-underground cable mixed lateral terminal when the distribution network was in service. The fault-originated voltage transient

signals were measured at a single observation point situated at the primary substation, which was 3.6 km away from the fault location. The live test results demonstrated that the EMTR-FCSE metric is capable of accurately identifying the fault location as well as the faulty phase in all tested fault cases. Moreover, according to the off-line analysis, the achievable fault location accuracy reached 10 m.

The present study has equally devoted attention to accommodating the demand for deploying EMTR-based fault location methods into a suitable hardware platform and also coupling it with a proper sensing and triggering system. In this respect, an embedded controller based fault location system has been developed, integrating the functions of fault detection, data acquisition, time-reversal processing, and electromagnetic transients (EMT) simulations.

In the pilot trial, a ruggedized prototype of the fault location system was deployed at the primary substation of the tested distribution feeder. It has been shown that the fault location system properly functioned in detecting all the tested fault events, including zero-crossing cases, and efficiently implementing the EMTR-FCSE method.

5 Electromagnetic Time Reversal Similarity Properties and Its Fault Location Application

The classical application of electromagnetic time reversal (EMTR) to fault location in power systems develops the category of so-called matched-media based fault location methods, proposing the use of various metrics, such as fault current signal energy (e.g., [79]) and fault current signal amplitude (e.g., [84]). The term 'matched-media' refers to the identity between the media of the forward-propagation stage (i.e., the fault occurrence stage) and backward-propagation stage (i.e., the fault location stage). The recent study has enriched the EMTR fault location methodology by proposing another category of methods correspondingly named EMTR mismatched-media based fault location methods (detailed in the next chapter).

The existing studies, considering either matched or mismatched media, generally devote attention to the assessment of the features (e.g., energy and amplitude) of the signals observed in the backward-propagation stage to determine the most-likely fault location. In contrast, the study in this chapter presents a rigorous integrated time-frequency domain analysis to prove a similarity characteristic contained in the matched-media based fault location process. A novel EMTR cross-correlation metric is proposed to quantitatively represent the time-domain similarity between the fault-originated transient signal (measured as a response to a fault occurrence) and the fault current signal in the backward stage simulated at the true fault location and, thus, to identify the location of a fault occurrence.

The chapter includes results of publications [85, 170, 171].

5.1 Time-Correlation Properties Inherent to Time-Reversal Process

5.1.1 General problem

Let us consider a medium in which transport phenomena are taking place. Let us also suppose that these transport phenomena can be modeled by wave equations. In a generic way, a functional transformation f exists and constrains the physical laws governing the system evolution in time. Formally, we can write (5.1), in which $\boldsymbol{x}$ represents the system states, $\boldsymbol{r}$ identifies the space coordinate, $\boldsymbol{x}|_{t_0}$ the array of initial conditions of the system state, $\boldsymbol{z}$ the array of the system parameters, and Υ, Π and Ξ the functional operators describing the system physical laws in the standard form of wave equations. These operators also include knowledge of boundary conditions.

$$f : \mathbb{R}^{n+1} \to \mathbb{R}^{n+1}$$
$$\Upsilon \left[\frac{\partial^2 \boldsymbol{x}(\boldsymbol{r},t)}{\partial t^2}, \boldsymbol{x}(\boldsymbol{r})|_{t_0}, \boldsymbol{z} \right] + \Pi \left[\frac{\partial \boldsymbol{x}(\boldsymbol{r},t)}{\partial t}, \boldsymbol{x}(\boldsymbol{r})|_{t_0}, \boldsymbol{z} \right] + \Xi \left[\boldsymbol{x}(\boldsymbol{r},t), \boldsymbol{x}(\boldsymbol{r})|_{t_0}, \boldsymbol{z} \right] = 0 \,. \tag{5.1}$$

Based on the system model, let us cast the general *time-correlation property* inherent to the time-reversal process.

As introduced in Chapter 2, the general application of time reversal to locate a source at an unknown position $\boldsymbol{r}_0 \in \mathbb{R}^n$ can be described as a two-stage process.

In the forward-propagation stage, assuming that the source is represented by a positive Dirac impulse and its originated signals are measured at a certain number of points, $\{\boldsymbol{r}_1, \ldots, \boldsymbol{r}_i, \ldots, \boldsymbol{r}_l\}$, the so-called observation points of the *time-reversal mirror*. At the ith element of the mirror, the impulse response reads $\boldsymbol{h}_i^{\mathrm{DT}}\big(t, \langle \boldsymbol{r}_0, \boldsymbol{r}_i \rangle\big)$ wherein $\boldsymbol{r}_0$ is the unknown location of the source and $\boldsymbol{r}_i$ the location of the ith observation point.

In the backward-propagation stage, the measured response at each observation point is time reversed, such as $\boldsymbol{h}_i^{\mathrm{DT}}\big(-t, \langle \boldsymbol{r}_0, \boldsymbol{r}_i \rangle\big)$, and back injected into the original medium. It is worth observing that, by virtue of the reciprocity (e.g., [158]), the impulse response in the backward stage (i.e., from $\boldsymbol{r}_i$ to the source point $\boldsymbol{r}_0$) is identical to the one obtained in the forward stage, namely

$$\boldsymbol{h}_i^{\mathrm{RT}}\big(t, \langle \boldsymbol{r}_i, \boldsymbol{r}_0 \rangle\big) = \boldsymbol{h}_i^{\mathrm{DT}}\big(t, \langle \boldsymbol{r}_0, \boldsymbol{r}_i \rangle\big) \,. \tag{5.2}$$

Considering the contributions from all the l observed points, the system impulse response, namely the signal received at the source location, reads

$$\boldsymbol{s}(t, \boldsymbol{r}_0) = \sum_{i=1}^{l} \boldsymbol{h}_i^{\mathrm{DT}}\big(-t, \langle \boldsymbol{r}_0, \boldsymbol{r}_i \rangle\big) \otimes \boldsymbol{h}_i^{\mathrm{RT}}\big(t, \langle \boldsymbol{r}_i, \boldsymbol{r}_0 \rangle\big) \,. \tag{5.3}$$

Substituting (5.2) into (5.3) produces

$$s(t, \boldsymbol{r}_0) = \sum_{i=1}^{l} \boldsymbol{h}_i^{\mathrm{DT}}\big(-t, \langle \boldsymbol{r}_0, \boldsymbol{r}_i \rangle\big) \otimes \boldsymbol{h}_i^{\mathrm{DT}}\big(t, \langle \boldsymbol{r}_0, \boldsymbol{r}_i \rangle\big). \tag{5.4}$$

It is readily found that (5.4) corresponds to the *auto-correlation* function of the forward-propagation-stage system impulse response. As it is in a matched filter, each individual convolution in (5.4) reaches a positive maximum at $t = 0$. The maximum can be physically interpreted as the energy of $\boldsymbol{h}_i^{\mathrm{DT}}\big(t, \langle \boldsymbol{r}_0, \boldsymbol{r}_i \rangle\big)$. It is evident that all contributions from different observation points interfere constructively at the source, resulting in (5.4) reaching a maximum at $t = 0$ as well.

5.1.2 Fault location problem

Let us now focus on the problem of fault location in power networks. In this case, the generic system function (5.1) reduces to the telegrapher's equations governing the voltage and current wave propagation along transmission lines. For the sake of simplicity and without loss of generality, let us consider a single-wire overhead line.

Figures 5.1a and 5.1b schematically depict respectively the forward-propagation system emulating a fault occurrence along the line and the backward-propagation system in which fault-originated transient signals (recorded in the previous stage) are time reversed and back injected into the network from the line left end, where the observation point is situated.

In Fig. 5.1a, the solid fault occurrence (at $x = x_f$) is equivalently described by a switch initiating a short-circuit between the phase conductor and the ground. γ and Z_C denote the propagation constant and the characteristic impedance, respectively. At the line terminals, the phase conductor is grounded through high impedance, namely Z_0 and Z_L, which represents the input impedance of power transformers (in the frequency range associated with the fault-generated high-frequency transients). Still, using a single observation point at $x = 0$, the recorded post-fault transient voltage reads $V_0^{\mathrm{DT}}(t)$. In the backward-propagation stage, as shown in Fig. 5.1b, $V_0^{\mathrm{DT}}(t)$ is time reversed and back injected by its Norton equivalent $I_0^{\mathrm{TR}}(t)$, and fault currents $I_{x_{\mathbb{G}}}^{\mathrm{RT}}(t)$ are observed at a series of *a priori* guessed fault locations:

$$x_{\mathbb{G}} = \big\{\, x_g \,\big|\, x_{g,0} = x_f,\, x_{g,1},\, x_{g,2},\, \dots \big\}. \tag{5.5}$$

Given this, the impulse response of the forward-propagation system can be obtained by injecting a Dirac-shaped voltage signal at the fault location and calculating the voltage across the terminal high impedance, and thus, it reads[1] $\boldsymbol{h}^{\mathrm{DT}}\big(t, \langle x_f, 0 \rangle\big)$.

---

[1] Since a single observation point is used, the subscript i of $\boldsymbol{h}^{\mathrm{DT}}\big(t, \langle x_f, 0 \rangle\big)$ equals one and is omitted. In what follows, unless otherwise emphasized, the coordinate $x = 0$ of the observation point will be not explicitly indicated either.

(a)

(b)
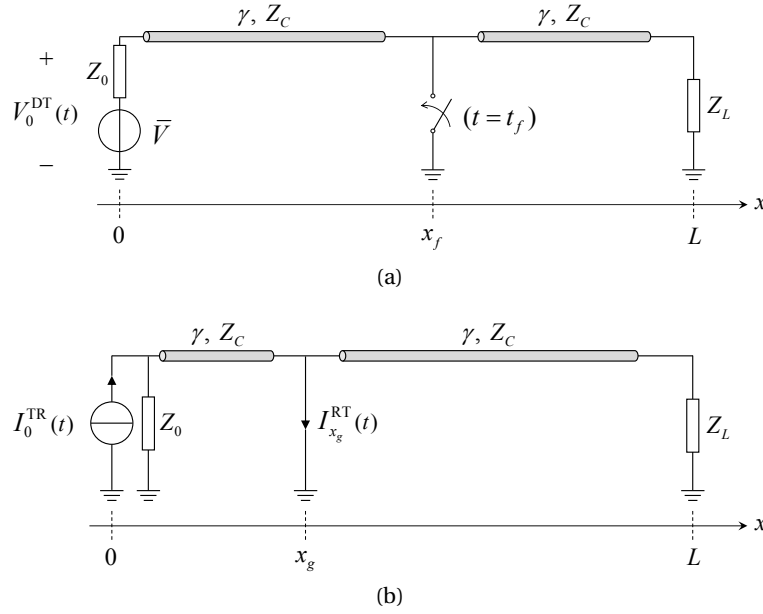
Figure 5.1 – Simplified representation of a solid fault event in power networks. (a) Forward-propagation stage: the stage of fault occurrence. The line is assumed to be supplied with a DC voltage (i.e., $\overline{V}$) at the line terminal $x = 0$. (b) Backward-propagation stage: the stage to locate the fault using EMTR.

As discussed in the previous section, the application of the time-reversal theory to identify an unknown source and its spatial location requires the knowledge of the system impulse responses. Note that $\boldsymbol{h}^{\mathrm{DT}}(t, x_f)$ is a function of the fault location x_f. However, x_f is actually the desired solution to the forward-backward-propagation system problem of fault location. More importantly, from a practical point of view, power systems generally monitor fault-generated transient signals [e.g., $V_0^{\mathrm{DT}}(t)$] responding to a fault occurrence, but not to the transfer function $\boldsymbol{h}^{\mathrm{DT}}(t, x_f)$. Thus, the fact that $\boldsymbol{h}^{\mathrm{DT}}(t, x_f)$ cannot be inferred either through calculation or from measurement poses an obstacle to applying straightforwardly the *time-correlation property* of (5.4) for carrying out the fault location task. For this reason, an alternative exploitation of (5.4) is needed to cope with the inaccessibility of $\boldsymbol{h}^{\mathrm{DT}}(t, x_f)$.

In the next section, we will demonstrate that the identity of (5.2) implies a similarity between the time-reversed fault-originated transient current I_0^{TR} and the fault current (denoted by $I_{x_f}^{\mathrm{RT}}$), which results from the back injection of I_0^{TR}, at the true fault location in both the time domain and the frequency domain. Furthermore, the fault location task can be performed through assessing the similarity between those observable variables without requiring the knowledge of $\boldsymbol{h}^{\mathrm{DT}}(t, x_f)$.

5.2 Time- and Frequency-Domain Analysis of Electromagnetic Time Reversal Based Similarity Properties

In this section, the similarity characteristic is first discussed and mathematically proved through an integrated time-frequency domain analysis. The proof is based on analytically deriving the target variables (I_0^{TR} and $I_{x_{\mathbb{G}}}^{\mathrm{RT}}$) with reference to the configured solid fault occurrence illustrated in Fig. 5.1a and applying the EMTR-based fault location process. Note that, for the sake of simplicity, the analysis in this section is carried out considering a lossless line. The applicability of the proved similarity characteristic to lossy media will be validated in the following sections in which realistic power network parameters are employed.

5.2.1 Frequency-domain analysis

1) Forward-propagation stage: fault occurrence

In the frequency domain, the solid fault occurrence in Fig. 5.1a can be represented by injecting an equivalent step-like voltage [54, 125]:

$$\overline{V} \cdot E(j\omega) = \overline{V} \cdot 1/(j\omega), \quad (\omega > 0), \tag{5.6}$$

into the line conductor at the fault location $x = x_f$. $E(j\omega)$ is the Fourier transform of the unit-step function $\varepsilon(t)$. The forward-stage line set-up is described using two-port networks, as shown in Fig. 5.2.
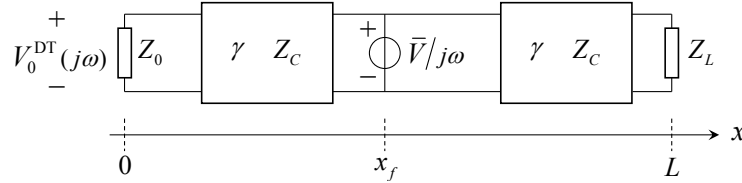
Figure 5.2 – Two-port representation of the forward-propagation-stage line set-up.

The fault response calculated at the observation point $x = 0$ reads

$$V_0^{\mathrm{DT}}(j\omega) = \frac{\left(1 + \rho_0^V\right) \cdot e^{-j[\beta(\omega) \cdot x_f]}}{1 + \rho_0^V \cdot e^{-j[\beta(\omega) \cdot 2x_f]}} \cdot \left[\overline{V} \cdot E(j\omega)\right], \tag{5.7}$$

in which ρ_0^V is the voltage reflection coefficient at $x = 0$, $\beta(\omega)$ is the phase constant as ω/v under the lossless-line assumption and v is the propagation speed along the line. Note that both the voltage reflection coefficient ρ_0^V and the characteristic impedance Z_C appear frequency independent by assuming a lossless line.

75

In the frequency domain, the impulse response $\boldsymbol{h}^{\mathrm{DT}}(t, x_f)$ is equivalent to a transfer function, given by

$$H^{\mathrm{DT}}(j\omega) = \frac{V_0^{\mathrm{DT}}(j\omega)}{\overline{V} \cdot E(j\omega)} = \frac{\left(1 + \rho_0^V\right) \cdot e^{-j[\beta(\omega) \cdot x_f]}}{1 + \rho_0^V \cdot e^{-j[\beta(\omega) \cdot 2x_f]}} \ . \tag{5.8}$$

By virtue of the general boundary condition of power networks with respect to the frequency content of typical fault-originated transient signals, where ρ_0^V approximates to $+1$ [79, 125], the following theorem is proposed.

Theorem 1 *provided that $\rho_0^V = +1$, the local maxima of $\left|V_0^{\mathrm{DT}}(j\omega)\right|$ coincide with the Fourier expansion coefficients of a periodic square wave with a period being quadruple of the fault time delay Γ_{x_f}.*

Γ_{x_f} is defined as the line one-way time delay caused by traveling-wave propagation from the fault location (i.e., $x = x_f$) to the observation point (i.e., $x = 0$) and *vice versa*.

To prove the magnitude-frequency characteristic of $V_0^{\mathrm{DT}}(j\omega)$ stated by *Theorem 1*, we first calculate the magnitude or modulus of the forward-propagation-stage transfer function $H^{\mathrm{DT}}(j\omega)$ as

$$\left|H^{\mathrm{DT}}(j\omega)\right| = \frac{1 + \rho_0^V}{\sqrt{1 + \left(\rho_0^V\right)^2 + 2\rho_0^V \cdot \cos\left[\beta(\omega) \cdot 2x_f\right]}} \ . \tag{5.9}$$

For the sake of numerical illustration, we specify the parameters of the overhead line in Fig. 5.1 by those of typical 380-kV transmission lines. As to the boundary conditions, the terminal impedance, namely Z_0 and Z_L, is set to 100 kΩ each. Meanwhile, the line length L and the fault location x_f are assumed to be 8 km and 5 km, respectively. Finally, without losing generality, we assume that the injected step-like voltage is of unit amplitude (i.e., $\overline{V} = 1$).

Given this, the magnitude spectrum of $H^{\mathrm{DT}}(j\omega)$ and that of the unit-step function $1/(j\omega)$ are together depicted in Fig. 5.3. As it can be observed, the frequency components of $H^{\mathrm{DT}}(j\omega)$ predominately concentrate at a number of narrow frequency bands. More specifically, it can be proved that $\left|H^{\mathrm{DT}}(j\omega)\right|$ features harmonic characteristic.

Property 1 *the local maxima of $\left|H^{\mathrm{DT}}(j\omega)\right|$ appear at the fault time delay dependent fundamental frequency f^0 and its odd harmonics. The set of the resonance frequencies is*

$$\mathbb{F}^{\mathrm{DT}} = \left\{ f_i = (2i - 1) \cdot f^0 \ \middle| \ f^0 = 1/\left(4\Gamma_{x_f}\right), \ i = 1, 2, 3, \ldots \right\}, \tag{5.10}$$

where f^0 is generally called the fault switching frequency.

More importantly, the local maxima are all equal, with

$$\left|H^{\mathrm{DT}}\right|^m = \left|H^{\mathrm{DT}}(j\omega)\right|_{\omega = 2\pi \cdot \mathbb{F}^{\mathrm{DT}}} = \frac{1 + \rho_0^V}{1 - \rho_0^V} = \frac{Z_0}{Z_C} \ . \tag{5.11}$$
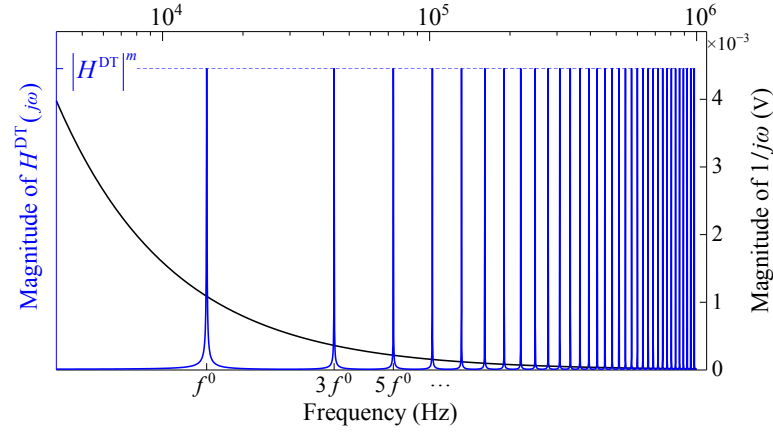
Figure 5.3 – Spectral magnitude representation of the forward-propagation-stage transfer function $H^{\mathrm{DT}}(j\omega)$ and the unit-step function $1/(j\omega)$. The value of the frequency f^0 for the considered fault case is 14.6 kHz.

Then, according to (5.7), the magnitude or modulus of $V_0^{\mathrm{DT}}(j\omega)$ reads

$$\left| V_0^{\mathrm{DT}}(j\omega) \right| = \frac{1 + \rho_0^V}{\omega \cdot \sqrt{1 + \left(\rho_0^V\right)^2 + 2\rho_0^V \cdot \cos\left[\beta(\omega) \cdot 2x_f\right]}} \, . \tag{5.12}$$

Under the boundary condition of $\rho_0^V = +1$, the resonance frequencies of $\left| V_0^{\mathrm{DT}}(j\omega) \right|$ coincide with the ones of $\left| H^{\mathrm{DT}}(j\omega) \right|$ at $\mathbb{F}^{\mathrm{DT}}$. The local maxima of $\left| V_0^{\mathrm{DT}}(j\omega) \right|$ are yielded

$$\left| V_0^{\mathrm{DT}}(j\omega) \right|_{\omega = 2\pi \cdot \mathbb{F}^{\mathrm{DT}}} = \left| H^{\mathrm{DT}}(j\omega) \right|_{\omega = 2\pi \cdot \mathbb{F}^{\mathrm{DT}}} \cdot \frac{4\Gamma_{x_f}}{(2i-1) \cdot 2\pi} = \frac{\xi}{n \cdot \pi} \, ,$$
$$i = 1, 2, 3, \dots, \quad \text{and} \quad n = 1, 3, 5, \dots, \tag{5.13}$$

where ξ is a defined magnitude coefficient.

Considering the Fourier series representation of a periodic square wave with an amplitude A and a duty cycle D as $1/2$, its complex-exponential expansion coefficients are

$$|c_n| = A \cdot D \cdot \left| \frac{\sin(n \cdot \pi \cdot D)}{n \cdot \pi \cdot D} \right| = \frac{A}{n \cdot \pi}, \quad n = 1, 3, 5, \dots \, . \tag{5.14}$$

In accordance with (5.10) to (5.14), the local maxima of $\left| V_0^{\mathrm{DT}}(j\omega) \right|$ fit the pattern $|c_n|$ at $\mathbb{F}^{\mathrm{DT}}$, proving *Theorem 1*.

As a numerical validation of the proved magnitude-frequency characteristics, we depict $\left| V_0^{\mathrm{DT}}(j\omega) \right|$ in Fig. 5.4 making use of the line parameters set previously. The superposition of the local maxima of $\left| V_0^{\mathrm{DT}}(j\omega) \right|$ upon $|c_n|$ can be explicitly observed.

77
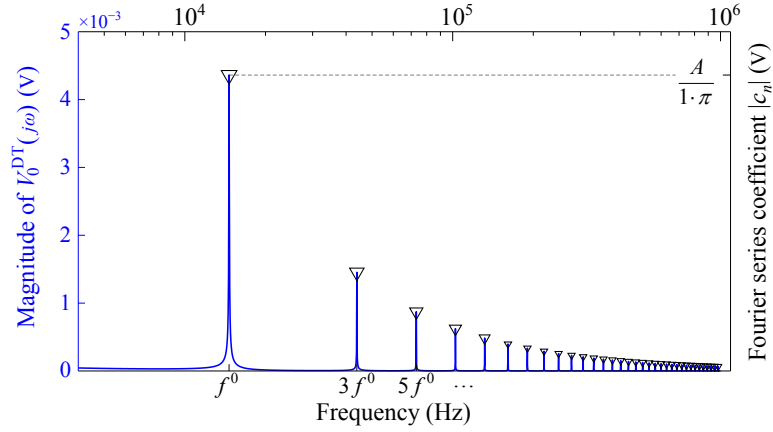
Figure 5.4 – Magnitude spectrum of $V_0^{\mathrm{DT}}(j\omega)$ and Fourier series coefficients (see the downward-pointing triangle markers) of a periodic square wave with an amplitude A and a duty cycle D as $1/2$.

Furthermore, since the cosine term in the denominator of $\left|H^{\mathrm{DT}}(j\omega)\right|$ [see (5.9)] is of even symmetry, it can be proved that f^0 and its odd harmonics also behave as the central frequency point of each narrow band. This fact, together with the foregoing discussed magnitude-frequency characteristics of $H^{\mathrm{DT}}(j\omega)$ and $V_0^{\mathrm{DT}}(j\omega)$, ensures that the time-domain counterpart of $V_0^{\mathrm{DT}}(j\omega)$ is a periodic square wave with a period of $4\Gamma_{x_f}$.

It is worth mentioning that the above analyses are in light of the frequencies ranging from the fault switching frequency of f^0. In other words, the derivation focuses on the fault-originated high-frequency transients (denoted as $\tilde{V}_0^{\mathrm{DT}}(t)$ in the time-domain analysis in the next section).

2) *Backward-propagation stage: fault location*

In order to identify the fault location, in the backward-propagation stage, the fault response $V_0^{\mathrm{DT}}(j\omega)$ observed in the forward stage is reversed in time and back injected into the line set-up from its original observation point (i.e., $x = 0$). The time-reversal operation in the frequency domain is realized by calculating the complex conjugate of $V_0^{\mathrm{DT}}(j\omega)$, namely

$$V_0^{\mathrm{DT}}(j\omega) \xrightarrow{\mathrm{TR}} V_0^{\mathrm{TR}}(j\omega): \quad V_0^{\mathrm{TR}}(j\omega) = \left[V_0^{\mathrm{DT}}(j\omega)\right]^*. \tag{5.15}$$

The backward-stage line set-up is illustrated by using the two-port network representation, as shown in Fig. 5.5.

In Fig. 5.5, $V_0^{\mathrm{TR}}(j\omega)$ is back injected by its Norton equivalent

$$I_0^{\mathrm{TR}}(j\omega) = V_0^{\mathrm{TR}}(j\omega)/Z_0. \tag{5.16}$$
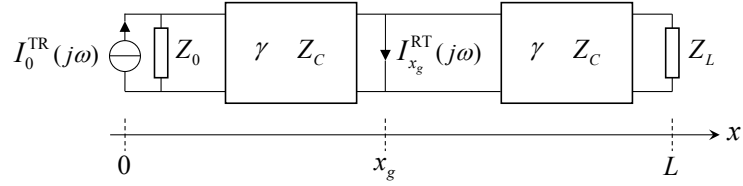
Figure 5.5 – Two-port representation of the backward-propagation-stage line set-up.

At the set of *a priori* locations $x_{\mathbb{G}}$, the fault currents are calculated as

$$I_{x_{\mathbb{G}}}^{\text{RT}}(j\omega) = \frac{\left(1+\rho_0^V\right) \cdot e^{-j\left[\beta(\omega) \cdot x_{\mathbb{G}}\right]}}{1+\rho_0^V \cdot e^{-j\left[\beta(\omega) \cdot 2x_{\mathbb{G}}\right]}} \cdot I_0^{\text{TR}}(j\omega) \,. \tag{5.17}$$

Similarly, we define the backward-propagation-stage transfer function as

$$H^{\text{RT}}(x_{\mathbb{G}}, \ j\omega) = \frac{I_{x_{\mathbb{G}}}^{\text{RT}}(j\omega)}{I_0^{\text{TR}}(j\omega)} = \frac{\left(1+\rho_0^V\right) \cdot e^{-j\left[\beta(\omega) \cdot x_{\mathbb{G}}\right]}}{1+\rho_0^V \cdot e^{-j\left[\beta(\omega) \cdot 2x_{\mathbb{G}}\right]}} \,, \tag{5.18}$$

which behaves as a function of the distance between the observation point and the guessed fault locations.

Lemma 1 *at a guessed fault location x_g, the local maxima of $\left|H^{\text{RT}}(x_g, \ j\omega)\right|$ occur at*

$$\mathbb{F}_{x_g}^{\text{RT}} = \left\{ (2i-1) \cdot f_{x_g}^0 \ \middle| \ f_{x_g}^0 = 1/\left(4\Gamma_{x_g}\right), \ i=1,2,3,\dots \right\}, \tag{5.19}$$

where Γ_{x_g} is the propagation delay between $x=0$ and $x=x_g$.

Figure 5.6 compares $\mathbb{F}^{\text{DT}}$ and $\mathbb{F}_{x_{\mathbb{G}}}^{\text{RT}}$ for $x_{\mathbb{G}}$ including the true fault location x_f (i.e., $x = 5$ km) and the locations $x_f \pm \Delta x$ with Δx being multiples of 100 m. The coincidence of $\mathbb{F}^{\text{DT}}$ with $\mathbb{F}_{x_f}^{\text{RT}}$ in Fig. 5.6 is consistent with the fact that the backward-stage transfer function $H^{\text{RT}}(x_g, \ j\omega)$ becomes identical to the forward-stage transfer function $H^{\text{DT}}(j\omega)$ when the true fault location is assumed, namely $x_g = x_f$. More importantly, because of the distance dependence of (5.8) and (5.18), the two transfer functions appear identical only at the true fault location.

From the above, $\left|I_0^{\text{TR}}(j\omega)\right|$ and $\left|I_{x_f}^{\text{RT}}(j\omega)\right|$ reach their respective local maxima at

$$\mathbb{F}^{\text{DT}} = \mathbb{F}_{x_f}^{\text{RT}} \,, \tag{5.20}$$

showing the maximal magnitudes

$$\left|I_0^{\text{TR}}(j\omega)\right|_{\omega=2\pi \cdot \mathbb{F}^{\text{DT}}} = \frac{\xi}{n \cdot \pi} \cdot \frac{1}{Z_0} \tag{5.21}$$

and

$$\left|I_{x_f}^{\text{RT}}(j\omega)\right|_{\omega=2\pi \cdot \mathbb{F}_{x_f}^{\text{RT}}} = \frac{\xi}{n \cdot \pi} \cdot \frac{1}{Z_0} \cdot \frac{Z_0}{Z_C} = \frac{\xi}{n \cdot \pi} \cdot \frac{1}{Z_C} \,, \tag{5.22}$$
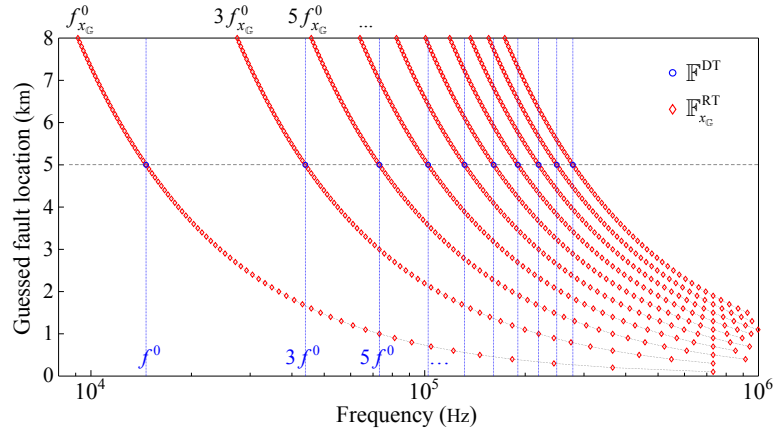
Figure 5.6 – Resonance frequencies of the forward- and backward-propagation-stage transfer functions.

with n being 1, 3, 5, ...

To sum up, according to (5.21) and (5.22), the frequency-domain analysis indicates that the magnitude-frequency characteristics of the back-injected current $I_0^{\mathrm{TR}}(j\omega)$ and the fault current $I_{x_f}^{\mathrm{RT}}(j\omega)$ equally fit the pattern of the Fourier series coefficients of a periodic square wave with a period of $4\Gamma_{x_f}$. Whereas at non-fault locations, as a result of the discrepancies between $\mathbb{F}^{\mathrm{DT}}$ and $\mathbb{F}^{\mathrm{RT}}_{x_{\mathrm{G}}}$, the magnitude-frequency behaviors of the transfer function (5.18) lose the harmonic characteristic, therefore the current waveforms are not square wave-like any more.

Note that the boundary condition of ρ_0^V being +1 is considered to reach the above conclusions. Taking the effects of reflection loss into consideration, the time-domain counterpart of $I_0^{\mathrm{TR}}(j\omega)$ [as well as that of $V_0^{\mathrm{DT}}(j\omega)$] and $I_{x_f}^{\mathrm{RT}}(j\omega)$ present damped oscillations. Nevertheless, given that ρ_0^V approaches +1, the time-domain waveforms are still dominated by the feature of a $4\Gamma_{x_f}$-period square wave. We clarify their time-domain attributes in the next section.

5.2.2 Time-domain analysis

1) Forward-propagation stage: fault occurrence

For the fault occurrence shown in Fig. 5.1, the transient voltage signal observed at $x = 0$ can be analytically calculated as (5.23) and depicted in Fig. 5.7.

$$V_0^{\mathrm{DT}}(t) = \overline{V} \cdot \varepsilon(t) + \sum_{i=1}^{m} \left\{ \left(1 + \rho_0^V\right) \cdot \left(\rho_0^V \rho_{x_f}^V\right)^{i-1} \cdot \left(-\overline{V}\right) \cdot \varepsilon\left[t - t_f - (2i-1) \cdot \Gamma_{x_f}\right] \right\},$$

$$m = 1, 2, \ldots, k, \ldots, M, \ldots, \tag{5.23}$$

where $\rho_{x_f}^V$ is the voltage reflection coefficient at the fault location $x = x_f$.
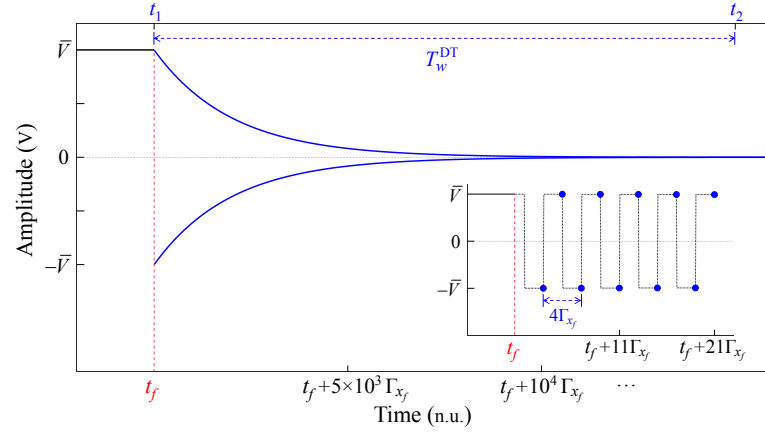
Figure 5.7 – Envelope of the fault-originated transient voltage signal observed at the line end $x = 0$. The oscillation of $V_0^{\mathrm{DT}}(t)$ is described by the sampling points at its positive and negative edges. The initial five-period oscillations are illustrated in the expanded view.

Recalling the line set-up, in which a typical 380-kV overhead line (with the characteristic impedance about 360 Ω) is grounded through a 100-kΩ impedance at each of the line terminals, ρ_0^V is about +0.99. Therefore, in agreement with the conclusions of the frequency-domain analysis, $V_0^{\mathrm{DT}}(t)$ has a damped oscillatory waveform. In Fig. 5.7, the oscillation of $V_0^{\mathrm{DT}}(t)$ is described by its envelope, which is composed of the sampling points at its positive and negative edges (see the blue dots in the expanded view). For the sake of clarity, the initial oscillations (in five periods) are shown with their detailed attributes in the expanded view of Fig. 5.7. As it can be observed, the oscillations of $V_0^{\mathrm{DT}}(t)$ have a period of $4\Gamma_{x_f}$.

The first term in (5.23), namely the product of the supplied voltage $\overline{V}$ and the unit-step function $\varepsilon(t)$, indicates that the line system has been in steady-state before the fault occurring instant t_f. The summation term quantifies the fact that the fault-originated transient response consists of multiple reflections. The upper limit m in the sum operation determines a long enough time length so that the oscillations of $V_0^{\mathrm{DT}}(t)$ sufficiently decay to 0.

Note that the time-domain time-reversal operation postulates that the signal under processing is of a certain duration. To this end, a time-window function[2] $W(t)$ is applied to truncate $V_0^{\mathrm{DT}}(t)$:

$$\tilde{V}_0^{\mathrm{DT}}(t) = \left[V_0^{\mathrm{DT}}(t) \cdot W(t) \Big|_{t_f + \Gamma_{x_f}}^{t_f + \Gamma_{x_f} + T_w^{\mathrm{DT}}} \right] \Bigg|_{t = t + t_f + \Gamma_{x_f}}, \tag{5.24}$$

where the starting instant t_1 of $W(t)$ is assigned to $t_f + \Gamma_{x_f}$ so that the steady-state component of $V_0^{\mathrm{DT}}(t)$ is filtered out.

---

[2] $W(t)\Big|_{t_2}^{t_1} = \varepsilon(t_1) - \varepsilon(t_2)$, where $\varepsilon(t)$ is the unit-step function.

Chapter 5. Electromagnetic Time Reversal Similarity Properties and Its Fault Location Application

In regard to the time-window length T_w^{DT}, we set it at an integral multiple of the time delay Γ_{x_f}, namely

$$T_w^{\text{DT}} = M \cdot 2\Gamma_{x_f}, \tag{5.25}$$

where M is large enough, ensuring that the whole transient process is contained in the time window. M is assigned 1.5×10^4 in the derivation.

It is worth mentioning that the above operation is not at the cost of losing generality. It is equivalent to extracting the fault-originated high-frequency transients. Identities of (5.24) and (5.25) allow concisely formulating the transients $\tilde{V}_0^{\text{DT}}(t)$ in an analytical expression as:

$$\tilde{V}_0^{\text{DT}}(t) = \overline{V} \cdot W(t)\big|_{M \cdot 2\Gamma_{x_f}}^{0} + \sum_{i=1}^{M} \left[\left(1 + \rho_0^V\right) \cdot \left(\rho_0^V \rho_{x_f}^V\right)^{i-1} \cdot \left(-\overline{V}\right) \cdot W(t) \Big|_{M \cdot 2\Gamma_{x_f}}^{(i-1)\cdot 2\Gamma_{x_f}} \right]. \tag{5.26}$$

2) Backward-propagation stage: fault location

Corresponding to the time-reversal operation (5.16) in the frequency domain, the transients $\tilde{V}_0^{\text{DT}}(t)$ observed in the forward stage is reversed in time and its Norton equivalent $I_0^{\text{TR}}(t)$ is determined:

$$V_0^{\text{TR}}(t) = \tilde{V}_0^{\text{DT}}(t)\big|_{t=-t+T_w^{\text{DT}}}, \quad I_0^{\text{TR}}(t) = V_0^{\text{TR}}(t)/Z_0. \tag{5.27}$$

At the guessed fault locations $x_{\mathbb{G}}$, the fault currents $I_{x_{\mathbb{G}}}^{\text{RT}}(t)$ can be calculated by:

$$
\begin{aligned}
I_{x_{\mathbb{G}}}^{\text{RT}}(t) &= \frac{Z_0}{Z_0 + Z_C} \cdot \sum_{j=1}^{n} \left\{ \left(1 + \rho_{x_{\mathbb{G}}}^I\right) \cdot \left(\rho_0^I \rho_{x_{\mathbb{G}}}^I\right)^{j-1} \cdot I_0^{\text{TR}}\left[t - (2j-1) \cdot 2\Gamma_{x_{\mathbb{G}}}\right] \right\} \\
&= \frac{1}{Z_0 + Z_C} \cdot \sum_{j=1}^{n} \Bigg\langle \left(1 + \rho_{x_{\mathbb{G}}}^I\right) \cdot \left(\rho_0^I \rho_{x_{\mathbb{G}}}^I\right)^{j-1} \cdot \\
&\qquad \left\{ \overline{V} \cdot W(t) \Big|_{(2j-1)\cdot\Gamma_{x_{\mathbb{G}}} + M \cdot 2\Gamma_{x_f}}^{(2j-1)\cdot\Gamma_{x_{\mathbb{G}}}} + \right. \\
&\qquad \left. \sum_{i=1}^{M} \left[\left(1 + \rho_0^V\right) \cdot \left(\rho_0^V \rho_{x_f}^V\right)^{i-1} \cdot \left(-\overline{V}\right) \cdot W(t) \Big|_{(2j-1)\cdot\Gamma_{x_{\mathbb{G}}} + (M-i+1)\cdot 2\Gamma_{x_f}}^{(2j-1)\cdot\Gamma_{x_{\mathbb{G}}}} \right] \right\} \Bigg\rangle \\
&\qquad n = 1, 2, \ldots, k, \ldots, N, \ldots,
\end{aligned}
\tag{5.28}
$$

in which ρ_0^I and $\rho_{x_{\mathbb{G}}}^I$ are the current reflection coefficients at $x = 0$ and $x = x_{\mathbb{G}}$, respectively. $\Gamma_{x_{\mathbb{G}}}$ refers to a collection of the propagation delays from $x = 0$ to the guessed fault locations $x_{\mathbb{G}}$.

In order to compensate for the quantitative difference in amplitude, $I_0^{\text{TR}}(t)$ and $I_{x_f}^{\text{RT}}(t)$ are normalized and depicted in Fig. 5.8. The normalization is with reference to their respective maximum amplitudes and is given by

$$Nor\left[I_0^{\text{TR}}(t)\right] \triangleq I_0^{\text{TR},nor}(t) = \frac{I_0^{\text{TR}}(t)}{Max\left[I_0^{\text{TR}}(t)\right]}, \tag{5.29}$$
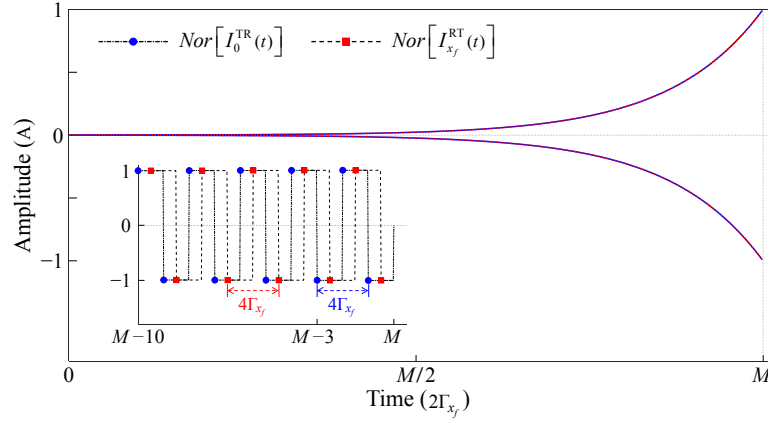
Figure 5.8 – Envelopes of the normalized waveforms of $I_0^{\text{TR}}(t)$ and $I_{x_f}^{\text{RT}}(t)$ in a duration of T_w^{DT}. The two waveforms are represented by sampling the positive and negative edges of $I_0^{\text{TR},nor}(t)$ and $I_{x_f}^{\text{RT},nor}(t)$. The expand view depicts the last five-period oscillations.

$$Nor\left[I_{x_f}^{\text{RT}}(t) \right] \triangleq I_{x_f}^{\text{RT},nor}(t) = \frac{I_{x_f}^{\text{RT}}(t)}{Max\left[I_{x_f}^{\text{RT}}(t) \right]} \ . \tag{5.30}$$

For the sake of comparison, $I_{x_f}^{\text{RT}}(t)$ is truncated to the duration of $I_0^{\text{TR}}(t)$ in Fig. 5.8. Like the approach employed in Fig. 5.7, we sample the positive and negative edges [of $I_0^{\text{TR},nor}(t)$ and $I_{x_f}^{\text{RT},nor}(t)$] and describe the two waveforms with their envelopes. According to the enlarged view of the last several period components shown in the inset, the oscillations of $I_{x_f}^{\text{RT}}(t)$ are also in a period of $4\Gamma_{x_f}$.

Let us consider the arbitrary k^{th} edge components of $I_0^{\text{TR},nor}(t)$ and $I_{x_f}^{\text{RT},nor}(t)$, which read

$$Nor\left[I_0^{\text{TR},k} \right] = Nor\left[I_0^{\text{TR}}(t) \right]\Big|_{t=t_0^{\text{TR},k}} \ , \tag{5.31}$$

$$Nor\left[I_{x_f}^{\text{RT},k} \right] = Nor\left[I_{x_f}^{\text{RT}}(t) \right]\Big|_{t=t_{x_f}^{\text{RT},k}} \ . \tag{5.32}$$

The time lag between the sampling instants stays constant:

$$\Delta t = t_{x_f}^{\text{RT},k} - t_0^{\text{TR},k} = (2k-1)\cdot\Gamma_{x_f} - (k-1)\cdot 2\Gamma_{x_f} = \Gamma_{x_f} \ . \tag{5.33}$$

After straightforward mathematical manipulations, the ratio of the two reference amplitudes can be calculated as

$$\eta(k) = \frac{Nor\left[I_0^{\text{TR},k} \right]}{Nor\left[I_{x_f}^{\text{RT},k} \right]} = \frac{1 - \left(\rho_0^V\right)^{2k}}{1 - \left(\rho_0^V\right)^{2M}} \ . \tag{5.34}$$
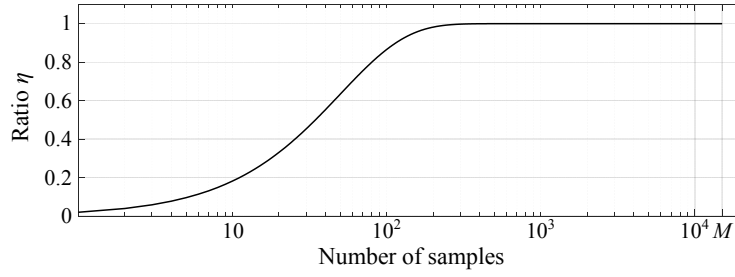
Figure 5.9 – Ratio of the sampling points at the positive and negative edges of $I_0^{\text{TR},nor}(t)$ and $I_{x_f}^{\text{RT},nor}(t)$. M is 1.5×10^4 in the derivation.

Given ρ_0^V being +0.99, $\eta(k)$ is plotted as a function of the number of samples in Fig. 5.9. As displayed, the ratio approximates to +1 except for the initial small percentage of samples, which are of relatively insignificant amplitudes. That is to say, most components of the two signals, with a constant time lag of Γ_{x_f}, are characterized by very similar amplitudes. The similarity can be noticed by the overlap of the envelopes of $I_0^{\text{TR},nor}(t)$ and $I_{x_f}^{\text{RT},nor}(t)$ in Fig. 5.8.

Thus far, (5.33) and (5.34) prove that $I_{x_f}^{\text{RT},nor}(t)$ behaves as a quasi-time-delayed copy of $I_0^{\text{TR},nor}(t)$.

The integrated time- and frequency-domain analysis in this section reveals the similarity properties existing in the classical EMTR (in matched media) based fault location process. Although the derivation makes reference to a simplified line set-up, it is clear that the theoretical foundation of the similarity characteristic lies in the generic identity of (5.4). Note that the identity is derived from the reciprocity principle and establishes when the guessed fault location coincides with the true one, irrespective of the topological complexity.

5.3 Electromagnetic Time Reversal Based Fault Location Method Using Similarity Properties

Based on the proved similarity property, we present in this section a single-end measurement based EMTR metric addressing the fault location problem in power networks.

5.3.1 Time-domain similarity quantitative representation

The time-domain similarity between $I_0^{\mathrm{TR}}(t)$ and $I_{x_\mathbb{G}}^{\mathrm{RT}}(t)$ is proposed to be quantitatively represented by calculating the metric of the maximum of the cross-correlation sequence (e.g., [170, 172]), under the denomination of MCCS, as

$$R^m(x_\mathbb{G},\, l) = Max \left\{ \sum_{k=0}^{K} I_0^{\mathrm{TR}}[(k+l)\cdot\Delta t] \cdot I_{x_\mathbb{G}}^{\mathrm{RT}}(k\cdot\Delta t) \right\},$$
$$K = T_w^{\mathrm{DT}}/\Delta t, \quad l = 0, \pm 1, \pm 2, \ldots, \pm(K-1). \tag{5.35}$$

The true fault location is identified by

$$x_{f,\,estimated} = arg\big|_{x_\mathbb{G}} \quad Max\left[R^m(x_\mathbb{G},\, l)\right]. \tag{5.36}$$

In (5.35), $I_0^{\mathrm{TR}}(t)$ and $I_{x_f}^{\mathrm{RT}}(t)$ are discretized with the sampling interval Δt. Given that the back-injected transients $I_0^{\mathrm{TR}}(t)$ are in a temporal duration of T_w^{DT}, the duration of the fault current $I_{x_\mathbb{G}}^{\mathrm{RT}}(t)$ is generally twice as long as T_w^{DT}. Note that, In (5.35), $I_{x_\mathbb{G}}^{\mathrm{RT}}(t)$ is truncated by T_w^{DT}.

According to the relation between the operation of cross correlation and the time-domain convolution (e.g., [172]), $R^m(x_\mathbb{G}, l)$ in (5.35) can be equivalently calculated using

$$R^m(x_\mathbb{G},\, l) = Max\left\{ I_0^{\mathrm{TR}}(-l\cdot\Delta t) \otimes I_{x_f}^{\mathrm{RT}}(l\cdot\Delta t) \right\}. \tag{5.37}$$

Thus, the evaluation of the time-domain similarity can be achieved through the convolution operation.

5.3.2 EMTR similarity property based fault location method

We introduce in this section the implementation of the proposed EMTR similarity property based fault location method, which relies on evaluating the maximum of the cross-correlation sequence (MCCS) metric.

The step-by-step process is summarized in a pseudo-algorithm presented in Table 5.1. As same as the classical EMTR-FCSE method, the time-domain similarity method requires the knowledge of the power-network topology as well as its line/cable wave propagation parameters to numerically represent the target network in a simulation environment, which is capable

Table 5.1 – Pseudo-algorithm of the EMTR cross-correlation metric

Input: network topology and parameters, guessed fault locations $x_{\mathbb{G}}$

$V_{0,ph}^{\mathrm{DT}}(t),\ t \in [0, T]^3$

$\tilde{V}_{0,ph}^{\mathrm{DT}}(t),\ t \in [0, T]$

$$V_{0,ph}^{\mathrm{TR}}(t) = \tilde{V}_{0,ph}^{\mathrm{DT}}\big(-t + T_w^{\mathrm{DT}}\big),\ t \in [0, T_w^{\mathrm{DT}}] \tag{5.38}$$

for each *a priori* guessed fault location $x_g \in x_{\mathbb{G}}$ **do**

1: simulate the fault current $I_{x_g}^{\mathrm{RT}}(t)$ using network model and $V_0^{\mathrm{TR}}(t)$

2: compute the MCCS metric $R^m(x_g)$

end

$x_{f,\,estimated} = arg\big|_{x_{\mathbb{G}}}\quad Max[R^m(x_{\mathbb{G}})]$

Output: $x_{f,estimated}$

of simulating the transient propagation. In addition, the true fault location being unknown, a set of guessed fault locations is *a priori* defined according to a desired accuracy.

Responding to a fault event, the fault-originated transient voltage $V_{0,ph}^{\mathrm{DT}}(t)$ (with $ph = a, b, c$ for three-phase systems) can be measured at a single observation point that is assumed to be deployed at the secondary winding of a power transformer. It is implied that the time-window length T is sufficient long (typically, one period of power frequency or longer) to record the full transient process of $V_{0,ph}^{\mathrm{DT}}(t)$.

As previously formulated, $\tilde{V}_{0,ph}^{\mathrm{DT}}(t)$ represents the fault-originated high-frequency transients, whose spectrum $[\tilde{V}_{0,ph}^{\mathrm{DT}}(j\omega)]$ contains the main components at the frequencies of the fault switching frequency (i.e., f^0 in Fig. 5.4) and beyond. $\tilde{V}_{0,ph}^{\mathrm{DT}}(t)$ is extracted from the original transient voltage $V_{0,ph}^{\mathrm{DT}}(t)$ by means of a high-pass (HP) filter to remove the low-frequency steady-state signal. The frequency f^0 is identified in the magnitude spectrum of $V_{0,ph}^{\mathrm{DT}}(t)$. Considering its maximally-flat frequency response and steep roll-off, the use of a high-order (4th or higher) Butterworth IIR filter is recommended.

Then, the extracted transients $\tilde{V}_{0,ph}^{\mathrm{DT}}(t)$ are truncated by a certain time-window T_w^{DT} and time reversed as $V_{0,ph}^{\mathrm{TR}}(t)$ through (5.38). The time-reversal operation consists of reversing the temporal sequence of $\tilde{V}_{0,ph}^{\mathrm{DT}}(t)$, namely $\tilde{V}_{0,ph}^{\mathrm{DT}}(-t + T_w^{\mathrm{DT}})$, and thus the signal in the pre-triggering stage is transformed into zero-padded components after the operation. For this reason, any point in time between $t = 0$ and $t = t_{triggering}$ can be selected as the starting instant of the time

---

[3]The recording time window can be divided into the pre-triggering stage, spanning from $t = 0$ to a fault triggering instant $t_{triggering}$, and the subsequent stage (i.e., post-triggering stage) from $t_{triggering}$ to T. The fault triggering strategy, which is employed in the embedded controller based fault location system (see Section 4.3), allows precisely reading the triggering instant and allocating the temporal length of the pre-triggering stage.

window T_w^{DT}.

For each pre-defined guessed fault location x_g, an independent electromagnetic transients simulation is performed by back injecting $V_{0,ph}^{\mathrm{TR}}(t)$ into the network model to compute the fault current signal $I_{x_g}^{\mathrm{RT}}(t)$.

The final procedure performing the fault location estimation consists of calculating the maximum of the cross-correlation sequence (MCCS) metric (5.35), with the global maximum of the metric indicating the fault location [i.e., (5.36)].

5.4 Numerical Validation

In this section, we numerically validate the proposed cross-correlation metric by implementing the algorithm of Table 5.1 to locate faults in the IEEE 34-bus test distribution feeder. Fig. 5.10 shows modeling the test distribution feeder in the EMTP-RV simulation environment.
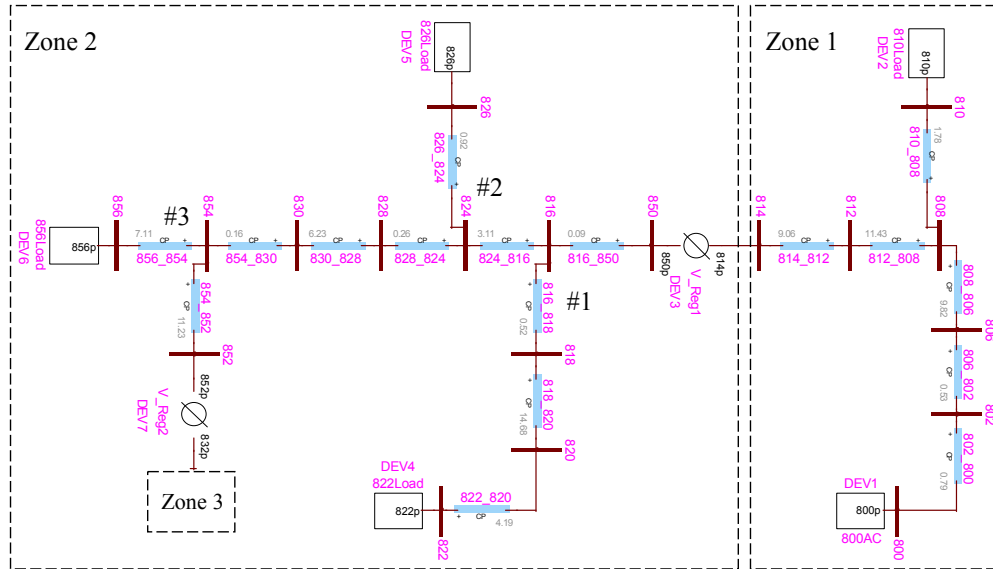
Figure 5.10 – IEEE 34-bus test distribution feeder modeled in the EMTP-RV simulation environment. The detailed configuration of Zone 3 is not plotted.

The IEEE 34-bus test distribution feeder is supplied with a nominal voltage of 24.9 kV from the terminal node (substation) numbered 800 and the buses are connected with two interconnection transformers situated at Nodes 814 and 852. In view of traveling wave propagation, the blocking behavior of the two transformers divides the network into three zones. Fig. 5.10 shows Zones 1 and 2 of the feeder modeled in the EMTP-RV environment. The detailed configuration of Zone 3 is not described. Note that the modeling has taken the transformer's winding-to-ground capacitive behaviors into consideration: the power distribution transformer in the network was modeled by means of a 50 Hz standard model in parallel with a

Π-network of capacitors, whose capacitance values were in the order of hundreds of picofarads (see more details in [127]).

The case study in this section consists of simulating single- and three-phase-to-ground fault (ph-g and 3 ph-g) occurrences in the first zone of the feeder (between Nodes 800 and 814). The secondary winding of the feeding transformer at Node 800 is considered as the single observation point. Moreover, given that fault occurrence in power networks is a stochastic event, the fault location performance of the cross-correlation metric is evaluated with respect to the uncertainties including:

i)   fault location,

ii)   fault impedance, and

iii) fault inception angle.

As summarized in Table 5.2, the simulation case studies consider two common types of faults at each node in the tested zone, with different values of fault impedance, namely 0 (solid fault), 10, 30 and 50 Ω. Additionally, the simulation is extended to a near zero-crossing fault case at each of the nodes. The tested fault inception angle (θ_f) is about 4 degrees. As a result, a total of 54 fault cases are studied. According to the step-by-step implementation of the algorithm of Table 5.1, the time-domain similarity method is shown to be able to accurately identify the true fault location in each tested fault case.

Table 5.2 – Fault cases simulated in Zone 1 of the IEEE 34-bus test distribution feeder

Fault type	Fault location (Node)	Fault impedance (Ω)	Num. of cases
ph-g (*a*-g)	802, 804, 806, 808, 812, 814	0, 10, 30, 50	24
3 ph-g			24
ph-g (*b*-g), $\theta_f \approx 4°$		0	6

5.4.1   Performance assessment with respect to fault inception angle

Figure 5.11 shows, as an example, the calculated metric of the maximum of the cross-correlation sequence (MCCS) for the single-phase-to-ground fault at Node 810. In agreement with (5.36), the true fault location, as well as the faulty phase (i.e., Phase *a*), are characterized by the MCCS metric with the global maximum among the guessed fault locations. For the sake of comparison, the calculated metric for the fault, which occurs on Phase *b* with a fault inception angle (θ_f) of about only four degrees, is superimposed in the same figure. As known, such a fault with an extremely small fault inception angle decreases the signal-to-noise-ratio of the extracted transients and therefore degrades the performance of some traveling-wave based fault location methods. Observe that the proposed time-domain similarity method demonstrates a comparable performance in locating the near zero-crossing fault.
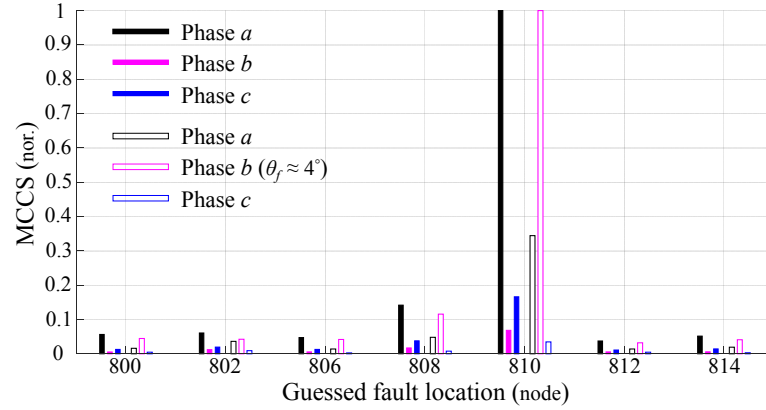
Figure 5.11 – Normalized cross-correlation metric calculated for the single-phase-to-ground fault cases at Node 810. The color-filled bars represent the phase (a)-to-ground fault case and the white-filled bars refer to the near zero-crossing phase (b)-to-ground fault case. The normalization is based on the maxima of the MCCS metric calculated for the respective fault cases.

5.4.2 Performance assessment with respect to fault impedance

Figure 5.12 compares the calculated MCCS metric for the phase (a)-to-ground fault at Node 812 between a solid fault case and two resistive fault cases varying in the fault impedance from 30 to 50 Ω. For the sake of simplicity, only the results for the faulty phase are shown. It can be seen that the proposed cross-correlation metric is robust against the variation of the fault impedance.
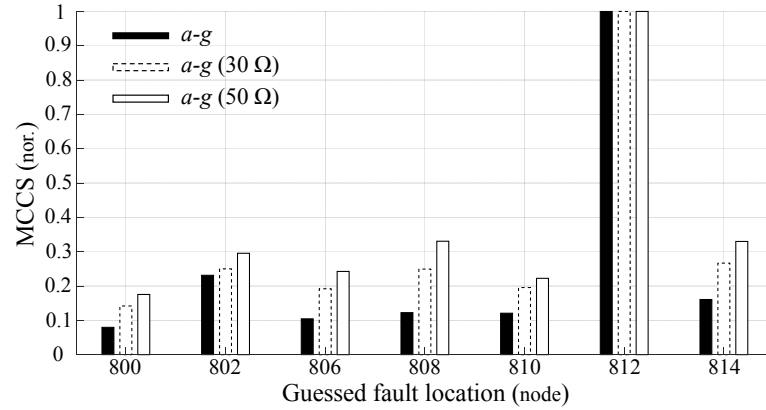
Figure 5.12 – Normalized cross-correlation metric calculated for the phase (a)-to-ground fault cases at Node 812 with different values for the fault impedance: 0, 30 and 50 Ω. The normalization is based on the maxima of the MCCS metric obtained in the respective fault cases.

As discussed in [79], the EMTR backward-propagation simulation does not require *a priori* estimation to the exact value of the fault impedance. In the above-mentioned cases, the fault

current is simulated by assuming a zero fault impedance.

5.4.3 Performance assessment with respect to fault type

Figure 5.13 presents the evaluation of the fault location performance of the MCCS metric for the three-phase-to-ground fault cases with respect to different fault locations and values for the fault impedance. As it can be seen, in spite of the uncertainties, the proposed time-domain similarity method is still effective in locating each of the faults by reaching a global maximum at the corresponding true fault location.
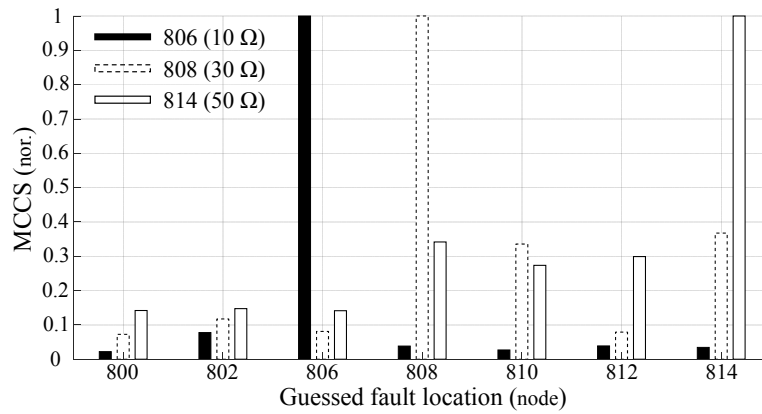
Figure 5.13 – Normalized cross-correlation metric calculated for the three-phase-to-ground fault cases: *i*) 10-Ω fault at Node 806, *ii*) 30-Ω fault at Node 808 and *iii*) 50-Ω fault at Node 814. The normalization is based on the maxima of the MCCS metric calculated for the respective fault cases.

The presented numerical validation case studies demonstrate that the proposed EMTR time-domain similarity method based on the MCCS metric is robust in terms of locating various faults differing in the fault type, the fault inception angle as well as the fault impedance.

5.5 Application Example

This section further assesses the fault location performance of the proposed time-domain similarity method in more topologically-complex power networks featuring multiple branches and nodes. In this respect, the second zone of the IEEE 34-bus test distribution feeder is considered.

The zone under study is terminated by the two interconnection transformers at Nodes 850 and 852 (see Fig. 5.10). The main feeder between the two nodes is 21.1 km in length with three laterals [of 19.4 km (♯1), 0.92 km (♯2), and 7.11 km (♯3)] branching off to connect power loads. The single observation end is the secondary winding of the transformer located at Node 850.

The foregoing simulation case studies, as well as the experimental validation to be presented in the next section, show the robustness of the cross-correlation metric against the fault impedance and the fault inception angle. The following simulations focus on illustrating and discussing the applicability of the metric to the radial power network with respect to various fault locations and types.

As summarized in Table 5.3, the fault types considered in the case studies include:

i)   single-phase-to-ground fault (ph-g),
ii) two-phase-to-ground fault (2 ph-g),
iii) three-phase-to-ground fault (3 ph-g),
iii) phase-to-phase-to-ground fault (ph-ph-g), and
iii) phase-to-phase fault (ph-ph).

The faults are assumed to occur at each node of the radial network. As a result, a total of 55 fault cases are tested.

Table 5.3 – Fault cases simulated in Zone 2 of the IEEE-34 bus test distribution feeder

Fault locations (Node)		Fault type	Num. of fault cases
Main feeder	Branch		
816, 824, 828, 830, 854, 852	818, 820, 822 (♯1) 826 (♯2) 856 (♯3)	ph-g (*a*-g)	11
		2 ph-g (*a,b*-g)	11
		3 ph-g	11
		ph-ph-g (*b-c*-g)	11
		ph-ph (*a-c*)	11

Among the 55 simulated fault cases, only in one case, the metric of MCCS exhibits lower performance in exactly identifying the true fault location. The case refers to the phase (*a*)-to-ground fault at Node 830, with a location error of 158 m. Even in this case, the location error can still be considered as tolerant since it represents only 3‰ of the total line length.

Except for the case, the proposed time-domain similarity method is capable of accurately identifying all the faults, which vary in the fault type, at each node. For example, Fig. 5.14 to Fig. 5.16 describe the calculated MCCS metric as a function of the guessed fault location for the following fault cases: *i*) single-phase-to-ground fault (*a*-g) at Node 822, *ii*) two-phase-to-ground fault (*a, b*-g) at Node 828, and *iii*) phase-to-phase-to-ground fault (*b-c*-g) at Node 852. As it can be observed, the MCCS metric achieves the global maximum at the corresponding location of the fault occurrence.
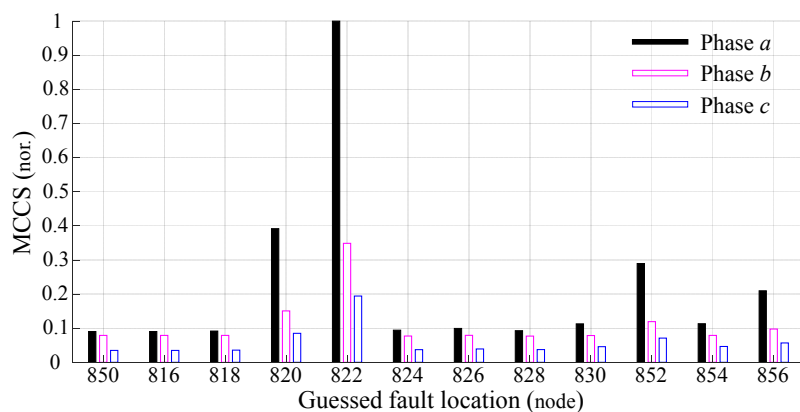
Figure 5.14 – Normalized cross-correlation metric calculated for the phase (*a*)-to-ground fault at Node 822. The normalization is based on the maximum of the calculated MCCS metric.
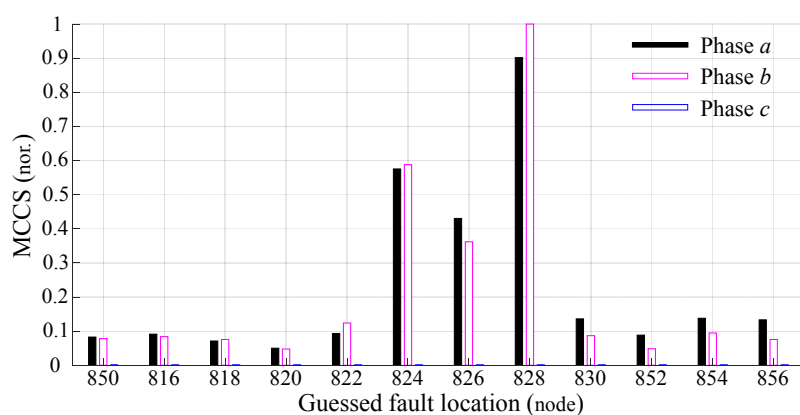
Figure 5.15 – Normalized cross-correlation metric calculated for the two-phase (*a, b*)-to-ground fault at Node 828. The normalization is based on the maximum of the calculated MCCS metric.
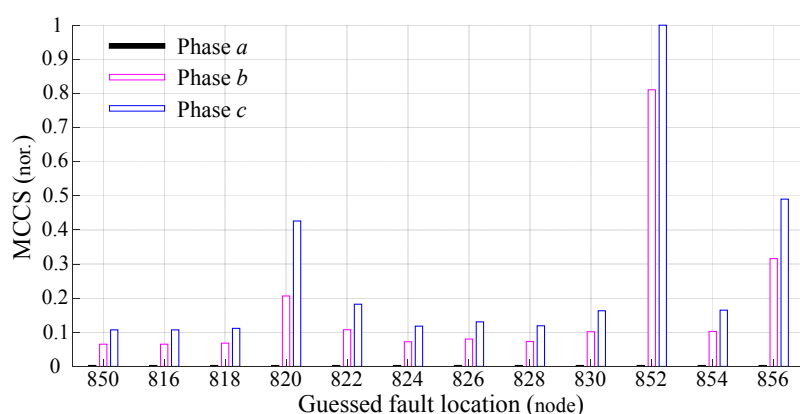
Figure 5.16 – Normalized cross-correlation metric calculated for the phase (*b*)-to-phase (*c*)-to-ground fault at Node 852. The normalization is based on the maximum of the calculated MCCS metric.

5.6 Experimental Validation

This section makes reference to the pilot test reported in Section 4.4 to assess the capability of the EMTR similarity property based method dealing with realistic fault events.

5.6.1 Fault cases and results

As detailed in Section 4.4, the pilot test was carried out by artificially triggering a real fault when a radial distribution feeder was under normal operation conditions (i.e., live power networks). The tested network was a primary distribution feeder consisting of an 11.9-km long double-circuit line operating at 18/60 kV and seven 18-kV three-phase laterals branching from the main feeder (see Fig. 4.14). The fault occurrence was initiated at an (overhead) line-(underground) cable mixed lateral terminal (indicated as the guessed fault location of No. 55 in Fig. 4.14), which was about 3.6 km away from the primary substation (substation A in Fig. 4.14). The primary substation A was also selected as a single observation end to record fault-originated transient signals during the pilot trial. The tested single-phase-to-ground fault cases are reported in Table. 4.3. The pilot test covered both solid and resistive faults, meanwhile taking various fault occurrence mechanisms into consideration. The phase-to-ground faults were caused by either a permanent short circuit or a single/intermittent transient arc discharge to ground.

The proposed EMTR similarity property based fault location method is validated in all the fault cases. For the sake of brevity, in what follows, the fault location performance of the MCCS metric in the cases of the solid and the resistive faults are reported.

Figure 5.17 presents the calculated MCCS metric as a function of the guessed fault location for the solid fault case of Fig. 4.17. The fault was triggered during the positive-half period of Phase-a voltage. A total of 123 electricity nodes in the tested network were defined as the guessed fault locations. As it can be seen, the true fault location, numbered 55, is characterized as the global maximum in agreement with the criterion of (5.36).

The simulation case study has devoted special attention to assessing the MCCS metric with respect to the fault with a relatively small inception angle. Further validation is conducted using the acquired data of the near zero-crossing case of Fig. 4.24. The distribution of the calculated MCCS metric as a function of the guessed fault location is illustrated in Fig. 5.18. It is evident that both the exact fault location and the faulty phase are identified. The above-discussed results (of Fig. 5.17 and Fig. 5.18) experimentally validate the robustness of the time-domain similarity property and the resultant MCCS metric against the fault inception angle.
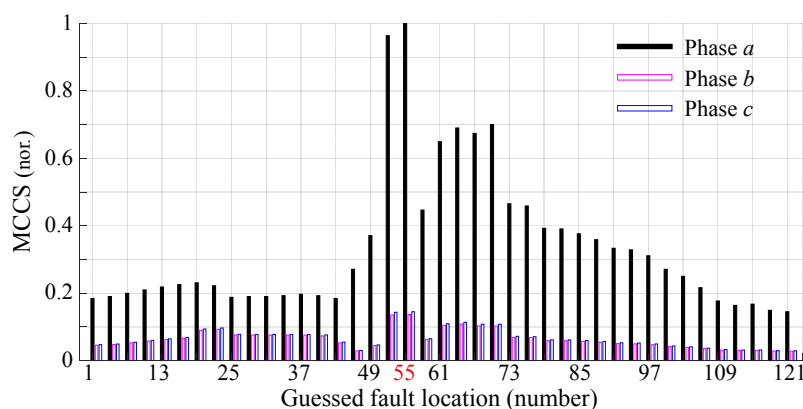
Figure 5.17 – Normalized cross-correlation metric calculated for the solid phase (*a*)-to-ground fault. The true fault location of the faulty phase is numbered 55.
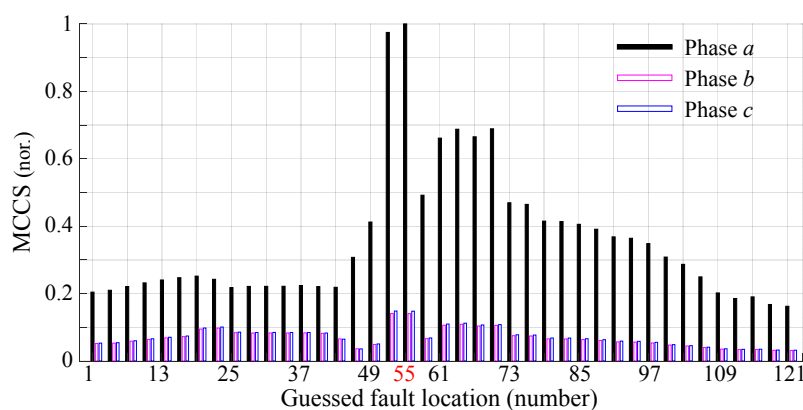
Figure 5.18 – Normalized cross-correlation metric calculated for the near zero-crossing phase (*a*)-to-ground fault. The true fault location of the faulty phase is numbered 55.
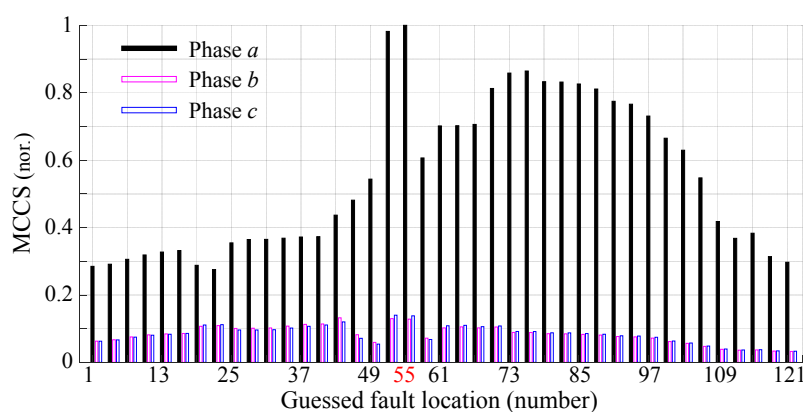
Figure 5.19 – Normalized cross-correlation metric calculated for the resistive phase (*a*)-to-ground fault. The true fault location of the faulty phase is numbered 55.

Figure 5.19 presents the calculated values of the MCCS metric at the respective guessed fault locations for the 30-Ω phase (a)-to-ground fault case of Fig. 4.21. In spite of the faster-damping high-frequency transients compared to those of the solid faults (see Fig. 4.18), the proposed MCCS metric is still effective in evaluating the similarity between the back-injected transients and the fault current simulated at the true fault location, which is thus indicated in Fig. 5.19 as the global maximum of the MCCS metric.

The presented analysis using the pilot test data experimentally validates the EMTR similarity property and demonstrate the capability of the MCCS metric in dealing with realistic faults.

5.6.2 Analysis

1) *Fault location accuracy*

As it can be seen from the presented results, reaching the global maximum at the true fault location (i.e., the guessed fault location numbered 55), the calculated MCCS metric also shows a second peak value at the adjacent guessed fault location numbered 52. These two locations are the two ends of the 230-m long faulty underground cable (see Fig. 4.14).

Like the location accuracy analysis performed in Section 4.4.5, the faulty cable model was subdivided into 23 sections. Then, the fault current signal was simulated at the junctions of each two adjacent 10-m cable sections. Fig. 5.20 shows the calculated MCCS metric at those junctions for the solid fault case of Fig. 4.17 and the resistive fault case of Fig 4.21. The obtained results confirm that the true fault location (i.e., the right end of the cable) still features the maximum of the MCCS metric and, thus, demonstrate a better-than-10-m location accuracy for the tested realistic faults.
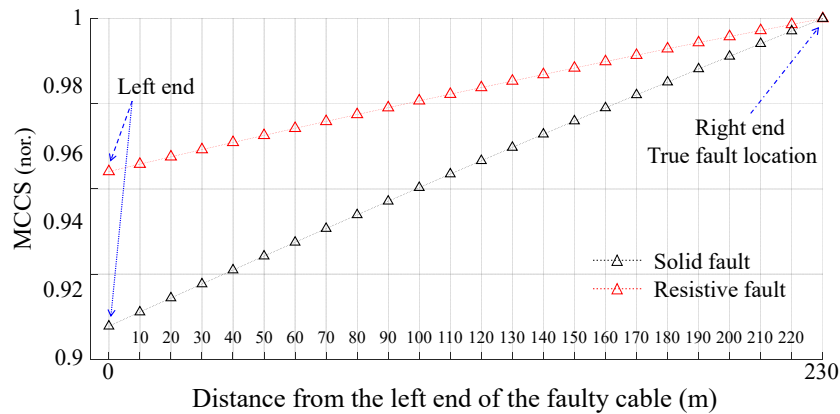
Figure 5.20 – Normalized cross-correlation metric as a function of the distance from the left end of the faulty cable.

It worth noting that a similar location accuracy was obtained in the rest of the realistic fault cases, such as the arcing-discharge caused faults of Figs. 4.20 and 4.21. Thus, the results are not reported here.

2) Computation efficiency

We now discuss the advantage of the proposed cross-correlation metric based on the similarity property over the other classical EMTR fault location metrics (e.g., [79, 84]), with a particular emphasis on computation efficiency.

As discussed, the proposed metric of the maximum of the cross-correlation sequence (MCCS) evaluates the similarity between $I_0^{\mathrm{TR}}(t)$ and $I_{x_{\mathbb{G}}}^{\mathrm{RT}}(t)$ in the time scale of the duration of the back-injected transients [e.g., T_w^{DT} of $I_0^{\mathrm{TR}}(t)$]. In other words, the MCCS metric requires simulating the fault current signals [e.g., $I_{x_{\mathbb{G}}}^{\mathrm{RT}}(t)$] only in the duration of T_w^{DT}, as opposed to the fault current signal amplitude or energy metric requiring the observation of the full waveforms of $I_{x_{\mathbb{G}}}^{\mathrm{RT}}(t)$ in the duration T_w^{RT}, which, in general, is twice as long as T_w^{DT}.

As a result, the proposed time-domain similarity method considerably reduces the simulation time consumption *per* guessed fault location and, therefore, benefits a faster response of identifying fault occurrences.

5.7 Conclusion

The study presented in this chapter performed an integrated time-frequency domain analysis to prove a similarity characteristic existing in the classical implementation of the EMTR technique to locating faults in power networks.

The time-domain similarity characteristic demonstrates that the fault current at the true fault location exclusively behaves as a quasi-scaled copy of the time-reversed back-injected transient current. For the sake of simplicity, the analysis made reference to a single-wire overhead-line set-up to formulate the similarity characteristic. Nevertheless, since the similarity is founded on the identity between the transfer functions of the forward-stage and the backward-stage, the development can be generalized to any linear network with arbitrary topology.

Based on the proved similarity characteristic, we proposed to calculate the cross-correlation between the back-injected current signal and the fault current signal simulated at a guessed fault location to quantify the level of the time-domain similarity and to identify the true fault location.

The similarity characteristic and the fault location performance of the proposed cross-correlation metric were validated through simulation case studies using the IEEE 34-bus test distribution feeder and also making reference to a live test triggering faults in a real and operational medium-voltage radial distribution network.

It has been shown that the proposed time-domain similarity method is applicable to locating various types of faults (including single-phase-to-ground faults, three-phase-to-ground faults, phase-to-phase faults, etc.), meanwhile, providing robust performance in coping with

uncertainties like the fault impedance and the fault inception angle.

Also, note that the proposed cross-correlation metric demonstrates similar fault location performances in terms of location accuracy and robustness, compared to the classical fault current signal energy metric. On the other hand, it is worth emphasizing that the cross-correlation metric is computationally more efficient as it simulates the fault current signal in a shorter duration (i.e., T_w^{DT}) *per* guessed fault location.

6 Electromagnetic Time Reversal in Mismatched Media and Its Fault Location Application

Based on the pioneering studies since the 1990s that shed light on time reversal in terms of basic principle and classical applications, recent research has given attention to studying the capability and quality of refocusing time-reversed signals (e.g., acoustic or electromagnetic waves) to the original source location in a mismatched or changing media. In contrast to time reversal in the conventional sense, the emerging concept of mismatched media refers to the scenario where the time-reversed waves are back injected and propagate through a medium that is different from the original forward-stage medium.

This chapter first presents an experimental study of the focusing property of electromagnetic time reversal (EMTR) in a scattering medium. Particular attention is given to the case when a moderate lumped mismatch between the forward-propagation and backward-propagation media exists.

Then, the presented research discusses the application of EMTR in mismatched media with reference to the problem of fault location in power networks. Compared to the classical implementation of EMTR (i.e., in matched media), it is proposed to remove the transverse branch representing a fault from the power network in the backward stage. We demonstrate that this modified backward-propagation medium satisfies different frequency- and time-domain properties (bounded phase, minimum squared modulus, mirrored minimum energy), which allows the identification of the fault location. The numerical and experimental validation demonstrates the performance of the mismatched-media based properties in terms of fault location accuracy and using a single-end measurement. More importantly, the proposed properties require only one single simulation for the backward propagation, thus reducing significantly the computational burden of running multiple independent backward simulations as it is in the classical methods.

The chapter includes results of publications [81, 82, 173].

6.1 Electromagnetic Time Reversal in Mismatched Media

6.1.1 Matched versus mismatched media in time reversal

As discussed in the previous chapters, the classical applications of time reversal adhere to the principle of *matched media*, namely the backward-propagation medium (in the *reversed time*) is strictly identical to the forward-propagation medium (in the *direct time*) [3, 6]. However, this may not be the case in some applications related, for instance, to biomedical engineering or communication systems (e.g., [16, 38, 39]) where changes in the medium are inevitable. Thereby, the concept of *mismatched* or *changing media* has emerged to describe the scenario where the time-reversed and back-injected signal, for example, acoustic or electromagnetic waves, propagates through a medium different from the one wherein it has been generated by its original source [44, 174, 175, 176, 177, 178].

In addition to the factor of the propagative medium itself featuring uncertainties due, for instance, to time-varying characteristics (e.g., [39]), the mismatched-media situation can also result from an incomplete or inaccurate representation of the original medium in numerical environments for some applications, in which the time-reversal backward propagation is numerically simulated.

A body of literature has reported encouraging research results, demonstrating that time reversal remains a powerful technique to refocus and localize the original source, in particular, tolerates some extent of a mismatch between the forward- and backward-propagation media. It can be expected that the complexity (i.e., the existence of scatterings) and inhomogeneity of the propagation medium would compensate for some amount of the loss of propagative attributes that are due to the mismatch between the forward- and backward-media [17, 20, 177, 179, 180]. Like most application scenarios of time reversal, the propagation medium of transverse electromagnetic waves in power networks is characterized by discontinuities and inhomogeneity, which opens up the possibility of extending the application of EMTR in mismatched media to the fault location.

In the next section, investigations reported in the literature (e.g., [178]) on the focusing properties of EMTR in shifted mismatched media are briefly summarized. Then, we present the results of an experimental study on the focusing property of EMTR in lumped mismatched media.

6.1.2 Focusing properties of EMTR in shifted mismatched media

The referenced experimental study was performed by Liu et al. on EMTR in a multiple-scattering medium with a particular focus on the source localization performance in shifted mismatched media [178].

As it is shown in Fig. 6.1, Liu et al. designed an experimental set-up consisting of a total of 750 dielectric rods randomly placed in a 1.2-m long and 2.4-m wide styrofoam baseboard with an average inter-rod spacing of 6.5 cm. Two Vivaldi antennas were used, one for the transmission of and the other for the reception of vertically-polarized electric fields over band ranging from 0.5 to 10.5 GHz.

(a)   (b)
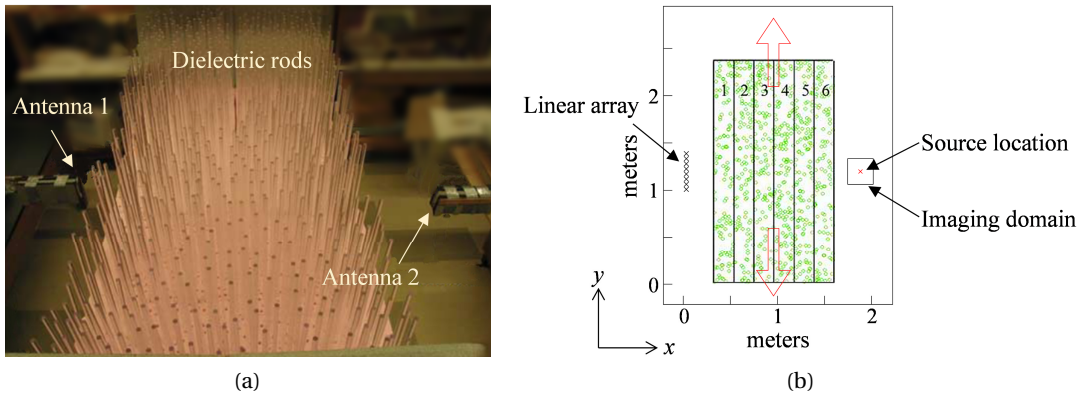
Figure 6.1 – Dielectric rod experimental set-up used in the study of time-reversal focusing property in shifted mismatched media (adopted from [178]). (a) Picture and (b) top schematic view. The dielectric rod is of 2.5-dielectric constant (ϵ_r), 1.25-cm diameter and 0.6-m length.

The mismatched-media scenario specified in the study refers to incrementally translating the rod set-up downwards or upwards relative to the antennas. In the forward-propagation stage, a single transmission antenna was situated at the center of a square imaging domain at the right side of the dielectric-rod set-up, as shown in 6.1b. The radiated electromagnetic fields were measured by an array of five antennas at the opposite side. In the backward-propagation stage, the measured fields were time reversed and re-radiated into the incrementally-translated medium. An EMTR space-time image was calculated using the measured Green's functions to represent the intensities of the received fields at the inter-grid locations within the imaging domain [178].

The experiment shows that the imaging quality is a function of the relative shift of the rod set-up and proves that the original source point can be distinguished even if there exists a certain degree of mismatch between the two stages' media. Moreover, Liu et al. proposed to use the average Green's function and the eigen Green's function, instead of the mismatched-media Green's function (from the measurement), to calculate the space-time image. The former Green's function results from the statistical processing of the measured Green's functions

across multiple realizations of mismatched media, while the latter one is based on a principle components analysis (PCA) [178, 181]. As a result, the two processed Green's functions both significantly improve the time-reversal imaging quality even in the cases of mismatching the original medium to a large extent. Thus, the experimental study confirms the effects of the multiple-scattering path in enhancing the time-reversal focusing quality against mismatch between the forward- and backward-propagation media.

6.1.3   Focusing properties of EMTR in lumped mismatched media

Inspired by the research of Liu et al., we performed an experimental study on the focusing property of EMTR in a scattering medium, in particular when a moderate lumped mismatch between the forward- and backward-propagation media occurs. Unlike the dielectric-rod set-up in [178] wherein the rods were employed in large quantities and distributed in an irregular pattern, we considered a simpler set-up. A total of 20 rods were employed and arranged regularly between the transmitting and receiving antennas, as illustrated in Fig. 6.2. The objective is to assess the time-reversal focusing property when a limited number of rods (1 or 2 out of 20) are removed from the medium in the backward-propagation stage. Indeed, the number of the scattering paths is largely reduced in comparison with that of the densely-distributed rods in [178], we hypothesize that a moderate lumped mismatch between the two stages' media would not impair the focusing property and the contributions associated with the remaining rods would still enable locating the source.

The experimental set-up shown in Fig. 6.2 was built in the EMC Laboratory of Amir Kabir University of Technology. It was composed of a 26×17.5 cm^2 area, in which 20 plexiglass dielectric rods (of 1-m length and 1-cm diameter) were evenly deployed in a matrix of 4×5 with a spacing distance between two adjacent rods being 6.5 cm. Each rod was labeled with a coordinate (r,c) according to the row and column numbers of its location (see Fig. 6.2b). The geometrical and electrical parameters of the set-up are reported in Table 6.1.

Table 6.1 – Geometrical and electrical parameters of the dielectric-rod set-up of Fig. 6.2a

Component	Parameter	Value
	Length	1 m
Rod	Diameter	1 cm
	Relative dielectric constant (ϵ_r) (methyl methacrylate)	2.7
Baseboard	Relative dielectric constant (ϵ_r) (expanded polystyrene)	2

Two double-ridged horn antennas, separated by a distance of 30 cm, were used as the transmitting and receiving antennas. The center point of the transmitting/receiving antenna's aperture was aligned with the half-length cross-section of the rods. Antenna 2 (i.e., the receiving antenna) was mounted on a stepper motor and could thus be moved vertically with a precision of one centimeter. In the forward-propagation stage, the radiated electric field was measured

(a)

(b)
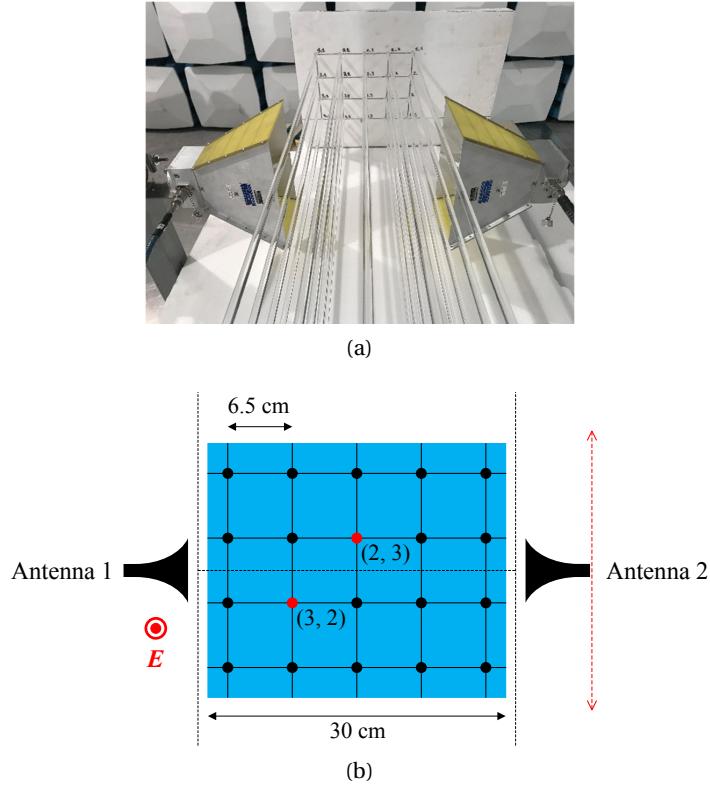
Figure 6.2 – Dielectric rod experimental set-up used in study of time-reversal focusing property in lumped mismatched media. (a) Picture and (b) schematic representation of the half-length cross-section of the rods.

by the receiving antenna in the presence of all 20 rods.

In the backward-propagation stage, we considered the following four experimental cases (summarized in Table 6.2):
Case 0: The forward- and backward-propagation media were matched (i.e., no rods removed),
Cases 1 and 2: One rod out of 20 was removed [either (2,3) or (3,2), see Fig. 6.2b],
Case 3: Two rods out of 20 [(2,3) and (3,2), see Fig. 6.2b] were removed.

Table 6.2 – Experimental cases for the backward-propagation medium

Case n		Rod(s) removed in the backward stage
0	Matched	None
1	Mismatched	$(2,3)$
2	Mismatched	$(3,2)$
3	Mismatched	$(2,3)$ and $(3,2)$

As illustrated in Fig. 6.3, in the forward-propagation stage, Antenna 1 was oriented to generating a vertically-polarized electric field. The S-parameter S_{21} (transmission coefficient) was

measured to quantify the transmitting-receiving characteristics in the frequency domain. To this end, a Rohde & Schwarz–ZVK type vector network analyzer (VNA) was used considering frequencies ranging from 7 to 18 GHz to intensify the interaction between the propagated fields with the rods.
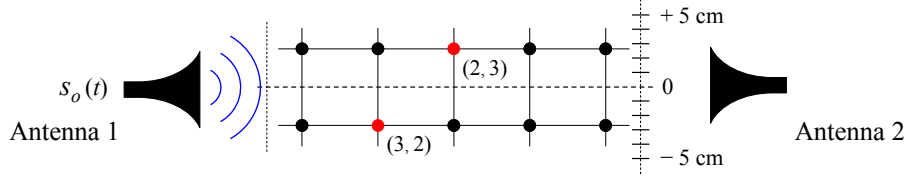
Figure 6.3 – Schematic representation of the experimental set-up in the forward-propagation stage.

To facilitate the description, we refer to the measured S_{21}-parameter as a transfer function

$$T_n^{0,h}(f) = S_{21}(f), \tag{6.1}$$

where 0 in the superscript refers to the height of the transmitting antenna (i.e., Antenna 1), which was fixed at $h = 0$ (the reference height). The second superscript h identifies the height of the receiving antenna (i.e., Antenna 2), which in the experiment varied from -5 cm to $+5$ cm, namely $h = -5, -4, \ldots, 0, \ldots, +4, +5$. The subscript n corresponds to one of the experimental cases proposed in Table 6.2 and thus it takes the following values: 0, 1, 2, 3. For example, $T_0^{0,-1}$ represents the S_{21}-parameter being measured when the receiving antenna is at the height of -1 cm with all the rods being present (i.e., *Case* 0 of the matched media).

In light of the four experimental cases of Table 6.2 and 11 considered heights for the receiving antenna, a total of 44 transfer functions were measured.

In the following analysis, we assume that the initial excitation signal $s_o(t)$ is a Morlet wavelet given by

$$s_o(t) = \cos\left(2\pi \cdot f_c \cdot t\right) \cdot e^{-\left(t/\sqrt{2}\delta\right)^2} \tag{6.2}$$

with

$$\delta = 1/f_c, \tag{6.3}$$

where f_c is the center frequency of the Gaussian function shaped magnitude spectrum of $s_o(t)$. It is assigned 12.5 GHz according to the considered frequency band ranging from 7 to 18 GHz.

The forward-propagation stage (indicated by the superscript 'DT' as the abbreviation of *direct time*) transfer function, in which both the antennas are at the reference height $h = 0$, is given by

$$T^{\mathrm{DT}}(f) = T_0^{0,0}(f) = S_{21}{}_0^0(f). \tag{6.4}$$

The received electric field reads in the frequency domain as

$$S^{\text{DT}}(f) = T^{\text{DT}}(f) \cdot S_o(f), \tag{6.5}$$

where, $S_o(f)$ is the Fourier transform of $s_o(t)$.

The time-reversal operation in the frequency domain corresponds to the complex conjugate transformation:

$$S^{\text{DT}*}(f) \triangleq \left[S^{\text{DT}}(f) \right]^*. \tag{6.6}$$

The backward propagation is schematically described in Fig. 6.4, taking *Case* 3 as an example, consisting of $S^{\text{DT}}(-t)$ being back injected from Antenna 2 meanwhile the two rods, $(2,3)$ and $(3,2)$, are removed from the original propagative medium.
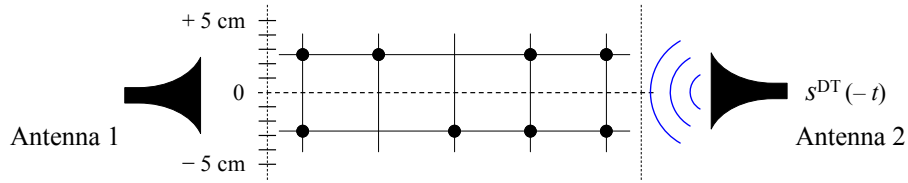
Figure 6.4 – Schematic representation of the experimental set-up for mismatched-media *Case* 3 in the backward-propagation stage.

Thus, the frequency spectrum of the field measured by Antenna 1 in the backward-propagation stage can be calculated by

$$S_n^{\text{RT}}(f, h) = S^{\text{DT}*}(f) \cdot T_n^{0,h}(f), \tag{6.7}$$

where n and h are in the ranges defined earlier.

Because of the low-loss medium, the field measured at the source location (specified in the present case by the reference height $h = 0$) is approximately a time-reversed copy of the original excitation [3, 6]. Thus, the source location can be identified in the frequency domain by using the mean square error (*MSE*) between the source excitation and the received field in the backward-prorogation stage:

$$h_o = \left. \arg \right|_h \quad Min \left\{ MSE(f, h) = \frac{1}{N} \cdot \sum_{f_{\text{lower}}}^{f_{\text{upper}}} \left| Nor\left\{ S_n^{\text{RT}*}(f, h) \right\} - S_o(f) \right|^2 \right\}, \tag{6.8}$$

where h_o is the estimated source location (i.e., the height of Antenna 1). N is the number of samples in the frequency band ranging from $f_{\text{lower}} = 7$ GHz to $f_{\text{upper}} = 18$ GHz, being set to 1601 in the experiment. The normalization operation with the notation *Nor* in (6.8) is given by

$$Nor\left\{ S_n^{\text{RT}*}(f, h) \right\} = \frac{S_n^{\text{RT}*}(f, h)}{\left| T_0^{0,0}(f) \right|^2}. \tag{6.9}$$

Figure 6.5 presents the calculated *MSE* metric as a function of the height of the receiving antenna for the cases of Table 6.2. As anticipated, the minimum of the *MSE* metric in Fig. 6.5a for the matched-media case obviously corresponds to the original source location as a result of considering the same medium in the two propagation stages.
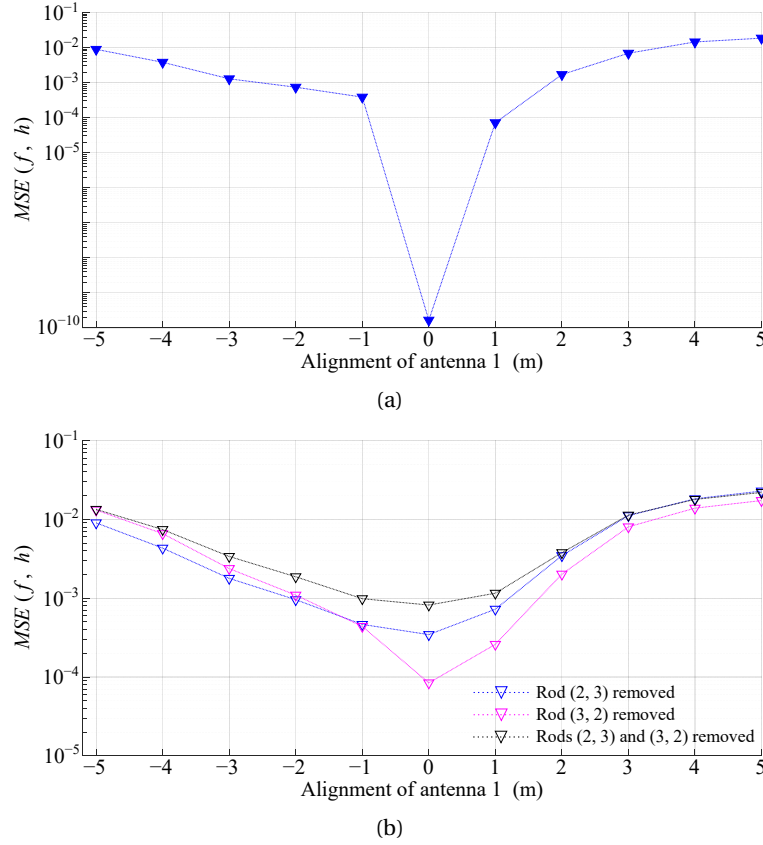
Figure 6.5 – Mean square error metric as a function of the alignment of Antenna 1 in the backward-propagation stage for (a) the matched-media case and (b) the mismatched-media cases.

It is worth noticing in Fig. 6.5b the profiles of the *MSE* metric for the respective mismatched-media cases. It is evident that, for the present study, the number of scattering paths is limited in comparison with that of the set-up in [178] wherein a total of 750 rods were distributed with an average inter-rod spacing of 6.5 cm. In spite of the fact, the absence of one or two rods in the backward-propagation medium does not dramatically compromise the time-reversal focusing property. As it can be observed, the source location still can be identified by means of the *MSE* metric formulated in (6.8).

The experimental studies presented in this section investigated the EMTR focusing property in mismatched media by considering different modifications to the backward-propagation medium. It goes without saying that either the shifted-type or the lumped-type modification

implies a controlled mismatch between the two stages' media. It is observed that as the mismatch is intensified, such as shifting the rod set-up to a larger distance (e.g., [178]) or removing an increasing number of rods, the focusing quality can be degraded.

6.2 Using Electromagnetic Time Reversal in Mismatched Media to Locate Faults in Transmission Lines

As mentioned previously, the general time-reversal application implies the use of the same propagation medium in the forward-and backward-propagation stages. In the application of EMTR to fault location, since the true fault location is unknown, the topology of the faulty network changes in the backward-propagation stage, depending on the location of the transverse branch that reproduces a fault occurrence. Inspired by the property of refocusing electromagnetic waves to the original source in lumped mismatched media, we extend the classical EMTR-based fault location methods by removing the transverse branch from the faulty power network in the backward-propagation stage.

6.2.1 General consideration

Let us recall the representation of a fault occurrence along a transmission line, as it is illustrated in Fig. 6.6a for the case of a single-wire line above the ground. With regard to the fault location problem, the propagation medium in the fault occurrence stage (i.e., forward-propagation stage) can be described in two main aspects of parameters:

i) *physical characteristics* of the line, namely its length L, characteristic impedance Z_C and propagation constant γ, and
ii) *boundary conditions* at the line terminals and the fault location.
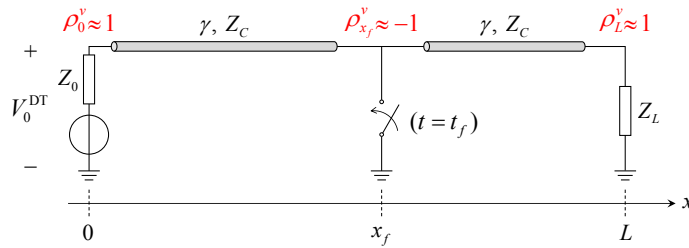
Figure 6.6 – Schematic representation of a fault occurrence in power networks. ρ_0^v, ρ_L^v and $\rho_{x_f}^v$ are the voltage reflection coefficients at the line terminals, $x = 0$ and $x = L$, and the fault location, $x = x_f$, respectively.

The boundary condition is generally quantitatively described by using the voltage (or current) reflection coefficient in the transmission-line theory. It has been explained in Chapter 2 that the line extremities constitute, to a first approximation, open circuits from the viewpoint of the frequency contents of fault-associated transient signals. As a result, $\rho_0^v \approx +1$ and $\rho_L^v \approx +1$.

Conversely, the voltage reflection coefficient associated with the fault location, $\rho_{x_f}^v$, is close to -1 when a solid or low-impedance fault is assumed.

In the classical EMTR-based fault location methods, a fault occurrence is reproduced in the backward stage, bringing about $\rho_{x_f}^v = -1$. Since the true fault location is unknown, a set of *a priori* guessed fault locations are assumed. The time-reversal inherent spatial correlation property allows the true fault location to be uniquely characterized among those guessed fault locations by the maximum amplitude or energy of the fault current signal [79, 84]. For this reason, the classical implementation of EMTR requires numerous independent backward-propagation simulations to estimate the most likely fault location. When a higher location accuracy is desired, the guessed fault locations need to be defined with increasing density. This way, the increasing number of guessed fault locations necessarily calls for an increasing computation time.
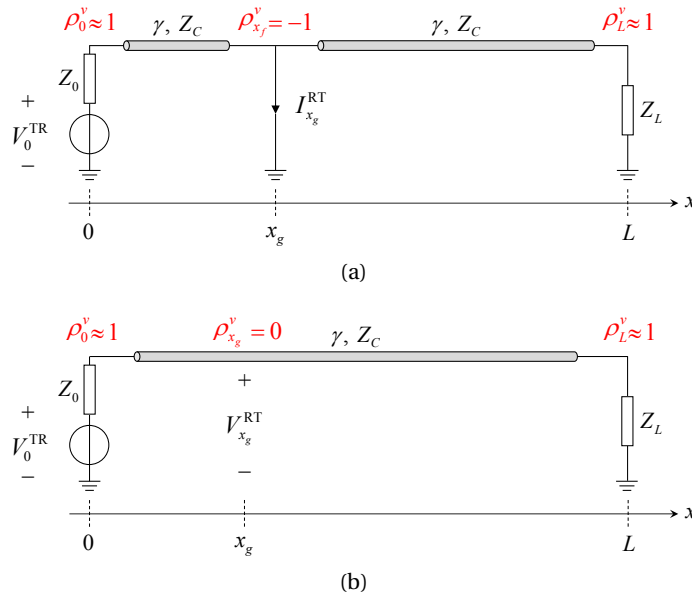
Figure 6.7 – Simplified representation of EMTR applied to locate faults in power networks based on (a) the matched-media condition and (b) the mismatched-media condition.

In view of the above, we propose to consider a fixed topology of a non-faulty power network in the backward-propagation stage, excluding the transverse branch associated with reproducing a fault, as it can be seen in Fig. 6.6b. This would effect a mismatch between the forward- and backward-propagation media as a result of changing the boundary condition at the fault location from the state of fault (i.e., $\rho_{x_f}^v = -1$) to that of non-fault (i.e., $\rho_{x_g}^v = 0$). This also constitutes a lumped mismatch in the sense that all the other line parameters and boundary conditions remain intact.

We hypothesize that the absence of the reflection and transmission processes at the fault location still allows the identification of the fault location. In other words, we assume that

the contributions associated with reflections from line terminals (and discontinuities, if any) would suffice to determine the location of the fault. This assumption can be justified by the fact that, in general, two types of components contribute to form the transient signal in response to a fault event:

i) the direct contribution coming from the fault (location) itself, and
ii) the indirect contribution coming from the reflection and transmission processes associated with the line terminals and junctions.

Let us assume to be in a hypothetical fully matched (non-reflective) medium in which the only contribution comes from the fault itself. In this case, the localization of the fault would simply not be possible by back-injecting the time-reversed transients. Thus, to locate the fault using EMTR-based methods, the components associated with the indirect contributions are by far more important than that from the fault itself.

Moreover, the proposed mismatched media also serves the purpose of realizing a faster fault response, since the multiple independent simulations at the guessed fault locations are no longer required in the backward-propagation stage. Specifically, only one simulation run is needed by considering the fixed line-topology without the transverse branch reproducing a fault. Instead of simulating the fault current as it is in the classical implementation of EMTR, the voltage along the line is considered as the characteristic quantity to infer the true fault location.

6.2.2 Transfer functions in mismatched media

For describing the proposed two-stage procedure of applying EMTR in mismatched media to locate faults in transmission-line networks, we first derive the solutions to the following variables in the frequency domain:

i) The voltage observed in the forward-propagation stage (i.e., *direct time*) at one of the line terminals, for example $x = 0$, in response to a fault occurrence at $x = x_f$:

$$V_0^{\text{DT}}(j\omega) \triangleq V(x = 0, j\omega) = \left(1 + \rho_0^v\right) \cdot \frac{e^{-\gamma(j\omega) \cdot x_f}}{1 + \rho_0^v \cdot e^{-\gamma(j\omega) \cdot 2x_f}} \cdot V_f(j\omega). \tag{6.10}$$

ii) The time-reversed voltage response that results from the complex conjugate operation

$$V_0^{\text{DT}}(j\omega) \xrightarrow{\text{TR}} V_0^{\text{TR}}(j\omega): \quad V_0^{\text{TR}}(j\omega) = \left[V_0^{\text{DT}}(j\omega)\right]^* . \tag{6.11}$$

iii) The voltage along the line with a source imposing $V_0^{\text{TR}}(j\omega)$ being applied at the observation

point in the backward-propagation stage (i.e., *reversed time*):

$$V^{\text{RT}}(x,\, j\omega) \triangleq V(x,\, j\omega) = \left(1 - \rho_0^v\right) \cdot \frac{e^{-\gamma(j\omega) \cdot x} + \rho_L^v \cdot e^{-\gamma(j\omega) \cdot (2L-x)}}{2\left[1 - \rho_0^v \cdot \rho_L^v \cdot e^{-\gamma(j\omega) \cdot 2L}\right]} \cdot V_0^{\text{TR}}(j\omega). \tag{6.12}$$

Next, to relate the above-formulated variables, we first introduce the *direct-time* transfer function as the ratio of the output variable $V_0^{\text{DT}}(j\omega)$ to the input variable $V_f(j\omega)$, namely

$$\mathcal{H}^{\text{DT}}(x_f,\, j\omega) = \frac{V_0^{\text{DT}}(j\omega)}{V_f(j\omega)}, \tag{6.13}$$

and, we define in a similar way the *reversed-time* transfer function

$$\mathcal{H}^{\text{RT}}(x,\, j\omega) = \frac{V^{\text{RT}}(x,\, j\omega)}{V_0^{\text{TR}}(j\omega)}. \tag{6.14}$$

It is important to underline that the output variable $V_0^{\text{DT}}(j\omega)$ in the *direct time* is time reversed and then behaves as the input in the *reversed time*. As a result, we write

$$V^{\text{RT}}(x,\, j\omega) = \mathcal{H}^{\text{RT}}(x,\, j\omega) \cdot \left[\mathcal{H}^{\text{DT}}(x_f,\, j\omega)\right]^* \cdot \left[V_f(j\omega)\right]^* \tag{6.15}$$

to relate the output in the *reversed time* to the input in the *direct time*.

Finally, we define the *direct-reversed-time* transfer function as

$$\mathcal{H}(x,\, j\omega) = \mathcal{H}^{\text{RT}}(x,\, j\omega) \cdot \left[\mathcal{H}^{\text{DT}}(x_f,\, j\omega)\right]^*. \tag{6.16}$$

According to (6.10) to (6.16), $\mathcal{H}(x,\, j\omega)$ can be analytically expressed as follows:

$$\mathcal{H}(x,\, j\omega) = (1 - \rho_0^v) \cdot \frac{e^{-\gamma(j\omega) \cdot x} + \rho_L^v \cdot e^{-\gamma(j\omega) \cdot (2L-x)}}{2\left[1 - \rho_0^v \cdot \rho_L^v \cdot e^{-\gamma(j\omega) \cdot 2L}\right]} \cdot \left[(1 + \rho_0^v) \cdot \frac{e^{-\gamma(j\omega) \cdot x_f}}{1 + \rho_0^v \cdot e^{-\gamma(j\omega) \cdot 2x_f}}\right]^*. \tag{6.17}$$

This way, the general task of locating faults in transmission-line networks can be accomplished through investigating the behavior of the *direct-reversed-time* transfer function as it behaves as a function of the longitudinal coordinate x.

6.3 Property: Bounded Phase of the *Direct-Reversed-Time* Transfer Function

In this section, we state a theorem according to which the phase angle of the *direct-reversed-time* transfer function $\mathcal{H}(x, j\omega)$ is bounded between $\pm\pi/2$ at the position of the fault. This theorem will be applied to develop an algorithm for fault location in transmission-line networks.

6.3.1 *Theorem 1: bounded phase of $\mathcal{H}(x, j\omega)$*

The phase angle of the *direct-reversed-time* transfer function of EMTR in mismatched media presents the following property.

Theorem 1 if $x = x_f$, $\angle\mathcal{H}(x_f, j\omega) \in (-\pi/2, \pi/2)$;

$$\forall\, x \neq x_f, \exists\, f = \omega/2\pi : \angle\mathcal{H}(x, j\omega) \notin (-\pi/2, \pi/2).$$

The symbol of $\angle$ denotes phase angle or argument in radians. The property described by *Theorem 1* hereafter is referred to as the *bounded phase* property.

In what follows, we present the mathematical proof of *Theorem 1*. For the sake of simplicity, the proof still makes reference to the lossless-line assumption, which results in the propagation constant γ being $j\beta(\omega)$, with $\beta(\omega)$ denoting the phase constant. In the same way, the characteristic impedance Z_C and the voltage reflection coefficients, ρ_0^v and ρ_L^v, turn out to be frequency independent. Besides, in view of the fact that $\rho_0^v \approx 1$ and $\rho_L^v \approx 1$, further simplification in the proof is applied by considering $\rho_0^v = \rho_L^v = \rho$. $\mathcal{H}(x, j\omega)$ consequently becomes

$$\mathcal{H}(x, j\omega) = (1 - \rho^2) \cdot \frac{e^{-j\beta(\omega)\cdot(x-x_f)} + \rho \cdot e^{-j\beta(\omega)\cdot(2L-x-x_f)}}{2\left[1 - \rho^2 \cdot e^{-2j\beta(\omega)\cdot L}\right] \cdot \left[1 + \rho \cdot e^{2j\beta(\omega)\cdot x_f}\right]}. \tag{6.18}$$

The complete proof of *Theorem 1* in a lossy medium is given in Appendix A.1.

Proof. Let $x_{\mathbb{G}}$ be a set of *a priori* guessed fault locations, namely

$$x_{\mathbb{G}} = \left\{ x_g \,\middle|\, x_{g,0} = x_f, x_{g,1}, x_{g,2}, \ldots \right\}, \tag{6.19}$$

where the transfer function $\mathcal{H}(x_g, j\omega)$ is calculated.

If the phase angle of the complex-valued function $\mathcal{H}(x_g = x_f, j\omega)$ satisfies the open interval $(-\pi/2, \pi/2)$, the real part of it is necessarily positive for all frequencies. Thus, proving *Theorem 1* can be carried out by distinguishing x_f from the guessed fault location, which is

$$x_g \in \complement_{x_{\mathbb{G}}} x_f, \tag{6.20}$$

through inspecting the sign of the real part of $\mathcal{H}(x_g, j\omega)$.

To this end, a straightforward manipulation provides the expression

$$Re\{\mathcal{H}(x_g, j\omega)\} =$$
$$(1-\rho^2)^2 \cdot$$

$$\frac{\overbrace{(1+\rho^2)\cdot\cos[\beta(\omega)\cdot(x_g-x_f)]}^{\mathcal{H}_a} + \overbrace{\rho\cdot\cos[\beta(\omega)\cdot(x_g+x_f)] + \rho\cdot\cos[\beta(\omega)\cdot(2L-x_g-x_f)]}^{\mathcal{H}_{bc}}}{2\left\{(1+2\rho)^2 + \rho^2\cdot\sin^2[\beta(\omega)\cdot L]\right\}\cdot\left\{(1-\rho^2)^2 + 4\rho\cdot\cos^2[\beta(\omega)\cdot x_f]\right\}}, \tag{6.21}$$

in which the symbol of *Re* denotes the real part function.

It is not trivial to observe that the term $(1-\rho^2)^2$ and the denominator in (6.21) appear always positive.

As it is indicated, we introduce the terms in the numerator as

$$\mathcal{H}_a = (1+\rho^2)\cdot\cos[\beta(\omega)\cdot(x_g-x_f)], \tag{6.22}$$

and

$$\mathcal{H}_{bc} = \rho\cdot\left\{\cos[\beta(\omega)\cdot(x_g+x_f)] + \cos[\beta(\omega)\cdot(2L-x_g-x_f)]\right\}. \tag{6.23}$$

It is worth observing that $\mathcal{H}_a$ varies in the closed interval between $\pm(1+\rho^2)$, while $\mathcal{H}_{bc}$ in the closed interval limited by $\pm2\rho$. The sign of (6.21) is determined by the sum of the two terms:

$$\mathcal{H}_a + \mathcal{H}_{bc}. \tag{6.24}$$

We divide the proof into two cases referring to $x_g = x_f$ and $x_g \neq x_f$, respectively.

i) $x_g = x_f$

When the guessed fault location x_g coincides with the true fault location x_f, (6.24) becomes

$$(1+\rho^2) + \rho\cdot\left\{\cos[\beta(\omega)\cdot 2x_f] + \cos[\beta(\omega)\cdot 2(L-x_f)]\right\}. \tag{6.25}$$

Applying the double-angle formulas, (6.25) can be written as

$$(1+\rho^2) + \rho\cdot\left\{2\cos^2[\beta(\omega)\cdot x_f] + 2\cos^2[\beta(\omega)\cdot(L-x_f)] - 2\right\}, \tag{6.26}$$

and

$$(1-\rho)^2 + 2\rho\cdot\left\{\cos^2[\beta(\omega)\cdot x_f] + \cos^2[\beta(\omega)\cdot(L-x_f)]\right\} > 0, \tag{6.27}$$

As it can be seen, the terms in (6.27) all appear non-negative, and above all the sum of the terms is always greater than zero as the addends do not reach zero simultaneously.

Thus, we prove that (6.24) is positive $\forall\omega\,(=2\pi\cdot f)$.

$ii)$ $x_g \neq x_f$

In this case, $\mathcal{H}_a$ is not always positive, while being in the closed interval limited by $\pm \left(1 + \rho^2\right)$. For proving *Theorem 1*, it suffices to find a special value of ω such that

$$\mathcal{H}_a + \mathcal{H}_{bc} < 0. \tag{6.28}$$

For instance, there exists $\omega = \dfrac{\nu}{x_g - x_f} \cdot (\pi + 2k\pi)$, with $k \in \mathbb{Z}$ and ν referring to the phase velocity, such that (6.22) and (6.23) can be written as follows:

$$\mathcal{H}_a = \left(1 + \rho^2\right) \cdot \cos(\pi) = -\left(1 + \rho^2\right), \tag{6.29}$$

and

$$\begin{aligned} \mathcal{H}_{bc} &= \rho \cdot \left[\cos\left(\pi \cdot \frac{x_g + x_f}{x_g - x_f}\right) + \cos\left(\pi \cdot \frac{2L - x_g - x_f}{x_g - x_f}\right) \right] \\ &= 2\rho \cdot \cos\left(\pi \cdot \frac{L}{x_g - x_f}\right) \cdot \cos\left(\pi \cdot \frac{L - x_g - x_f}{x_g - x_f}\right). \end{aligned} \tag{6.30}$$

$\mathcal{H}_{bc}$ ranges from -2ρ to 2ρ and, therefore, there exists

$$\mathcal{H}_a + \mathcal{H}_{bc} = -\left(1 + \rho^2\right) + \mathcal{H}_{bc} < -\left(1 + \rho^2\right) - 2\rho < 0, \tag{6.31}$$

which is satisfied $\forall x_g \neq x_f$.

At this point *Theorem 1* is proved.

6.3.2 Numerical validation

In this section, we present the first numerical example to validate the bounded phase property suggested by *Theorem 1*. We make reference to a single-conductor transmission line specified by the per-unit-length parameters of typical 20-kV overhead lines, which are reported in Table 6.3.

Table 6.3 – Typical transmission-line parameters of 20-kV overhead lines and coaxial cables

Line parameter	Overhead line	Coaxial cable
Per-unit-length inductance l	1.1 μH/m	0.309 μH/m
Per-unit-length capacitance c	10.7 pF/m	302 pF/m
Per-unit-length resistance r	0.268 mΩ/m	0.0995 mΩ/m
Per-unit-length conductance g	$--$	0.285 nS/m

The line is assumed to be connected at both ends to power transformers, which are represented by their high-frequency input impedance ($Z_0 = Z_L = 100$ kΩ in this example.) The line length

113

L is 6.5 km and the fault is assumed to occur at 3.6 km away from the line terminal $x = 0$, where the observation point is located.

Figure 6.8a shows the computed phase angle of $\mathcal{H}(x_g, j\omega)$ for Case i) wherein the guessed fault location x_g is exactly the true fault location x_f. As it can be observed, the phase angle of $\mathcal{H}(x_f, j\omega)$ is bounded by $\pm\pi/2$, confirming the formulated phase property. The computation involves a frequency range between 100 Hz and 5 MHz, considering a frequency step df equal to 10 Hz.

(a)

(b)

(c)
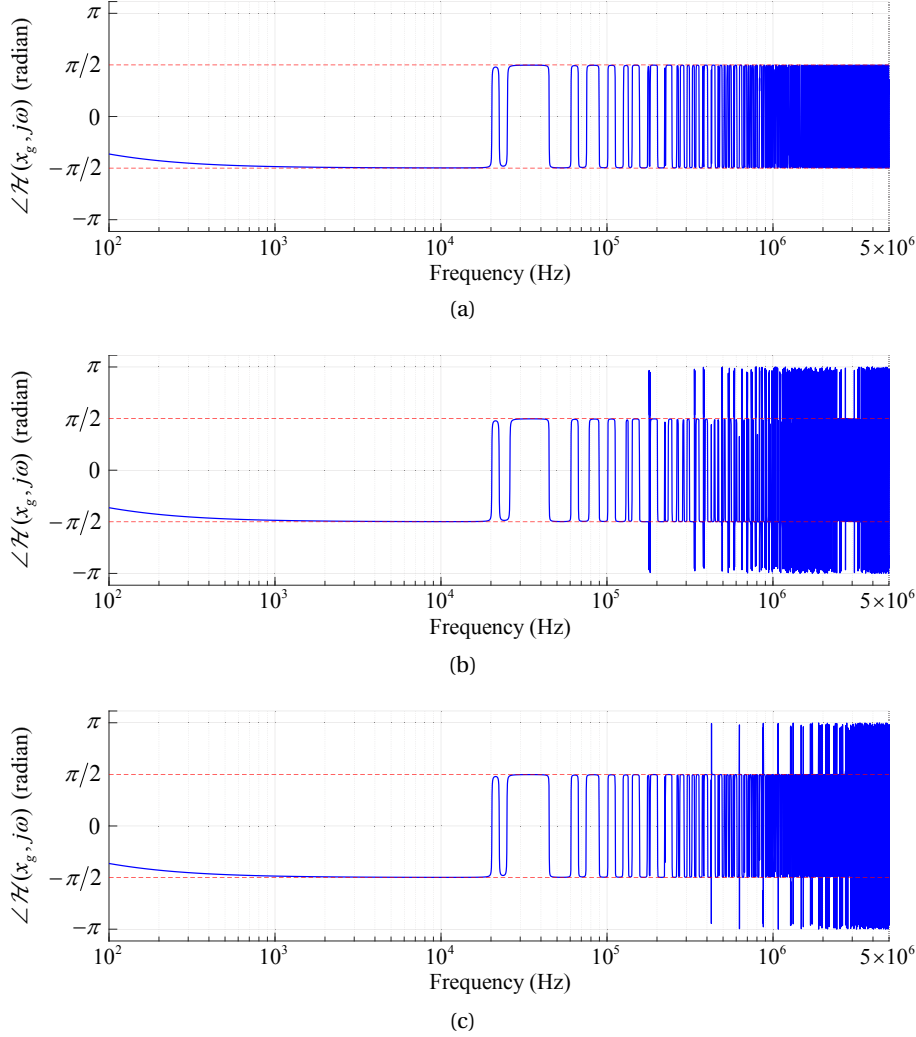
Figure 6.8 – Phase angle of the transfer function $\mathcal{H}(x_g, j\omega)$ for a 20-kV single-conductor overhead line ($L = 6.5$ km, $x_f = 3.6$ km), for (a) $x_g = x_f$, (b) $x_g = x_f + 100$ m, and (c) $x_g = x_f - 20$ m, with f ranging from 100 Hz to 5 MHz and the frequency step being 10 Hz.

In Cases ii) and iii), x_g is assumed to be $x_f + \Delta x$, with Δx being respectively $+100$ m (see Fig. 6.8b) and -20 m (see Fig. 6.8c). Δx denotes a difference between the guessed fault location x_g and the true fault location x_f. It is evident that, in these two cases, the argument of $\mathcal{H}(x_g, j\omega)$

exhibits some out-of-range values at higher frequencies even though it is still bounded by $\pm\pi/2$ at lower frequencies.

The numerical validation is extended to further observe the distribution of $\mathcal{H}(x_g, j\omega)$ in the complex plane. As it is suggested in the proof, only if x_g coincides with x_f is the real part of $\mathcal{H}(x_g, j\omega)$ positive. Fig. 6.9 compares the four-quadrant distribution of the complex-valued $\mathcal{H}(x_g, j\omega)$ as a function of $\omega = 2\pi \cdot f$ for three cases: *i*) $x_g = x_f$ (i.e., Fig. 6.9a), *ii*) $x_g = x_f + 15$ m (i.e., Fig. 6.9b), and *iii*) $x_g = x_f - 100$ m (i.e., Fig. 6.9c). f ranges from 100 Hz to 5 MHz and is discretized by an increment $df = 100$ Hz.

(a)

(b)

(c)
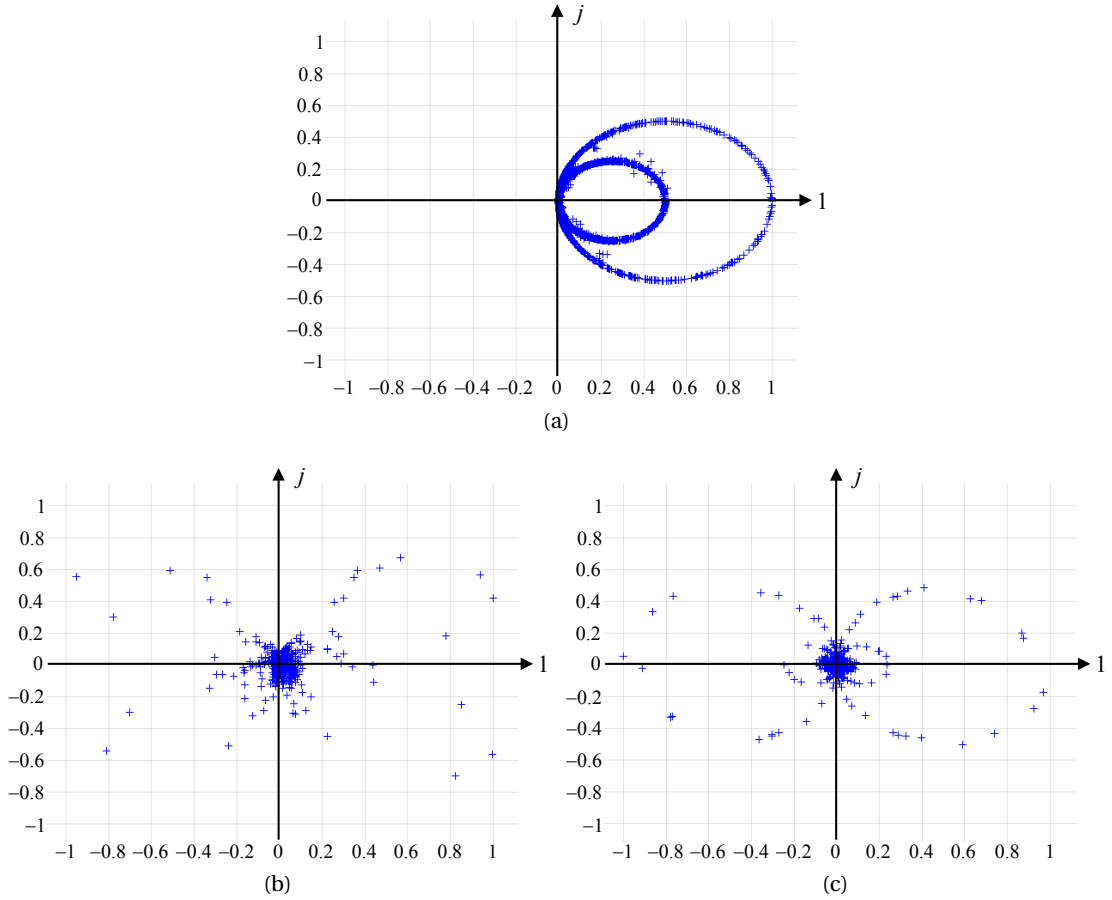
Figure 6.9 – Four-quadrant distribution of the normalized transfer function $Nor\left\{\mathcal{H}(x_g, j\omega)\right\}$ for a 20-kV single-conductor overhead line ($L = 6.5$ km, $x_f = 3.6$ km), for (a) $x_g = x_f$, (b) $x_g = x_f + 15$ m, and (c) $x_g = x_f - 100$ m. f ranges from 100 Hz to 5 MHz with $df = 100$ Hz.

For the sake of comparison, we define a normalization function $Nor\{\cdot\}$ that consists of the operation:

$$Nor\{\cdot\} \triangleq \frac{\cdot}{Max\left\{Abs\left\{Re\{\cdot\}\right\},\ Abs\left\{Im\{\cdot\}\right\}\right\}}, \tag{6.32}$$

where the symbols of *Max, Abs, Re* and *Im* denote the functions of maximum, absolute value,

real part and imaginary part, respectively.

As it can be observed, the real and imaginary parts of $Nor\left\{\mathcal{H}(x_g, j\omega)\right\}$ are confined within the region of $[-1,1] \times [-j, j]$ in the complex plane. In particular, for the case of Fig. 6.9a, $\left(Re\{\mathcal{H}(x_g = x_f, j\omega)\}, Im\{\mathcal{H}(x_g = x_f, j\omega)\}\right)$ is only located in Quadrants I and II, thus ensuring the phase angle of $\mathcal{H}(x_f, j\omega)$ not being over the limit of $\pm\pi/2$.

6.3.3 *Lemma 1: inverse relation*

A close observation of $\angle\mathcal{H}(x_f + \Delta x, j\omega)$ illustrated in Fig. 6.8 shows that the larger the distance $|\Delta x|$, the smaller the $\pm\pi/2$ bounded region. For example, in the case of $\Delta x = -20$ m (see Fig. 6.8c), the frequency point corresponding to the first out-of-range phase angle, denoted by f_o, appears to be 0.425 MHz, while if $\Delta x = +100$ m (see Fig. 6.8b), f_o is reduced to 0.177 MHz.

We formally define the first out-of-range frequency f_o as: for a given fault occurrence at $x = x_f$, a generic location along the line can be expressed as $x = x_f + \Delta x$, there exists f_o, such that

$$
\begin{aligned}
\angle\mathcal{H}(x_f + \Delta x, j\omega) \in (-\pi/2, \pi/2), &\quad \forall f < f_o, \\
\angle\mathcal{H}(x_f + \Delta x, j\omega) \notin (-\pi/2, \pi/2), &\quad \forall f \geq f_o,
\end{aligned}
\tag{6.33}
$$

where $\omega = 2\pi \cdot f$. We write f_o as

$$
\begin{aligned}
f_{o, +|\Delta x|}, &\quad for\ \Delta x > 0, \\
f_{o, -|\Delta x|}, &\quad for\ \Delta x < 0.
\end{aligned}
\tag{6.34}
$$

And there is

Lemma 1 $\quad f_{0, \pm|\Delta x|} \propto \dfrac{1}{|\Delta x|}$,

which states that the first-out-of-range frequency $f_{0, \pm|\Delta x|}$ is inversely proportional to the distance between a generic location along the line and the true fault location.

This behavior, as explained in the proof in Section 6.3.1, is due to the fact that the sign of the real part of $\mathcal{H}(x_g, j\omega)$ is determined by that of $\mathcal{H}_a + \mathcal{H}_{bc}$. Moreover, $\mathcal{H}_a$ appears dominant as a guessed fault location approaches x_f. The smaller $|\Delta x|$, the wider the frequency band (ranging from $f = 0$) wherein the sign of $\mathcal{H}_a$ remains positive.

Dealing with the fault location problem, $|\Delta x|$ represents the location accuracy, with which the true fault location x_f is allowed to be distinguished from its neighboring locations $x_f \pm \Delta x$. The property suggested by *Lemma 1* leads the investigation:

i) to assess the achievable fault location accuracy $|\Delta x|$ by means of the bounded phase property;

ii) to correlate the achieved accuracy $|\Delta x|$ with its required least frequency bandwidth $f_{o, |\Delta x|}$,

which is determined by the first out-of-range frequencies $f_{o,\pm|\Delta x|}$. To be specific,

$$f_{o,|\Delta x|} = Max\left\{ f_{o,+|\Delta x|},\ f_{o,-|\Delta x|} \right\}. \tag{6.35}$$

Relating $f_{o,|\Delta x|}$ to Δx benefits the deployment of the proposed phase property in a real application wherein any digital sampling system is band limited.

We propose a pseudo algorithm (see Table 6.4), which is compatible with discretized time- and frequency-domain quantities, to estimate the least bandwidth allowing reaching a corresponding desired location accuracy $|\Delta x|$.

Table 6.4 – Pseudo-algorithm of estimating $f_{o,|\Delta x|}$ as a function of $|\Delta x|$

Input:	network topology and parameters, the true fault location x_f, and the frequency vector
	$$\mathbb{F} = \left\{ f_j = j \cdot \mathrm{d}f \right\},\ j = 0, 1, \dots, M. \tag{6.36}$$
for	each *a priori* Δx_i **do**
	1: compute $\angle \mathcal{H}(x_f + \Delta x_i, j\omega_j)$, $\omega_j = 2\pi \cdot f_j$, $\forall j$
	2: $f_{o,\pm|\Delta x_i|} = f_{i^\pm}$
	3: $f_{o,|\Delta x_i|} = Max\left\{ f_{i^+},\ f_{i^-} \right\}$
end	
Output:	$|\Delta x_i|$ and $f_{o,|\Delta x_i|}$

For a fault occurrence at $x = x_f$ in a transmission-line network under study. We define a frequency vector as $\mathbb{F}$ in (6.36), in which $\mathrm{d}f$ is dependent on the given sampling rate and the number of samples while M is related to the system bandwidth. The algorithm links $f_{o,|\Delta x_i|}$ to the corresponding accuracy $|\Delta x_i|$, clarifying that there exists a least requirement for the bandwidth, below which it is impossible to identify the true fault location with the desired location accuracy.

Figure 6.10 reports the first out-of-range frequency $f_{o,|\Delta x|}$ as a function of Δx for the line set-up considered in Section 6.3.2 with $x_f = 3.6$ km (see Fig. 6.10a) and an additional case wherein $x_f = 545$ m. The desired fault location accuracy $|\Delta x|$ is assumed to be 10 m in the case of Fig. 6.10a and 5 m for the case of Fig. 6.10b. The calculation identifies the least frequency $f_{o,|\Delta x|}$ respectively as 0.829 MHz and 1.456 MHz.

(a)

(b)
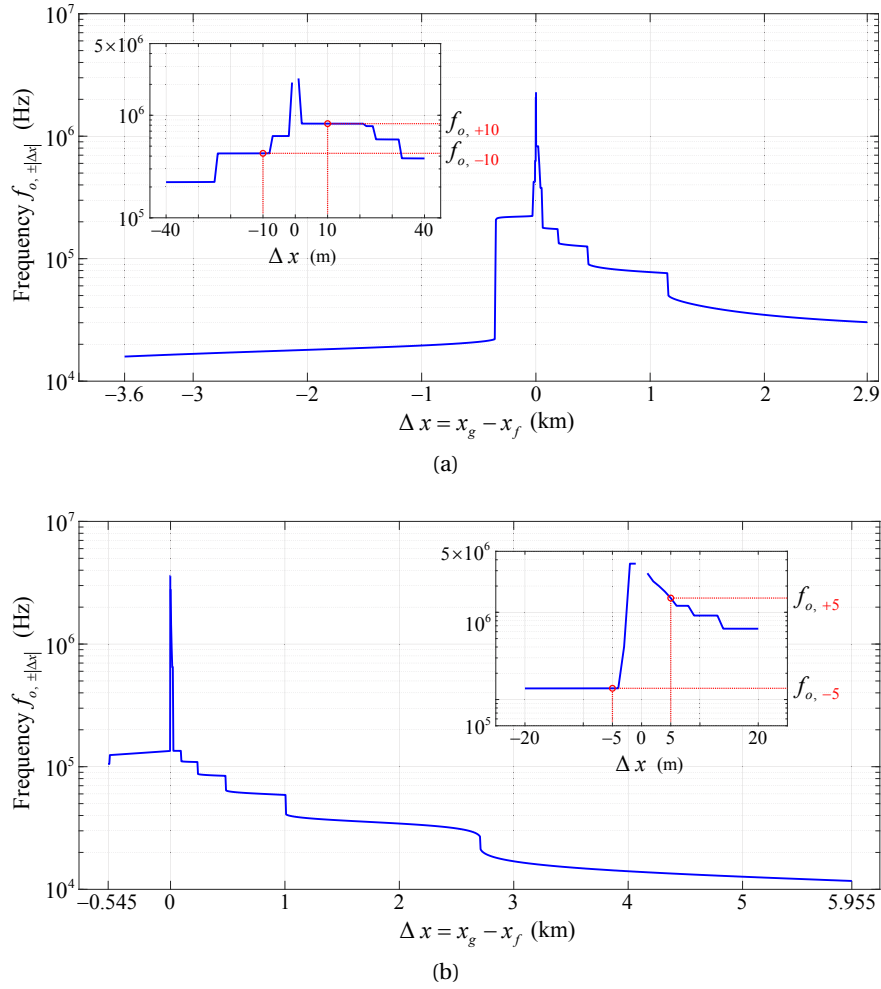
Figure 6.10 – First out-of-range frequency $f_{o,\pm|\Delta x|}$ as a function of Δx for (a) $x_f = 3.6$ km and (b) $x_f = 545$ m. The line length L is 6.5 km. f ranges from 100 Hz to 5 MHz with $\mathrm{d}f = 10$ Hz.

6.3.4   Application example

Although the formulation of *Theorem 1* in Section 6.3.1 makes reference to a simplified line setup, namely a non-branched homogeneous overhead line, we show two examples in this section that the proposed bounded phase property is applicable to more topologically-complex networks. To be specific, a single-phase line composed of mixed overhead-coaxial cable lines and a Y-shaped inhomogeneous network are considered. The adopted parameters refer to those of typical line/cables in distribution/transmission networks and the line losses are also taken into account in these simulations.

1) *Single-phase inhomogeneous transmission line*

The first simulation case considers an inhomogeneous transmission line with an overall length $L_1 + L_2 = 15$ km, consisting of an overhead line of length $L_1 = 6$ km and a coaxial cable of length $L_2 = 9$ km, as shown in Fig. 6.11. The adopted 20-kV line/cable parameters are summarized in Table 6.3. The line is terminated at each of the ends with a power transformer, whose high-frequency input impedance, Z_0 or Z_L, is assumed to be 100 kΩ. The line terminal $x = 0$ constitutes the single observation point.
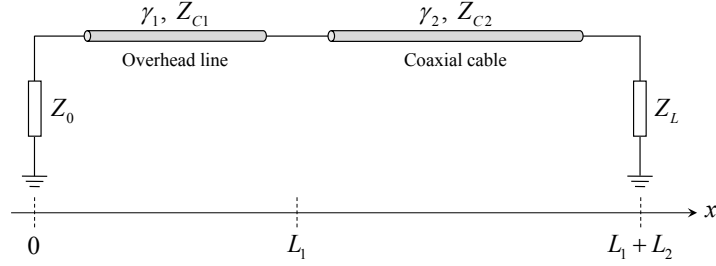
Figure 6.11 – Schematic representation of a single-phase transmission line composed of mixed overhead-coaxial cable lines.

To demonstrate the reliability of the proposed bounded phase property, two fault cases are considered to cover faults respectively occurring along the overhead line (i.e., $0 < x = x_f < L_1$) and the coaxial cable (i.e., $L_1 < x = x_f < L_1 + L_2$).

a) Fault occurrence along the overhead line at $x = x_f = 2.1$ km

Figure 6.12 illustrates the calculated phase angle of the transfer function $\mathcal{H}(x_g, j\omega)$ as a function of the guessed fault location x_g and the frequency f. x_g is defined along both the overhead line and the underground cable with an increment (dx) of 100 m. f ranges from 1 kHz to 1 MHz with df equaling 100 Hz. For the sake of observation, Fig. 6.12 plots at each x_g only the out-bounded phase angle, namely $\angle\mathcal{H}(x_g, j\omega) \notin (-\pi/2, \pi/2)$. The true fault location $x_g = x_f$ can be clearly distinguished from the other guessed fault locations. To be specific, x_f exclusively features a bounded phase angle among the guessed fault locations, displaying a null distribution of $\angle\mathcal{H}(x_f, j\omega)$ throughout the considered frequency range. That is to say, it confirms that $\angle\mathcal{H}(x_f, j\omega)$ is bounded by $\pm\pi/2$.

Moreover, according to the curve of $f_{o, \pm|\Delta x|}-\Delta x$ shown in Fig. 6.13, the true fault location x_f can be identified with a desired accuracy $|\Delta x|$ of 1 m by means of the bounded phase property when $f > 0.503$ MHz.
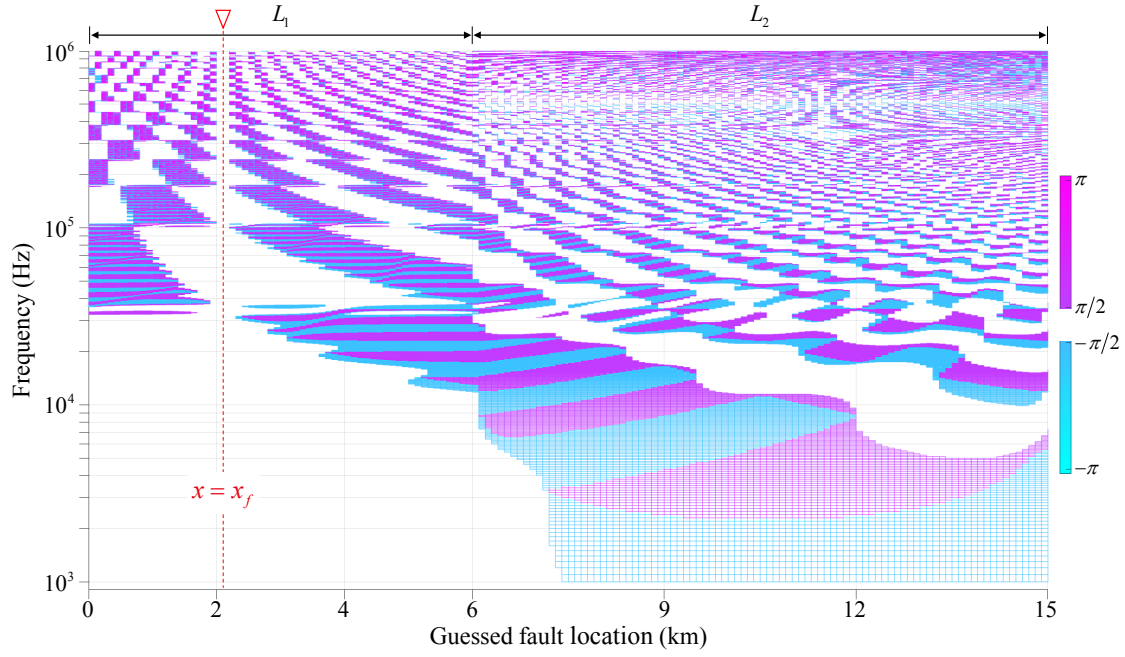
Figure 6.12 – Phase angle of the transfer function $\mathcal{H}(x_g, j\omega)$ for the case $x_f = 2.1$ km as a function of the guessed fault location x_g and the frequency f. $0 < x_g < L_1 + L_2$ with $dx = 100$ m and 1 kHz $< f < 1$ MHz with $df = 100$ Hz.

Figure 6.13 – First out-of-range frequency $f_{o, \pm|\Delta x|}$ as a function of Δx ($0 < x_g < L_1$) for the case $x_f = 2.1$ km. f ranges from 100 Hz to 1 MHz with $df = 10$ Hz.

b) **Fault occurrence along the coaxial cable at** $x = x_f = 10.8$ **km**

We consider now a fault event along the cable section with $x_f = 10.8$ km. Fig. 6.14 shows the phase angle of the transfer function versus frequency for each guessed fault location. Again, it is confirmed that the only location rendering $\angle \mathcal{H}(j\omega)$ bounded appears at the true fault location. Moreover, calculating the first out-of-range frequency $f_{o,\pm|\Delta x|}$ with a finer distance-difference Δx, a better-than-1-m location accuracy is achievable when the frequency is greater than 0.215 MHz
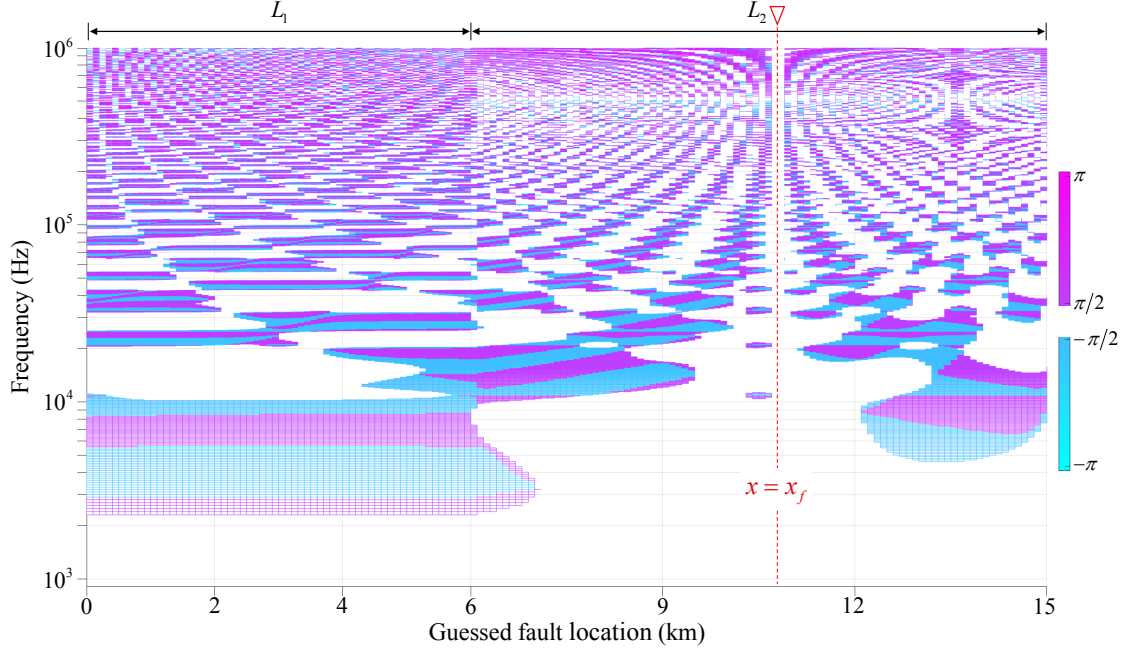
Figure 6.14 – Phase angle of the transfer function $\mathcal{H}(x_g, j\omega)$ for the case $x_f = 10.8$ km as a function of the guessed fault location x_g and the frequency f. $0 < x_g < L_1 + L_2$ with $\mathrm{d}x = 100$ m and 1 kHz $< f < 1$ MHz with $\mathrm{d}f = 100$ Hz.

2) *Y-Shaped inhomogeneous network*

The applicability of the formulated transfer function property is further discussed by taking account of:

i) The topological complexity of transmission-line networks, thereby a Y-shaped network (see Fig. 6.15) is considered to represent generic teed networks that contain an arbitrary number of line branches and nodes.

ii) The inhomogeneity of transmission-line networks. To this end, the Y-shaped network is composed of overhead lines and coaxial cables, as it is indicated in Fig. 6.15

iii) The location of a single observation point. Each of the network terminals is considered to be a single observation point in response to separate fault occurrences along the three line
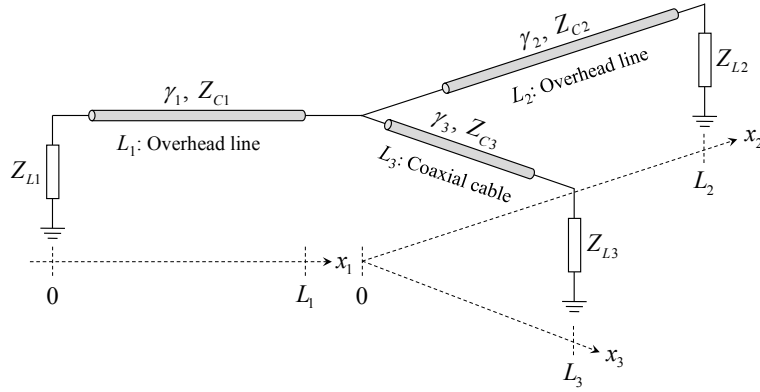
Figure 6.15 – Schematic representation of the Y-shaped inhomogeneous transmission-line network.

branches.

To be specific, the line/cable sections are respectively 6 km (L_1 = 6 km), 11 km (L_2 = 11 km), and 5 km (L_3 = 5 km) in length. To facilitate the description, the three line branches hereafter are referred to by their respective lengths.

The inhomogeneity of the network is enhanced by characterizing the line branches with diverse types of lines/cables. As it is shown in Fig. 6.15, the adopted parameters are extended beyond that of the 20-kV line/cable (see Table 6.3) employed in the previous cases. Specifically, Branches L_1 and L_3 are respectively 380-kV overhead line and coaxial cable, whose per-unit-length parameters are reported in Table 6.5. Meanwhile, Branch L_2 is a 20-kV overhead line.

Table 6.5 – Typical transmission-line parameters of 380-kV overhead lines and coaxial cables

Line parameter	Overhead line	Coaxial cable
Per-unit-length inductance l	0.853 μH/m	0.71 μH/m
Per-unit-length capacitance c	13.7 pF/m	266 pF/m
Per-unit-length resistance r	0.02 mΩ/m	0.025 mΩ/m
Per-unit-length conductance g	0.007 nS/m	0.194 nS/m

We assume that a solid fault occurs at an arbitrary location along the three line branches. Then the transfer function $\mathcal{H}(x_g, j\omega)$ is calculated based on the single observation point being separately located at the left end of Branch L_1 (i.e., $x_1 = 0$), the right end of Branch L_2 (i.e., $x_2 = 11$ km) and the right end of Branch L_3 (i.e., $x_3 = 5$ km). The network is grounded at the three ends with the high impedance, showing $Z_{L1} = Z_{L2} = Z_{L3} = 100$ kΩ, to model the input impedance of the terminal transformer.

In what follows, we report the assessment of the bounded phase property in two fault cases:

i) fault occurrence along the 20-kV overhead line (i.e., Branch L_2) at $x_2 = x_f = 7.9$ km, and

ii) fault occurrence along the 380-kV coaxial cable (i.e., Branch L_3) at $x_3 = x_f = 3.7$ km.

a) **Fault occurrence along Branch L_2 at $x_2 = x_f = 7.9$ km**

The three subgraphs in Fig. 6.16 show in the x_g–f plane the calculated and color-coded phase angle of the transfer function $\mathcal{H}(x_g, j\omega)$, corresponding to the guessed fault locations being defined along Branches L_1, L_2 and L_3 with a distance step dx of 100 m. The terminals of the two non-faulty line branches, namely $x_1 = 0$ and $x_3 = 5$ km, are referred to as the far ends relative to defining the terminal of the faulty line branch itself as the near end (i.e., $x_2 = 11$ km).

The presented results in Fig. 6.16 are associated with using the far end $x_1 = 0$ as the single observation point. As it can be seen in Fig. 6.16, in spite of the enhanced topological complexity and inhomogeneity of the network, the proposed transfer function property is still validated, showing that $\angle\mathcal{H}(x_g = x_f, j\omega)$ is bounded by $\pm\pi/2$. It is worth noting that a similar distribution of $\angle\mathcal{H}(x_g, j\omega)$ along Branch L_2 can be obtained when formulating the transfer function based on another far end (e.g., $x_3 = 5$ km) as the observation point.
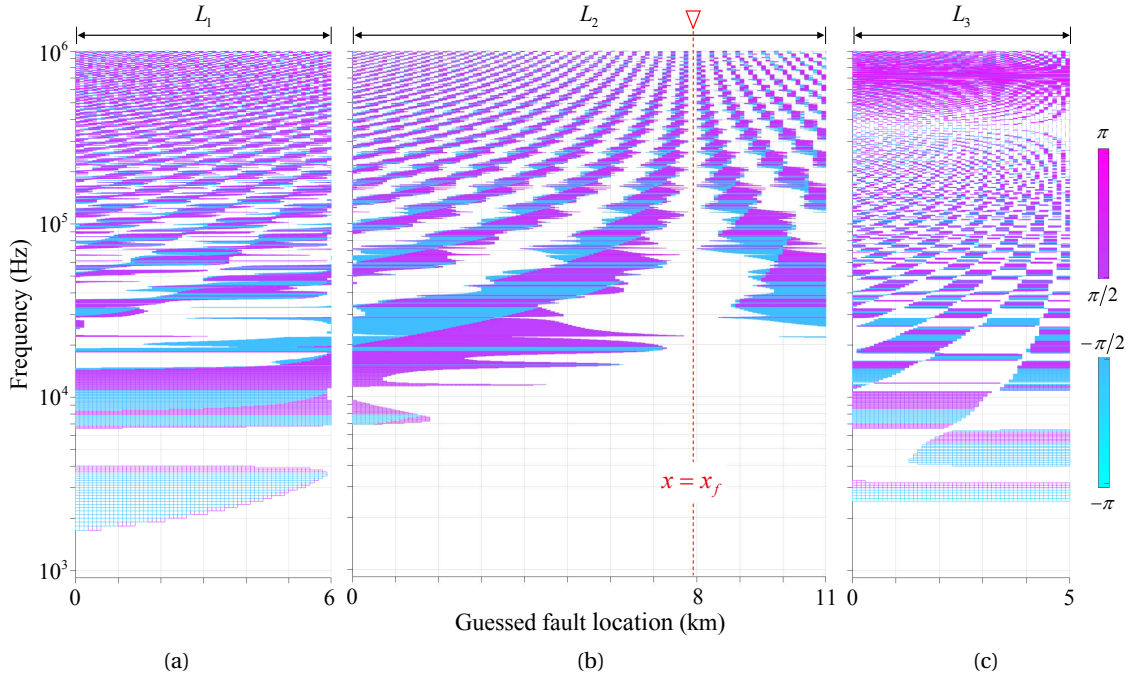
Figure 6.16 – Phase angle of the transfer function $\mathcal{H}(x_g, j\omega)$ for the case $x_2 = x_f = 7.9$ km based on the far end $x_1 = 0$ as the single observation point. (a) $0 < x_g < L_1$, (b) $0 < x_g < L_2$, and (c) $0 < x_g < L_3$ (d$x = 100$ m). f ranges from 1 kHz to 1 MHz and df equals 100 Hz.

Chapter 6. Electromagnetic Time Reversal in Mismatched Media and Its Fault Location Application

In addition to the scenario of situating the observation point at each of the far ends, Fig. 6.17 plots $\angle \mathcal{H}(x_g, j\omega)$ in the x_g–f plane for the foregoing fault case but with the observation point being switched to the near end $x_2 = 11$ km. Clearly, the proposed property is still applicable, showing a null distribution of $\angle \mathcal{H}(x_f, j\omega)$ throughout the considered frequency range. Thus, the results shown above demonstrate that the bounded phase property is robust against the location of the observation point.
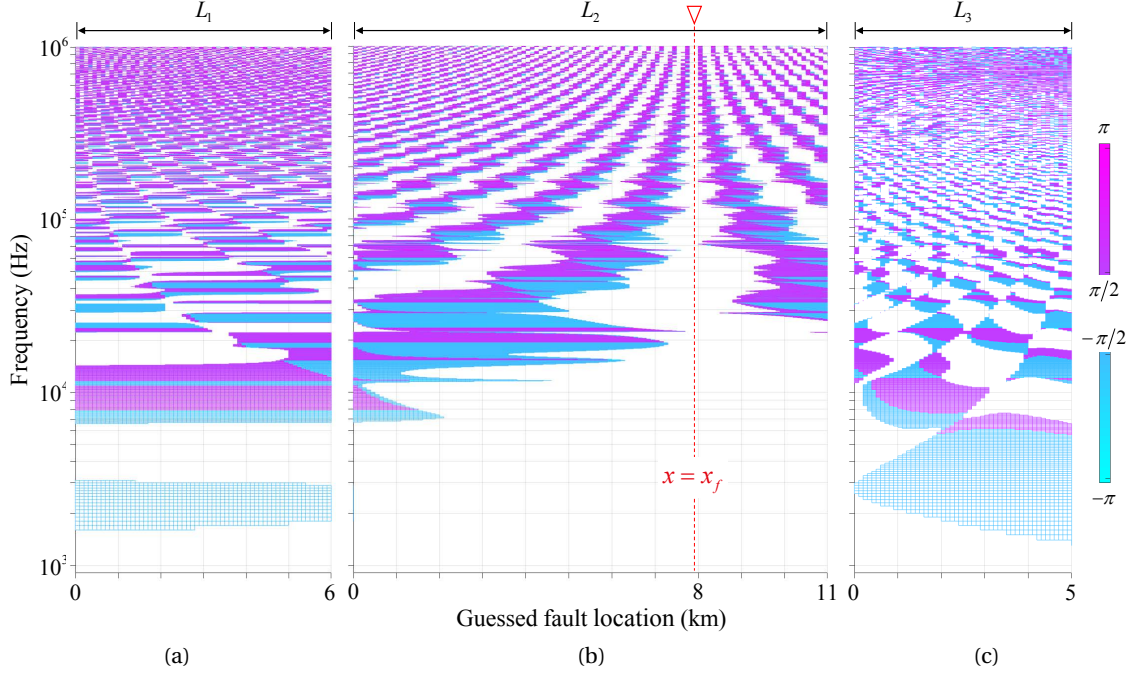
Figure 6.17 – Phase angle of the transfer function $\mathcal{H}(x_g, j\omega)$ for the case $x_2 = x_f = 7.9$ km based on the near end $x_2 = 11$ km as the single observation point. (a) $0 < x_g < L_1$, (b) $0 < x_g < L_2$, and (c) $0 < x_g < L_3$ (d$x = 100$ m). f ranges from 1 kHz to 1 MHz and df equals 100 Hz.

Finally, according to the curves of $f_{o,\pm|\Delta x|}$–Δx plotted in Fig. 6.18, a location accuracy of 1 m is allowed to be reached if the frequency band is wider than 1.105 MHz.

b) Fault occurrence along Branch L_3 at $x_3 = x_f = 3.7$ km

The final example assumes a fault occurrence along the coaxial cable L_3 at $x_3 = x_f = 3.7$ km. As discussed earlier, the proposed phase property is independent of the location of the single observation point. Here, we present the calculation resulting from deploying the observation point at the far end $x_2 = 11$ km. As it can be seen in Fig. 6.19, at the true fault location, the transfer function $\mathcal{H}(x_f, j\omega)$ displays the bounded phase angle between $\pm \pi/2$. What is more, in virtue of the bounded phase property, x_f can be distinguished from its neighboring locations $x_f \pm 1$ m, as long as a frequency bandwidth larger than 0.882 MHz is achievable.
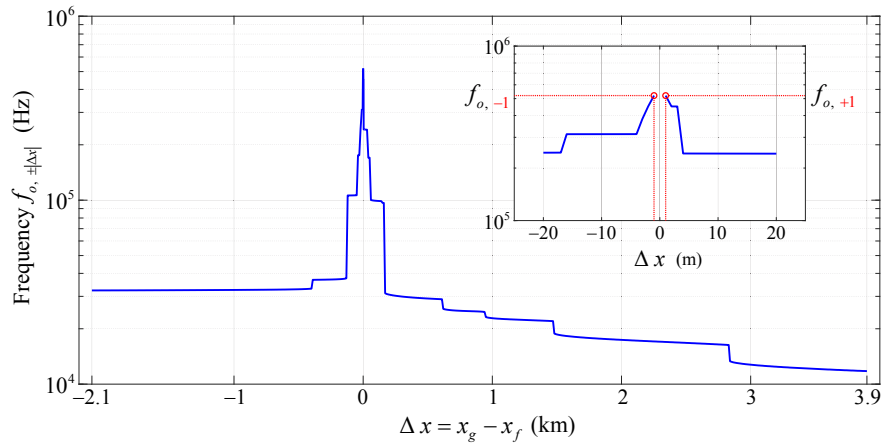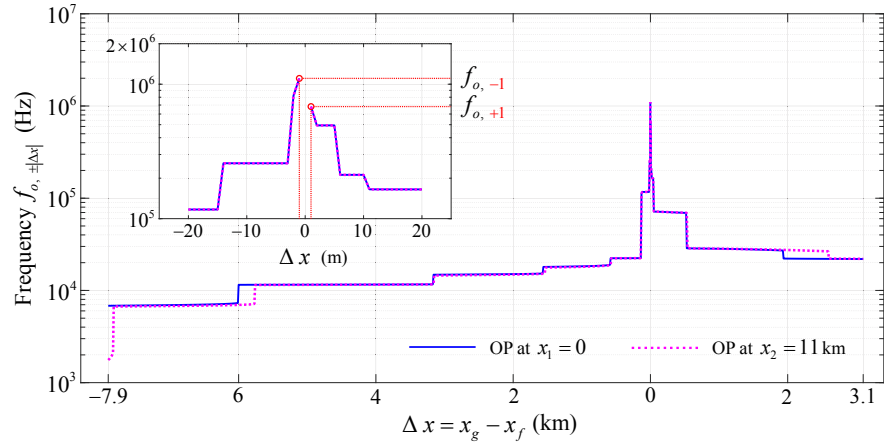
Figure 6.18 – First out-of-range frequency $f_{o,\pm|\Delta x|}$ as a function of Δx ($0 < x_g < L_2$) for the case $x_2 = x_f = 7.9$ km. The single observation point is respectively located at the far end $x_1 = 0$ (blue solid line) and the near end $x_2 = 11$ km (magenta dot line). f ranges from 100 Hz to 1 MHz with $df = 10$ Hz.
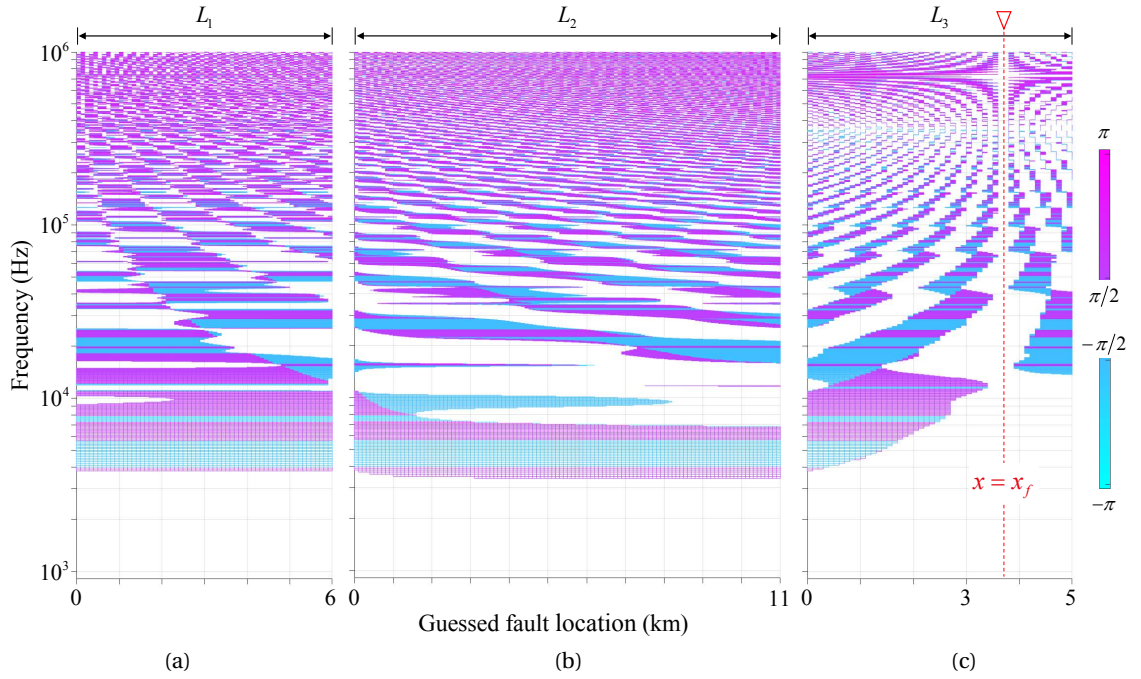
Figure 6.19 – Phase angle of the transfer function $\mathcal{H}(x_g, j\omega)$ for the case $x_3 = x_f = 3.7$ km based on the far end $x_2 = 11$ km as the single observation point. (a) $0 < x_g < L_1$, (b) $0 < x_g < L_2$, and (c) $0 < x_g < L_3$ ($dx = 100$ m). f ranges from 1 kHz to 1 MHz and df equals 100 Hz.

6.4 Property: Mirrored Minimum Squared Modulus of the *Direct-Reversed-Time* Transfer Function

6.4.1 *Theorem 2: mirrored minimum squared modulus of $\mathcal{H}(x, j\omega)$*

The *direct-reversed-time* transfer function of EMTR in mismatched media presents the following property.

Theorem 2 $\forall f_i \in \mathbb{F}^{DT} = \left\{ f_i = (2i - 1) \cdot f^0 \mid f^0 = 1 / \left(4\Gamma_{x_f} \right), \; i = 1, 2, 3, \dots \right\}$,

$$ x_{min} \triangleq \underset{0 < x < L}{Min} \left\{ \left| \mathcal{H}(x, j\omega) \right|^2 \Big|_{\omega = 2\pi \cdot f_i} \right\} = L - x_f. $$

$\mathbb{F}^{DT}$ contains the fault inherent switching frequency and its odd harmonics.

Theorem 2 explains that, at each single frequency among $\mathbb{F}^{DT}$, the squared modulus of $\mathcal{H}(x, j\omega)$ reaches its minimum always at the location x_{mirror}, which is the mirror image point of the true fault location x_f with respect to the line center, namely $x_{mirror} = L - x_f$.

The complete proof of *Theorem 2* in a lossy medium is left in Appendix A.1. The following mathematical proof makes reference to the lossless line and its related simplification discussed in Section 6.3.1.

Proof. Considering the expression of the *direct-reversed-time* transfer function $\mathcal{H}(x, j\omega)$ in (6.17), we rewrite its simplified form in (6.18) as follows to facilitate the proof.

$$ \mathcal{H}(x, j\omega) = \overbrace{\left[1 + \rho \cdot e^{-j\beta(\omega) \cdot 2(L-x)} \right]}^{\mathcal{H}_d(x, j\omega)} \cdot \frac{(1 - \rho^2) \cdot e^{-j\beta(\omega) \cdot (x - x_f)}}{2 \left[1 - \rho^2 \cdot e^{-j\beta(\omega) \cdot 2L} \right] \cdot \left[1 + \rho \cdot e^{j\beta(\omega) \cdot 2x_f} \right]} \, . \tag{6.37} $$

The squared modulus of $\mathcal{H}(x, j\omega)$ then reads

$$ \left| \mathcal{H}(x, j\omega) \right|^2 = \overbrace{\left| 1 + \rho \cdot e^{-j\beta(\omega) \cdot 2(L-x)} \right|^2}^{\left| \mathcal{H}_d(x, j\omega) \right|^2} \cdot \frac{(1 - \rho^2)^2}{4 \left| 1 - \rho^2 \cdot e^{-j\beta(\omega) \cdot 2L} \right|^2 \cdot \left| 1 + \rho \cdot e^{j\beta(\omega) \cdot 2x_f} \right|^2} \, . \tag{6.38} $$

Obviously, only the term $\left| \mathcal{H}_d(x, j\omega) \right|^2$ in (6.38) behaves as a function of the longitudinal coordinate x, which directs the attention of the proof to discussing the behavior of $\left| \mathcal{H}_d(x, j\omega) \right|^2$ at those frequencies of $\mathbb{F}^{DT}$.

It is obtained that

$$ \left| \mathcal{H}_d(x, j\omega) \right|^2 \Big|_{\omega = 2\pi \cdot \mathbb{F}^{DT}} = 1 + \rho^2 + 2\rho \cdot \cos \left[\frac{4\pi \cdot (L - x) \cdot \Gamma_{x_f}}{x_f} \cdot \mathbb{F}^{DT} \right] , \tag{6.39} $$

and at $\forall f_i \in \mathbb{F}^{DT}$

$$\left|\mathcal{H}_{d,i}(x)\right|^2 \triangleq \left|\mathcal{H}_d(x, j\omega)\right|^2\bigg|_{\omega=2\pi \cdot f_i} = 1 + \rho^2 + 2\rho \cdot \cos\left[(2i-1)\cdot \pi \cdot \frac{L-x}{x_f}\right], \quad i = 1, 2, 3, \dots .$$

(6.40)

There exists

$$\left|\mathcal{H}_{d,i}(x)\right|^2 \geqslant (1-\rho)^2, \quad i = 1, 2, 3, \dots .$$

(6.41)

Especially, the equality is established if

$$(2i-1)\cdot \pi \cdot \frac{L-x}{x_f} = (2k-1)\cdot \pi,$$

$$i = 1, 2, 3, \dots , \quad \text{and} \quad k = 0, \pm 1, \pm 2, \pm 3, \dots .$$

(6.42)

In other words, $\left|\mathcal{H}_{d,i}(x)\right|^2$ reaches its local minima at the locations

$$x = L - \frac{2k-1}{2i-1}\cdot x_f,$$

$$i = 1, 2, 3, \dots , \quad \text{and} \quad k = 0, \pm 1, \pm 2, \pm 3, \dots .$$

(6.43)

Since $0 < L - x_f$, $x_f < L$, there exist two constraints on the values of i and k.

First,

$$i = 1, 2, 3, \dots, N \quad \text{with} \quad N = Floor\,(f_{max}/f^0),$$

(6.44)

where *Floor* denotes the floor function and f_{max} refers to the maximum of the frequency of interest.

Moreover,

$$k = 1, 2, 3, \dots, K \quad \text{with} \quad K = Floor\left\{\,[\,(2i-1)\cdot (L/x_f) + 1\,]/2\,\right\}.$$

(6.45)

We introduce a case study and take advantage of lattice diagrams to render (6.43) intuitive. To be specific, it is assumed $L = 4x_f$, namely that the fault occurs at the location of a quarter of the line length. In consequence, the mirror image point is at $x = L - x_f = 3x_f$. We consider the frequencies including f^0 and its odd harmonics up to 7-th order in such a way that $i \leqslant (N = 4)$.

The lattice diagrams, 6.20a to 6.20d, show the mapping, among i, k and x, governed by (6.43). It can be observed that, along the x-axis, the number as well as the locations of the local minima of $\left|\mathcal{H}_{d,i}(x)\right|^2$ differ in accordance with the value of i. For instance, in the case of Fig. 6.20a where $i = 1$ and $f = f_0$, there exist two minima of $\left|\mathcal{H}_{d,i}(x)\right|^2$, which respectively appear at $x = x_f$ and $x = 3x_f$.

Note that, as a particular case, the location $x = 3x_f$, which is exactly the mirror image point of the fault location $x = x_f$, features the local minimum of $\left|\mathcal{H}_{d,i}(x)\right|^2$ for each of the considered frequencies that include f^0 and its odd harmonics. As highlighted by the red lines in each of
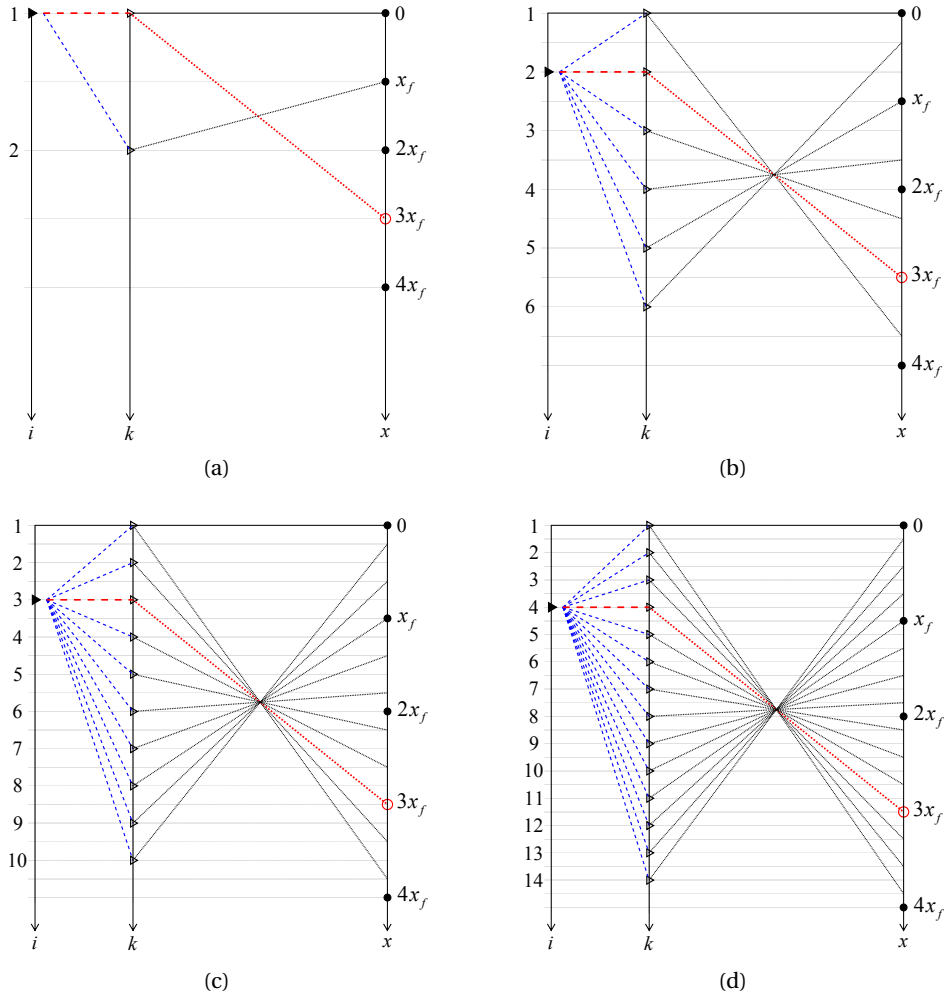
Figure 6.20 – Mapping among i, k and x of the fault case $L = 4x_f$ for: (a) $i = 1$, $f = f^0$, $K = 2$; (b) $i = 2$, $f = 3f^0$, $K = 6$; (c) $i = 3$, $f = 5f^0$, $K = 10$, and (d) $i = 4$, $f = 7f^0$, $K = 14$.

the diagrams, the mapping between i and $k = i$, resulting in $x = 3x_f$ always being the location characterized by the local minimum of $\left|\mathcal{H}_{d,i}(x)\right|^2$.

To be more general, the distribution of the local minima of $\left|\mathcal{H}_{d,i}(x)\right|^2$ for an arbitrary fault occurrence is shown in Fig. 6.21. The fault cases are exemplified by

$$ x_f/L = \left\{ 1/10,\ 1/5,\ 1/4,\ 1/3,\ 1/2,\ 2/3,\ 3/4,\ 4/5,\ 9/10,\ 1 \right\}. \tag{6.46} $$

Figures 6.21a to 6.21d respectively correspond to the distributions at f^0 and its odd harmonics up to the 7-th order. In agreement with *Theorem 2*, the red dots, which appear along the downward diagonal, demonstrate that the mirror image point is always a local minimum of $\left|\mathcal{H}_{d,i}(x)\right|^2$ at each f_i and for each x_f.
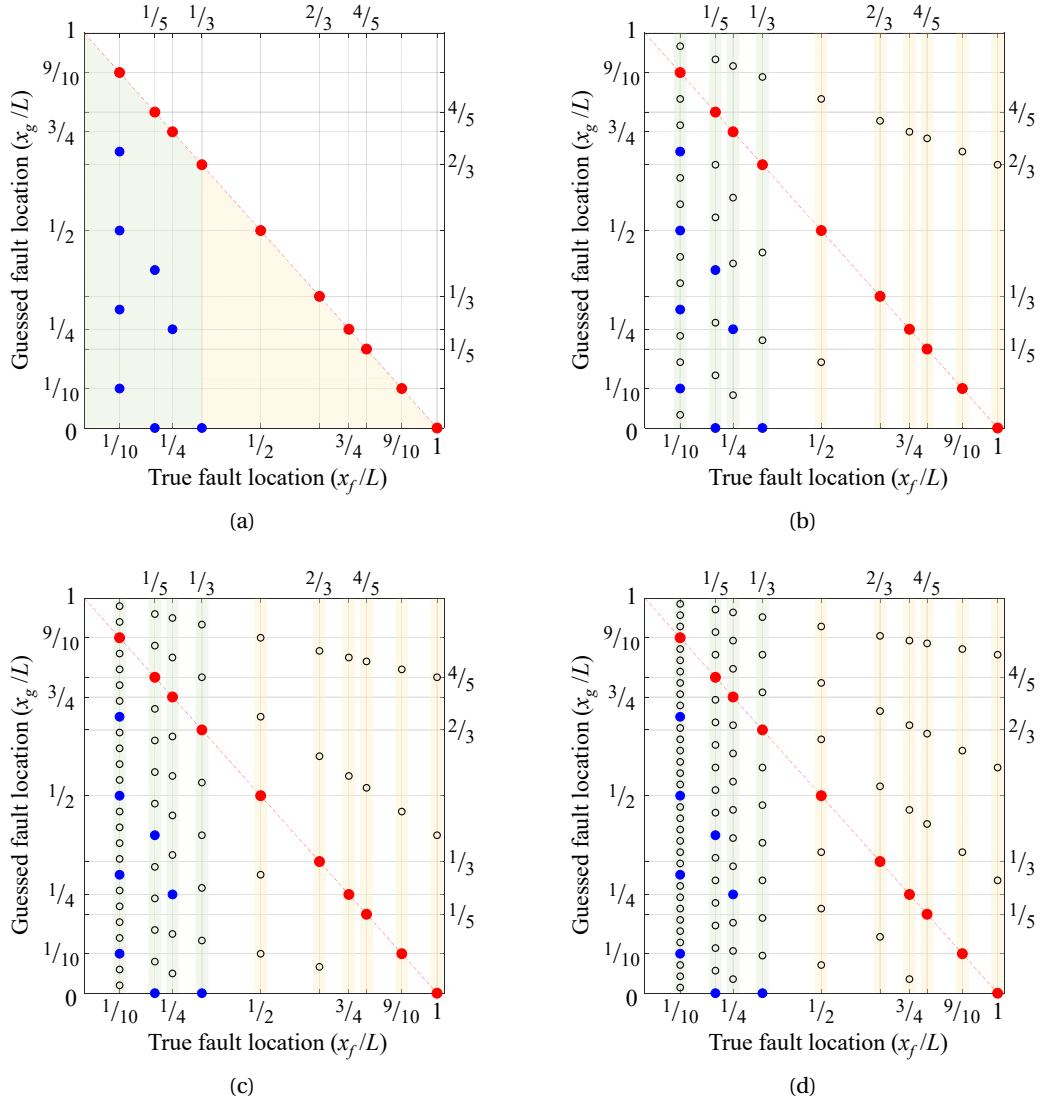
Figure 6.21 – Distribution of local minima of $\left|\mathcal{H}_{d,i}(x)\right|^2$ for the fault cases $x_f/L = \{1/10, 1/5, 1/4, 1/3, 1/2, 2/3, 3/4, 4/5, 9/10, 1\}$ at (a) $i = 1$, $f = f^0$; (b) $i = 2$, $f = 3f^0$; (c) $i = 3$, $f = 5f^0$, and (d) $i = 4$, $f = 7f^0$. Among the dots, which represent the local minima, the red dots are the mirror image points of the respective fault locations. In addition, for the fault case where $x_f \in (0, L/3]$ the blue dots further indicate the locations of (6.47) that feature the local minimum of $\left|\mathcal{H}_{d,i}(x)\right|^2$ for each f_i.

It is also worth noting that for the fault location $x = x_f$ that belongs to the interval $(0, L/3]$, in addition to the mirror image point $x = L - x_f$, the locations

$$x = (L - x_f) - m \cdot 2x_f,$$
$$m = 1, 2, 3, \ldots, M \quad \text{with} \quad M = Floor\left\{(L - x_f)/2x_f\right\},$$

(6.47)

which are indicated by the blue dots in the subgraphs, feature the local minimum of $\left|\mathcal{H}_{d,i}(x)\right|^2$ for each f_i as well. Taking the fault case of Fig. 6.20 as an example, $\left|\mathcal{H}_{d,i}(x)\right|^2$ reaches its local minima at both $x = L - x_f = 3x_f$ and $x = L - 3x_f = x_f$.

Without limiting i to a finite arithmetic number N, the foregoing fact applies to $\left|\mathcal{H}_d(x, j\omega)\right|^2$ at $\mathbb{F}^{\mathrm{DT}}$, and thus *Theorem 2* is proved.

6.4.2 *Corollary 1 and 2: mirrored minimum energies of* $\mathcal{H}(x, j\omega)$ *and* $V^{\mathrm{RT}}(x, j\omega)$

The transfer function constitutes the frequency-domain representation to the unit impulse response of a linear time invariant system. According to Parseval's theorem, we calculate the energy of the impulse response of the *direct-reversed-time* system at $\mathbb{F}^{\mathrm{DT}}$ as follows:

$$E\left\{\mathcal{H}|_{\mathbb{F}^{\mathrm{DT}}}\right\} \triangleq E\left\{\left.\mathcal{H}(x, j\omega)\right|_{\omega=2\pi\cdot\mathbb{F}^{\mathrm{DT}}}\right\} = \sum_{i=1}^{N}\left\{\left.\left|\mathcal{H}(x, j\omega)\right|^2\right|_{\omega=2\pi\cdot f_i}\right\}. \tag{6.48}$$

Corollary 1 $\exists\, \mathbb{F}^{\mathrm{DT}} = \left\{ f_i = (2i-1)\cdot f^0 \,\middle|\, f^0 = 1/\left(4\Gamma_{x_f}\right),\ i = 1, 2, 3, \ldots, N \right\}$,

$$x_{min} \triangleq \operatorname*{Min}_{0 < x < L}\left\{ E\left\{\mathcal{H}|_{\mathbb{F}^{\mathrm{DT}}}\right\}\right\} = L - x_f.$$

To prove *Corollary 1*, let us recall the proof of *Theorem 2* in lossy medium in Section A.1.3.

It is suggested that, for each $f_i \in \mathbb{F}^{\mathrm{DT}}$, $\left|\mathcal{H}_d(x, j\omega)\right|^2$, as well as $\left|\mathcal{H}(x, j\omega)\right|^2$, always reach their local minima at

$$x_{\mathbb{M}} = \left\{ x_m = (L - x_f) - m\cdot 2x_f \,\middle|\, m = 0, 1, 2, \ldots, M \right\}, \tag{6.49}$$

with

$$M = Floor\left\{ (L - x_f)/2x_f \right\}. \tag{6.50}$$

At those locations,

$$\left|\mathcal{H}_{d,i}(x_m)\right|^2 = e^{-\alpha\cdot 2x_m}\cdot\left[1 - \rho_L^v\cdot e^{-\alpha\cdot 2(L-x_m)}\right]^2. \tag{6.51}$$

Moreover, $\left|\mathcal{H}_{d,i}(x_m)\right|^2$ monotonically decreases as x_m increases, namely

$$\left|\mathcal{H}_{d,i}(L - x_f - M\cdot 2x_f)\right|^2 > \ldots > \left|\mathcal{H}_{d,i}(L - x_f - 1\cdot 2x_f)\right|^2 > \left|\mathcal{H}_{d,i}(L - x_f)\right|^2. \tag{6.52}$$

Let us consider that x_f respectively belongs to $(0, L/3]$ and $(L/3, L]$.

As discussed in Sections 6.4.1 and A.1.3, for $x_f \in (L/3, L]$

$$x_{\mathbb{M}} = \left\{ x_0 = L - x_f \right\}, \tag{6.53}$$

while, in the former scenario,

$$x_{\mathbb{M}} = \{\, x_0 = L - x_f, \; x_2 = L - 3x_f, \; \dots, \; x_M = L - x_f - M \cdot 2x_f \,\}. \tag{6.54}$$

It can be readily found in Figs 6.21a to 6.21d, $x_0 = L - x_f$ is always shown at the downward diagonal. The additional locations $\complement_{x_{\mathbb{M}}} x_0$, if any, are all distributed below the diagonal, as represented by the blue dots. That is to say, among those locations that belong to $x_{\mathbb{M}}$, $x_0 = L - x_f$, which is also named the mirror image point of the fault location x_f, is characterized as the global minimum of $\left|\mathcal{H}_{d,i}(x)\right|^2$ for each f_i.

To sum up,

i) Among those locations determined by (6.43) to (6.45), $x_{\mathbb{M}}$ of (6.49) allows $\left|\mathcal{H}(x, j\omega)\right|^2$ to reach its local minimum at each $f_i \in \mathbb{F}^{\mathrm{DT}}$;

ii) Among $x_{\mathbb{M}}$ of (6.49), the mirror image point $x = L - x_f$ allows $\left|\mathcal{H}(x, j\omega)\right|^2$ to reach its global minimum at each $f_i \in \mathbb{F}^{\mathrm{DT}}$;

iii) At the fault switching frequency f_0, the *cos* term of $\left|\mathcal{H}_{d,i}(x)\right|^2$ in (A.27) reaches its last local minimum at the mirror image point $x = L - x_f$.

In this way, the operation (6.48) at $x = L - x_f$ in particular consists of summating the multiple minima of $\left|\mathcal{H}(x, j\omega)\right|^2$ at $\mathbb{F}^{\mathrm{DT}}$, and thereby results in the summation logically being the minimum as well.

In conclusion, *Corollary 1* is deduced from the foregoing properties.

Similarly, the energy of the *reversed-time* voltage $V^{\mathrm{RT}}(x, j\omega)$ derived in (6.15) can be calculated at $\mathbb{F}^{\mathrm{DT}}$ as:

$$E\Big\{ V^{\mathrm{RT}}\big|_{\mathbb{F}^{\mathrm{DT}}} \Big\} \triangleq E\Big\{ V^{\mathrm{RT}}(x, j\omega)\big|_{\omega = 2\pi \cdot \mathbb{F}^{\mathrm{DT}}} \Big\} = \sum_{i=1}^{N} \Big\{ \left|V^{\mathrm{RT}}(x, j\omega)\right|^2 \Big|_{\omega = 2\pi \cdot f_i} \Big\}, \tag{6.55}$$

and

Corollary 2 $\exists\, \mathbb{F}^{\mathrm{DT}} = \Big\{ f_i = (2i - 1) \cdot f^0 \,\big|\, f^0 = 1/\big(4\Gamma_{x_f}\big), \; i = 1, 2, 3, \dots, N \Big\}$,

$$x_{min} \triangleq \underset{0 < x < L}{Min} \Big\{ E\Big\{ V^{\mathrm{RT}}\big|_{\mathbb{F}^{\mathrm{DT}}} \Big\} \Big\} = L - x_f.$$

It can be found in (6.15) that the excitation of $V_f(j\omega)$ at each f_i is a constant, and, as such, *Corollary 2* is inferred from *Corollary 1*.

Based on the above established properties named *mirrored minimum squared modulus and*

energy, the true fault location can be identified by its mirror image point through

$$x_f = L - x_{min}$$

$$= L - \underset{0 < x < L}{Min} \left\{ \left| \mathcal{H}(x, j\omega) \right|^2 \Big|_{\mathbb{F}^{DT}} \right\} = L - \underset{0 < x < L}{Min} \left\{ E\left\{ \mathcal{H} |_{\mathbb{F}^{DT}} \right\} \right\} = L - \underset{0 < x < L}{Min} \left\{ E\left\{ V^{RT} |_{\mathbb{F}^{DT}} \right\} \right\}.$$

(6.56)

6.4.3   Numerical validation

In this section, we numerically illustrate the properties stated in *Theorem 2* and its two corollaries. To this end, an 11-km-long single-phase overhead line of the 380-kV per-unit-length parameters (see Table. 6.5) is considered. At the line terminals, the high-frequency input impedance of Z_0 (and Z_L) is assigned 100 kΩ. The single observation point is located at $x = 0$. The fault occurrence is assumed to be at $x = x_f = 7$ km.

We first observe the squared modulus of $\mathcal{H}(x_g, j\omega)$ in Fig. 6.22a as a function of the guessed fault location x_g together with the order of harmonics $2i - 1$. For defining the values of the former independent variable x_g, the 11-km-long line is discretized by an increment step dx of 10 m. As to the latter one, we consider the maximum value of i as 20 to include f^0 and its odd harmonics up to the 39-th order. f^0 is 10.4 kHz for the fault case. For the sake of comparison, at each harmonic, the calculated squared moduli at the guessed fault locations are normalized with reference to the global maximum.

As it is shown in Fig. 6.22a, at a given harmonic f_i, the squared modulus of $\mathcal{H}(x_g, j\omega = j2\pi \cdot f_i)$ reaches its minimum at the locations satisfying the mapping relation of (6.43). Even though, in agreement with *Theorem 2*, the mirror image point $x_g = L - x_f = 4$ km is indicated at each harmonic by the color signifying the minimum squared modulus of $\mathcal{H}(x_g, j\omega)$.
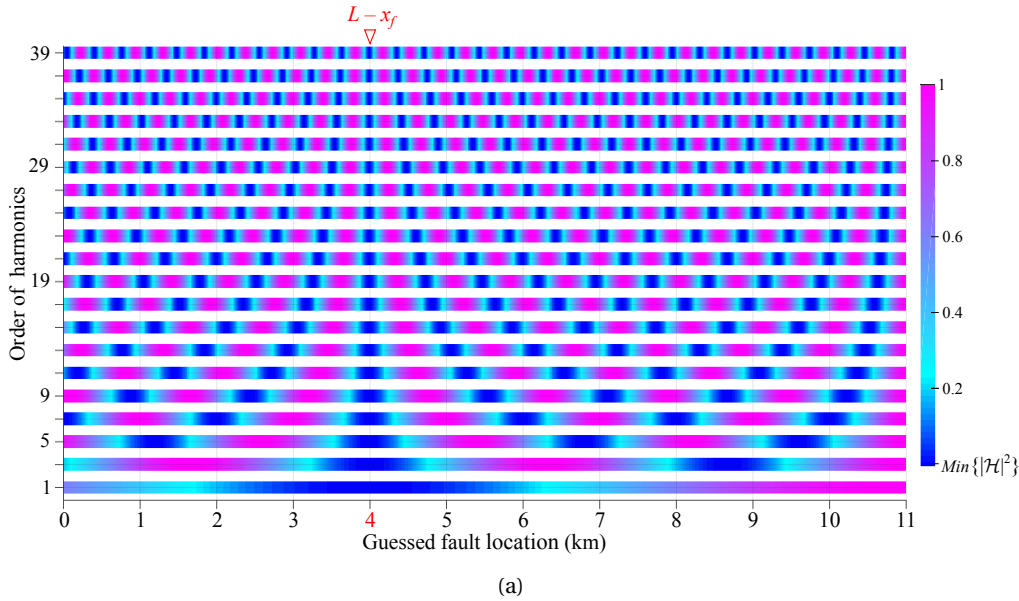
(a)

(b)
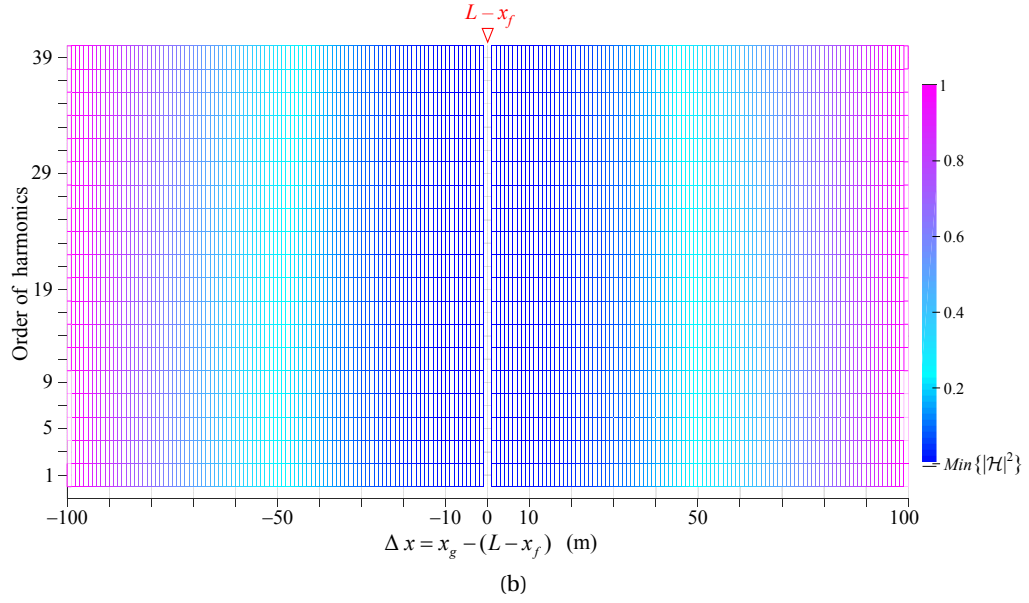
Figure 6.22 – Normalized squared modulus of $\mathcal{H}(x_g, j\omega)$ calculated at f^0 and its odd harmonics up to the 39-th order. The line length L is 11 km and the fault location is $x_f = 7$ km. f^0 is 10.4 kHz for the fault case. The guessed fault locations are defined: (a) every 10 m along the line and (b) every 1 m in the spacing between $(L - x_f) \pm 100$ m.

Figure 6.22b presents a finer observation of the behavior of $\left|\mathcal{H}(x_g, j\omega)\right|^2$ at the locations adjacent to the mirror image point $L - x_f$. The discretization step dx is reduced to 1 m to define the guessed fault locations in the spacing between $x = 4$ km ± 100 m. It confirms, on a meter scale, that the mirror image point uniquely features the property of *Theorem 2*.

We proceed to validate the mirrored minimum energy properties formulated in *Corollary 1* and *2*.

Figure 6.23 presents the calculated energy of the *direct-reversed-time* transfer function, namely $E\left\{\mathcal{H}|_{\mathbb{F}DT}\right\}$, for the foregoing fault case wherein $L = 11$ km and $x_f = 7$ km. The curves of $E\left\{\mathcal{H}|_{\mathbb{F}DT}\right\}$ versus x_g shown in the subgraphs of Fig. 6.23 respectively result from summating $\left|\mathcal{H}(x_g, j\omega = j2\pi \cdot f_i)\right|^2$ for f_i up to the first 2, 10, and 20 order odd harmonics. Note that the normalization results in the calculated maximum energy at the unit value. In all the three scenarios, $E\left\{\mathcal{H}|_{\mathbb{F}DT}\right\}$ reaches its minimum at $x_g = 4$ km, which is the mirror image point of the true fault location.

Following the approach assessing the quality of refocusing time-reversed acoustic or electromagnetic waves to the original source point, we define the focal spot in the fault location case as the spacing $S = |x_{+50\%} - x_{-50\%}|$, as it is indicated in Fig. 6.23a. Correspondingly, the focal spot size refers to $S_r = |x_{+50\%} - x_{min}|$. For the three scenarios varying in the number of harmonics N from 2, 10 to 20, the focal spot sizes are yielded as 2390 m, 335 m and 170 m respectively. That is to say, the summation of $E\left\{\mathcal{H}|_{\mathbb{F}DT}\right\}$ with a larger N to contain

133

$\left| \mathcal{H}(x_g, j\omega = j2\pi \cdot f_i) \right|^2$ of higher order harmonics provides a higher resolution in distinguishing the mirror image point by means of the mirrored minimum energy property.
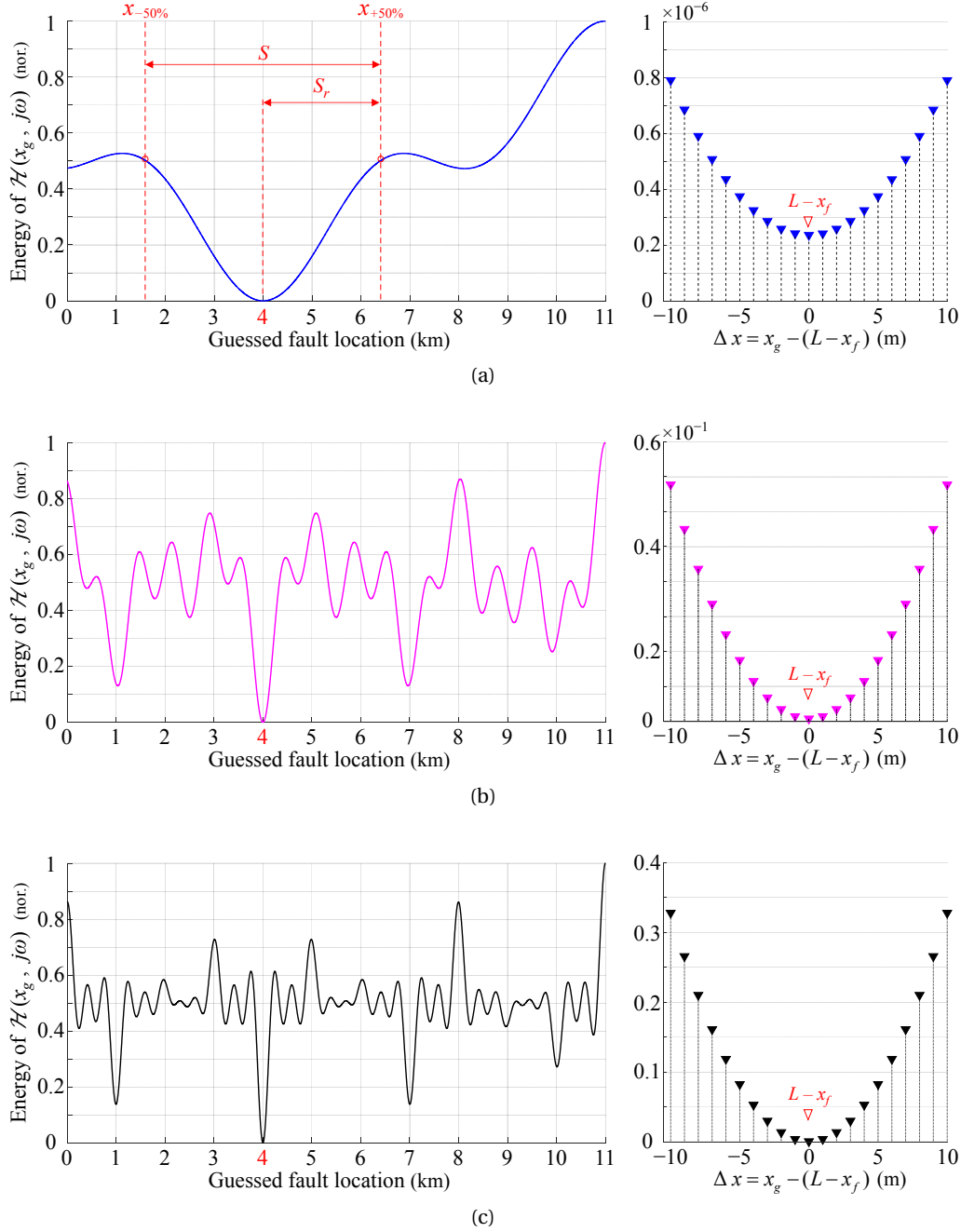
Figure 6.23 – Normalized energy of $\mathcal{H}(x_g, j\omega)$ calculated at $\mathbb{F}^{DT}$ for: (a) $N = 2$, (b) $N = 10$, and (c) $N = 20$. The fault location is assumed to be $x_f = 7$ km. In the subgraphs on the left, the guessed fault locations are defined per 5 m along the line. The subgraphs on the right refer to dx as 1 m in the neighboring region of $L - x_f$.

Additionally, as it is in the previous analysis, the guessed fault locations are defined at the neighboring locations of $x_g = L - x_f$ with a finer distance increment ($\mathrm{d}x = 1$ m) to examine the property on a meter scale. As it can be observed in each subgraph on the right in Figs. 6.23a, b, and c, the minimum energy remains at the mirror image point.

Given the present fault case, the energy of the *reversed-time* voltage, $E\left\{V^{\mathrm{RT}}\big|_{\mathbb{F}^{\mathrm{DT}}}\right\}$, is calculated and described as a function of the guessed fault location in Fig. 6.24. *Corollary 2* is numerically validated in the example, observing that the minimum energy is located at the mirror image point $x_g = L - x_f = 4$ km. According to Fig. 6.24b, it allows identifying the mirror image point with a better-than-1-m accuracy.

(a)

(b)
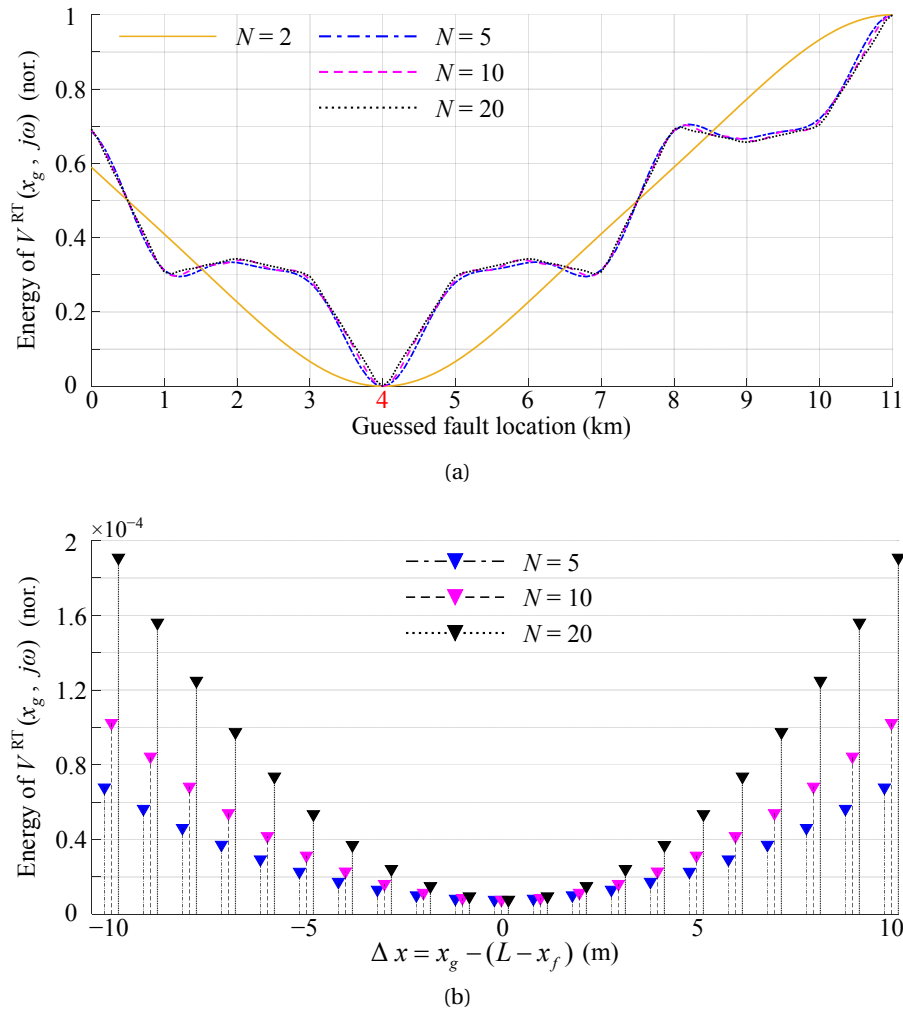
Figure 6.24 – Normalized energy of $V^{\mathrm{RT}}(x_g, j\omega)$ calculated at $\mathbb{F}^{\mathrm{DT}}$ for the fault case $x_f = 7$ km. The guessed fault locations are defined: (a) along the line with $\mathrm{d}x = 5$m and (b) in the neighboring region of $L - x_f$ with $\mathrm{d}x = 1$ m.

Finally, drawing a comparison between the energies calculated with different upper limits N in the summation of $E\left\{V^{\mathrm{RT}}\big|_{\mathbb{F}_{\mathrm{DT}}}\right\}$ in (6.55), Fig. 6.24a shows that the energy of $V^{\mathrm{RT}}(x, j\omega)$ is dominated by its components at lower frequencies, such as f^0. While, the components at the higher-order harmonics contribute to enhancing the resolution in terms of distinguishing the mirror image point $L - x_f$ from its adjacent locations.

6.4.4 Experimental validation

This section presents an experimental validation of the property formulated in *Corollary 2* by means of a reduced-scale coaxial-cable set-up.

The experiment made use of a 477-m-long standard RG-58 cable composed of two sections being 73 m and 404 m in length respectively. At the two ends of the set-up, the inner and shielding conductors of the cable were connected to lumped resistors with relatively high resistances, namely $Z_0 = 560\ \Omega$ and $Z_L = 1\ \mathrm{k\Omega}$, in comparison with the 50-Ω characteristic impedance of the RG-58 cable. In this way, we considered asymmetrical reflective boundary conditions. A DC voltage of 6 V supplied the cable set-up from the line end at $x = 0$, which also served as the single observation point.

In order to emulate a real fault, a short circuit was artificially triggered between the inner and shielding conductors of the cable. The fault location was the junction of the two cable sections, namely $x_f = 73$ m. Note that the fault-initiated traveling waves propagate along the cable at speed of about 65.9 % of the speed of light and are reflected at the cable ends terminated on high resistances as well as at the junction with the presence of the short circuit. Considering that the fault location was tens of meters away from the observation point situated at the cable end $x = 0$, the resultant one-way propagation delay was in the order of hundreds of nanoseconds. That is to say, for correctly emulating the fault in such a reduced-scale cable set-up, the hardware fault emulator needs to feature a high-speed switch, which is capable of changing its status in a few nanoseconds. To address this constraint, we adopted a metal-oxide semiconductor field-effect transistor (MOSFET) with a turn-on time of 3 ns. In the experiment, the MOSFET was driven by a NI digital input/output (I/O) card C/series 9402 that is able to generate a gate signal to the MOSFET with a sub-nanosecond rise time. It should note that the emulated fault referred to the solid-type fault since no resistor was set between the MOSFET drain and the cable inner conductor.

In the *direct time*, the fault-originated transients were measured as the voltage $V_0^{\mathrm{DT}}(t)$ across Z_0 at the observation point $x = 0$, as it can be seen in Fig. 6.25a. The waveform of $V_0^{\mathrm{DT}}(t)$ explains that the MOSFET acted after the cable system had been in the steady state. A 14-bit NI PCI-5122 high-speed digitizer was used to perform the measurement at a sampling rate of 1 MSamples/s. Note that the 3-dB bandwidth of the digitizer reaches up to 100 MHz, which is sufficient to cover the frequency spectrum of $V_0^{\mathrm{DT}}(t)$, which contains the fault switching frequency of 0.66 MHz, as it is shown in Fig. 6.25b.
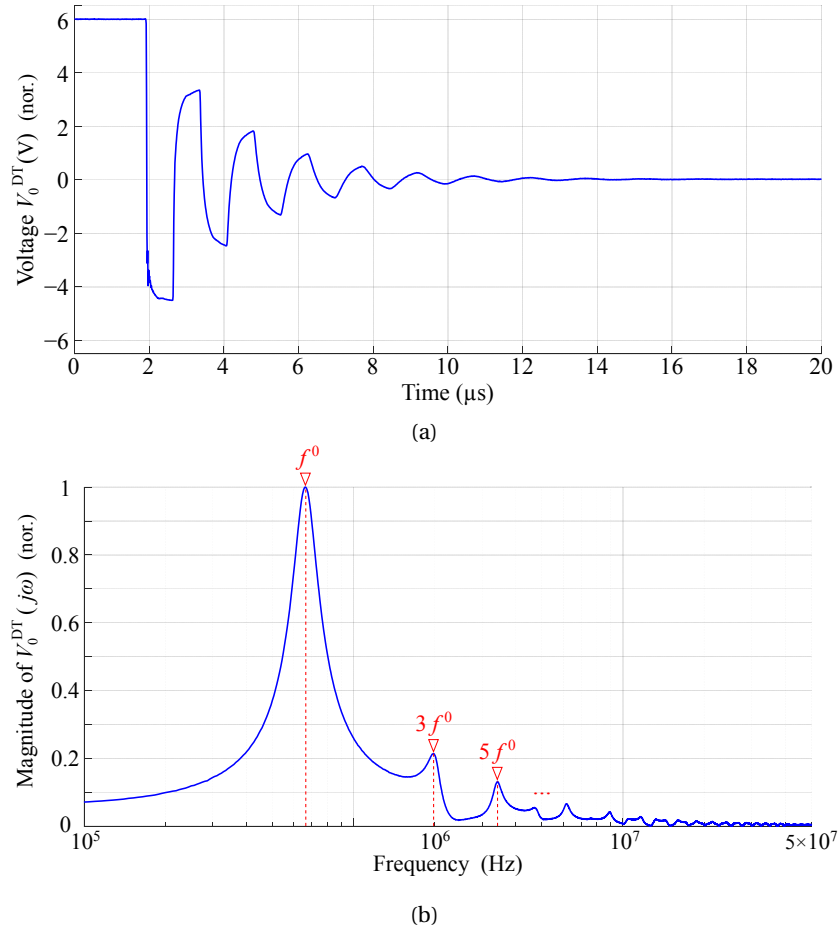
Figure 6.25 – (a) Waveform and (b) frequency spectrum of $V_0^{\mathrm{DT}}(t)$ in response to the emulated fault at $x_f = 73$ m. The components with relatively insignificant magnitudes present in the frequencies below 100 kHz are not plotted in (b).

In the *reversed time*, we simulated the backward propagation in both the time domain and frequency domain. The experimental set-up was numerically represented by using the constant-parameter (CP) line module in the EMTP-RV environment. In the time domain, the fault-originated transients $V_0^{\mathrm{DT}}(t)$ were time reversed as $V_0^{\mathrm{DT}}(-t + T)$ with $T = 20\mu$s and back injected to its EMTP-RV model to simulate the *reversed-time* voltage $V^{\mathrm{RT}}(x_g, t)$ at each of the guessed fault locations. While, in the frequency domain, the backward propagation scenario was described by making use of the transmission-line equation wherein the complex conjugate of $V_0^{\mathrm{DT}}(j\omega)$ excited the cable from the end $x = 0$, and then $V^{\mathrm{RT}}(x_g, j\omega)$ was calculated.

In view of that the main component of $V_0^{\mathrm{DT}}(j\omega)$ largely concentrates at f^0 together with the conclusion that $E\left\{V^{\mathrm{RT}}\big|_{\mathbb{F}^{\mathrm{DT}}}\right\}$ is dominated by the components of $V^{\mathrm{RT}}(j\omega)$ at lower f_i, we directly calculated the energy of $V^{\mathrm{RT}}(j\omega)$ in the full frequency range. This way, the application of *Corollary 2* to fault location appears fairly straightforward. The considered frequency range was between 1 kHz and 50 MHz.

Figure 6.26 presents the profile of the voltage energy as a function of the guessed fault location. The normalization is implemented with respect to the maximum energy. As discussed earlier, the voltage energy was calculated in the frequency domain by summating the overall squared moduli of the components distributed in the frequency range between 1 kHz and 50 MHz. Among the guessed fault locations, which are separated from each other by 1m, the location with the coordinate $x = 404$ m is characterized by the minimum energy. The location exactly behaves as the mirror image point $L - x_f$ corresponding to the emulated fault at $x_f = 73$ m with $L = 477$ m.
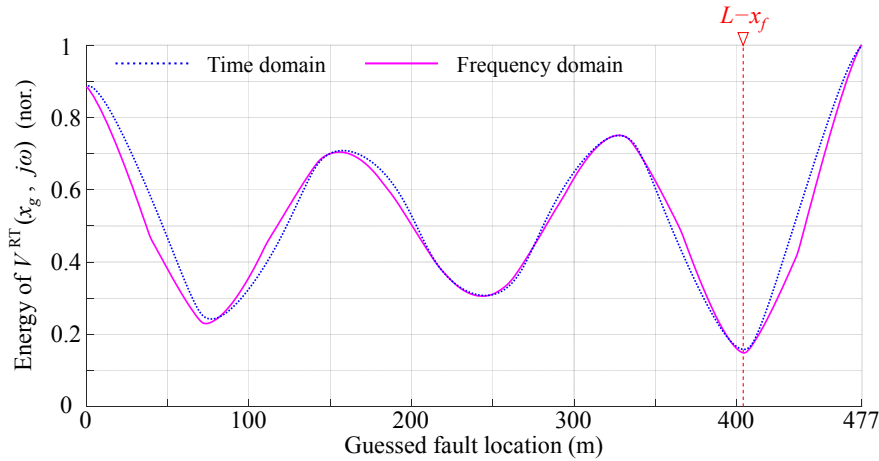
Figure 6.26 – Normalized energy of $V^{\mathrm{RT}}(x_g, j\omega)$ as a function of the guessed fault location for the emulated fault at $x_f = 73$ m.

Using Parseval's theorem, we also calculated the voltage energy in the time domain without the attention to identifying the switching frequency f^0 in the frequency domain. As illustrated by the blue dotted line superimposed in Fig. 6.26, the time-domain calculation produces a similar performance in terms of distributing the voltage energies at the guessed fault locations along the cable. The minimum energy again appears at the mirror image point $x = 404$ m.

6.5 Conclusion

The research presented in this chapter discussed EMTR in mismatched media with respect to:

- Assessing EMTR focusing property in a scattering medium, in particular when a moderate lumped mismatch between the media in the stages of the forward- and backward-propagation exists.

- Illustrating the concept in the application of locating faults in power networks.

With regard to the first focus, we designed an experimental set-up consisting of a 26×17.5 cm^2 area, in which 20 plexiglass dielectric rods were evenly deployed in a matrix of 4×5 with a separation distance between two adjacent rods of 6.5 cm. The proposed lumped mismatch referred to a limited number of rods (1 or 2 out of 20) being removed in the backward-propagation stage from the original medium. The focusing property of EMTR in the proposed cases of mismatched media was investigated experimentally in the frequency domain using two double-ridged horn antennas and a vector network analyzer, considering the frequencies ranging from 7 to 18 GHz.

The experimental analysis confirmed that the absence of one or two rods in the backward-propagation medium does not compromise the focusing property of EMTR. The focusing performance was found to be lower than that achieved in the matched-media case. However, the contributions associated with the fixed rods still allowed locating the source using EMTR-based techniques.

Based on the experimental investigations demonstrating the effectiveness of EMTR in the cases of lumped mismatches between the forward- and backward-propagation media, we proposed in the problem of fault location to remove the transverse branch representing a fault from the backward propagation medium. This way, the backward-stage medium consists of a fixed topology, namely the non-faulty transmission-line network itself.

The proposed realization of the mismatch between the media of the forward and backward stages brings two significant advantages compared to classical EMTR methods.

First, in contrast to the classical methods that require multiple independent simulations considering different guessed fault locations, the proposed backward-stage medium based on a fixed topology requires only one single simulation to observe the voltage along the network, thus reducing considerably the computation burden and further facilitating a faster fault response.

More importantly, we demonstrated that the modified backward-propagation medium satisfies various properties, which can be used to identify the fault location.

The bounded phase property stated in *Theorem 1* describes that the phase angle of the *direct-re* -*versed-time* transfer function $\mathcal{H}(x, j\omega)$ at the true function $x = x_f$ is bounded by $\pm\pi/2$. Even though the theorem was formulated for a single-phase transmission line, the numerical vali-

dation suggests that the property also holds in the case of inhomogeneous transmission-line networks, ranging from basic single-line configurations to more complex multiple branched topology. It was also shown that the phase property holds irrespective of deploying the single observation point at any one of the network terminals.

As a lemma of *Theorem 1*, we also presented an inversely-proportional relation, stating that the larger the distance $|\Delta x|$ the smaller the $\pm \pi/2$ bounded region at a guessed fault location $x_g = x_f \pm |\Delta x|$. Mathematically, the property states that the first-out-of-range frequency is inversely proportional to the distance between a guessed fault location and the true fault location. This way, the property can be used as a criterion to select an adequate frequency bandwidth for a given desired fault location accuracy.

Next, we proposed *Theorem 2* named mirrored minimum squared modulus. It shows that, at the frequencies $\mathbb{F}^{DT}$ including the fault switching frequency and its odd harmonics, the squared modulus of the *direct-reversed-time* transfer function shows its minimum always at the location, which is the mirror image point of the true fault location with respect to the line center. Moreover, based on Parseval's theorem, *Theorem 2* was extended to *Corollary 1* and *Corollary 2*, which respectively state that the mirror image point is also characterized by the minimum energy of the transfer function $\mathscr{H}(x, j\omega)$ as well as that of the reversed-time voltage $V^{RT}(x, j\omega)$.

The properties of the mirrored minimum squared modulus and energy were numerically validated and it was shown that both the properties are able to provide better-than-1-m accuracy. Besides, an experiment was particularly performed to validate the property of the mirrored minimum energy of $V^{RT}(x, j\omega)$ by means of a reduced-scale single-phase line set-up. It was shown that the hardware-emulated fault was identified using the property and reaching a 1-m location accuracy.

7 Conclusion

7.1 Summary and Conclusions

The focus of the thesis was on the study of the theory of *electromagnetic time reversal* (EMTR) and its application to fault location in power networks.

Chapter 3 of the thesis challenged the widely accepted understanding that a *closed time-reversal cavity* is a purely theoretical concept and that its experimental realization is impossible. In the thesis, a theoretical proof supported by experiments was presented to demonstrate that a time-reversal cavity for electromagnetic waves can be realized using a transmission-line network. In addition, the *interfering* effect associated with the so-called diverging wave in the backward-propagation stage was discussed. Also, an active realization of a *time-reversal sink* was presented to effectively overcome the interfering effect.

With regard to the classical EMTR-based fault location, in which the medium in the backward-propagation stage is required to be identical to that in the forward-propagation stage, in a sense, being described as *matched media*, an assessment of the performance of the EMTR technique along with the fault current signal energy (FCSE) metric was presented in Chapter 4. The study made reference to full-scale experiments, consisting of a field experiment on an unenergized distribution line and a pilot test on a live-medium voltage distribution feeder. The applicability and fault location performance of the EMTR-FCSE metric were for the first time validated in real power system environments. Chapter 4 also presented a development of an embedded controller based fault location system addressing the demand of efficiently implementing EMTR-based fault location methods in power systems by a suitable hardware platform coupled with proper sensing and triggering units.

In Chapter 5, the thesis proposed a new metric for identifying the focusing point of the back-injected transients using the *time-correlation property*. A comprehensive time-frequency domain analysis was performed, proving a *similarity* characteristic contained in the EMTR matched-media based fault location process. A novel *cross-correlation* metric was proposed to

quantitatively represent the similarity characteristic and thus to identify the location of a fault occurrence. The applicability and robustness of the proposed cross-correlation metric were numerically and experimentally validated. More importantly, compared to the classical fault current signal energy or amplitude metric, the cross-correlation metric is characterized by superior performance in terms of computation efficiency.

Chapter 6 was devoted to the study of EMTR in *mismatched media*. An experiment was designed and presented, the results of which suggest that the focusing property of EMTR remains intact when a moderate lumped *mismatch* between the media of the forward- and backward-propagation stages exists. The concept of EMTR in mismatched media was then applied for the first time to the fault location problem in power networks. It was proposed to remove the transverse branch (reproducing a fault) from the power network in the backward stage, thus creating a lumped mismatch between the media respectively in the fault occurrence stage and the fault location stage. The modified backward-propagation medium was proved to satisfy different frequency- and time-domain properties, which can be used to characterize the fault location by three proposed criteria (*bounded phase, mirrored minimum squared modulus* and *mirrored minimum energy*). More importantly, the proposed methods based on the derived mismatched-media criteria require only one single simulation for the backward propagation, thus reducing significantly the computational burden of running multiple independent backward simulations as it is in the classical methods.

7.2   Original Contributions

The original theoretical and experimental contributions of the thesis, covering both the theoretical aspect of electromagnetic time reversal and its application to fault location, are summarized as follows:

- For the first time, a closed time-reversal cavity for electromagnetic waves was realized experimentally using a network of transmission lines. The cavity allows reproducing in the future the past behavior of signals along a transmission-line network. To achieve this, only a finite number of responses need to be monitored at the network terminals.

- A time-reversal sink, which allows effectively overcoming the interfering effects caused by the diverging waves, was realized.

- The first field experiment and the first live pilot test were performed, validating EMTR-based fault location methods in real power system environments. The performance of the EMTR-FCSE metric was assessed considering faults of different natures (e.g., fault types and fault inception angles) occurring in live power networks (i.e., under normal operating conditions).

- An embedded controller-based fault location system, which integrates the functions of fault detection, data acquisition, time-reversal algorithm implementation, and electro-

magnetic transient simulations, was developed. The efficiency and robustness of the fault location system were assessed in the live pilot test.

- Development of a novel metric identifying the focusing point of the time-reversed back-injected transients. Unlike the classical EMTR methods depending on the attributes of the signal observed in the backward-propagation stage, the proposed metric analyzes the cross-correlation between the fault-originated transients (in the forward stage) and the fault current (in the backward stage), meanwhile, demonstrates an improved computation efficiency.

- Experimental evidence of the EMTR focusing property in case of lumped mismatch between the media respectively in the forward- and backward-propagation stages.

- A new category of EMTR based fault location methods was developed eliminating the need of reproducing a fault in the backward propagation stage and, thus, allowing considerably reducing the fault response delay.

7.3   Future Works

In continuation of the work presented in the thesis, the following topics are suggested for further investigation and potential industrial applications:

The proposed closed time-reversal cavity in transmission lines in Chapter 3 can find useful applications including:

- On-line monitoring of communication networks. Such networks can also include point-to-point wireless communication systems, which can be represented by their equivalent models in the backward-propagation stage.

- Preventive maintenance and monitoring of cables to detect and locate incipient faults before their occurrence.

- Detecting and locating intentional electromagnetic interference (IEMI) attacks.

- Facilitating the investigation of incidents in flight-data recorders.

The proposed EMTR in matched-media based fault location method using the metric of the maximum of the cross-correlation sequence in Chapter 5 can be further studied in the following aspects:

- Considering frequency-dependent transmission-line models.

- Sensitivity analysis considering uncertainties in line parameters and network models.

- Application to locate other sources of transients such as direct lightning strike originated flashovers along power networks or conducted intentional electromagnetic interference.

Finally, further research is needed to apply the developed properties and metrics based on EMTR in mismatched media in Chapter 6 to more topologically-complex power networks, including:

- Extending the derived properties to multi-conductor transmission lines.

- Extending the properties of mirrored minimum squared modulus and energy in power networks featuring inhomogeneity.

A Appendix

A.1 Proof of *Theorem 1 and 2* in Lossy Medium

A.1.1 Low-loss line approximation

By low loss, the per-unit-length parameters for two-conductor lines satisfy

$$r \ll \omega \cdot l, \tag{A.1}$$

and

$$g \ll \omega \cdot c. \tag{A.2}$$

According to the condition, the propagation constant reads [153]

$$
\begin{aligned}
\gamma(j\omega) &= \alpha + j\beta(\omega) \\
&= j\omega \cdot \sqrt{l \cdot c} \cdot \sqrt{\left(1 - \frac{r \cdot g}{\omega^2 \cdot l \cdot c}\right) - j\left(\frac{r}{\omega \cdot l} + \frac{g}{\omega \cdot c}\right)} \\
&\cong j\omega \cdot \sqrt{l \cdot c} \cdot \sqrt{1 - j\left(\frac{r}{\omega \cdot l} + \frac{g}{\omega \cdot c}\right)} \quad \left\{ \begin{aligned} r &\ll \omega \cdot l \\ g &\ll \omega \cdot c \end{aligned} \right\} \\
&\cong j\omega \cdot \sqrt{l \cdot c} \cdot \left[1 - j\left(\frac{r}{2\omega \cdot l} + \frac{g}{2\omega \cdot c}\right)\right],
\end{aligned}
\tag{A.3}
$$

from which the attenuation and phase constants appear to be

$$\alpha \cong \frac{1}{2}\left(\frac{r}{Z_C} + g \cdot Z_C\right), \tag{A.4}$$

and

$$\beta(\omega) \cong \omega \cdot \sqrt{l \cdot c}, \tag{A.5}$$

where the characteristic impedance is obtained under the approximation as

$$Z_C = \sqrt{\frac{r + j\omega \cdot l}{g + j\omega \cdot c}} \cong \sqrt{\frac{l}{c}} \quad \left\{ \begin{array}{l} r \ll \omega \cdot l \\ g \ll \omega \cdot c \end{array} \right\} \; . \tag{A.6}$$

Hence, for a low-loss line where (A.1) and (A.2) are satisfied, the phase constant and the characteristic impedance are independent of frequency and essentially the same as for a lossless line.

Note that the low-loss approximation is justified for typical overhead lines and underground cables considering the significant range of frequencies for electromagnetic transients originated by faults in power systems. Those transients are characterized by a spectrum dominating across the frequencies ranging from some kilohertz.

A.1.2 Proof of *Theorem 1*: *bounded Phase of* $\mathcal{H}(x, j\omega)$

The *direct-reversed-time* transfer function in (6.17) is rewritten for a low-loss line as

$$\mathcal{H}(x, j\omega)$$
$$= \left(1 - \rho_0^v\right) \cdot \frac{e^{-[\alpha + j\beta(\omega)] \cdot x} \cdot \left\{1 + \rho_L^v \cdot e^{-[\alpha + j\beta(\omega)] \cdot 2(L-x)}\right\}}{2\left\{1 - \rho_0^v \cdot \rho_L^v \cdot e^{-[\alpha + j\beta(\omega)] \cdot 2L}\right\}} \cdot \left\{(1 + \rho_0^v) \cdot \frac{e^{-[\alpha + j\beta(\omega)] \cdot x_f}}{1 + \rho_0^v \cdot e^{-[\alpha + j\beta(\omega)] \cdot 2x_f}}\right\}^*$$
$$= \left[1 - (\rho_0^v)^2\right] \cdot \frac{e^{-j\beta(\omega) \cdot (x - x_f)} \cdot \left[1 + \rho_L^v \cdot e^{-\alpha \cdot 2(L-x)} \cdot e^{-j\beta(\omega) \cdot 2(L-x)}\right]}{2e^{\alpha \cdot (x + x_f)} \cdot \left[1 - \rho_0^v \cdot \rho_L^v \cdot e^{-\alpha \cdot 2L} \cdot e^{-j\beta(\omega) \cdot 2L}\right] \cdot \left[1 + \rho_0^v \cdot e^{-\alpha \cdot 2x_f} \cdot e^{j\beta(\omega) \cdot 2x_f}\right]} \; . \tag{A.7}$$

Note that, (A.7) applies to asymmetrical boundary conditions respectively at the line ends, which are represented by different voltage reflection coefficients, ρ_0^v and ρ_L^v.

Substituting x by $x_f + \Delta x$ with Δx representing a deviation from the true fault location, (A.7) reads

$$\mathcal{H}(x_f + \Delta x, j\omega) =$$

$$\left[1 - (\rho_0^v)^2\right] \cdot \frac{e^{-j\beta(\omega) \cdot \Delta x} \cdot \overbrace{\left[1 + \rho_L^v \cdot e^{-\alpha \cdot 2(L - x_f - \Delta x)} \cdot e^{-j\beta(\omega) \cdot 2(L - x_f - \Delta x)}\right]}^{\mathcal{H}_a}}{2e^{\alpha \cdot (2x_f + \Delta x)} \cdot \underbrace{\left[1 - \rho_0^v \cdot \rho_L^v \cdot e^{-\alpha \cdot 2L} \cdot e^{-j\beta(\omega) \cdot 2L}\right]}_{\mathcal{H}_b} \cdot \underbrace{\left[1 + \rho_0^v \cdot e^{-\alpha \cdot 2x_f} \cdot e^{j\beta(\omega) \cdot 2x_f}\right]}_{\mathcal{H}_c}} \; . \tag{A.8}$$

Defining the terms $\mathcal{H}_a$, $\mathcal{H}_b$, and $\mathcal{H}_c$, (A.8) can be expressed as

$$\mathcal{H}(x_f + \Delta x, j\omega) = \left[1 - (\rho_0^v)^2\right] \cdot \frac{e^{-j\beta(\omega) \cdot \Delta x}}{2e^{\alpha \cdot (2x_f + \Delta x)}} \cdot \frac{\mathcal{H}_a}{\mathcal{H}_b \cdot \mathcal{H}_c} \; . \tag{A.9}$$

According to the equivalent transform

$$\mathcal{H}(x_f + \Delta x,\, j\omega) = \left[1 - (\rho_0^v)^2\right] \cdot \frac{e^{-j\beta(\omega)\cdot\Delta x}}{2e^{\alpha\cdot(2x_f+\Delta x)}} \cdot \frac{\mathcal{H}_a \cdot \mathcal{H}_b^* \cdot \mathcal{H}_c^*}{\mathcal{H}_b \cdot \mathcal{H}_b^* \cdot \mathcal{H}_c \cdot \mathcal{H}_c^*}, \tag{A.10}$$

the denominator of $\mathcal{H}(x_f + \Delta x,\, j\omega)$ appears to be a positive real number $\forall \omega\,(=2\pi\cdot f)$. Thus, the polarity of the real part of $\mathcal{H}(x_f + \Delta x,\, j\omega)$ is dependent on its numerator. We denote the numerator of $\mathcal{H}(x_f + \Delta x,\, j\omega)$

$$\mathcal{H}^N(x_f + \Delta x,\, j\omega) = \left[1 - (\rho_0^v)^2\right] \cdot e^{-j\beta(\omega)\cdot\Delta x} \cdot \mathcal{H}_a \cdot \mathcal{H}_b^* \cdot \mathcal{H}_c^*. \tag{A.11}$$

It is obtained that

$$\mathcal{H}^N(x_f + \Delta x,\, j\omega) = \left[1 - (\rho_0^v)^2\right] \cdot (M + jN) \cdot e^{-j\beta(\omega)\cdot\Delta x}, \tag{A.12}$$

where

$$
\begin{aligned}
M =\ & 1 - (\rho_0^v)^2 \cdot (\rho_L^v)^2 \cdot e^{\alpha\cdot2(\Delta x - 2L)} \cdot \cos[\beta(\omega)\cdot 2\Delta x] \\
& + \rho_0^v \cdot \rho_L^v \cdot e^{-\alpha\cdot2L} \cdot \left\{ e^{\alpha\cdot2\Delta x} \cdot \cos[\beta(\omega)\cdot 2(\Delta x - L)] - \cos[\beta(\omega)\cdot 2L] \right\} \\
& + \rho_0^v \cdot e^{-\alpha\cdot2x_f} \cdot \left\{ \cos[-\beta(\omega)\cdot 2x_f] - (\rho_L^v)^2 \cdot e^{\alpha\cdot2(2x_f+\Delta x - 2L)} \cdot \cos[\beta(\omega)\cdot 2(x_f + \Delta x)] \right\} \\
& + \rho_L^v \cdot e^{-\alpha\cdot2(L+x_f)} \cdot \left\{ e^{\alpha\cdot2(2x_f+\Delta x)} \cdot \cos[\beta(\omega)\cdot 2(x_f + \Delta x - L)] - (\rho_0^v)^2 \cdot \cos[\beta(\omega)\cdot 2(L - x_f)] \right\},
\end{aligned}
\tag{A.13}
$$

and

$$
\begin{aligned}
N =\ & -(\rho_0^v)^2 \cdot (\rho_L^v)^2 \cdot e^{\alpha\cdot2(\Delta x - 2L)} \cdot \sin[\beta(\omega)\cdot 2\Delta x] \\
& + \rho_0^v \cdot \rho_L^v \cdot e^{-\alpha\cdot2L} \cdot \left\{ e^{\alpha\cdot2\Delta x} \cdot \sin[\beta(\omega)\cdot 2(\Delta x - L)] - \sin[\beta(\omega)\cdot 2L] \right\} \\
& + \rho_0^v \cdot e^{-\alpha\cdot2x_f} \cdot \left\{ \sin[-\beta(\omega)\cdot 2x_f] - (\rho_L^v)^2 \cdot e^{\alpha\cdot2(2x_f+\Delta x - 2L)} \cdot \sin[\beta(\omega)\cdot 2(x_f + \Delta x)] \right\} \\
& + \rho_L^v \cdot e^{-\alpha\cdot2(L+x_f)} \cdot \left\{ e^{\alpha\cdot2(2x_f+\Delta x)} \cdot \sin[\beta(\omega)\cdot 2(x_f + \Delta x - L)] - (\rho_0^v)^2 \cdot \sin[\beta(\omega)\cdot 2(L - x_f)] \right\}.
\end{aligned}
\tag{A.14}
$$

This way, (A.12) further reads

$$
\begin{aligned}
\mathcal{H}^N(x_f + \Delta x,\, j\omega) = {} & \left[1 - (\rho_0^v)^2\right] \cdot \left\{ M \cdot \cos[\beta(\omega)\cdot \Delta x] + N \cdot \sin[\beta(\omega)\cdot \Delta x] \right\} \\
& + j\left[1 - (\rho_0^v)^2\right] \cdot \left\{ N \cdot \cos[\beta(\omega)\cdot \Delta x] - M \cdot \sin[\beta(\omega)\cdot \Delta x] \right\}.
\end{aligned}
\tag{A.15}
$$

Appendix A. Appendix

Still, the proof is separated into two scenarios respectively considering $x = x_f$ and $x \neq x_f$.

i) $x = x_f$

When the guessed fault location coincides with the true fault location x_f, namely $\Delta x = 0$, the real part of $\mathcal{H}^N(x_f, j\omega)$ shows

$$Re\{\mathcal{H}^N(x_f, j\omega)\} = \left[1 - (\rho_0^v)^2\right] \cdot M. \tag{A.16}$$

Especially,

$$
\begin{aligned}
M =& 1 - (\rho_0^v)^2 \cdot (\rho_L^v)^2 \cdot e^{-\alpha \cdot 4L} \\
&+ \rho_0^v \cdot e^{-\alpha \cdot 2x_f} \cdot \left[1 - (\rho_L^v)^2 \cdot e^{-\alpha \cdot 4(L-x_f)}\right] \cdot \cos[\beta(\omega) \cdot 2x_f] \\
&+ \rho_L^v \cdot e^{-\alpha \cdot 2(L-x_f)} \cdot \left[1 - (\rho_0^v)^2 \cdot e^{-\alpha \cdot 4x_f}\right] \cdot \cos[\beta(\omega) \cdot 2(L-x_f)].
\end{aligned}
\tag{A.17}
$$

Applying the double-angle formulas,

$$
\begin{aligned}
M =& \left(1 - \rho_0^v \cdot e^{-\alpha \cdot 2x_f}\right) \cdot \left[1 - \rho_L^v \cdot e^{-\alpha \cdot 2(L-x_f)}\right] \cdot \left(1 - \rho_0^v \cdot \rho_L^v \cdot e^{-\alpha \cdot 2L}\right) \\
&+ 2\rho_0^v \cdot e^{-\alpha \cdot 2x_f} \cdot \left[1 - (\rho_L^v)^2 \cdot e^{-\alpha \cdot 4(L-x_f)}\right] \cdot \cos^2[\beta(\omega) \cdot x_f] \\
&+ 2\rho_L^v \cdot e^{-\alpha \cdot 2(L-x_f)} \cdot \left[1 - (\rho_0^v)^2 \cdot e^{-\alpha \cdot 4x_f}\right] \cdot \cos^2[\beta(\omega) \cdot (L-x_f)].
\end{aligned}
\tag{A.18}
$$

All the terms in (A.18) appear non-negative and do not reach zero simultaneously. That is to say, the real part of $\mathcal{H}^N(x_f, j\omega)$ is positive $\forall \omega (= 2\pi \cdot f)$. Moreover, according to (A.10), it is thus proved that the real part of $\mathcal{H}(x_f, j\omega)$ is positive $\forall \omega (= 2\pi \cdot f)$.

ii) $x \neq x_f$, $x = x_f + \Delta x$

In this case, the real part of $\mathcal{H}^N(x_f + \Delta x, j\omega)$ appears to be

$$Re\{\mathcal{H}^N(x_f, j\omega)\} = \left[1 - (\rho_0^v)^2\right] \cdot \left\{M \cdot \cos[\beta(\omega) \cdot \Delta x] + N \cdot \sin[\beta(\omega) \cdot \Delta x]\right\}. \tag{A.19}$$

There exists a certain frequency $\omega_o (= 2\pi \cdot f_o)$ such that

$$\beta(\omega_o) \cdot \Delta x = \frac{3}{2}\pi + 2k\pi, \quad k \in \mathbb{Z} \tag{A.20}$$

and, thus

$$Re\{\mathcal{H}^N(x_f + \Delta x, j\omega)\} = \left[1 - (\rho_0^v)^2\right] \cdot (-N). \tag{A.21}$$

There exists

$$-N = -\rho_0^v \cdot e^{-\alpha \cdot 2x_f} \cdot \left[1 - \rho_L^v \cdot e^{-\alpha \cdot 2(L-x_f)+\alpha \cdot 2\Delta x}\right] \cdot \left[1 + \rho_L^v \cdot e^{-\alpha \cdot 2(L-x_f)}\right]. \tag{A.22}$$

Considering the range of Δx:

$$
\begin{aligned}
&- x_f < \Delta x < L - x_f \\
\Longleftrightarrow &- \alpha \cdot 2(L - x_f) + \alpha \cdot 2\Delta x < 0 \\
\Longleftrightarrow &1 - \rho_L^v \cdot e^{-\alpha \cdot 2(L - x_f) + \alpha \cdot 2\Delta x} > 0 \\
\Longleftrightarrow &- N < 0
\end{aligned}
\tag{A.23}
$$

It states that $\exists\, \omega_o = 2\pi \cdot f_o$, at which the real parts of $\mathcal{H}^N(x_f + \Delta x,\, j\omega)$ and $\mathcal{H}(x_f + \Delta x,\, j\omega)$ appear negative.

At this point *Theorem 1* in low-loss medium is proved.

A.1.3 Proof of *Theorem 2*: *mirrored minimum squared modulus of $\mathcal{H}(x,\, j\omega)$*

To facilitate the proof, (A.7) is rewritten as

$$
\mathcal{H}(x,\, j\omega) = \overbrace{\left[1 + \rho_L^v \cdot e^{-\alpha \cdot 2(L-x)} \cdot e^{-j\beta(\omega) \cdot 2(L-x)} \right]}^{\mathcal{H}_d(x,\, j\omega)} \cdot e^{-\alpha \cdot x} \cdot
$$
$$
\frac{\left[1 - (\rho_0^v)^2 \right] \cdot e^{-\alpha \cdot x_f} \cdot e^{-j\beta(\omega) \cdot (x - x_f)}}{2 \left[1 - \rho_0^v \cdot \rho_L^v \cdot e^{-\alpha \cdot 2L} \cdot e^{-j\beta(\omega) \cdot 2L} \right] \cdot \left[1 + \rho_0^v \cdot e^{-\alpha \cdot 2x_f} \cdot e^{j\beta(\omega) \cdot 2x_f} \right]} \, .
\tag{A.24}
$$

The squared modulus of $\mathcal{H}(x,\, j\omega)$ is thus expressed as

$$
\left| \mathcal{H}(x,\, j\omega) \right|^2 = \overbrace{\left| 1 + \rho_L^v \cdot e^{-\alpha \cdot 2(L-x)} \cdot e^{-j\beta(\omega) \cdot 2(L-x)} \right|^2}^{\left| \mathcal{H}_d(x,\, j\omega) \right|^2} \cdot e^{-\alpha \cdot 2x} \cdot
$$
$$
\frac{\left[1 - (\rho_0^v)^2 \right]^2 \cdot e^{-\alpha \cdot 2x_f}}{4 \left| 1 - \rho_0^v \cdot \rho_L^v \cdot e^{-\alpha \cdot 2L} \cdot e^{-j\beta(\omega) \cdot 2L} \right|^2 \cdot \left| 1 + \rho_0^v \cdot e^{-\alpha \cdot 2x_f} \cdot e^{j\beta(\omega) \cdot 2x_f} \right|^2} \, .
\tag{A.25}
$$

It can be observed that the term denoted as $\left| \mathcal{H}_d(x,\, j\omega) \right|^2$ in (A.25) appears to be a function of the longitudinal coordinate x. There exists

$$
\left| \mathcal{H}_d(x,\, j\omega) \right|^2 = e^{-\alpha \cdot 2x} + (\rho_L^v)^2 \cdot e^{-\alpha \cdot 2(2L-x)} + 2\rho_L^v \cdot e^{-\alpha \cdot 2L} \cdot \cos[\beta(\omega) \cdot 2(L - x)].
\tag{A.26}
$$

Moreover, at $\forall f_i \in \mathbb{F}^{\mathrm{DT}} = \left\{ f_i = (2i - 1) \cdot f^0 \,\middle|\, f^0 = 1 / \left(4\Gamma_{x_f} \right),\ i = 1, 2, 3, \dots \right\}$,

$$
\begin{aligned}
\left| \mathcal{H}_{d,i}(x) \right|^2 &\triangleq \left| \mathcal{H}_d(x,\, j\omega) \right|^2 \Big|_{\omega = 2\pi \cdot f_i} \\
&= e^{-\alpha \cdot 2x} + (\rho_L^v)^2 \cdot e^{-\alpha \cdot 2(2L-x)} + 2\rho_L^v \cdot e^{-\alpha \cdot 2L} \cdot \cos\left[(2i - 1) \cdot \pi \cdot \frac{L - x}{x_f} \right],
\end{aligned}
\tag{A.27}
$$
$$
i = 1, 2, 3, \dots \, .
$$

Considering (A.4) together with that power networks are characterized by a line length in the order of tens to hundreds of kilometers, it is allowed that $\left|\mathcal{H}_{d,i}(x)\right|^2$ reaches its local minimum when

$$(2i-1)\cdot\pi\cdot\frac{L-x}{x_f}=(2k-1)\cdot\pi,$$

$$i=1,2,3,\dots,\quad\text{and}\quad k=0,\pm1,\pm2,\pm3,\dots\ . \tag{A.28}$$

This way, the conclusion drawn in Section 6.4.1 applies, suggesting that $\left|\mathcal{H}_{d,i}(x)\right|^2$ reaches its local minima at the locations

$$x=L-\frac{2k-1}{2i-1}\cdot x_f, \tag{A.29}$$

where

$$i=1,2,3,\dots,N\quad\text{with}\quad N=\mathit{Floor}\left(f_{max}/f^0\right), \tag{A.30}$$

and

$$k=1,2,3,\dots,K\quad\text{with}\quad K=\mathit{Floor}\left\{\left[\,(2i-1)\cdot(L/x_f)+1\,\right]/2\right\}. \tag{A.31}$$

Floor denotes the floor function and f_{max} refers to the maximum of the frequency of interest.

We further define a set $x_\mathbb{M}$ to categorize those locations, at which for a given fault occurrence at $x=x_f$ the local minimum of $\left|\mathcal{H}_{d,i}(x)\right|^2$ can be obtained at each f_i. There exists

$$x_\mathbb{M}=\left\{\,x_m=(L-x_f)-m\cdot 2x_f\,\middle|\,m=0,1,2,\dots,M\,\right\}, \tag{A.32}$$

with

$$M=\mathit{Floor}\left\{\,(L-x_f)/2x_f\,\right\}. \tag{A.33}$$

It points to that for $x_f\in(L/3,L]$ $x_\mathbb{M}$ contains the mirror image point $x=L-x_f$ as a single element while multiple points of local minimum exist for $x_f\in(0,L/3]$.

In conclusion, *Theorem 2* under the low-loss line approximation is proved.

A.2 Electrical and Geometrical Parameters of Pilot Distribution Network

This section provides the detailed configuration and electrical parameters of the pilot distribution feeder. For the ease of description, we re-draw the schematic diagram of Fig. 4.14 to name and number the overhead-line towers (pylons) and the underground cables present in the network. As illustrated in Fig. A.1, the pylons (abbreviated to P) are numbered from 1 to 33, meanwhile, the cables (abbreviated to C) are numbered from 1 to 9. Tables A.1 and A.2 summarize the geometrical and electrical parameters of the overhead lines. Table A.3 presents the types of the underground cables.
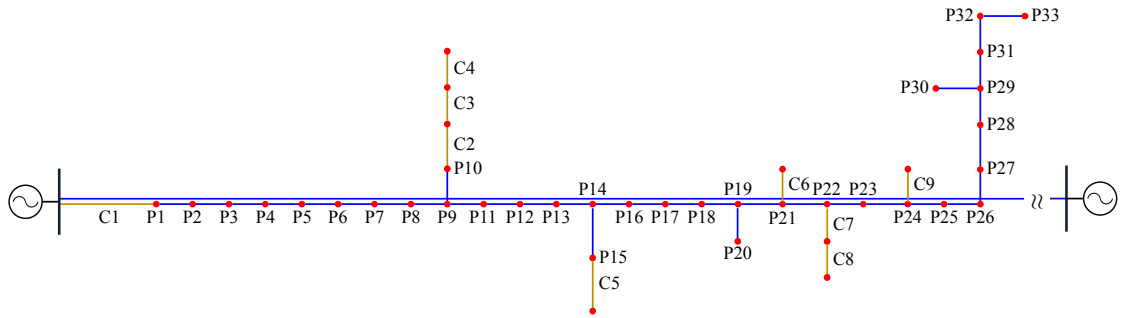
Figure A.1 – Simplified schematic representation of the medium-voltage distribution feeder employed in the pilot test. P: Pylons. C: Underground Cables.
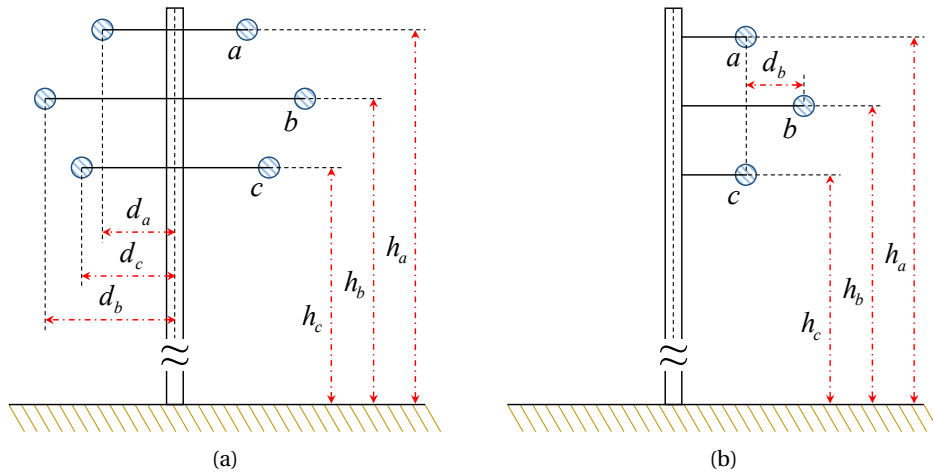
Figure A.2 – Cross-section geometry of the overhead-line conductors for (a) double-circuit overhead-line tower and (b) single-circuit overhead-line tower.

151

Table A.1 – Geometrical parameters of the overhead-line towers

Tower			h (m)			d (m)		
Type	No.		h_a	h_b	h_c	d_a	d_b	d_c
Double circuit	A	1-9, 11-14, 21, 25-29	18.1	15.6	13.1	1.4	2.5	1.8
	B	16-19	21.5	19	16.5	1.4	2.5	1.8
	C	22	17.9	15.4	12.9	1.7	3	2.1
	D	23, 31-32	21	18.5	16	1.4	2.5	1.8
	E	24	20.6	18.1	15.6	1.7	3	2.1
Single circuit	–	10, 20, 30, 33	13	12.4	11.8	–	0.75	–

h: vertical height. d: horizontal distance.

Table A.2 – Electrical characteristics of the overhead-line conductors

Section	Conductor (solid)	
	Material	Diameter (mm)
P1-P9, P9-P14, P14-P19, P19-P21, P21-P22, P22-P24, P24-P29, P29-32	Aluminum	13.82
P9-P10, P19-P20, P29-P30, P32-P33	Copper	2.52
P14-P15	Copper	3.19

Table A.3 – Types of the underground cables

No.	Type
1, 5	Nexans GKT-F 3×1×150/25
2, 3	Nexans GKT 3×1×95/16
4, 6, 7 ,9	Nexans GKT-F 3×1×50/16
8	Nexans XKDT 3×1×150/25

Bibliography

[1] B. Bogert, "Demonstration of delay distortion correction by time-reversal techniques," *IRE Transactions on Communications Systems*, vol. 5, pp. 2–7, Dec. 1957.

[2] F. Rachidi, M. Rubinstein, and M. Paolone, *Electromagnetic Time Reversal: Application to EMC and Power Systems.* John Wiley & Sons, 2017.

[3] M. Fink, "Time reversal of ultrasonic fields. i. basic principles," *IEEE Transactions on Ultrasonics, Ferroelectrics, and Frequency Control*, vol. 39, pp. 555–566, Sept. 1992.

[4] P. M. Morse and K. U. Ingard, *Theoretical Acoustics.* Princeton University Press, 1987.

[5] D. Cassereau, F. Wu, and M. Fink, "Limits of self-focusing using closed time-reversal cavities and mirrors-theory and experiment," in *IEEE Symposium on Ultrasonics*, pp. 1613–1618 vol.3, Dec. 1990.

[6] D. Cassereau and M. Fink, "Time-reversal of ultrasonic fields. iii. theory of the closed time-reversal cavity," *IEEE Transactions on Ultrasonics, Ferroelectrics, and Frequency Control*, vol. 39, pp. 579–592, Sept. 1992.

[7] D. Cassereau and M. Fink, "Theoretical modelisation of time-reversal cavities, application to self-focussing in inhomogeneous media," *Acoustical Imaging*, vol. 19, pp. 141–147, 1992.

[8] F. Wu, J. Thomas, and M. Fink, "Time reversal of ultrasonic fields. ii. experimental results," *IEEE Transactions on Ultrasonics, Ferroelectrics, and Frequency Control*, vol. 39, pp. 567–578, Sept. 1992.

[9] M. Fink, "Time-reversal mirrors," *Journal of Physics D: Applied Physics*, vol. 26, pp. 1333–1350, Sept. 1993.

[10] M. Fink and C. Prada, "Acoustic time-reversal mirrors," *Inverse Problems*, vol. 17, pp. R1–R38, Feb. 2001.

[11] M. Fink, D. Cassereau, A. Derode, C. Prada, P. Roux, M. Tanter, J. L. Thomas, and F. Wu, "Time-reversed acoustics," *Reports on Progress in Physics*, vol. 63, pp. 1933–1995, Nov. 2000.

Bibliography

[12] C. Prada, F. Wu, and M. Fink, "The iterative time-reversal mirror: a solution to self-focusing in the pulse echo mode," *Journal of the Acoustical Society of America*, vol. 90, pp. 1119–1129, Aug. 1991.

[13] C. Prada, J. Thomas, and M. Fink, "The iterative time reversal process: analysis of the convergence," *Journal of the Acoustical Society of America*, vol. 97, pp. 62–71, Jan. 1995.

[14] A. Derode, P. Roux, and M. Fink, "Robust acoustic time reversal with high-order multiple scattering," *Physical Review Letters*, vol. 75, pp. 4206–4209, Dec. 1995.

[15] L. Borcea, G. Papanicolaou, C. Tsogka, and J. Berryman, "Imaging and time reversal in random media," *Inverse Problems*, vol. 18, pp. 1247–1279, Oct. 2002.

[16] A. Derode, A. Tourin, J. de Rosny, M. Tanter, S. Yon, and M. Fink, "Taking advantage of multiple scattering to communicate with time-reversal antennas," *Physical Review Letters*, vol. 90, p. 014301, Jan. 2003.

[17] G. Bal and L. Ryzhik, "Time reversal and refocusing in random media," *Journal on Applied Mathematics*, vol. 63, no. 5, pp. 1475–1498, 2003.

[18] J. Fouque and K. Solna, "Time-reversal aperture enhancement," *Multiscale Modeling and Simulation*, vol. 1, no. 2, pp. 239–259, 2003.

[19] S. Kim, W. A. Kuperman, W. S. Hodgkiss, H. C. Song, G. Edelmann, and T. Akal, "Echo-to-reverberation enhancement using a time reversal mirror," *Journal of the Acoustical Society of America*, vol. 115, pp. 1525–1531, Apr. 2004.

[20] P. Blomgren, G. Papanicolaou, and H. Zhao, "Super-resolution in time-reversal acoustics," *Journal of the Acoustical Society of America*, vol. 111, pp. 230–248, Jan. 2002.

[21] C. Tsogka and G. Papanicolaou, "Time reversal through a solid-liquid interface and super-resolution," *Inverse Problems*, vol. 18, pp. 1639–1657, Dec. 2002.

[22] S. K. Lehman and A. J. Devaney, "Transmission mode time-reversal super-resolution imaging," *Journal of the Acoustical Society of America*, vol. 113, pp. 2742–2753, May 2003.

[23] G. Lerosey, J. De Rosny, A. Tourin, and M. Fink, "Focusing beyond the diffraction limit with far-field time reversal," *Science*, vol. 315, pp. 1120–1122, Feb. 2007.

[24] M. Fink, "Time-reversal waves and super resolution," *Journal of Physics: Conference Series*, vol. 124, p. 012004, July 2008.

[25] C. Draeger and M. Fink, "One-channel time reversal of elastic waves in a chaotic 2d-silicon cavity," *Physical Review Letters*, vol. 79, pp. 407–410, July 1997.

[26] C. Draeger and M. Fink, "One-channel time-reversal in chaotic cavities: theoretical limits," *Journal of the Acoustical Society of America*, vol. 105, pp. 611–617, Feb. 1999.

154

[27] C. Draeger, J. Aime, and M. Fink, "One-channel time-reversal in chaotic cavities: experimental results," *Journal of the Acoustical Society of America*, vol. 105, pp. 618–625, Feb. 1999.

[28] C. Prada and M. Fink, "Eigen modes of the time-reversal operator: a solution to selective focusing in multiple-target media," *Wave Motion*, vol. 20, pp. 151–163, Sept. 1994.

[29] C. Prada, S. Manneville, D. Spoliansky, and M. Fink, "Decomposition of the time reversal operator: detection and selective focusing on two scatterers," *Journal of the Acoustical Society of America*, vol. 99, pp. 2067–2076, Apr. 1996.

[30] N. Mordant, C. Prada, and M. Fink, "Highly resolved detection and selective focusing in a waveguide using the d.o.r.t. method," *Journal of the Acoustical Society of America*, vol. 105, pp. 2634–2642, May 1999.

[31] J.-L. Robert and M. Fink, "Spatio-temporal invariants of the time reversal operator," *Journal of the Acoustical Society of America*, vol. 127, pp. 2904–2912, May 2010.

[32] H. Lev-Ari and A. J. Devancy, "The time-reversal technique re-interpreted: subspace-based signal processing for multi-static target location," in *Proceedings of 2000 IEEE Sensor Array and Multichannel Signal Processing Workshop.*, pp. 509–513, Mar. 2000.

[33] A. J. Devaney and M. Dennison, "Inverse scattering in inhomogeneous background media," *Inverse Problems*, vol. 19, pp. 855–870, June 2003.

[34] M. Dennison and A. Devaney, "Inverse scattering in inhomogeneous background media: ii. multi-frequency case and SVD formulation," *Inverse Problems*, vol. 20, pp. 1307–1324, Aug. 2004.

[35] F. K. Gruber, E. A. Marengo, and A. J. Devaney, "Time-reversal imaging with multiple signal classification considering multiple scattering between the targets," *Journal of the Acoustical Society of America*, vol. 115, pp. 3042–3047, June 2004.

[36] A. J. Devaney, "Time reversal imaging of obscured targets from multistatic data," *IEEE Transactions on Antennas and Propagation*, vol. 53, pp. 1600–1610, May 2005.

[37] A. J. Devaney, E. A. Marengo, and F. K. Gruber, "Time-reversal-based imaging and inverse scattering of multiply scattering point targets," *Journal of the Acoustical Society of America*, vol. 118, pp. 3129–3138, Nov. 2005.

[38] J. L. Thomas, F. Wu, and M. Fink, "Time reversal focusing applied to lithotripsy," *Ultrasonic Imaging*, vol. 18, no. 2, pp. 106 – 121, 1996.

[39] M. Fink, G. Montaldo, and M. Tanter, "Time-reversal acoustics in biomedical engineering," *Annual Review of Biomedical Engineering*, vol. 5, no. 1, pp. 465–497, 2003. PMID: 14527319.

[40] J. Gateau, L. Marsac, M. Pernot, J. Aubry, M. Tanter, and M. Fink, "Transcranial ultrasonic therapy based on time reversal of acoustically induced cavitation bubble signature," *IEEE Transactions on Biomedical Engineering*, vol. 57, pp. 134–144, Jan. 2010.

[41] M. Tanter and M. Fink, "Ultrafast imaging in biomedical ultrasound," *IEEE Transactions on Ultrasonics Ferroelectrics and Frequency Control*, vol. 61, pp. 102–119, Jan. 2014.

[42] O. Couture, V. Hingot, B. Heiles, P. Muleki-Seya, and M. Tanter, "Ultrasound localization microscopy and super-resolution: a state of the art," *IEEE Transactions on Ultrasonics Ferroelectrics and Frequency Control*, vol. 65, pp. 1304–1320, Aug. 2018.

[43] N. Chakroun, M. A. Fink, and F. Wu, "Time reversal processing in ultrasonic nondestructive testing," *IEEE Transactions on Ultrasonics, Ferroelectrics, and Frequency Control*, vol. 42, pp. 1087–1098, Nov. 1995.

[44] G. F. Edelmann, T. Akal, W. S. Hodgkiss, S. Kim, W. A. Kuperman, and H. C. Song, "An initial demonstration of underwater acoustic communication using time reversal," *IEEE Journal of Oceanic Engineering*, vol. 27, pp. 602–609, July 2002.

[45] S. Kim, W. Kuperman, W. Hodgkiss, H. Song, G. Edelmann, and T. Akal, "Robust time reversal focusing in the ocean," *Journal of the Acoustical Society of America*, vol. 114, pp. 145–157, July 2003.

[46] C. Larmat, J. P. Montagner, M. Fink, Y. Capdeville, A. Tourin, and E. Clevede, "Time-reversal imaging of seismic sources and application to the great Sumatra earthquake," *Geophysical Research Letters*, vol. 33, pp. 1–4, Oct. 2006.

[47] C. S. Larmat, R. A. Guyer, and P. A. Johnson, "Time-reversal methods in geophysics," *Physics Today*, vol. 63, pp. 31–35, Aug. 2010.

[48] A. Przadka, S. Feat, P. Petitjeans, V. Pagneux, A. Maurel, and M. Fink, "Time reversal of water waves," *Physical Review Letters*, vol. 109, p. 064501, Aug. 2012.

[49] G. Lerosey, J. de Rosny, A. Tourin, A. Derode, G. Montaldo, and M. Fink, "Time reversal of electromagnetic waves," *Physical Review Letters*, vol. 92, p. 193904, May 2004.

[50] B. E. Henty and D. D. Stancil, "Multipath-enabled super-resolution for rf and microwave communication using phase-conjugate arrays," *Physical Review Letters*, vol. 93, p. 243904, Dec. 2004.

[51] G. Lerosey, J. de Rosny, A. Tourin, A. Derode, and M. Fink, "Time reversal of wideband microwaves," *Applied Physics Letters*, vol. 88, Apr. 2006.

[52] R. Carminati, R. Pierrat, J. de Rosny, and M. Fink, "Theory of the time reversal cavity for electromagnetic fields," *Optics Letters*, vol. 32, pp. 3107–3109, Nov. 2007.

[53] J. de Rosny, G. Lerosey, and M. Fink, "Theory of electromagnetic time-reversal mirrors," *IEEE Transactions on Antennas and Propagation*, vol. 58, pp. 3139–3149, Oct. 2010.

[54] H. H, W. Hayt, and J. Buck, *Engineering Electromagnetics.* Electrical engineering series, McGraw-Hill, 2001.

[55] R. Snieder, "Time-reversal invariance and the relation between wave chaos and classical chaos," in *Imaging of Complex Media with Acoustic and Seismic Waves*, pp. 1–15, Springer-Verlag Berlin, 2002.

[56] F. Rachidi and M. Rubinsein, "Time reversal of electromagnetic fields and its application to lightning location," in *2013 International Symposium on Lightning Protection (XII SIPDA)*, pp. 378–383, 2013.

[57] M. Davy, J. de Rosny, and M. Fink, "Focusing and amplification of electromagnetic waves by time-reversal in an leaky reverberation chamber," in *2009 IEEE Antennas and Propagation Society International Symposium*, pp. 1–4, June 2009.

[58] P. Kosmas and C. M. Rappaport, "Time reversal with the fdtd method for microwave breast cancer detection," *IEEE Transactions on Microwave Theory and Techniques*, vol. 53, pp. 2317–2323, July 2005.

[59] M. D. Hossain and A. S. Mohan, "Coherent time reversal minimum variance beamforming for the localization of tissue malignancies in dense breast phantoms," in *2013 Asia-Pacific Microwave Conference Proceedings (APMC)*, pp. 377–379, Nov. 2013.

[60] M. G. Aram, M. Haghparast, M. S. Abrishamian, and A. Mirtaheri, "Comparison of imaging quality between linear sampling method and time reversal in microwave imaging problems," *Inverse Problems in Science and Engineering*, vol. 24, no. 8, pp. 1347–1363, 2016.

[61] D. Liu, G. Kang, L. Li, Y. Chen, S. Vasudevan, W. Joines, Q. Liu, J. Krolik, and L. Carin, "Electromagnetic time-reversal imaging of a target in a cluttered environment," *IEEE Transactions on Antennas and Propagation*, vol. 53, pp. 3058–3066, Sept. 2005.

[62] W. Zhang, A. Hoorfar, and L. Li, "Through-the-wall target localization with time reversal music method," *Progress in Electromagnetics Research-Pier*, vol. 106, pp. 75–89, 2010.

[63] V. C. Odedo, M. E. Yavuz, F. Costen, R. Himeno, and H. Yokota, "Time reversal technique based on spatiotemporal windows for through the wall imaging," *IEEE Transactions on Antennas and Propagation*, vol. 65, pp. 3065–3072, June 2017.

[64] H. Zhai, S. Sha, V. K. Shenoy, S. Jung, M. Lu, K. Min, S. Lee, and D. S. Ha, "An electronic circuit system for time-reversal of ultra-wideband short impulses based on frequency-domain approach," *IEEE Transactions on Microwave Theory and Techniques*, vol. 58, pp. 74–86, Jan. 2010.

[65] Y. Chen, Y. Yang, F. Han, and K. J. R. Liu, "Time-reversal wideband communications," *IEEE Signal Processing Letters*, vol. 20, pp. 1219–1222, Dec. 2013.

[66] A. Cozza and B. Abou, "Accurate radiation-pattern measurements in a time-reversal electromagnetic chamber," *IEEE Antennas and Propagation Magazine*, vol. 52, pp. 186–193, Apr. 2010.

[67] A. Cozza and F. Monsef, "Multiple-source time-reversal transmissions in random media," *IEEE Transactions on Antennas and Propagation*, vol. 62, pp. 4269–4281, Aug. 2014.

[68] L. Abboud, A. Cozza, and L. Pichon, "A matched-pulse approach for soft-fault detection in complex wire networks," *IEEE Transactions on Instrumentation and Measurement*, vol. 61, pp. 1719–1732, June 2012.

[69] L. Abboud, A. Cozza, and L. Pichon, "A noniterative nethod for locating soft faults in complex wire networks," *Transactions on Vehicular Technology*, vol. 62, pp. 1010–1019, Mar. 2013.

[70] M. Kafal, A. Cozza, and L. Pichon, "Locating multiple soft faults in wire networks using an alternative dort implementation," *IEEE Transactions on Instrumentation and Measurement*, vol. 65, pp. 399–406, Feb. 2016.

[71] M. Kafal, A. Cozza, and L. Pichon, "Locating faults with high resolution using single-frequency tr-music processing," *IEEE Transactions on Instrumentation and Measurement*, vol. 65, pp. 2342–2348, Oct. 2016.

[72] M. Kafal and A. Cozza, "Multifrequency tr-music processing to locate soft faults in cables subject to noise," *IEEE Transactions on Instrumentation and Measurement*, vol. 69, pp. 411–418, Feb. 2020.

[73] N. Mora, F. Rachidi, and M. Rubinstein, "Application of the time reversal of electromagnetic fields to locate lightning discharges," *Atmospheric Research*, vol. 117, no. SI, pp. 78–85, 2012.

[74] G. Lugrin, N. M. Mora, F. Rachidi, M. Rubinstein, and G. Diendorfer, "On the location of lightning discharges using time reversal of electromagnetic fields," *IEEE Transactions on Electromagnetic Compatibility*, vol. 56, pp. 149–158, Feb 2014.

[75] T. Wang, S. Qiu, L. Shi, and Y. Li, "Broadband vhf localization of lightning radiation sources by emtr," *IEEE Transactions on Electromagnetic Compatibility*, vol. 59, pp. 1949–1957, Dec. 2017.

[76] A. Mostajabi, H. Karami, M. Azadifar, A. Ghasemi, M. Rubinstein, and F. Rachidi, "Single-sensor source localization using electromagnetic time reversal and deep transfer learning: Application to lightning," *Scientific Reports*, vol. 9, p. 17372, Nov. 2019.

[77] R. Razzaghi, M. Scatena, K. Sheshyekani, M. Paolone, F. Rachidi, and G. Antonini, "Locating lightning strikes and flashovers along overhead power transmission lines using electromagnetic time reversal," *Electric Power Systems Research*, vol. 160, pp. 282 – 291, 2018.

[78] Z. Wang, F. Gerini, M. Paolone, C. A. Nucci, and F. Rachidi, "Using electromagnetic time reversal similarity metric to locate lightning-originated flashovers on overhead transmission lines," in *2019 International Symposium on Lightning Protection (XV SIPDA)*, pp. 1–6, Sept. 2019.

[79] R. Razzaghi, G. Lugrin, H. Manesh, C. Romero, M. Paolone, and F. Rachidi, "An efficient method based on the electromagnetic time reversal to locate faults in power networks," *IEEE Transactions on Power Delivery*, vol. 28, pp. 1663–1673, July 2013.

[80] R. Razzaghi, G. Lugrin, M. Paolone, and F. Rachidi, "On the use of electromagnetic time reversal to locate faults in series-compensated transmission lines," in *2013 IEEE Grenoble PowerTech*, pp. 1–5, June 2013.

[81] A. Codino, Z. Wang, R. Razzaghi, M. Paolone, and F. Rachidi, "An alternative method for locating faults in transmission line networks based on time reversal," *IEEE Transactions on Electromagnetic Compatibility*, vol. 59, pp. 1601–1612, Oct. 2017.

[82] Z. Wang, A. Codino, R. Razzaghi, M. Paolone, and F. Rachidi, "Using electromagnetic time reversal to locate faults in transmission lines: Definition and application of the "mirrored minimum energy" property," in *2017 International Symposium on Electromagnetic Compatibility - EMC EUROPE*, pp. 1–6, Sept. 2017.

[83] Z. Wang, S. He, Q. Li, B. Liu, R. Razzaghi, M. Paolone, Y. Xie, M. Rubinstein, and F. Rachidi, "A full-scale experimental validation of electromagnetic time reversal applied to locate disturbances in overhead power distribution lines," *IEEE Transactions on Electromagnetic Compatibility*, vol. 60, pp. 1562–1570, Oct. 2018.

[84] S. He, Y. Xie, Z. Wang, F. Rachidi, B. Liu, Q. Li, and X. Kong, "Norm criteria in the electromagnetic time reversal technique for fault location in transmission lines," *IEEE Transactions on Electromagnetic Compatibility*, vol. 60, pp. 1240–1248, Oct. 2018.

[85] Z. Wang, R. Razzaghi, M. Paolone, and F. Rachidi, "Electromagnetic time reversal similarity characteristics and its application to locating faults in power networks," *IEEE Transactions on Power Delivery*, pp. 1–1, 2019.

[86] Z. Wang, R. Razzaghi, M. Paolone, and F. Rachidi, "Time reversal applied to fault location in power networks: pilot test results and analyses," *International Journal of Electrical Power and Energy Systems*, vol. 114, p. 105382, 2020.

[87] S. He, A. Cozza, and Y. Xie, "Electromagnetic time reversal as a correlation estimator: Improved metrics and design criteria for fault location in power grids," *IEEE Transactions on Electromagnetic Compatibility*, vol. 62, pp. 598–611, Apr. 2020.

[88] M. M. Saha, J. J. Izykowski, and E. Rosolowski, *Fault Location on Power Networks*. Springer Science & Business Media, 2009.

[89] *IEEE Guide for Determining Fault Location on Ac Transmission and Distribution Lines.* IEEE Std C37.114-2014 (Revision of IEEE Std C37.114-2004), Jan. 2015.

[90] *Power System Stability and Control.* EPRI power system engineering series, McGraw-Hill, 1994.

[91] *IEEE Guide for Electric Power Distribution Reliability Indices.* IEEE Std 1366-2012 (Revision of IEEE Std 1366-2003), 2012.

[92] A. A. Chowdhury and D. O. Koval, "Current practices and customer value-based distribution system reliability planning," *IEEE Transactions on Industry Applications*, vol. 40, pp. 1174–1182, Sept. 2004.

[93] F. Soudi and K. Tomsovic, "Optimized distribution protection using binary programming," *IEEE Transactions on Power Delivery*, vol. 13, pp. 218–224, Jan. 1998.

[94] T. W. Stringfield, D. J. Marihart, and R. F. Stevens, "Fault location methods for overhead lines," *Transactions of the American Institute of Electrical Engineers. Part III: Power Apparatus and Systems*, vol. 76, pp. 518–529, Apr. 1957.

[95] L. Eriksson, M. M. Saha, and G. D. Rockefeller, "An accurate fault locator with compensation for apparent reactance in the fault resistance resulting from remote-end infeed," *IEEE Power Engineering Review*, vol. PER-5, pp. 44–44, Feb. 1985.

[96] M. B. Djuric, Z. M. Radojevic, and V. V. Terzija, "Distance protection and fault location utilizing only phase current phasors," *IEEE Transactions on Power Delivery*, vol. 13, pp. 1020–1026, Oct. 1998.

[97] T. Kawady and J. Stenzel, "A practical fault location approach for double circuit transmission lines using single end data," *IEEE Transactions on Power Delivery*, vol. 18, pp. 1166–1173, Oct. 2003.

[98] C. E. de Morais Pereira and L. C. Zanetta, "Fault location in transmission lines using one-terminal postfault voltage data," *IEEE Transactions on Power Delivery*, vol. 19, pp. 570–575, Apr. 2004.

[99] A. D. Filomena, M. Resener, R. H. Salim, and A. S. Bretas, "Fault location for underground distribution feeders: An extended impedance-based formulation with capacitive current compensation," *International Journal of Electrical Power & Energy Systems*, vol. 31, pp. 489 – 496, Oct. 2009.

[100] Z. Xu and T. S. Sidhu, "Fault location method based on single-end measurements for underground cables," *IEEE Transactions on Power Delivery*, vol. 26, pp. 2845–2854, Oct. 2011.

[101] K. Jia, D. Thomas, and M. Sumner, "A new single-ended fault-location scheme for utilization in an integrated power system," *IEEE Transactions on Power Delivery*, vol. 28, pp. 38–46, Jan. 2013.

[102] J. Izykowski, R. Molag, E. Rosolowski, and M. M. Saha, "Accurate location of faults on power transmission lines with use of two-end unsynchronized measurements," *IEEE Transactions on Power Delivery*, vol. 21, pp. 627–633, Apr. 2006.

[103] A. L. Dalcastagne, S. N. Filho, H. H. Zurn, and R. Seara, "An iterative two-terminal fault-location method based on unsynchronized phasors," *IEEE Transactions on Power Delivery*, vol. 23, pp. 2318–2329, Oct. 2008.

[104] Y. Liao and N. Kang, "Fault-location algorithms without utilizing line parameters based on the distributed parameter line model," *IEEE Transactions on Power Delivery*, vol. 24, pp. 579–584, Apr. 2009.

[105] J. Izykowski, E. Rosolowski, P. Balcerek, M. Fulczyk, and M. M. Saha, "Accurate noniterative fault-location algorithm utilizing two-end unsynchronized measurements," *IEEE Transactions on Power Delivery*, vol. 26, pp. 547–555, Apr. 2011.

[106] S. M. Brahma and A. A. Girgis, "Fault location on a transmission line using synchronized voltage measurements," *IEEE Transactions on Power Delivery*, vol. 19, pp. 1619–1622, Oct. 2004.

[107] C. W. Liu, T. C. Lin, C. S. Yu, and J. Z. Yang, "A fault location technique for two-terminal multisection compound transmission lines using synchronized phasor measurements," *IEEE Transactions on Smart Grid*, vol. 3, pp. 113–121, Mar. 2012.

[108] P. Dutta, A. Esmaeilian, and M. Kezunovic, "Transmission-line fault analysis using synchronized sampling," *IEEE Transactions on Power Delivery*, vol. 29, pp. 942–950, Apr. 2014.

[109] T. P. S. Bains, T. S. Sidhu, Z. Xu, I. Voloh, and M. R. D. Zadeh, "Impedance-based fault location algorithm for ground faults in series-capacitor-compensated transmission lines," *IEEE Transactions on Power Delivery*, vol. 33, pp. 189–199, Feb. 2018.

[110] V. A. Stanojević, G. Preston, and V. Terzija, "Synchronised measurements based algorithm for long transmission line fault analysis," *IEEE Transactions on Smart Grid*, vol. 9, pp. 4448–4457, Sept. 2018.

[111] S. Hussain and A. Osman, "Fault location scheme for multi-terminal transmission lines using unsynchronized measurements," *International Journal of Electrical Power and Energy Systems*, vol. 78, pp. 277 – 284, 2016.

[112] S. M. Brahma, "Fault location scheme for a multi-terminal transmission line using synchronized voltage measurements," *IEEE Transactions on Power Delivery*, vol. 20, pp. 1325–1331, Apr. 2005.

[113] G. Manassero, E. C. Senger, R. M. Nakagomi, E. L. Pellini, and E. C. N. Rodrigues, "Fault-location system for multiterminal transmission lines," *IEEE Transactions on Power Delivery*, vol. 25, pp. 1418–1426, July 2010.

[114] T. C. Lin, P. Y. Lin, and C. W. Liu, "An algorithm for locating faults in three-terminal multisection nonhomogeneous transmission lines using synchrophasor measurements," *IEEE Transactions on Smart Grid*, vol. 5, pp. 38–50, Jan. 2014.

[115] S. Azizi and M. Sanaye-Pasand, "A straightforward method for wide-area fault location on transmission networks," *IEEE Transactions on Power Delivery*, vol. 30, pp. 264–272, Feb. 2015.

[116] G. Feng and A. Abur, "Fault location using wide-area measurements and sparse estimation," *IEEE Transactions on Power Systems*, vol. 31, pp. 2938–2945, July 2016.

[117] A. S. Dobakhshari, "Fast accurate fault location on transmission system utilizing wide-area unsynchronized measurements," *International Journal of Electrical Power & Energy Systems*, vol. 101, pp. 234 – 242, Oct. 2018.

[118] A. S. Dobakhshari, "Wide-area fault location of transmission lines by hybrid synchronized/unsynchronized voltage measurements," *IEEE Transactions on Smart Grid*, vol. 9, pp. 1869–1877, May 2018.

[119] C. A. Peñuela Meneses and J. R. S. Mantovani, "Improving the grid operation and reliability cost of distribution systems with dispersed generation," *IEEE Transactions on Power Systems*, vol. 28, pp. 2485–2496, Aug. 2013.

[120] P. G. McLaren and S. Rajendra, "Travelling-wave techniques applied to the protection of teed circuits: - multi-phase/multi-circuit system," *IEEE Transactions on Power Apparatus and Systems*, vol. PAS-104, pp. 3551–3557, Dec. 1985.

[121] A. O. Ibe and B. J. Cory, "A travelling wave-based fault locator for two- and three-terminal networks," *IEEE Transactions on Power Delivery*, vol. 1, pp. 283–288, Apr. 1986.

[122] G. B. Ancell and N. C. Pahalawaththa, "Maximum likelihood estimation of fault location on transmission lines using travelling waves," *IEEE Transactions on Power Delivery*, vol. 9, pp. 680–689, Apr. 1994.

[123] F. H. Magnago and A. Abur, "Fault location using wavelets," *IEEE Transactions on Power Delivery*, vol. 13, pp. 1475–1480, Oct. 1998.

[124] F. H. Magnago and A. Abur, "A new fault location technique for radial distribution systems based on high frequency signals," in *1999 IEEE Power Engineering Society Summer Meeting. Conference Proceedings*, vol. 1, pp. 426–431 vol.1, July 1999.

[125] A. Borghetti, M. Bosetti, C. A. Nucci, M. Paolone, and A. Abur, "Integrated use of time-frequency wavelet decompositions for fault location in distribution networks: theory and experimental validation," *IEEE Transactions on Power Delivery*, vol. 25, pp. 3139–3146, Oct. 2010.

[126] Z. He, K. Liao, X. Li, S. Lin, J. Yang, and R. Mai, "Natural frequency-based line fault location in hvdc lines," *IEEE Transactions on Power Delivery*, vol. 29, pp. 851–859, Apr. 2014.

[127] A. Borghetti, M. Bosetti, M. D. Silvestro, C. A. Nucci, and M. Paolone, "Continuous-wavelet transform for fault location in distribution power networks: definition of mother wavelets inferred from fault originated transients," *IEEE Transactions on Power Systems*, vol. 23, pp. 380–388, May 2008.

[128] D. Spoor and J. G. Zhu, "Improved single-ended traveling-wave fault-location algorithm based on experience with conventional substation transducers," *IEEE Transactions on Power Delivery*, vol. 21, pp. 1714–1720, July 2006.

[129] L. Rui, F. Guoqing, Z. Xueyuan, and X. Xue, "Fault location based on single terminal travelling wave analysis in radial distribution network," *International Journal of Electrical Power and Energy Systems*, vol. 66, pp. 160–165, Mar. 2015.

[130] M. Gilany, D. k. Ibrahim, and E. S. Tag Eldin, "Traveling-wave-based fault-location scheme for multiend-aged underground cable system," *IEEE Transactions on Power Delivery*, vol. 22, pp. 82–89, Jan. 2007.

[131] C. Yu, "An unsynchronized measurements correction method for two-terminal fault-location problems," *IEEE Transactions on Power Delivery*, vol. 25, pp. 1325–1333, July 2010.

[132] F. V. Lopes, K. M. Silva, F. B. Costa, W. L. A. Neves, and D. Fernandes, "Real-time traveling-wave-based fault location using two-terminal unsynchronized data," *IEEE Transactions on Power Delivery*, vol. 30, pp. 1067–1076, June 2015.

[133] L. Yuansheng, W. Gang, and L. Haifeng, "Time-domain fault-location method on hvdc transmission lines under unsynchronized two-end measurement and uncertain line parameters," *IEEE Transactions on Power Delivery*, vol. 30, pp. 1031–1038, June 2015.

[134] F. V. Lopes, "Settings-free traveling-wave-based earth fault location using unsynchronized two-terminal data," *IEEE Transactions on Power Delivery*, vol. 31, pp. 2296–2298, Oct. 2016.

[135] F. V. Lopes, P. Lima, J. P. G. Ribeiro, T. R. Honorato, K. M. Silva, E. J. S. Leite, W. L. A. Neves, and G. Rocha, "Practical methodology for two-terminal traveling wave-based fault location eliminating the need for line parameters and time synchronization," *IEEE Transactions on Power Delivery*, vol. 34, pp. 2123–2134, Dec. 2019.

[136] Y. Chen, D. Liu, and B. Xu, "Wide-area traveling wave fault location system based on iec61850," *IEEE Transactions on Smart Grid*, vol. 4, pp. 1207–1215, June 2013.

[137] M. B. Dewe, S. Sankar, and J. Arrillaga, "The application of satellite time references to hvdc fault location," *IEEE Transactions on Power Delivery*, vol. 8, pp. 1295–1302, July 1993.

[138] I. Daubechies, "The wavelet transform, time-frequency localization and signal analysis," *IEEE Transactions on Information Theory*, vol. 36, pp. 961–1005, Sept. 1990.

[139] A. Graps, "An introduction to wavelets," *IEEE Computational Science and Engineering*, vol. 2, no. 2, pp. 50–61, 1995.

[140] W. A. Wilkinson and M. D. Cox, "Discrete wavelet analysis of power system transients," *IEEE Transactions on Power Systems*, vol. 11, pp. 2038–2044, Nov 1996.

[141] F. B. Costa, "Fault-induced transient detection based on real-time analysis of the wavelet coefficient energy," *IEEE Transactions on Power Delivery*, vol. 29, pp. 140–153, Feb. 2014.

[142] S. Huang and C. Hsieh, "High-impedance fault detection utilizing a Morlet wavelet transform approach," *IEEE Transactions on Power Delivery*, vol. 14, pp. 1401–1410, Oct. 1999.

[143] A. Borghetti, M. Bosetti, M. Di Silvestro, C. A. Nucci, and M. Paolone, "Continuous-wavelet transform for fault location in distribution power networks: definition of mother wavelets inferred from fault originated transients," *IEEE Transactions on Power Systems*, vol. 23, pp. 380–388, May 2008.

[144] Z. He, L. Fu, S. Lin, and Z. Bo, "Fault detection and classification in ehv transmission line based on wavelet singular entropy," *IEEE Transactions on Power Delivery*, vol. 25, pp. 2156–2163, Oct. 2010.

[145] Y. Hsu, F. C.Lu, Y. Chien, J. P. Liu, J. T. Lin, P. H. S. Yu, and R. R. T. Kuo, "An expert system for locating distribution system faults," *IEEE Transactions on Power Delivery*, vol. 6, pp. 366–372, Jan. 1991.

[146] M. M. Tawfik and M. M. Morcos, "Ann-based techniques for estimating fault location on transmission lines using prony method," *IEEE Transactions on Power Delivery*, vol. 16, pp. 219–224, Apr. 2001.

[147] Z. Jiao and R. Wu, "A new method to improve fault location accuracy in transmission line based on fuzzy multi-sensor data fusion," *IEEE Transactions on Smart Grid*, vol. 10, pp. 4211–4220, July 2019.

[148] M. Kezunovic and Y. Liao, "Fault location estimation based on matching the simulated and recorded waveforms using genetic algorithms," in *2001 Seventh International Conference on Developments in Power System Protection*, pp. 399–402, Apr. 2001.

[149] H. Jiang, J. J. Zhang, W. Gao, and Z. Wu, "Fault detection, identification, and location in smart grid based on data-driven computational methods," *IEEE Transactions on Smart Grid*, vol. 5, pp. 2947–2956, Nov. 2014.

[150] D. Srinivasan, R. Cheu, Y. Poh, and A. Ng, "Automated fault detection in power distribution networks using a hybrid fuzzy-genetic algorithm approach," *Engineering Applications of Artificial Intelligence*, vol. 13, pp. 407–418, Aug. 2000.

[151] W. H. Chen, C. W. Liu, and M. S. Tsai, "On-line fault diagnosis of distribution substations using hybrid cause-effect network and fuzzy rule-based method," *IEEE Transactions on Power Delivery*, vol. 15, pp. 710–717, Apr. 2000.

[152] H. Livani and C. Y. Evrenosoglu, "A machine learning and wavelet-based fault location method for hybrid transmission lines," *IEEE Transactions on Smart Grid*, vol. 5, pp. 51–59, Jan. 2014.

[153] C. R. Paul, *Analysis of Multiconductor Transmission Lines*. Wiley-IEEE Press, 2nd ed., 2007.

[154] G. Lugrin, R. Razzaghi, F. Rachidi, and M. Paolone, "Electromagnetic time reversal applied to fault detection: The issue of losses," in *2015 IEEE International Symposium on Electromagnetic Compatibility (EMC)*, pp. 209–212, Aug. 2015.

[155] R. Razzaghi, G. Lugrin, F. Rachidi, and M. Paolone, "Assessment of the influence of losses on the performance of the electromagnetic time reversal fault location method," *IEEE Transactions on Power Delivery*, vol. 32, pp. 2303–2312, Oct. 2017.

[156] A. Greenwood, *Electrical Transients in Power Systems*. New York, NY (USA); John Wiley and Sons Inc., 1991.

[157] M. H. J. Bollen, E. Styvaktakis, and I. Y. H. Gu, "Categorization and analysis of power system transients," *IEEE Transactions on Power Delivery*, vol. 20, pp. 2298–2306, July 2005.

[158] C. Altman and K. Suchy, *Reciprocity, Spatial Mapping and Time Reversal in Electromagnetics*. Springer Netherlands, 2011.

[159] Z. Wang, F. Rachidi, M. Paolone, M. Rubinstein, and R. Razzaghi, "A closed time-reversal cavity for electromagnetic waves in transmission line networks," *Under review*, pp. 1–8.

[160] F. Tesche, M. Ianoz, and T. Karlsson, *EMC Analysis Methods and Computational Models*. A Wiley-Interscience publication, Wiley, 1996.

[161] H. W. Dommel, "Digital computer solution of electromagnetic transients in single-and multiphase networks," *IEEE Transactions on Power Apparatus and Systems*, 1969.

[162] J. Mahseredjian, S. Dennetière, L. Dubé, B. Khodabakhchian, and L. Gérin-Lajoie, "On a new approach for the simulation of transients in power systems," *Electric Power Systems Research*, vol. 77, no. 11, pp. 1514 – 1520, 2007.

[163] J. de Rosny and M. Fink, "Overcoming the diffraction limit in wave physics using a time-reversal mirror and a novel acoustic sink," *Physical Review Letters*, vol. 89, p. 124301, Aug. 2002.

[164] W. A. Radasky, C. E. Baum, and M. W. Wik, "Introduction to the special issue on high-power electromagnetics (hpem) and intentional electromagnetic interference (iemi)," *IEEE Transactions on Electromagnetic Compatibility*, vol. 46, pp. 314–321, Aug. 2004.

[165] R. Smolenski, *Conducted Electromagnetic Interference (EMI) in Smart Grids.* Power Systems, Springer London, 2012.

[166] Z. Wang, S. He, Q. Li, B. Liu, R. Razzaghi, M. Paolone, Y. Xie, M. Rubinstein, and F. Rachidi, "A full-scale experimental test of electromagnetic time reversal applied to locate faults in power lines," in *Asian Electromagnetics Conference 2017 (ASIAEM 2017)*, pp. 1–5, July 2017.

[167] L. Peretto, P. Rinaldi, R. Sasdelli, and R. Tinarelli, "A system for the measurement of the starting instant of impulsive transients," in *Proceedings of the 21st IEEE Instrumentation and Measurement Technology Conference*, vol. 2, pp. 1394–1398 Vol.2, May 2004.

[168] M. Paolone, A. Borghetti, and C. A. Nucci, "An automatic system to locate phase-to-ground faults in medium voltage cable networks based on the wavelet analysis of high-frequency signals," in *2011 IEEE Trondheim PowerTech*, pp. 1–7, June 2011.

[169] R. Razzaghi, M. Paolone, F. Rachidi, J. Descloux, B. Raison, and N. Retiere, "Fault location in multi-terminal hvdc networks based on electromagnetic time reversal with limited time reversal window," in *Power Systems Computation Conference (PSCC)*, June 2014.

[170] Z. Wang, R. Razzaghi, M. Paolone, and F. Rachidi, "Electromagnetic time reversal applied to fault location: on the properties of back-injected signals," in *2018 Power Systems Computation Conference (PSCC)*, pp. 1–7, June 2018.

[171] Z. Chen, Z. Wang, M. Paolone, and F. Rachidi, "Properties of direct-time and reversed-time transfer functions to locate disturbances along power transmission lines," in *2019 IEEE Milan PowerTech*, pp. 1–6, June 2019.

[172] J. G. Proakis and D. G. Manolakis, *Digital Signal Processing: Principles, Algorithms, and Applications.* Pearson Prentice Hall, 2007.

[173] Z. Wang, H. R. Karami, A. Lowenstein, S. Rahimi, P. Dehkhoda, R. Razzaghi, M. Paolone, M. Rubinstein, and F. Rachidi, "Time reversal focusing property in mismatched media," in *American Electromagnetics Conference 2018 (AMEREM 2018)*, pp. 1–7, Aug. 2018.

[174] J. L. Krolik, "Matched-field minimum variance beamforming in a random ocean channel," *Journal of the Acoustical Society of America*, vol. 92, pp. 1408–1419, Sept. 1992.

[175] J. L. Krolik, "The performance of matched-field beamformers with mediterranean vertical array data," *IEEE Transactions on Signal Processing*, vol. 44, pp. 2605–2611, Oct. 1996.

[176] J. de Rosny, A. Tourin, A. Derode, B. van Tiggelen, and M. Fink, "Relation between time reversal focusing and coherent backscattering in multiple scattering media: A diagrammatic approach," *Physical Review E*, vol. 70, p. 046601, Oct. 2004.

[177] G. Bal and R. Verástegui, "Time reversal in changing environments," *Multiscale Modeling & Simulation*, vol. 2, no. 4, pp. 639–661, 2004.

[178] D. Liu, S. Vasudevan, J. Krolik, G. Bal, and L. Carin, "Electromagnetic time-reversal source localization in changing media: Experiment and analysis," *IEEE Transactions on Antennas and Propagation*, vol. 55, pp. 344–354, Feb. 2007.

[179] D. R. Jackson and D. R. Dowling, "Phase conjugation in underwater acoustics," *Journal of the Acoustical Society of America*, vol. 89, pp. 171–181, Jan. 1991.

[180] A. Ishimaru, *Wave Propagation and Scattering in Random Media*. Wiley, 1999.

[181] A. Basilevsky, *Statistical Factor Analysis and Related Methods: Theory and Applications*. Wiley Series in Probability and Statistics, Wiley, 2009.

Curriculum Vitae

Zhaoyang Wang

Nationality: China
Date of birth: 05. 07. 1988
Email: zhaoyang.wang@epfl.ch
Address: EPFL-SCI-STI-FR, Station 11, CH-1015 Lausanne

Education

École Polytechnique Fédérale de Lausanne, EPFL   *Oct. 2015 - present*
Lausanne, Switzerland
Ph.D. in Electrical Engineering

• Thesis title: *Electromagnetic Time Reversal: Theory, Application to Fault Location in Power Networks and Experimental Validation*

Xi'an Jiaotong University, XJTU   *Sept. 2012 - June. 2015*
Xi'an, China
M.Sc. in Electrical Engineering

• Thesis title: *Study on Directional Radiation Technology of Electromagnetic Pulse Based on Marx Generator and TEM Antenna*

Professional Experience

Doctoral assistant   *Oct. 2015 - present*

Electromagnetic Compatibility Laboratory, EMC-EPFL
Lausanne, Switzerland

Distributed Electrical Systems Laboratory, DESL-EPFL
Lausanne, Switzerland

Research Interests

- Electromagnetic transients in power systems
- Electromagnetic time reversal
- Power system fault location
- Power system protection

Awards

1. ***Best Student Paper Award*** in 2017 Asian Electromagnetics Conference, ASIAEM, July 2017

   Z. Wang, S. He, Q. Li, B. Liu, R. Razzaghi, M. Paolone, Y. Xie, M. Rubinstein, and F. Rachidi, "A full-scale experimental test of electromagnetic time reversal applied to locate faults in Power Lines."

2. ***2018 Richard B. Shultz Best Transaction Paper Award of***
   IEEE Transactions on Electromagnetic Compatibility

   Z. Wang, S. He, Q. Li, B. Liu, R. Razzaghi, M. Paolone, Y. Xie, M. Rubinstein, and F. Rachidi, "A full-scale experimental validation of electromagnetic time reversal applied to locate disturbances in overhead power distribution lines," *IEEE Transactions on Electromagnetic Compatibility*, vol. 60, pp. 1562–1570, Oct. 2018

Scientific Publications

Journal papers

1. A. Codino*, **Z. Wang***, R. Razzaghi, M. Paolone, and F. Rachidi, "An alternative method for locating faults in transmission line networks based on time reversal," *IEEE Transactions on Electromagnetic Compatibility*, vol. 59, pp. 1601–1612, Oct. 2017

   (* The first two authors contributed equally to this research work.)

2. **Z. Wang**, S. He, Q. Li, B. Liu, R. Razzaghi, M. Paolone, Y. Xie, M. Rubinstein, and F. Rachidi, "A full-scale experimental validation of electromagnetic time reversal applied to locate disturbances in overhead power distribution lines," *IEEE Transactions on Electromagnetic Compatibility*, vol. 60, pp. 1562–1570, Oct. 2018

3. S. He, Y. Xie, **Z. Wang**, F. Rachidi, B. Liu, Q. Li, and X. Kong, "Norm criteria in the electromagnetic time reversal technique for fault location in transmission lines," *IEEE Transactions on Electromagnetic Compatibility*, vol. 60, pp. 1240–1248, Oct. 2018

4. **Z. Wang**, R. Razzaghi, M. Paolone, and F. Rachidi, "Electromagnetic time reversal similarity characteristics and its application to locating faults in power networks," *IEEE Transactions on Power Delivery*, DOI: 10.1109/TPWRD.2019.2952207, 2019

5. **Z. Wang**, R. Razzaghi, M. Paolone, and F. Rachidi, "Time reversal applied to fault location in power networks: pilot test results and analyses," *International Journal of Electrical Power and Energy Systems*, vol. 114, p. 105382, 2020

6. **Z. Wang**, F. Rachidi, M. Paolone, M. Rubinstein, and R. Razzaghi, "A closed time-reversal cavity for electromagnetic waves in transmission line networks," *IEEE Transactions on Antennas and Propagation*, accepted, 2020

7. M. Azadifar, H. Karami, **Z. Wang**, M. Rubinstein, F. Rachidi, H. Karami, A. Ghassemi and G. B. Gharehpetian, "Partial discharge localization using electromagnetic time reversal: a performance analysis," *IEEE Access*, DOI: 10.1109/ISCAS.1989.100818, 2020

Journal papers under revision

8. Q. Li, **Z. Wang**, Y. Xie, and F. Rachidi, "A novel correlation criterion based on electromagnetic time reversal technique to locate transient radiation source in reflection environment."

9. **Z. Wang**, Z. Chen, M. Paolone, and F. Rachidi, "Mirrored minimum properties of electromagnetic time reversal in mismatched media applied to locate faults along transmission lines."

Conference proceedings

10. **Z. Wang**, S. He, Q. Li, B. Liu, R. Razzaghi, M. Paolone, Y. Xie, M. Rubinstein, and F. Rachidi, "A full-scale experimental test of electromagnetic time reversal applied to locate faults in power lines," in *2017 Asian Electromagnetics Conference*, ASIAEM, pp. 1–5, July 2017

11. **Z. Wang**, A. Codino, R. Razzaghi, M. Paolone, and F. Rachidi, "Using electromagnetic time reversal to locate faults in transmission lines: definition and application of the 'mirrored minimum energy' property," in *2017 International Symposium on Electromagnetic Compatibility*, EMC EUROPE, pp. 1–6, Sept. 2017

12. **Z. Wang**, R. Razzaghi, M. Paolone, and F. Rachidi, "Electromagnetic time reversal applied to fault location: on the properties of back-injected signals," in *2018 Power Systems Computation Conference*, PSCC, pp. 1–7, June 2018

13. **Z. Wang**, H. Karami, A. Lowenstein, S. Rahimi, P. Dehkhoda, R. Razzaghi, M. Paolone, M. Rubinstein, and F. Rachidi, "Time reversal focusing property in mismatched media," in *2018 American Electromagnetics Conference*, AMEREM, pp. 1–7, Aug. 2018

14. Z. Chen, **Z. Wang**, M. Paolone, and F. Rachidi, "Properties of direct-time and reversed-time transfer functions to locate disturbances along power transmission lines," in *2019 IEEE PowerTech*, pp. 1–6, June 2019

15. **Z. Wang**, F. Gerini, M. Paolone, C. A. Nucci, and F. Rachidi, "Using electromagnetic time reversal similarity metric to locate lightning-originated flashovers on overhead transmission lines," in *2019 International Symposium on Lightning Protection*, XV SIPDA, pp. 1–6, Sept. 2019

16. H. Karami, A. Mostajabi, M. Azadifar, **Z. Wang**, M. Rubinstein, and F. Rachidi, "Locating lightning using electromagnetic time reversal: application of the minimum entropy criterion," in *2019 International Symposium on Lightning Protection*, XV SIPDA, pp. 1–4, Sept. 2019

Presentations at conferences

Poster presentations

1. **Z. Wang**, R. Razzaghi, F. Rachidi, M. Paolone, F. Richoz, Y. Fritsche, J. B. Frain, and J. Zahnbrecher, "Experimental validation of the electromagnetic time reversal based fault location technique," in *2017 SCCER-FURIES Annual Conference*, Nov. 2017

Oral presentations

2. **Z. Wang**, R. Razzaghi, M. Paolone, F. Rachidi, M. Rubinstein, S. He, Q. Li, B. Liu, Y. Xie, A. Codino, J.B. Frain, F. Richoz, and Y. Fritsche, "Time reversal applied to fault location: a summary of experimental validations," in *2018 American Electromagnetics Conference*, AMEREM, Aug. 2018

3. N. Mora, **Z. Wang**, C. Romero, M. Nyffeler, and F. Rachidi, "Study of the electromagnetic protection of infrastructures with alternative shielding strategies," in *2019 Asian Electromagnetics Conference*, ASIAEM, Sept. 2019

4. **Z. Wang**, N. Mora, C. Romero, M. Nyffeler, and F. Rachidi, "Effect of penetrating conductors on shielding effectiveness of metallic enclosures," in *2019 Asian Electromagnetics Conference*, ASIAEM, Sept. 2019

Teaching Experience (Teaching Assistant)

1. *Circuits and Systems* course, B.Sc. in Electrical Engineering, EPFL
2. *Electromagnetic Compatibility* course, M.Sc. in Electrical Engineering, EPFL
2. *Wave Propagation along Transmission Lines* course, M.Sc. in Electrical Engineering, EPFL

Supervised Student Projects

Master thesis

1. K. Ameer, "Analysis of the effect of uncertainties on the performance of electromagnetic time reversal fault location," Summer 2017-2018
2. F. Gerini, "Locating lightning strikes and flashovers in power networks using electromagnetic time reversal based correlation (similarity) property," Winter 2018-2019

Master semester project

1. A. Lowenstein, "Electromagnetic time reversal applied to fault detection in power networks," Winter 2016-2017
2. Z. Zhen, "Electromagnetic time reversal in changing media based fault location methods extended to multi-conductor power networks," Summer 2017-2018
3. Z. Zhen, "Applying DORT-based methods to locate electrical faults in multi-terminal inhomogeneous power networks," Winter 2017-2018
4. C. Bourion, "Reciprocity property and its application in electromagnetic time reversal based fault location methods," Winter 2017-2018
5. D. F. Guillaume, "DORT-based method applied to locating resistive electrical faults," Winter 2018-2019

Peer Reviews

- IEEE Transactions on Electromagnetic Compatibility, since 2018
- International Journal of Electrical Power and Energy Systems, since 2019
- IEEE Sensors Journal, since 2019
- IEEE Transactions on Power Delivery, since 2019
- IET Generation, Transmission & Distribution, since 2020